THE UNIVERSITY OF CHICAGO

MEASUREMENT OF INCLUSIVE JET AND DIJET PRODUCTION USING THE ATLAS DETECTOR

A DISSERTATION SUBMITTED TO
THE FACULTY OF THE DIVISION OF THE PHYSICAL SCIENCES
IN CANDIDACY FOR THE DEGREE OF
DOCTOR OF PHILOSOPHY

DEPARTMENT OF PHYSICS

BY
ERIC J. FENG

CHICAGO, ILLINOIS
JUNE 2012

For my parents, whose sacrifices let me chase my dreams

"Twenty years from now, you will be more disappointed by the things you didn't do than by the ones you did do. So throw off the bowlines. Sail away from the safe harbor. Catch the trade winds in your sails. Explore. Dream. Discover."

— Mark Twain

TABLE OF CONTENTS

List of Figures x

List of Tables xviii

Acknowledgments xx

Abstract xxiii

Preface xxiv

Chapter

1 Introduction **1**
- 1.1 Overview 1
- 1.2 Thesis Outline 3
- 1.3 Standard Model 4
- 1.4 Quantum Chromodynamics 9
  - 1.4.1 Quantum Field Theory of the Strong Interaction 9
  - 1.4.2 Hard Scattering 12
  - 1.4.3 Parton Shower 14
  - 1.4.4 Matching the Matrix Element and Parton Shower 16
  - 1.4.5 Hadronization 17
  - 1.4.6 Parton Distribution Functions 17
  - 1.4.7 Underlying Event 18
  - 1.4.8 Jet Definition 19

2 Large Hadron Collider **23**
- 2.1 Overview 23
- 2.2 Accelerator Complex 24
- 2.3 Luminosity 26

3 The ATLAS Detector 28
3.1 Overview . . . 28
3.2 Coordinate System . . . 32
3.3 Inner Detector . . . 32
3.3.1 Overview and Performance . . . 32
3.3.2 Solenoid . . . 35
3.3.3 Pixel Detector . . . 36
3.3.4 Semiconductor Tracker . . . 37
3.3.5 Transition Radiation Tracker . . . 38
3.4 Calorimeters . . . 39
3.4.1 Overview and Performance . . . 39
3.4.2 Electromagnetic Calorimeter . . . 44
3.4.3 Hadronic Calorimeters . . . 47
3.4.4 Forward Calorimeter . . . 51
3.5 Muon Spectrometer . . . 52
3.5.1 Overview and Performance . . . 52
3.5.2 Toroids . . . 55
3.5.3 Precision Chambers . . . 56
3.5.4 Trigger Chambers . . . 57
3.6 Forward Detectors . . . 58
3.6.1 Minimum Bias Trigger Scintillators . . . 58
3.6.2 Beam Condition Monitors . . . 59
3.6.3 Luminosity Cerenkov Integrating Detector . . . 60
3.7 Trigger and Data Acquisition . . . 60
3.7.1 Level-1 Trigger . . . 61
3.7.2 Level-2 Trigger . . . 62
3.7.3 Event Filter . . . 62
3.7.4 Data Acquisition . . . 63
3.8 Detector Conditions and Data Quality . . . 64
3.9 Detector Simulation . . . 66

4 Monte Carlo Simulations and Theory Predictions 67
4.1 Overview . . . 67
4.2 Leading Order Monte Carlo Simulations . . . 68
4.2.1 Detector Corrections and Systematic Uncertainties . . . 68
4.2.2 Non-perturbative Corrections . . . 69
4.3 Next-to-leading Order Theory Predictions . . . 71
4.3.1 NLO Fixed-order Predictions . . . 71
4.3.2 NLO Monte Carlo Simulations . . . 75

5 Jet Reconstruction and Calibration 77
5.1 Jet Reconstruction . . . 77
5.2 Jet Calibration . . . 78
  5.2.1 Pile-up Correction . . . 79
  5.2.2 Origin Correction . . . 80
  5.2.3 Energy Correction . . . 81
  5.2.4 Position Correction . . . 81
  5.2.5 Jet Energy Scale and Resolution . . . 82
  5.2.6 Jet Angular Bias and Resolution . . . 83
5.3 Missing Transverse Momentum . . . 84

6 Data Analysis and Detector Corrections 88
6.1 Observables Measured . . . 88
6.2 Data Sample . . . 89
  6.2.1 Data Quality . . . 91
  6.2.2 Primary Vertex . . . 92
  6.2.3 Trigger . . . 92
6.3 Jet Selection . . . 95
  6.3.1 Acceptance . . . 95
  6.3.2 Jet Quality . . . 96
6.4 Backgrounds . . . 98
  6.4.1 Non-collision Backgrounds . . . 98
  6.4.2 Pile-up . . . 99
  6.4.3 Physics Backgrounds . . . 99
6.5 Luminosity . . . 99
  6.5.1 Overview . . . 99
  6.5.2 Absolute Calibration . . . 99
  6.5.3 Results . . . 102
6.6 Correction for Detector Effects . . . 103
  6.6.1 Unfolding . . . 103
  6.6.2 Iterative Dynamically Stabilized Technique . . . 103

7 Systematic Uncertainties 106
7.1 Overview . . . 106
7.2 Primary Vertex Position . . . 106
7.3 Trigger Efficiency . . . 107
7.4 Jet Reconstruction Efficiency . . . 107
7.5 Jet Selection Efficiency . . . 108
7.6 Jet Energy Scale . . . 108
7.6.1 Overview . . . 108
7.6.2 Calorimeter Response . . . 109
7.6.3 Detector Simulation . . . 113
7.6.4 η Intercalibration . . . 114
7.6.5 Pile-up . . . 116
7.6.6 Non-closure of the Calibration . . . 119
7.6.7 Summary . . . 119
7.7 In-situ Validation of JES . . . 119
7.7.1 Transverse Momentum Balance of Calorimeter Jets vs. Tracks . . . 122
7.7.2 Photon-jet Transverse Momentum Balance . . . 125
7.7.3 Multijet Transverse Momentum Balance . . . 129
7.7.4 Summary . . . 133
7.8 Jet Energy Resolution . . . 134
7.8.1 Techniques . . . 134
7.8.2 Event Selection . . . 137
7.8.3 Systematic Uncertainties . . . 137
7.8.4 Results . . . 138
7.9 Unfolding . . . 138
7.9.1 Data-driven Closure Test . . . 138
7.9.2 Cross-check with Bin-by-bin Method . . . 140
7.9.3 Cross-check with Jet Shapes . . . 140
7.10 Uncertainty Propagation . . . 141
7.11 Magnitude of Systematic Uncertainties . . . 143
7.12 Luminosity . . . 148
7.13 Systematic Correlations . . . 152

8 Results 156
8.1 Inclusive Jet Cross Sections . . . 156
8.2 Dijet Cross Sections . . . 170

9 Conclusions 182

Appendix

A Displays of Interesting Events 185

B Tables 190
B.1 Inclusive Jet Tables . . . 190
B.2 Dijet Tables . . . 205

References 224

LIST OF FIGURES

1.1 Kinematic reach of the inclusive jet cross section measured in this analysis compared to that of the previous study. 3
1.2 The quarks, leptons, and gauge bosons comprising the particles in the Standard Model. 5
1.3 Cross sections for different physics processes as a function of center-of-mass energy. 8
1.4 The strong coupling constant, α_{S}, as a function of the scale, Q, at which it is probed. 11
1.5 Leading-order ($2 \to 2$) Feynman diagrams for jet production in proton-proton scattering at the LHC. 13
1.6 Two types of NLO Feynman diagrams for jet production. 13
1.7 Leading-order ($1 \to 2$) Feynman diagrams for the splitting of quarks and gluons. 15
1.8 Projections on the $y - \phi$ plane of jets reconstructed from partons in a HERWIG event, using four different jet algorithms. 22

2.1 Schematic diagram of the CERN accelerator complex, which consists of the LINAC 2, PSB (BOOSTER), PS, SPS, and LHC accelerators. . . . 25

3.1 Illustration of the ATLAS detector showing the subsystems of the inner detector, calorimeters, and muon spectrometer, as well as the magnet systems. 29
3.2 Interactions of different types of particles in the various detector subsystems. 30
3.3 Illustration of the subsystems of the inner detector: the pixel detector, semiconductor tracker, and transition radiation tracker. 33
3.4 Illustration with a radial view of the barrel portions of the detectors that constitute the inner detector. 34
3.5 Illustration of the calorimeters: the barrel and endcap electromagnetic calorimeters, the barrel (tile) and endcap hadronic calorimeters, and the forward calorimeter. 40
3.6 Accordion absorbers and electrodes in the barrel of the electromagnetic calorimeter. 46
3.7 Predicted and measured pulse shapes for a signal deposited by a cosmic ray muon in the second layer of the barrel portion of the electromagnetic calorimeter. 47

3.8 Material in units of nuclear interaction lengths in each layer of the barrel (Tile), endcap (HEC), and forward (FCal) hadronic calorimeters, as well as in the electromagnetic (EM) calorimeter, as a function of pseudorapidity. 49
3.9 Illustration of the tile calorimeter structure showing the staggered steel absorber plates and scintillators. 50
3.10 Cut-away drawing of an FCal electrode (a). A close-up view of the cross-section of the electrode gap in FCal1, the first layer of the FCal, is also shown (b). 53
3.11 Illustration of the subsystems of the muon spectrometer: the monitored drift tubes, thin gap chambers, resistive plate chambers, and cathode strip chambers. 54
3.12 Illustration of 16 plastic scintillation counters forming one of the two MBTS disks on each side of the detector. 59
3.13 Flow chart of the online event selection in the trigger and data acquisition system. 61
3.14 Data-taking efficiency in 2010. 64

4.1 Non-perturbative correction factors, $c = \sigma_{\text{Had, UE on}}/\sigma_{\text{Parton, UE off}}$, for inclusive jets identified using the anti-k_t algorithm. 71
4.2 Values of the renormalization and factorization scales used for the dijet predictions obtained using NLOJET++, as a function of y^*, half the rapidity separation between the two leading jets. 74

5.1 Offset in energy at the EM scale due to pile-up, shown for calorimeter towers (a) and jets (b) as a function of pseudorapidity in bins of the number of reconstructed primary vertices. 80
5.2 Average jet energy scale correction obtained from the Monte Carlo simulation, shown as a function of the calibrated transverse momentum of anti-k_t jets with $R = 0.6$ in three representative η regions. 82
5.3 Average simulated jet response at the electromagnetic scale as a function of pseudorapidity, shown for different bins of the jet energy calibrated using the EM+JES scheme. 83
5.4 Difference between the calorimeter jet pseudorapidity, calculated after a correction has been applied to account for the origin of the jet, and the true jet pseudorapidity. 84
5.5 The fractional p_{T} response (a) and resolution (b) as a function of the p_{T} of anti-k_t truth jets with $R = 0.6$. 85
5.6 The absolute bias (a) and resolution (b) in jet y as a function of the p_{T} of anti-k_t truth jets with $R = 0.6$ in each of the seven rapidity bins used in the measurement. 86

5.7 The absolute bias (a) and resolution (b) in jet ϕ as a function of the p_{T} of anti-k_t truth jets with $R = 0.6$ in each of the seven rapidity bins used in the measurement. 87

6.1 Peak instantaneous luminosity per day delivered by the LHC to ATLAS as a function of time during stable beam operation (a). Cumulative integrated luminosity delivered by the LHC and collected by the ATLAS detector as a function of time (b). 90
6.2 The average number of pp interactions per beam crossing at the start of an LHC fill as a function of time. 91
6.3 Combined L1+L2 jet trigger efficiency as a function of reconstructed jet p_{T} for anti-k_t jets with $R = 0.6$ in the central region $|y| < 0.3$ (a) and the barrel-endcap transition region $1.2 \leq |y| < 2.1$ (b). 93
6.4 Efficiencies for the central and forward jet triggers with a L1 E_{T} threshold of 10 GeV, and for their logical OR, as a function of the rapidity y of the reconstructed jet in the transition region between the two trigger systems. 94
6.5 Inclusive jet p_{T} distribution for anti-k_t jets with $R = 0.4$ after successive cleaning criteria are applied. 97
6.6 Efficiency ϵ for passing the jet quality selection as a function of p_{T} for anti-k_t jets with $R = 0.6$ in the rapidity region $|y| < 0.3$. 98
6.7 Specific interaction rate versus nominal beam separation for the LUCID_EventOR algorithm during van der Meer scan IV in the x plane. . . 101

7.1 Mean E/p response as a function of the track momentum for tracks with $0.6 < |\eta| < 1.1$. 110
7.2 Ratio of the calorimeter response, determined from in-situ and test beam response measurements, with respect to the calorimeter jet response predicted by the Monte Carlo simulation. 112
7.3 Average jet response for anti-k_t jets with $R = 0.6$ measured relative to a central reference jet within $|\eta| < 0.8$ using collision data and various Monte Carlo simulations. 117
7.4 Fractional uncertainty in the jet energy scale due to pile-up, shown for anti-k_t jets with $R = 0.6$ for events containing two measured primary vertices, $N_{\mathrm{PV}} = 2$. 118
7.5 Fractional uncertainty in the jet energy scale as a function of the transverse momentum of jets in the region $0.3 \leq |\eta| < 0.8$ in the calorimeter barrel. 120
7.6 Fractional uncertainty in the jet energy scale as a function of the transverse momentum of jets in the region $2.1 \leq |\eta| < 2.8$ in the calorimeter endcap (a) and in the forward region $3.6 \leq |\eta| < 4.5$ (b). 121

7.7 The average charged-to-total momentum ratio, $\langle r_{\mathrm{trk}} \rangle$, obtained using collision data and the Monte Carlo simulation, shown as a function of the transverse momentum of anti-k_t jets with $R = 0.6$ that are in the region $|\eta| < 1.2$ and that have been calibrated using the EM+JES scheme. . . . 124
7.8 Double ratio of the mean track to calorimeter response ratio in data and Monte Carlo simulation, $R_{r_{\mathrm{trk}}} = [r_{\mathrm{trk}}]_{\mathrm{Data}}/[r_{\mathrm{trk}}]_{\mathrm{MC}}$. 125
7.9 Average jet response as determined by the direct p_{T} balance technique for anti-k_t jets with $R = 0.6$ calibrated with the EM+JES scheme as a function of the photon transverse momentum for both data and Monte Carlo simulation. 129
7.10 Ratio of the jet response in data and Monte Carlo simulation using the direct p_{T} balance technique (a) and the MPF method (b) as a function of the photon transverse momentum. 130
7.11 Multijet balance MJB as a function of the recoil system p_{T} for data and Monte Carlo simulation for anti-k_t jets with $R = 0.6$. 132
7.12 Ratio of data to Monte Carlo simulation for the multijet balance (MJB) as a function of the recoil system p_{T} for anti-k_t jets with $R = 0.6$. 133
7.13 Double-ratio of the jet response in data and the Monte Carlo simulation obtained using several in-situ techniques, shown as a function of the transverse momentum of anti-k_t jets with $R = 0.6$ in the region $|\eta| < 1.2$. 135
7.14 Schematic diagram defining the variables used in the bisector technique. . 136
7.15 Jet energy resolution determined using the dijet balance and bisector techniques as a function of the jet transverse momentum of anti-k_t jets with $R = 0.6$ that have been calibrated using the EM+JES scheme. . . . 139
7.16 The jet shape $\rho(r) = \frac{1}{\Delta r}\frac{p_{\mathrm{T}}^{r}}{p_{\mathrm{T}}^{R}}$, where p_{T}^{R} is the transverse momentum within a radius R of the jet axis, and p_{T}^{r} is the transverse momentum contained within a ring of thickness $\Delta r = 0.1$ at a mean radius $r = \sqrt{(\Delta y)^2 + (\Delta\phi)^2}$ from the jet axis. 142
7.17 The magnitude (a) and correlation between p_{T}-bins (b) of the total systematic uncertainty on the inclusive jet cross section measurement for anti-k_t jets with $R = 0.6$ in the bin $|y| < 0.3$. 145
7.18 The magnitude (left) and correlation between p_{T}-bins (right) of the total systematic uncertainty on the inclusive jet cross section measurement for anti-k_t jets with $R = 0.6$ in the bin $2.1 < |y| < 2.8$. 146
7.19 The magnitude (left) and correlation between p_{T}-bins (right) of the total systematic uncertainty on the inclusive jet cross section measurement for anti-k_t jets with $R = 0.6$ in the bin $3.6 < |y| < 4.4$. 147
7.20 Deviation of each set of van der Meer scans from the combined average (a). Residuals of the σ_{vis} ratios between algorithms for each van der Meer scan as a relative deviation from the mean ratio based on $\overline{\sigma}_{\mathrm{vis}}$ (b). 149

7.21 Fractional deviation in the average value of μ obtained using different algorithms with respect to the LUCID_EventOR value as a function of time. 151

8.1 Inclusive jet double-differential cross section as a function of jet p_{T} in different regions of $|y|$ for jets identified using the anti-k_t algorithm with $R = 0.4$. 157
8.2 Inclusive jet double-differential cross section as a function of jet p_{T} in different regions of $|y|$ for jets identified using the anti-k_t algorithm with $R = 0.6$. 158
8.3 Ratio of inclusive jet cross section to the theoretical prediction obtained using NLOJET++ with the CT10 PDF set. The current result is compared to that published in Ref. [21]. 159
8.4 Ratios of inclusive jet double-differential cross section to the theoretical prediction obtained using NLOJET++ with the CT10 PDF set. The ratios are shown as a function of jet p_{T} in central regions of $|y|$ for jets identified using the anti-k_t algorithm with $R = 0.4$. The theoretical error bands obtained by using NLOJET++ with different PDF sets (CT10, MSTW 2008, NNPDF 2.1, HERAPDF 1.5) are shown. 161
8.5 Ratios of inclusive jet double-differential cross section to the theoretical prediction obtained using NLOJET++ with the CT10 PDF set. The ratios are shown as a function of jet p_{T} in forward regions of $|y|$ for jets identified using the anti-k_t algorithm with $R = 0.4$. The theoretical error bands obtained by using NLOJET++ with different PDF sets (CT10, MSTW 2008, NNPDF 2.1, HERAPDF 1.5) are shown. 162
8.6 Ratios of inclusive jet double-differential cross section to the theoretical prediction obtained using NLOJET++ with the CT10 PDF set. The ratios are shown as a function of jet p_{T} in central regions of $|y|$ for jets identified using the anti-k_t algorithm with $R = 0.6$. The theoretical error bands obtained by using NLOJET++ with different PDF sets (CT10, MSTW 2008, NNPDF 2.1, HERAPDF 1.5) are shown. 163
8.7 Ratios of inclusive jet double-differential cross section to the theoretical prediction obtained using NLOJET++ with the CT10 PDF set. The ratios are shown as a function of jet p_{T} in forward regions of $|y|$ for jets identified using the anti-k_t algorithm with $R = 0.6$. The theoretical error bands obtained by using NLOJET++ with different PDF sets (CT10, MSTW 2008, NNPDF 2.1, HERAPDF 1.5) are shown. 164

8.8 Ratios of inclusive jet double-differential cross section to the theoretical prediction obtained using NLOJET++ with the CT10 PDF set. The ratios are shown as a function of jet p_{T} in central regions of $|y|$ for jets identified using the anti-k_t algorithm with $R = 0.4$. The ratios of POWHEG predictions showered using either PYTHIA or HERWIG to the NLOJET++ predictions corrected for non-perturbative effects are shown. 166
8.9 Ratios of inclusive jet double-differential cross section to the theoretical prediction obtained using NLOJET++ with the CT10 PDF set. The ratios are shown as a function of jet p_{T} in forward regions of $|y|$ for jets identified using the anti-k_t algorithm with $R = 0.4$. The ratios of POWHEG predictions showered using either PYTHIA or HERWIG to the NLOJET++ predictions corrected for non-perturbative effects are shown. 167
8.10 Ratios of inclusive jet double-differential cross section to the theoretical prediction obtained using NLOJET++ with the CT10 PDF set. The ratios are shown as a function of jet p_{T} in central regions of $|y|$ for jets identified using the anti-k_t algorithm with $R = 0.6$. The ratios of POWHEG predictions showered using either PYTHIA or HERWIG to the NLOJET++ predictions corrected for non-perturbative effects are shown. 168
8.11 Ratios of inclusive jet double-differential cross section to the theoretical prediction obtained using NLOJET++ with the CT10 PDF set. The ratios are shown as a function of jet p_{T} in forward regions of $|y|$ for jets identified using the anti-k_t algorithm with $R = 0.6$. The ratios of POWHEG predictions showered using either PYTHIA or HERWIG to the NLOJET++ predictions corrected for non-perturbative effects are shown. 169
8.12 Dijet double-differential cross section as a function of dijet mass, binned in half the rapidity separation between the two leading jets, $y^* = |y_1 - y_2|/2$. The results are shown for jets identified using the anti-k_t algorithm with $R = 0.4$. 171
8.13 Dijet double-differential cross section as a function of dijet mass, binned in half the rapidity separation between the two leading jets, $y^* = |y_1 - y_2|/2$. The results are shown for jets identified using the anti-k_t algorithm with $R = 0.6$. 172

8.14 Ratios of dijet double-differential cross section to the theoretical prediction obtained using NLOJET++ with the CT10 PDF set. The results are shown for jets identified using the anti-k_t algorithm with $R = 0.4$ that are in the region $y^* < 2.5$. The theoretical error bands obtained by using NLOJET++ with different PDF sets (CT10, MSTW 2008, NNPDF 2.1, HERAPDF 1.5) are shown. 173
8.15 Ratios of dijet double-differential cross section to the theoretical prediction obtained using NLOJET++ with the CT10 PDF set. The results are shown for jets identified using the anti-k_t algorithm with $R = 0.4$ that are in the region $2.5 \leq y^* < 4.4$. The theoretical error bands obtained by using NLOJET++ with different PDF sets (CT10, MSTW 2008, NNPDF 2.1, HERAPDF 1.5) are shown. 174
8.16 Ratios of dijet double-differential cross section to the theoretical prediction obtained using NLOJET++ with the CT10 PDF set. The results are shown for jets identified using the anti-k_t algorithm with $R = 0.6$ that are in the region $y^* < 2.5$. The theoretical error bands obtained by using NLOJET++ with different PDF sets (CT10, MSTW 2008, NNPDF 2.1, HERAPDF 1.5) are shown. 175
8.17 Ratios of dijet double-differential cross section to the theoretical prediction obtained using NLOJET++ with the CT10 PDF set. The results are shown for jets identified using the anti-k_t algorithm with $R = 0.6$ that are in the region $2.5 \leq y^* < 4.4$. The theoretical error bands obtained by using NLOJET++ with different PDF sets (CT10, MSTW 2008, NNPDF 2.1, HERAPDF 1.5) are shown. 176
8.18 Ratios of dijet double-differential cross section to the theoretical prediction obtained using NLOJET++ with the CT10 PDF set. The results are shown for jets identified using the anti-k_t algorithm with $R = 0.4$ that are in the region $y^* < 2.5$. The ratios of POWHEG predictions showered using either PYTHIA or HERWIG to the NLOJET++ predictions corrected for non-perturbative effects are shown. 178
8.19 Ratios of dijet double-differential cross section to the theoretical prediction obtained using NLOJET++ with the CT10 PDF set. The results are shown for jets identified using the anti-k_t algorithm with $R = 0.4$ that are in the region $2.5 \leq y^* < 4.4$. The ratios of POWHEG predictions showered using either PYTHIA or HERWIG to the NLOJET++ predictions corrected for non-perturbative effects are shown. 179

8.20 Ratios of dijet double-differential cross section to the theoretical prediction obtained using NLOJET++ with the CT10 PDF set. The results are shown for jets identified using the anti-k_t algorithm with $R = 0.6$ that are in the region $y^* < 2.5$. The ratios of POWHEG predictions showered using either PYTHIA or HERWIG to the NLOJET++ predictions corrected for non-perturbative effects are shown. 180
8.21 Ratios of dijet double-differential cross section to the theoretical prediction obtained using NLOJET++ with the CT10 PDF set. The results are shown for jets identified using the anti-k_t algorithm with $R = 0.6$ that are in the region $2.5 \leq y^* < 4.4$. The ratios of POWHEG predictions showered using either PYTHIA or HERWIG to the NLOJET++ predictions corrected for non-perturbative effects are shown. 181

A.1 Display of Run 167607, Event 63115223. This shows one of the highest-p_{T} jets collected during 2010, which has p_{T} of 1.5 TeV. 186
A.2 Display of Run 167607, Event 36526763. This shows one of the highest-energy jets collected during 2010, which is in the FCal and has an energy of 3.4 TeV. 187
A.3 Display of Run 167607, Event 40296085. This shows one of the highest-mass (3.1 TeV) central dijet events, with two leading jets within $|y| < 0.8$, that was collected during 2010. 188
A.4 Display of Run 167607, Event 9435121. This shows one of the highest-mass (4.0 TeV) forward dijet events, with two leading jets within $|y| < 2.8$, that was collected during 2010. 189

LIST OF TABLES

3.1 Luminosity-weighted relative fraction of good quality data delivered by the various ATLAS subsystems during LHC fills with stable beams in pp collisions at $\sqrt{s} = 7$ TeV, and after switching the tracking detectors on. . 65

5.1 Calorimeter regions used for jet calibration. 78

6.1 Best estimate of the visible cross section determined from van der Meer scan data. 103

7.1 The effect of the dominant systematic uncertainty sources on the inclusive jet cross section measurement, for representative p_{T} and y regions for anti-k_t jets with $R = 0.6$. 144
7.2 The effect of the dominant systematic uncertainty sources on the dijet cross section measurement, for representative m_{12} and y^* regions for anti-k_t jets with $R = 0.6$. 144
7.3 Description of bin-to-bin uncertainty correlations for the inclusive jet measurement. 153
7.4 Description of bin-to-bin uncertainty correlations for the dijet measurement. 154

B.1 Measured jet cross section for $R = 0.4$ and $|y| < 0.3$. 191
B.2 Measured jet cross section for $R = 0.4$ and $0.3 < |y| < 0.8$. 192
B.3 Measured jet cross section for $R = 0.4$ and $0.8 < |y| < 1.2$. 193
B.4 Measured jet cross section for $R = 0.4$ and $1.2 < |y| < 2.1$. 194
B.5 Measured jet cross section for $R = 0.4$ and $2.1 < |y| < 2.8$. 195
B.6 Measured jet cross section for $R = 0.4$ and $2.8 < |y| < 3.6$. 196
B.7 Measured jet cross section for $R = 0.4$ and $3.6 < |y| < 4.4$. 197
B.8 Measured jet cross section for $R = 0.6$ and $|y| < 0.3$. 198
B.9 Measured jet cross section for $R = 0.6$ and $0.3 < |y| < 0.8$. 199
B.10 Measured jet cross section for $R = 0.6$ and $0.8 < |y| < 1.2$. 200
B.11 Measured jet cross section for $R = 0.6$ and $1.2 < |y| < 2.1$. 201
B.12 Measured jet cross section for $R = 0.6$ and $2.1 < |y| < 2.8$. 202
B.13 Measured jet cross section for $R = 0.6$ and $2.8 < |y| < 3.6$. 203
B.14 Measured jet cross section for $R = 0.6$ and $3.6 < |y| < 4.4$. 204
B.15 Measured dijet cross section for $R = 0.4$ and $y^* < 0.5$. 206
B.16 Measured dijet cross section for $R = 0.4$ and $0.5 < y^* < 1.0$. 207
B.17 Measured dijet cross section for $R = 0.4$ and $1.0 < y^* < 1.5$. 208
B.18 Measured dijet cross section for $R = 0.4$ and $1.5 < y^* < 2.0$. 209

B.19 Measured dijet cross section for $R = 0.4$ and $2.0 < y^* < 2.5$. 210
B.20 Measured dijet cross section for $R = 0.4$ and $2.5 < y^* < 3.0$. 211
B.21 Measured dijet cross section for $R = 0.4$ and $3.0 < y^* < 3.5$. 212
B.22 Measured dijet cross section for $R = 0.4$ and $3.5 < y^* < 4.0$. 213
B.23 Measured dijet cross section for $R = 0.4$ and $4.0 < y^* < 4.4$. 214
B.24 Measured dijet cross section for $R = 0.6$ and $y^* < 0.5$. 215
B.25 Measured dijet cross section for $R = 0.6$ and $0.5 < y^* < 1.0$. 216
B.26 Measured dijet cross section for $R = 0.6$ and $1.0 < y^* < 1.5$. 217
B.27 Measured dijet cross section for $R = 0.6$ and $1.5 < y^* < 2.0$. 218
B.28 Measured dijet cross section for $R = 0.6$ and $2.0 < y^* < 2.5$. 219
B.29 Measured dijet cross section for $R = 0.6$ and $2.5 < y^* < 3.0$. 220
B.30 Measured dijet cross section for $R = 0.6$ and $3.0 < y^* < 3.5$. 221
B.31 Measured dijet cross section for $R = 0.6$ and $3.5 < y^* < 4.0$. 222
B.32 Measured dijet cross section for $R = 0.6$ and $4.0 < y^* < 4.4$. 223

ACKNOWLEDGMENTS

> *"I am mindful that scientific achievement is rooted in the past, is cultivated to full stature by many contemporaries and flourishes only in a favorable environment. No individual is alone responsible . . . ."*
>
> — Ernest Lawrence (Nobel Prize in Physics, 1939)

This doctoral work would not have been possible without the support of a great number of people. First and foremost among these is my advisor, Jim Pilcher. Jim taught me how to be a prudent scientist and stressed the importance of producing robust results. He instilled deeply in me the principle that a true experimentalist should be fluent in both detector hardware and data analysis. I'm grateful to Jim for trusting me to work independently, but also providing sound guidance whenever I needed it.

I spent two years taking and teaching classes at the University of Chicago. Sasha Paramonov, Lindsey Bleem, Paul Spyridis, Arun Thalapillil, Anton Kapliy, Tudor Costin, and others shared with me joys and sorrows in the challenging life of a physics graduate student. They supported me steadfastly whenever I felt down and celebrated with me when things went well.

During the course of my research, I worked with various graduate students, postdocs, and faculty in the Chicago ATLAS group. Imai Jen-La Plante was the first student I met, and we took classes and did research together. Erik Brubaker helped me navigate the maze of ATLAS software when I started. Giulio Usai was a quiet source of knowledge about the detector. Martina Hurwitz bequeathed her thesis topic on dijets to me when she switched to CDF. Monica Dunford and I worked together on the MBTS. Georgios Choudalakis shared his enthusiasm for data analysis and statistics. Chris Meyer was my protégé on jet measurements, which he will carry on for his thesis. Peter Onyisi, Antonio Boveia, and Joe Tuggle each provided a listening ear and sound advice. Mel Shochet, Kelby Anderson, Mark Oreglia, Frank Merritt, and Florencia Canelli helped and gave advice on my hardware work and physics analyses. Rob Gardner and Mary Heintz ensured that my computing experience was smooth. Nobuko McNeill and Aspasia Sotir-Plutis helped me deal with administrative issues.

I spent most of my graduate career based at CERN. Thanks to the LHC and the ATLAS Collaboration, I shared in the excitement of commissioning the ATLAS detector and analyzing the first LHC data. I'm grateful to Koji Terashi and Jon Butterworth, who invited me to join the Standard Model Jets group and help lead the jet cross section measurements. They and Mario Campanelli, Paolo Francavilla, Dag Gillberg, and Kerstin Perez served as co-editors with me on various conference notes and publications. Along with Tancredi Carli, Caterina Doglioni, Esteban Fullana, Bogdan Malaescu, Chris Meyer, Shima Shimizu, and Pavel Starovoitov, we all spent countless hours working to understand and solve myriad problems related to the experimental measurements and theory. Together we published the first jet cross sections measured at the LHC, and now those in this thesis, which are the best measurements to date.

The conveners of the Standard Model group, Kevin Einsweiler and Jon, provided prescient guidance and gave our analysis visibility in ATLAS meetings. The Editorial Board members – especially Sasha Glazov, the chair – patiently supplied constructive criticism. My thesis committee at Chicago – Jim, Mel, Carlos Wagner, and Sid Nagel – read and gave valuable feedback on this dissertation.

My office mates at CERN – Imai, Hyeonjin Kim, and Rishi Pravahan – always kept the office a friendly work environment. My friends back in the Bay Area, especially Gilbert Lip and Tina Zhang, welcomed me back whenever I went home as if I'd never left.

In my undergraduate research, the ATLAS group at Berkeley provided a nurturing environment where it was exciting to learn about particle detectors. This inspired me to pursue a Ph.D in high-energy physics, a decision I haven't regretted.

As a graduate student I was financially supported by the Robert Sachs Fellowship, Robert McCormick Fellowship, GAANN Fellowship, U.S. LHC Award, and the Gaurang & Kanwal Yodh Prize. I'm also grateful to Jim, Kevin, Tancredi, Mel, Fabiola Gianotti, and Rik Yoshida for supporting my postdoctoral fellowship applications.

During the last few years, I struggled with serious health problems. Many people, who are too many to list here, went out of their way to reach out with encouragement. I will never forget their amazing demonstrations of kindness.

Finally I would like to thank my family for always supporting me, particularly my parents. They provided me the opportunity to pursue a higher education that they never had, and this thesis is dedicated to them.

ABSTRACT

Inclusive jet and dijet cross sections have been measured in proton-proton collisions at a center-of-mass energy of 7 TeV using the ATLAS detector at the Large Hadron Collider. The cross sections are measured using jets clustered with the anti-k_t algorithm with parameters $R = 0.4$ and $R = 0.6$. These measurements are based on the 2010 data sample, consisting of a total integrated luminosity of 37 pb^{-1}. Inclusive jet double-differential cross sections are presented as a function of jet transverse momentum, in bins of jet rapidity. Dijet double-differential cross sections are studied as a function of the dijet invariant mass, in bins of half the rapidity separation of the two leading jets. The measurements are performed in the jet rapidity range $|y| < 4.4$, covering jet transverse momenta from 20 GeV to 1.5 TeV and dijet invariant masses from 70 GeV to 5 TeV, the highest ever measured. The data are compared to expectations based on next-to-leading order QCD calculations corrected for non-perturbative effects, as well as to next-to-leading order Monte Carlo predictions. The measurements test QCD in a new kinematic regime, providing sensitivity to new exotic phenomena that may exist and helping to determine parton distribution functions in a region where they are currently not well-constrained.

PREFACE

> *"My real education began when I entered the University of Chicago in September 1951 as a graduate student."*
>
> — James Cronin (Nobel Prize in Physics, 1980)

I started graduate work in physics at the University of Chicago in 2005. Since that time, my work on the ATLAS experiment has spanned detector hardware and software, detector performance, and physics analysis. My hardware experience is primarily based on work on the minimum bias trigger and the tile calorimeter. I have studied the detector performance using cosmic ray muons, tracks, and jets. My physics analyses have focused on final states with jets, involving both searches for new physical phenomena and cross section measurements. The latter are the subject of this thesis.

From 2005–2007, I worked on readout electronics for the minimum bias trigger scintillators [1]. With the collision data taken in 2009 and 2010, I calibrated them in-situ using their response to single charged particles in pp collision data at $\sqrt{s} = 900$ GeV [2] and 7 TeV [3, 4, 5]. During that time I also helped to commission the tile calorimeter using cosmic ray muons [6] and studied the calorimeter calibration with collision data [7].

In 2007 and 2008, I worked on computing infrastructure for monitoring and data preparation. I proposed and implemented the remote monitoring system, consisting of hardware and software infrastructure [8, 9]. I also helped to develop DESD, a new derived data format [10].

In 2008 and 2009, I worked on a series of jet performance studies. The first was a proposal to mitigate the effects of calorimeter defects through the use of track jets [11]. The second was a study of the performance of different jet algorithms [12]. The third was a proposal to calibrate jets using transverse momentum balance in γ+jet events [13]. The last study was later used in collision data at 7 TeV to validate the jet energy scale [14, 15].

In 2009 and 2010, I studied the sensitivity of searches for exotic new physics decaying to dijet final states [16]. I contributed to the first searches for dijet resonances [17] and contact interactions [18] using collision data at 7 TeV. I was also closely involved in the observation of jet quenching in lead ion collisions at $\sqrt{s_{NN}} = 2.76$ TeV [19].

From 2010–2012, I focused on jet cross section measurements using proton-proton collision data. Using the first 7 TeV data, I studied the jet reconstruction, calibration, and properties [7], as well as kinematic distributions of inclusive jet and dijet production [20]. Then I measured the inclusive jet and dijet cross sections using an early data sample [21, 22] and later with the full 2010 data sample [23, 24]. The latter is described in this dissertation.

To date this doctoral work has either directly produced or substantially contributed to five physics publications [17, 18, 19, 21, 23] and two publications on detector performance [3, 14]. This thesis focuses only on the latest inclusive jet and dijet cross section measurements, which have been submitted for publication [23]. The other work is described in the publications, conference notes, and internal notes cited above.

CHAPTER 1

INTRODUCTION

> *"Basic research is designed to increase our understanding of the nature of the universe in which we live. . . . Research is a venture, literally, into the unknown."*
>
> — Leon Lederman (Nobel Prize in Physics, 1988)

1.1 Overview

The Large Hadron Collider (LHC) in Geneva, Switzerland, collides protons together at the highest man-made energies in the world. At the LHC, the production of "jets" – collimated sprays of hadrons – through the strong interaction is the dominant high transverse-momentum (p_{T}) process. "Inclusive jet" and "dijet" production involve final states containing at least one or two jets, respectively. Jet cross sections serve as one of the main observables in high-energy particle physics, providing precise information on the structure of the proton. They are an important tool for understanding the strong interaction and searching for physics beyond the Standard Model [25, 26, 27, 28, 29, 30, 31, 32, 33, 34, 35, 36, 37, 38, 39, 40, 41, 42, 43, 44].

The ATLAS (A Toroidal LHC ApparatuS) experiment is one of two general-purpose high-energy physics experiments at the LHC. The ATLAS Collaboration has published a first measurement of inclusive jet and dijet production cross sections at $\sqrt{s} = 7$ TeV, using an integrated luminosity of 17 nb^{-1} [21]. This first measurement, which was performed during the course of this thesis work, only considered jets with transverse momentum larger than 60 GeV and in a rapidity interval $|y| < 2.8$.[1]

This thesis now extends the existing measurement using the full 2010 data sample of (37.3 ± 1.2) pb^{-1}, an integrated luminosity more than 2000 times larger than that of the previous study. This more than doubles the kinematic reach at high jet transverse momentum and large dijet invariant mass, exploring the shortest distances ever probed by man-made experiments. There are strong physics reasons to measure jets of lower transverse momentum and larger rapidity as well. Jets at lower p_{T} are more sensitive to effects in quantum chromodynamics (QCD), the theory of the strong interaction, that cannot be calculated using perturbation theory. In addition, forward jets may be sensitive to different dynamics in QCD than central jets. Moreover, LHC experiments have much wider rapidity coverage than those at the Fermilab Tevatron, so forward jet measurements at the LHC cover a region of phase space that has not been explored before.

The kinematic reach of this analysis is compared to that of the previous ATLAS study in Fig. 1.1. This data sample extends the existing inclusive jet p_{T} measurement from 700 GeV to 1.5 TeV and the existing dijet mass measurement from 1.8 TeV to 5 TeV. The results span approximately $7 \times 10^{-5} < x < 0.9$ in x, the fraction of the proton momentum carried by each of the partons involved in the hard interaction. Thus this analysis probes next-to-leading order (NLO) perturbative QCD (pQCD) and parton distribution functions (PDFs) in a large new kinematic regime of Q^2, the square of the momentum transfer, and x. The measurements are also sensitive to potential exotic phenomena that produce jet final states, including possible heavy resonances [17] and quark contact interactions [18].

---

[1] The coordinate system of the ATLAS detector is described in Sec. 3.2.

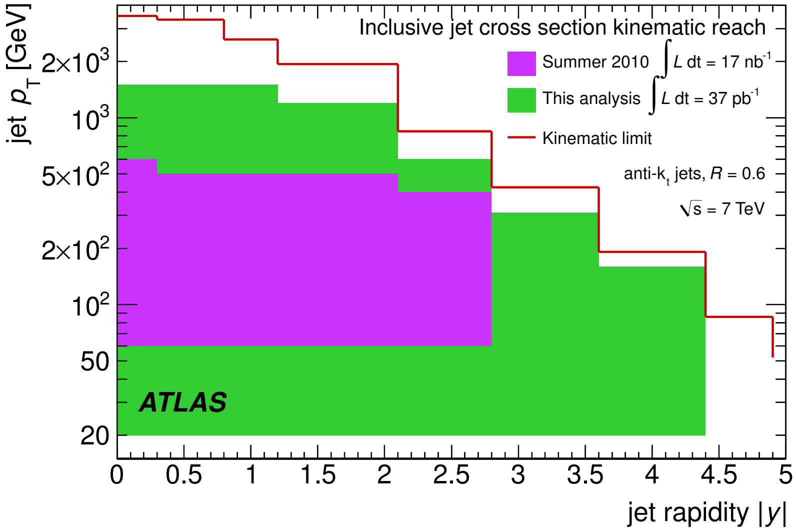

Figure 1.1: Kinematic reach of the inclusive jet cross section measured in this analysis compared to that of the previous study [21] for jets identified using the anti-k_t algorithm with $R = 0.6$. The kinematic limit for the center-of-mass energy of 7 TeV is also shown.

1.2 Thesis Outline

This thesis presents measurements of inclusive jet and dijet production at the LHC with the ATLAS detector. The analysis uses the full 2010 data sample of 37 pb^{-1} collected between April and November, 2010, and has been submitted for publication in Ref. [23]. Measurements using the first 17 nb^{-1} of data collected between April and June, 2010 were published in Ref. [21].

Chapter 1 provides an introduction to the Standard Model and QCD. Chapter 2 describes the LHC accelerator. Chapter 3 describes the ATLAS detector, with particular emphasis on the calorimeters used for these jet cross section measurements. Chapter 4 describes the theoretical predictions used for comparison with the experimental measurements, as well as their uncertainties. It also describes the Monte Carlo simulation used to correct for detector effects. Chapter 5 describes the reconstruction of physics objects, focusing on jet reconstruction and calibration which are critical for this analysis. Chapter 6 defines the experimental observables measured, namely the inclusive jet p_{T} and dijet mass double-differential cross sections. The data analysis and corrections for detector effects are also described. Chapter 7 discusses all systematic uncertainties that affect the measurements, with particular focus on the jet energy scale, the dominant source of uncertainty. The systematic correlations are also described. Chapter 8 presents the experimental results and compares them to a variety of theory predictions. Chapter 9 summarizes the measurements performed and briefly discusses the outlook.

1.3 Standard Model

The Standard Model, a relativistic quantum field theory, has been remarkably successful in describing almost all the known particles and interactions in physics. The strong, weak, and electromagnetic forces are described by the SU(3)×SU(2)×U(1) gauge groups. The generators of each gauge group, which are manifested as gauge bosons, mediate the interactions between the particles (quarks and leptons), which correspond to eigenvectors of the gauge groups. The respective eigenvalues are quantum numbers that characterize the coupling between the particles due to each interaction. The quantum numbers of the three gauge groups comprising the SM are termed color, weak isospin, and weak hypercharge, respectively. A quantum description of gravity remains an elusive goal that has not been achieved yet in the Standard Model.

The particles in the Standard Model are illustrated in Fig. 1.2. The fermions are grouped into three "generations" that are ordered by mass. There are six quarks (up, down, charm, strange, top, and bottom) and six leptons (electron, electron neutrino, muon, muon neutrino, tau, quark neutrino). The "up-type" quarks (up, charm, top) have

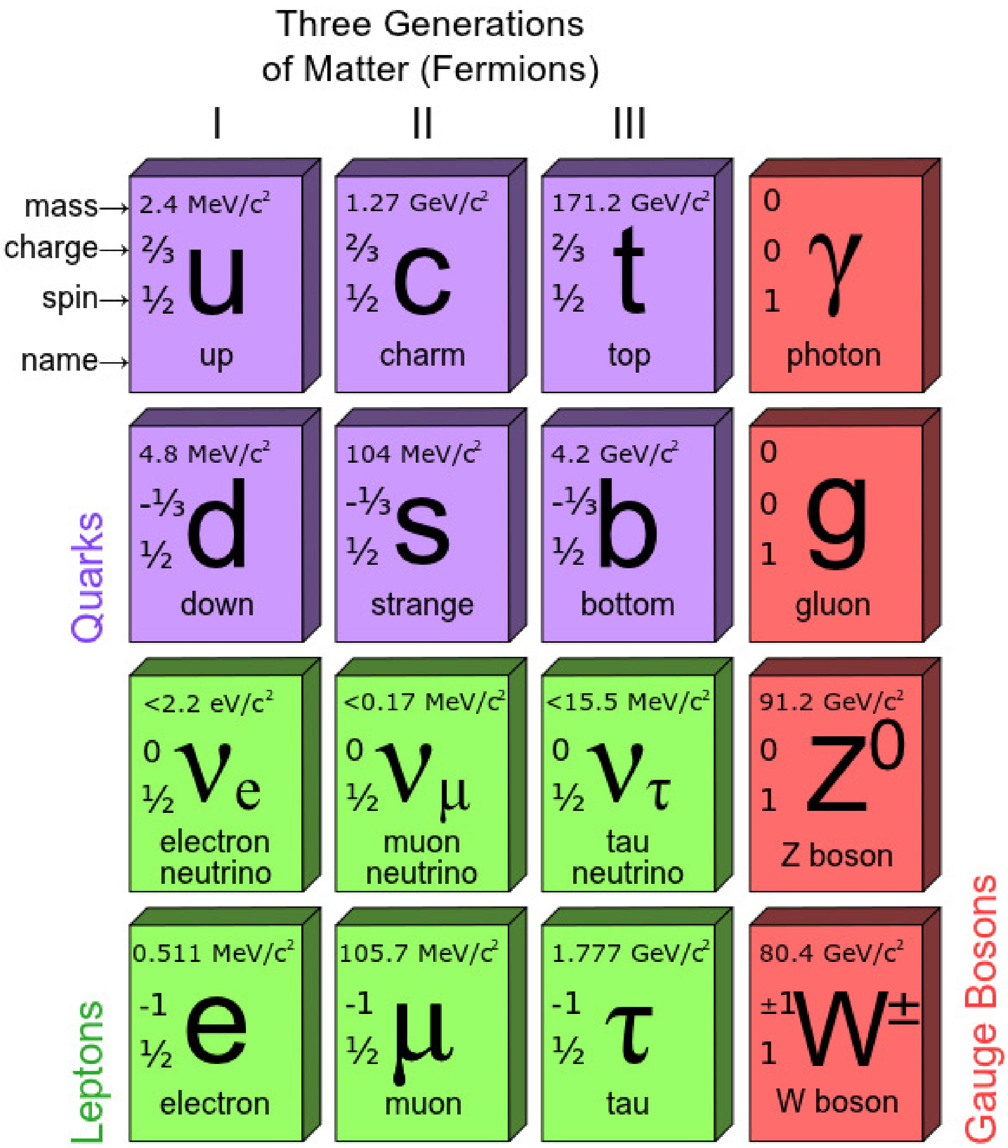

Figure 1.2: The quarks, leptons, and gauge bosons comprising the particles in the Standard Model [45]. The gauge bosons mediate the electromagnetic, strong, and weak forces.

charge of $+\frac{2}{3}e$, while the "down-type" quarks have charge of $-\frac{1}{3}e$. Each particle has an associated "anti-particle" with opposite quantum numbers to the particle.

At the very high temperatures in the early universe, all particles were massless. However below a critical temperature, the electroweak symmetry is broken spontaneously. This is believed to occur via the Higgs mechanism, where a scalar field called the Higgs field acquires a vacuum expectation value of 246 GeV. Particles acquire a mass by coupling to the Higgs boson, which has not been observed yet. A major goal of the ATLAS experiment is to discover the Higgs boson, if it exists, or otherwise to rule out its existence.

Leptons interact via the weak and electromagnetic forces, which are represented by the SU(2)×U(1) gauge group. The breaking of the symmetry of this gauge group produces the photon (γ), W, and Z gauge bosons as linear combinations of its generators. The photon is massless and carries the electromagnetic force. The W and Z bosons are massive and carry the weak force. Two W bosons are produced, one with positive charge and another with negative charge, while the Z boson is neutral.

Quarks couple to all force carriers, so they interact via the strong force (QCD) according to the $SU(3)$ group, as well as through weak and electromagnetic interactions. The conserved quantum number associated with QCD is "color", which may be red, blue, or green. The strong force is mediated by the gluon, which is neutral, massless, and contains both a color and anti-color charge. Its strength, as described through its coupling constant α_{S}, is large compared to that of the weak force, giving rise to their names.

The gravitational force, which is postulated to be mediated by a hypothetical particle called a "graviton", is not described in the Standard Model. Besides lacking a description of quantum gravity, the Standard Model has other limitations. It is viewed as an effective field theory that is valid at the lower energy scales where measurements have been performed, but which arises from a more fundamental theory at higher energy scales.

One of the main reasons for this is that the Standard Model does not contain a fundamental explanation for the particular values of its parameters. For example, some parameters related to the mass of the Higgs boson must be “finely” tuned to take certain values. There is also a “hierarchy problem”, in which the Higgs mass is expected to be at the energy scale where electroweak processes occur despite being subject to quantum corrections which are expected to be of the order of the Planck energy scale. It is therefore expected that a more fundamental theory exists beyond the TeV energy scale that explains these features. Other fundamental questions that remain to be answered regard the nature of dark matter, the unification of all the forces at higher energy scales, or the possible existence of additional spatial dimensions.

Any experimental search for the Higgs boson or other new interactions or particles that have not been observed requires a detailed understanding of QCD. An optimal observable to understand QCD is a “jet”, a collimated spray of hadrons that originates from partons (quarks or gluons) [46]. Since partons interact strongly, jet production is the dominant hard scattering process in the Standard Model. Figure 1.3 shows the production cross section for various processes as a function of the center-of-mass energy, $\sqrt{s}$, of an accelerator. The production cross section for energetic jets with $E_T > 100$ GeV (rising pink curve) at $\sqrt{s} = 7$ TeV, the center-of-mass energy of the LHC, is much larger than those for other processes (W and Z) involving leptons, which interact only through the electromagnetic and weak forces.

Because of their large cross sections, jet production provides an ideal avenue to probe QCD and parton distribution functions, which describe the distribution of the momenta of quarks and gluons within a proton [47]. Moreover, new models of physics where heavy particles decay into quark pairs may be observable as an unexpected increase in the rate of jet production compared to the expectations from QCD [17]. Other models such as

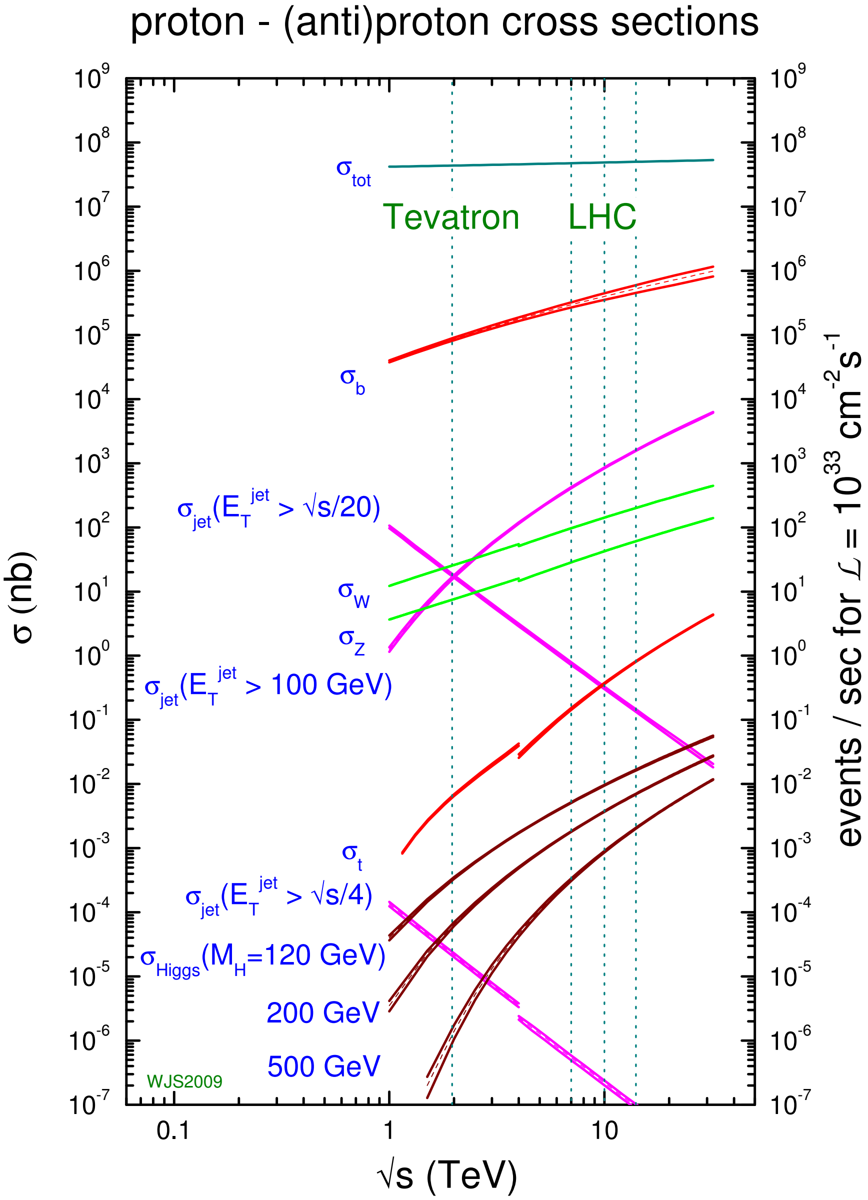

Figure 1.3: Cross sections for different physics processes as a function of center-of-mass energy [47]. The dashed vertical lines indicate the center-of-mass energies of the Tevatron (1.96 TeV), LHC (7 TeV), and two possible future LHC scenarios (10 and 14 TeV).

quark compositeness – quarks have heretofore been believed to be point-like particles – may manifest themselves through "contact interactions" between quarks, altering the kinematic distributions of jets produced compared to those expected [18]. Processes involving the production of jets also serve as large backgrounds in many other searches for new physics.

1.4 Quantum Chromodynamics

1.4.1 Quantum Field Theory of the Strong Interaction

Hadrons are composed of quarks and bound by gluons, an idea that arose historically from the $\mathrm{SU}(3)_\mathrm{f}$ flavor symmetry of up, down, and strange quarks in light hadrons such as pions and kaons [48]. The properties of the quarks are listed in Fig. 1.2. The "color" quantum number [49, 50], corresponding to the $\mathrm{SU}(3)_\mathrm{c}$ gauge group, was introduced in order to ensure that spin-$\frac{3}{2}$ hadrons have an anti-symmetric wavefunction as required for fermions.

Experiments studying deep inelastic scattering of electrons off a proton have demonstrated that protons are made of point-like particles called quarks [51]. The quarks exhibit "asymptotic freedom" such that they appear to be free inside the proton. However, free quarks have never been observed in nature, but rather have been found only in bound states (hadrons), a feature known as "color confinement". These two features can be understood through the running of the strong coupling constant.

QCD was first developed in 1973 as a non-Abelian Yang-Mills quantum field theory [52, 53]. Its Lagrangian describes the dynamics of quarks and gluons, and can be written [54]:

$$\mathcal{L} = \bar{\psi}(i\gamma^\mu \mathcal{D}_\mu - m)\psi - \frac{1}{4}G_{\mu\nu}G^{\mu\nu} \tag{1.1}$$

where the first term describes the kinematics and mass of the quarks, ψ_i, while the second term corresponds to the gluon force fields, $G_a^{\mu\nu}$. A summation over the quark and gluon fields is implied. The term $\gamma^\mu \mathcal{D}_\mu$ is the covariant derivative.

Renormalization is a mathematical tool in perturbation theory that is used in order to cancel infinities arising from "ultraviolet divergences", namely Feynman diagrams containing loops of virtual particles having arbitrarily large energy. An arbitrary scale is introduced where a perturbative calculation is performed, which may be different than the scale at which an experimental measurement is performed. The requirement that any physical observable must not depend on the "renormalization scale" causes the strong coupling constant:

$$\alpha_{\mathrm{S}} = g_s^2/4\pi \tag{1.2}$$

to "run" or to become dependent on the renormalization scale at which it is evaluated. The coupling constant becomes smaller as the scale increases, as shown in Fig. 1.4. It attains a value of 0.118 when probed at the mass of the Z boson, $Q = M_Z = 91.2$ GeV. The decreasing strength of the force allows quarks at higher energies, or equivalently smaller distances, to become asymptotically free. Similarly, the increase in strength of the strong interaction at lower energies, or equivalently larger distances, makes it more energetically favorable to produce a quark-anti-quark pair than to separate the quarks further. This results in "hadronization" (described in Sec. 1.4.5), whereby the quarks are confined within hadrons.

The increase of α_{S} at low energies makes perturbative calculations less reliable, so complex phenomenological models are used. These are used in order to attempt to describe "non-perturbative" effects arising from the colliding protons, the interactions of their constituent partons, and the process through which the scattered partons "shower" and "hadronize" into bound states.

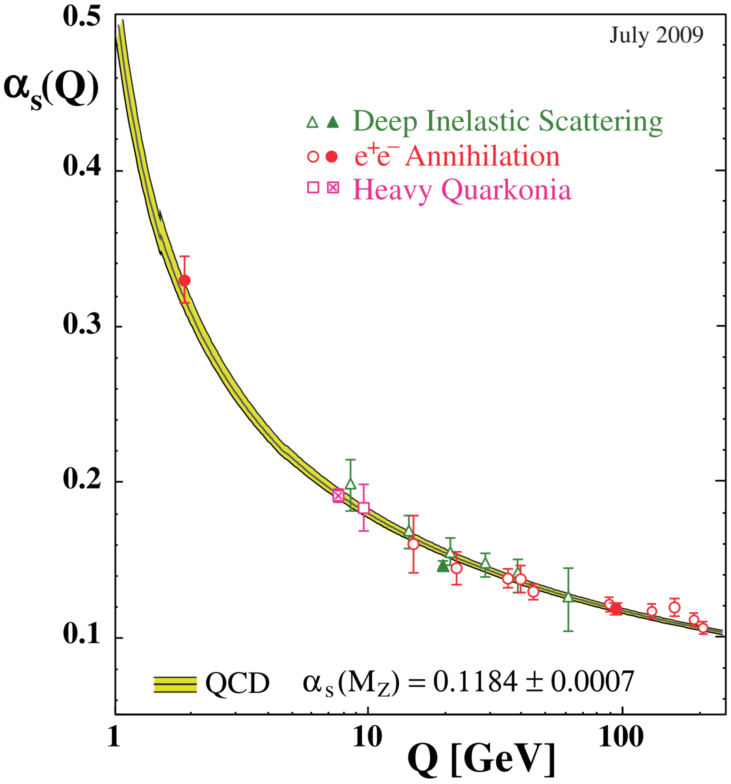

Figure 1.4: The strong coupling constant, α_S, as a function of the scale, Q, at which it is probed [55].

A perturbative calculation at all orders of α_S will produce results independent of the renormalization scale. However a "fixed-order" calculation, namely a calculation including only Feynman diagrams up to a particular order of the coupling constant, will depend on this scale due to the higher order terms that have been omitted. This results in an uncertainty on the theoretical prediction from the particular choice of renormalization scale.

QCD contains many unique features involving long-range interactions, which cannot be calculated using perturbation theory since the coupling constant of the theory is large in this regime. Many of these effects are described using phenomenological models that are constrained by experimental data. The most important effects involved in the calculation of cross sections for jet production at the LHC are described in the following sections.

The measurements performed in this thesis are compared to parton calculations performed at NLO in the strong coupling constant α_{S}, that have been corrected for non-perturbative effects. They are also compared to NLO Monte Carlo simulations, in which a parton shower is introduced. The various theoretical predictions are described in Chapter 4.

1.4.2 Hard Scattering

In perturbation theory, the dominant contributions to jet cross sections arise from Feynman diagrams that contribute to jet production at leading order (LO) in α_{S}. These are known as $2 \to 2$ diagrams because there are two incoming partons, and then after scattering there are two outgoing partons, along with the "beam remnants", which are the remnants of the interacting protons. Some examples of these LO diagrams are shown for quark-quark t-channel scattering in Fig. 1.5(a), quark-anti-quark s-channel annihilation in Fig. 1.5(b), and gluon-gluon t-channel scattering in Fig. 1.5(c).

The calculations of the amplitudes of the Feynman diagrams associated with the hard scattering process is referred to as a "matrix element calculation". A matrix element calculation performed at a fixed order, e.g. NLO, in the coupling constant is referred to as a "fixed-order calculation" or sometimes just "NLO calculation".

Compared to the leading order Feynman diagrams, an NLO calculation of a $2 \to 2$ hard scattering process also includes $2 \to 2$ diagrams with one virtual loop and $2 \to 3$ diagrams where one of the incoming or outgoing partons radiates a third parton. Figure 1.6 shows a representative example of each of these two types of NLO diagrams.

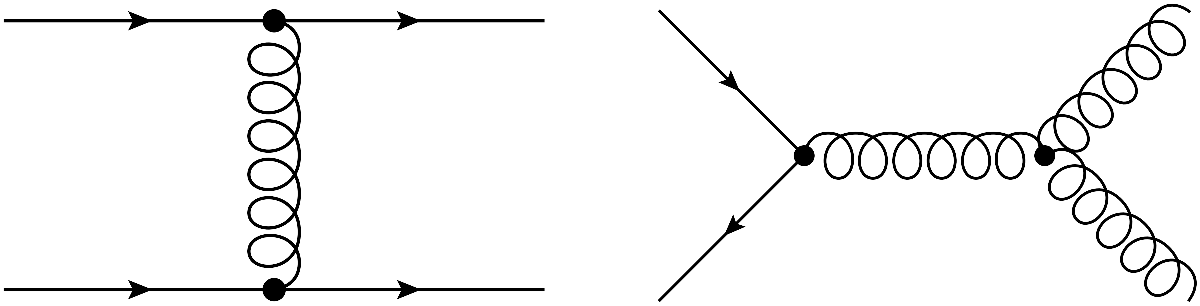

(a) quark-quark

(b) quark-anti-quark

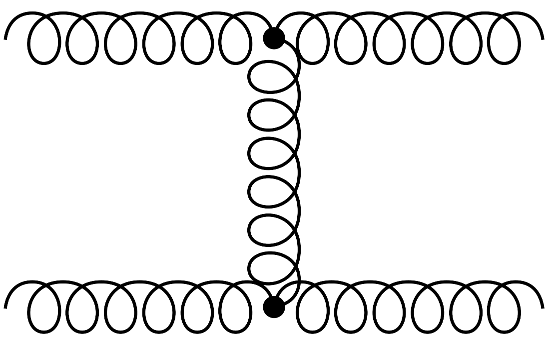

(c) gluon-gluon

Figure 1.5: Leading-order (2 → 2) Feynman diagrams for jet production in proton-proton scattering at the LHC. Examples are shown for quark-quark *t*-channel scattering (a), quark-anti-quark *s*-channel annihilation (b), and gluon-gluon *t*-channel scattering (c).

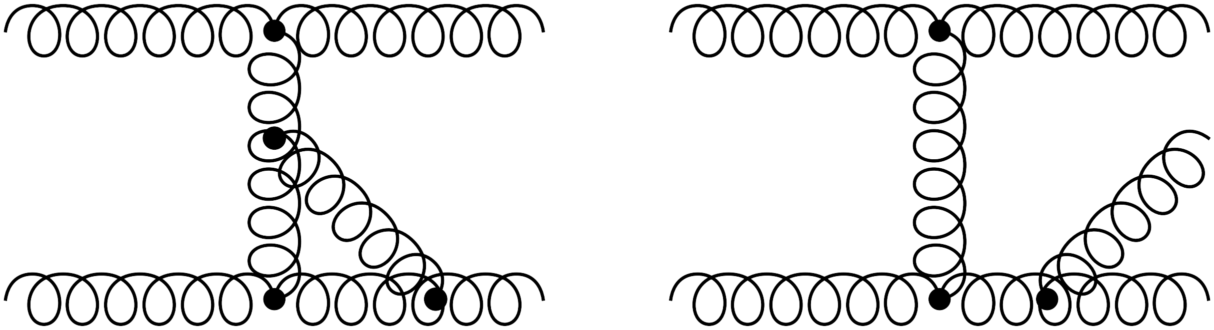

(a) Virtual loop

(b) Real emission

Figure 1.6: Two types of NLO Feynman diagrams for jet production, the first being a 2 → 2 diagram with a virtual loop (a) and the second being a 2 → 3 diagram where the third outgoing parton is produced via real emission from another parton (b).

1.4.3 Parton Shower

The “parton shower” is a phenomenological model that is used to describe the recursive radiation of quarks and gluons from partons, including soft and collinear emissions. Perturbative calculations suffer in these kinematic configurations due to large logarithmic terms that persist at all orders in the calculation [56]. The parton shower approximation effectively resums these logarithms according to the power of the logarithm. The various parton shower models in use and their parameter values are based on measurements of observables in minimum bias events and underlying event activity.

The parton shower uses “splitting functions” that describe the probability for a parent parton to emit a quark or gluon [57]. The leading-order Feynman diagrams corresponding to the splitting of quarks and gluons are shown in Fig. 1.7. Each splitting function is expressed in terms of the “Sudakov form factor”, which represents the probability for the parent parton *not* to radiate [58]. Because the Sudakov form factor is singular for soft and collinear emissions, an infrared cut-off is introduced to avoid these divergences, which would normally be cancelled by virtual diagrams in a calculation to all orders. The cut-off is typically chosen to be at the energy scale where partons hadronize, which is in the large vicinity of 100 MeV.

The Sudakov form factor serves as the basis for the parton shower model. It is implemented using a Monte Carlo simulation, which is referred to as a “generator”, that models the probability for a parton to radiate as it evolves from the “hard scattering process” to the infrared cut-off scale. Thus it produces a shower of partons through a recursive process of radiation, which gives rise to the name of the model. In different implementations, the showering is ordered from largest to smallest in either the p_{T} or angle of the emitted partons (see Sec. 4.2). The radiation is termed “final state radiation”.

A similar procedure, but where the ordering parameter of the shower is reversed, is

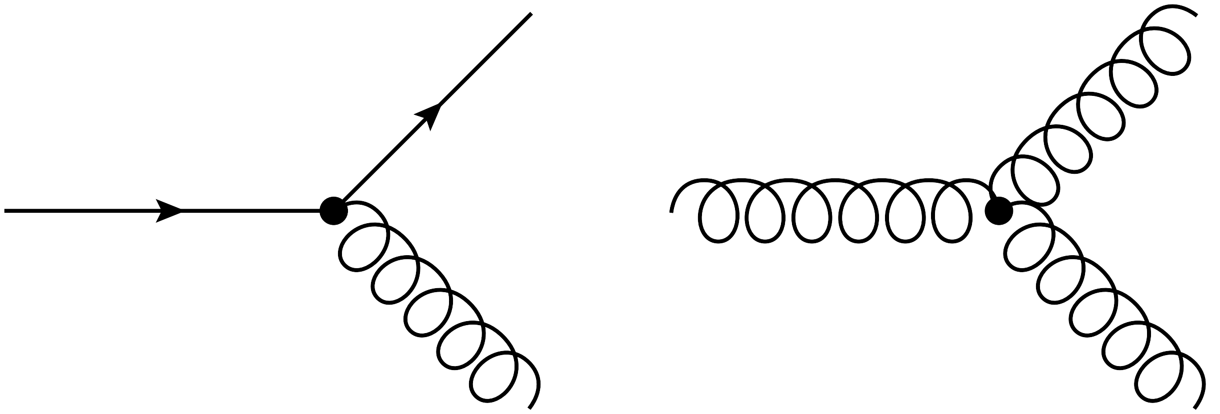

(a) $q \to qg$

(b) $g \to gg$

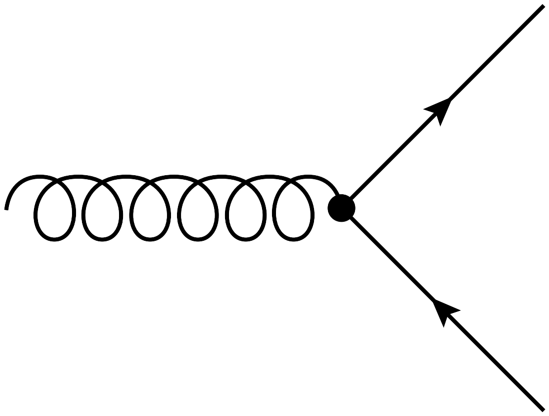

(c) $g \to q\bar{q}$

Figure 1.7: Leading-order ($1 \to 2$) Feynman diagrams for the splitting of quarks and gluons. Examples are shown for a quark emitting a gluon (a), a gluon emitting another gluon (b), and a gluon splitting into a quark-anti-quark pair (c).

used to evolve a parton "backwards" from the hard scattering to the scale at which it is probed in the proton. The cut-off scale here is termed the "factorization scale", which corresponds to the scale at which the parton distribution functions are "factorized" from the matrix element in the matrix element calculation (see Sec. 1.4.6).

The various models of the parton shower are designed, and the parameter values for each model are fit, based on measurements of observables sensitive to the modeling of minimum bias events and the underlying event. These fits are performed using data taken at the LEP and Tevatron colliders [59], as well as ATLAS measurements at the LHC [60, 61, 62, 63]. Together with the models and parameter values for hadronization (see Sec. 1.4.5) and the underlying event (Sec. 1.4.7), the parton shower model and parameter values constitute a "tune" of a Monte Carlo simulation. Several parton shower models and tunes are used in order to estimate the uncertainty associated with the modeling of the parton shower in the Monte Carlo simulation.

1.4.4 Matching the Matrix Element and Parton Shower

When a matrix element calculation is interfaced to a parton shower, a procedure is required in order not to "double-count" final states with a given jet multiplicity. For example, in a $2 \rightarrow 2$ hard scattering process, the matrix element calculation includes $2 \rightarrow 3$ diagrams of the type shown in Fig. 1.6, where the third outgoing parton has been radiated from the other two outgoing partons. However such a final state can also be produced by a $2 \rightarrow 2$ LO diagram in which the radiation of the third parton is produced through the parton shower.

Since jet production at leading order in the Standard Model occurs through $2 \rightarrow 2$ diagrams, this problem does not affect $2 \rightarrow 2$ LO Monte Carlo simulations.[2] It does

---

[2] It does affect LO "matrix element generators", which refer to parton shower Monte Carlo

impact the POWHEG NLO Monte Carlo simulation 4.3.2 used as a theory prediction in this analysis. This is avoided in POWHEG by requiring the radiative emissions in the parton showers to be less energetic ("softer") than the most energetic ("hardest") parton emission in the matrix element calculation.

1.4.5 Hadronization

Hadronization is the process through which hadrons are produced from partons. Due to confinement, partons cannot exist individually, but rather combine with quarks and gluons from the vacuum to form hadrons. This typically occurs at low energy scales where α_S is large, so it cannot be predicted using perturbation theory. Different phenomenological models of hadronization have been developed based on measurements of hadron spectra. These include the "Lund string model" implemented in the PYTHIA Monte Carlo simulation [64], which models gluons using field lines or "strings" that are attracted to each other, as well as the "cluster model" in the HERWIG generator [65], where gluons split into quark pairs that are grouped into color-neutral "clusters".

1.4.6 Parton Distribution Functions

In the "parton model" [66], a hadron is composed of partons. A parton distribution function or "PDF" encodes the probability for a parton of a given flavor to carry a fraction x of a proton's momentum, when the proton is probed at a momentum scale Q^2. In a cross section calculation for a proton-proton collision, the Factorization Theorem [54] in QCD allows one to separate non-perturbative effects occurring within the proton, which are

---

simulations that implement LO matrix element calculations of $2 \to N$ final states, where $N \geq 3$. These are not used for the theory predictions in this analysis.

encoded in the "proton structure function", from the hard scattering of the partons calculable by perturbation theory. This is done through the factorization scale, an infrared cutoff that removes the singularity from collinear emission (see Sec. 1.4.3). This factorizes the long-range interactions into a multiplicative term within the proton structure function that is determined using global fits to experimental data. In this way the non-perturbative effects within the proton, which are not calculable by perturbation theory, can be measured using data for each x and Q^2.

Requiring that experimentally determined observables must not depend on the factorization scale causes the parton distribution functions to run logarithmically with energy, where the energy dependence is captured by the DGLAP equations [67, 68, 69]. Data from lower energy colliders and deep inelastic scattering experiments are used to constrain the parton distribution functions at particular values of x and Q^2, and then the DGLAP evolution allows the PDFs to be predicted at the higher energies accessed by the LHC. However the parton distribution functions contain a residual dependence on the choice of factorization scale that results in an uncertainty on the theoretical prediction, whose calculation uses the PDFs.

1.4.7 Underlying Event

In events where protons are collided, interactions typically occur amongst multiple partons. The interactions of "spectator partons" that do not participate in the hard scatter, which are termed "underlying event" (UE), are described using phenomenological models [70]. In Monte Carlo generators, the color flow of these interactions may be implemented as occurring between color-charged partons (as in PYTHIA) or between color-neutral clusters of partons (HERWIG).

As with the parton shower, the parameters of each particular UE model are tuned to experimental data. Several UE models and tunes are used in order to estimate the uncertainty associated with the modeling of the UE in the Monte Carlo simulation.

1.4.8 Jet Definition

There is no unique technique to group objects into a jet, though many algorithms have been developed [46, 71]. Moreover, there is no one-to-one correspondence between the stable hadrons and the partons from which they derive; this is determined by the jet algorithm used. For example, a gluon that splits into a pair of quarks may be identified as one or two jets depending on the angular separation of the quarks, their momenta, and the parameters of the jet algorithm. Each jet algorithm has its own advantages and disadvantages.

Each jet algorithm generally groups input objects, which are termed "constituents", into jets. These constituents may be experimental objects such as calorimeter energy clusters, or theoretical objects such as partons or hadrons. Each algorithm has a fundamental parameter that describes the characteristic size of the jet produced.

In this thesis, jets are identified using the anti-k_t jet algorithm [72] implemented in the FastJet [73] package. This algorithm constructs, for each input object (e.g. a parton, particle or energy cluster) i, the quantities d_{ij} and d_{iB} as follows:

$$d_{ij} = \min(k_{ti}^{-2}, k_{tj}^{-2}) \frac{(\Delta R)^2_{ij}}{R^2}, \tag{1.3}$$

$$d_{iB} = k_{ti}^{-2}, \tag{1.4}$$

where

$$(\Delta R)^2_{ij} = (y_i - y_j)^2 + (\phi_i - \phi_j)^2, \tag{1.5}$$

k_{ti} is the transverse momentum of object i with respect to the beam direction, ϕ_i is its azimuthal angle, and y_i is its rapidity, defined as $y = \frac{1}{2}\ln[(E + p_z)/(E - p_z)]$, where E denotes the energy and p_z is the component of the momentum along the z-axis. A list containing all the d_{ij} and d_{iB} values is compiled. If the smallest entry is a d_{ij}, objects i and j are combined (their four-vectors are added) and the list is updated. If the smallest entry is a d_{iB}, this object is considered a complete "jet" and is removed from the list. As defined above, d_{ij} is a distance measure between two objects, and d_{iB} is a similar distance between the object and the beam. Thus the variable R is a resolution parameter which sets the relative distance at which jets are resolved from each other as compared to the beam. It can also be seen intuitively as the radius of a circular jet in the plane (ϕ, y) of azimuthal angle and rapidity. In this analysis, jet cross section measurements are performed using both a narrow ($R = 0.4$) and wide ($R = 0.6$) size.

The anti-k_t jet algorithm is used because it exhibits both theoretical [74] and experimental [12] properties that are desirable. For the theoretical side, it is "collinear safe", where the same jets should be identified in an event if any constituent is replaced with two objects with the same direction, but half the energy, of the original constituent. It is also "infrared safe", where the identification of any jet should be stable with respect to any soft radiation nearby. Finally, it produces geometrically well-defined ("cone-like") jets. For experimental measurements, the algorithm is able to measure a jet's energy with fine resolution. It is also insensitive to soft interactions arising from the UE and additional proton-proton interactions (see Sec. 6.4.2).

Two anti-k_t jet sizes are used because they are sensitive to different systematic and theoretical effects. Narrow jets have the advantage of being less affected by particles from other proton-proton interactions, as well as by spectator partons. They are also able to resolve small angular separations between jets due to their narrow size. However, wide jets are less susceptible to losing energy “out of cone” through parton radiation, hadronization, and showering in the calorimeter. This results in better resolution in measurements of the jet energy, as well as smaller uncertainties associated with missing higher order Feynman diagrams in the theoretical prediction. The use of two sizes also helps to understand the relative importance of different non-perturbative effects that are corrected for in the theoretical prediction (see Sec. 4.2.2). Underlying event impacts wide jets more severely, while hadronization is more important for narrow jets.

Figure 1.8 shows the jets reconstructed from partons in a HERWIG event, using four different jet algorithms. The anti-k_t algorithm, which is used in this thesis, produces well-defined jets with a circular projection on the $y - \phi$ plane. The other algorithms, Cambridge/Aachen [75, 76], k_t [77, 78], and SIS-Cone [79], produce jets with much more irregular shapes.

In this thesis, jet cross sections are measured at the “particle-level” final state of a proton-proton collision [80]. Particle-level jets are built from stable particles, which are defined as those with a proper lifetime longer than 10 ps. This definition includes muons and neutrinos from decaying hadrons.

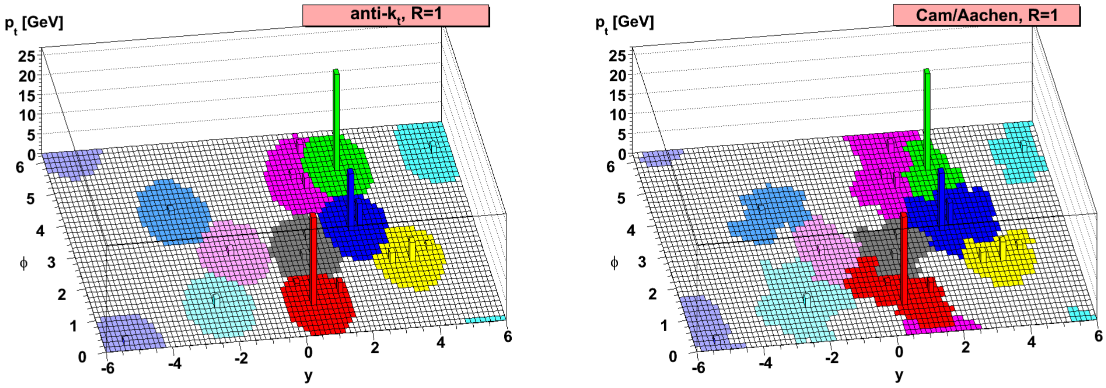

(a) anti-k_t (b) Cambridge/Aachen

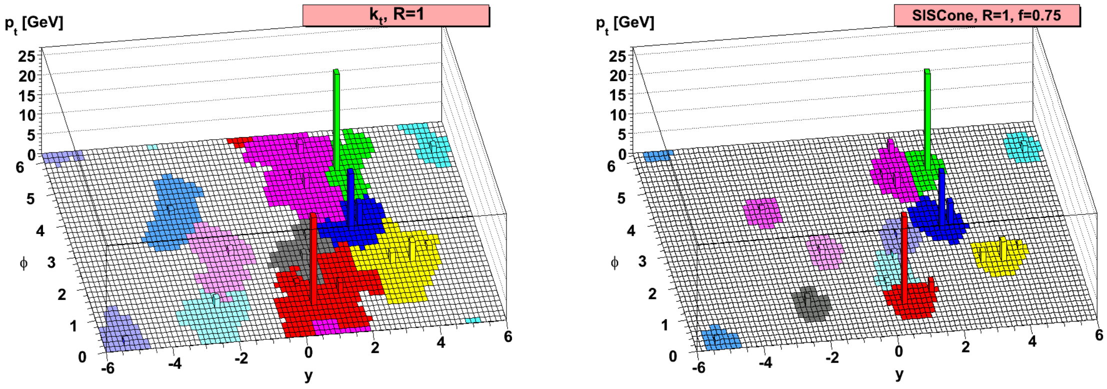

(c) k_t (d) SIS-Cone

Figure 1.8: Projections on the $y-\phi$ plane of jets reconstructed from partons in a HERWIG event, using four different jet algorithms [72]. The anti-k_t algorithm (a), which is used in this thesis, is shown in comparison to the Cambridge/Aachen (b), k_t (c), and SIS-Cone (d) algorithms.

CHAPTER 2

LARGE HADRON COLLIDER

"The day when the scientist, no matter how devoted, may make significant progress alone and without material help is past. . . . The attack on the atomic nucleus has required the development and construction of great instruments on an engineering scale."

— Ernest Lawrence (Nobel Prize in Physics, 1939)

2.1 Overview

The Large Hadron Collider (LHC) [81, 82, 83, 84] is a proton-proton collider in Geneva, Switzerland that collides two beams of protons together at very high energies. The ATLAS detector, which is designed to measure the output of these collisions, is located at one of four collision points on the LHC accelerator ring. During 2010, the first year of operation, the proton-proton collisions have been produced at a center-of-mass energy of $\sqrt{s} = 7$ TeV with 3.5 TeV per proton. This center-of-mass energy has been chosen to ensure a safe operating margin for the magnets in the accelerator, avoiding damage due to resistive connections [85]. The design center-of-mass energy of the LHC is $\sqrt{s} = 14$ TeV.

2.2 Accelerator Complex

The LHC was built in the tunnel previously housing the Large Electron-Positron (LEP) collider [86, 87]. The acceleration chain was previously used by the Super Proton Synchrotron (SPS) and includes the SPS itself. It consists of a series of particle accelerators that sequentially increase the energy of the protons. The LHC accelerator complex is illustrated in Fig. 2.1.

Protons are produced by ionizing hydrogen atoms in an electric field. They are accelerated to 50 MeV by the LINAC 2, a linear accelerator. The linear accelerator creates bunches of protons, which are combined and then accelerated in a series of four parallel storage rings. These are synchotron accelerators that "lock" bunches close to the local minima of an oscillating electric field in radio frequency (RF) cavities. These minima are stable points where protons are not accelerated, and protons nearby are accelerated or decelerated until they are bunched around these stable points. The bunches are then accelerated by changing the phase of the electric field with respect to the protons. This increases the momentum of the local minima, driving the protons to higher energies. The protons are accelerated to 1.4 GeV by the Proton Synchrotron Booster (PSB), also known as the BOOSTER, and then further to 26 GeV by the Proton Synchrotron (PS). The Super Proton Synchrotron (SPS) accelerates the protons to 450 GeV, the minimum energy required to maintain a stable beam in the LHC. Finally the LHC accelerates them to the operating energy of 3.5 TeV per beam.

The RF accelerators produce bunches centered around the stable points of the electric field, each with a longitudinal spread of about 0.75 m. There are 35,640 stable points, only one-tenth of which can be filled with protons. In 2010, up to 368 out of the 3564

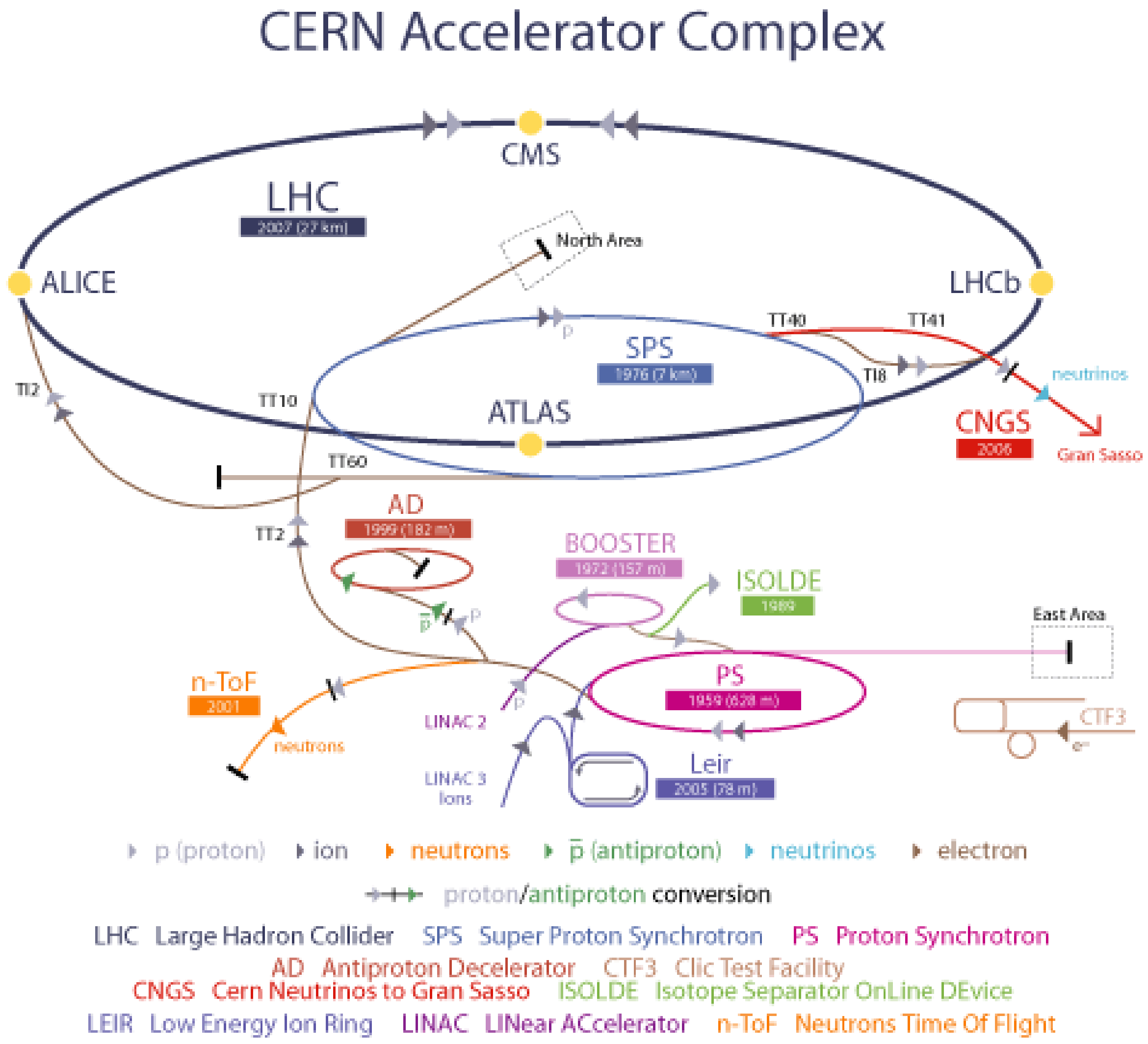

Figure 2.1: Schematic diagram of the CERN accelerator complex, which consists of the LINAC 2, PSB (BOOSTER), PS, SPS, and LHC accelerators [81].

bunch sites were filled, where each bunch contains up to 10^{11} protons [88].[1] The bunches are organized into up to 48 "bunch trains", each of which is a group of up to 8 bunches, where the bunches within a train are separated by 150 ns.

After the protons have been accelerated to an energy of 3.5 TeV, the beams are declared to be stable and the ATLAS detector begins to record data. The beam intensity decays with time as bunches collide and as protons are lost from the stable orbit. When the intensity has dropped sufficiently, the beam is "dumped" into a large thermal sink that absorbs its energy. This cycle is referred to as a "fill", typically lasting around 10 hours. Beam injection for a new fill typically occurs within 24 hours for the data reported here.

2.3 Luminosity

Besides the beam energy, the luminosity is the other characteristic that determines the operating conditions of the LHC. The luminosity L reflects the density and rate of proton bunches that are collided. The number of collisions per unit time, N, for a process with a cross section σ, is determined as:

$$N = L\sigma \tag{2.1}$$

The luminosity is determined from the beam parameters of the accelerator:

$$L = \frac{N_{\mathrm{b}}^2 F}{4\pi\beta^*}\frac{\gamma}{\epsilon_{\mathrm{n}}} n_{\mathrm{b}} f_{\mathrm{rev}} \tag{2.2}$$

where N_{b} is the number of protons per bunch. The correction factor F arises due to the LHC crossing angle at the interaction point, which reduces the luminous region and

---

[1] In the design LHC configuration, up to 2808 bunches of protons are accelerated and stored, with the rest being used to inject and abort the beams.

prevents “parasitic collisions” between unintended bunches. The value of the beam envelope function β evaluated at the interaction point, β^*, characterizes the beam size and focusing distance at the collision point. The normalized transverse beam emittance, ϵ_{n}, characterizes the phase and momentum space occupied by the beam, and γ is the relativistic factor of the protons. Finally n_{b} is the number of bunches and $f_{\mathrm{rev}} = c/26.7$ km $= 11.2$ kHz is the LHC revolution frequency, where c is the speed of light.

CHAPTER 3

THE ATLAS DETECTOR

"Soon I knew the craft of experimental physics was beyond me — it was the sublime quality of patience — patience in accumulating data, patience with recalcitrant equipment — which I sadly lacked."

— Abdus Salam (Nobel Prize in Physics, 1979)

3.1 Overview

The ATLAS detector is a large, general-purpose particle detector that is located at Interaction Point 1 (IP1) on the LHC accelerator ring. It is 44 m long and 25 m in diameter, weighing about 7000 tons. It is illustrated in Fig. 3.1 and described in detail in Ref. [89].

The overall detector has a cylindrical shape that consists of a series of many subdetectors designed to measure the momenta of different types of particles produced in each proton-proton collision. These subdetectors are grouped into three primary systems, which are arranged in concentric layers around the beam axis.

The inner detector [90, 91, 92, 93] is a system of tracking detectors surrounded by a 2 T solenoidal magnetic field. It is used for charged particle identification and position and momentum measurements. The calorimeter system [94, 95] is a set of calorimeters that are used to measure the energies of charged and neutral particles. The muon spectrometer [96, 97, 98] consists of detectors located within a large air-core toroidal magnetic field that are used to measure the position and momentum of muons.

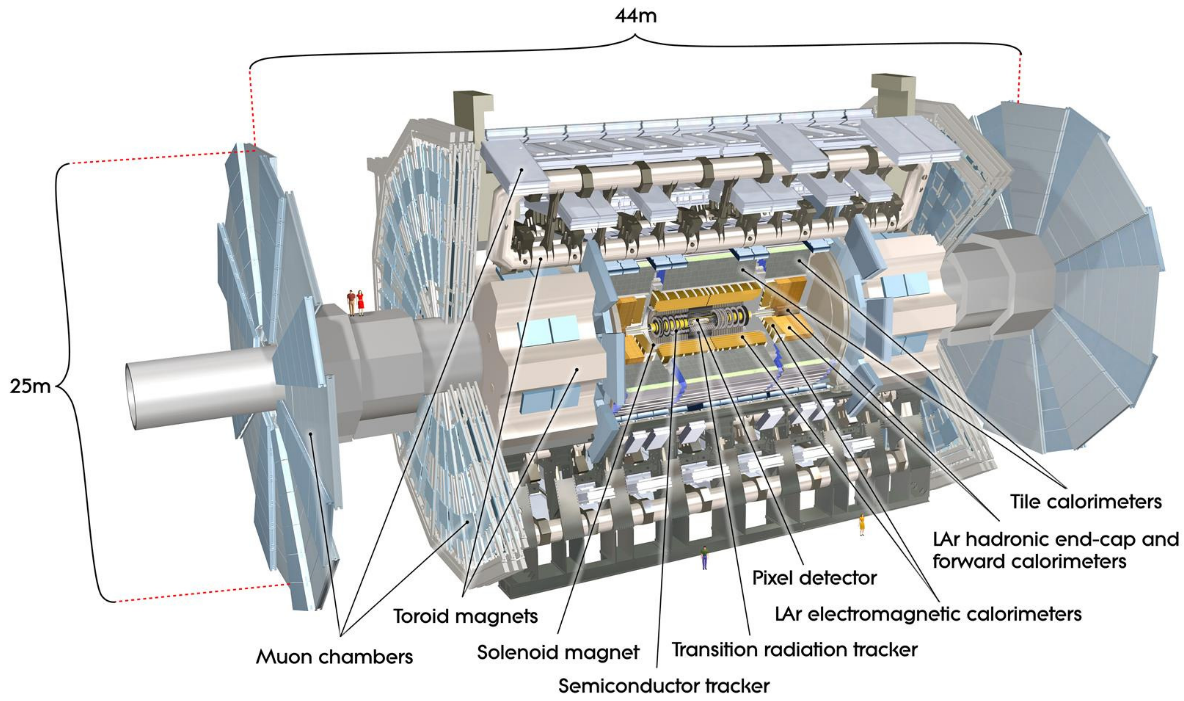

Figure 3.1: Illustration of the ATLAS detector showing the subsystems of the inner detector, calorimeters, and muon spectrometer, as well as the magnet systems [89].

A particle produced in a proton-proton collision interacts sequentially with different detector subsystems, depending on the type of particle. These interactions are illustrated in Fig. 3.2. Each particle first crosses the inner detector (ID), which is composed of the pixel detector (Pixel), the semiconductor tracker (SCT), and the transition radiation tracker (TRT). Each of these detectors has several layers that measure the position of a charged particle as it crosses each layer. The detectors are contained within a 2 T magnetic field generated by a solenoid in front of the calorimeter, which bends the trajectories of the charged particle. The radius of curvature and orientation of a charged particle's "track" through the detectors allows its momentum to be inferred.

Next the particle crosses and deposits energy in the electromagnetic (EM) calorime-

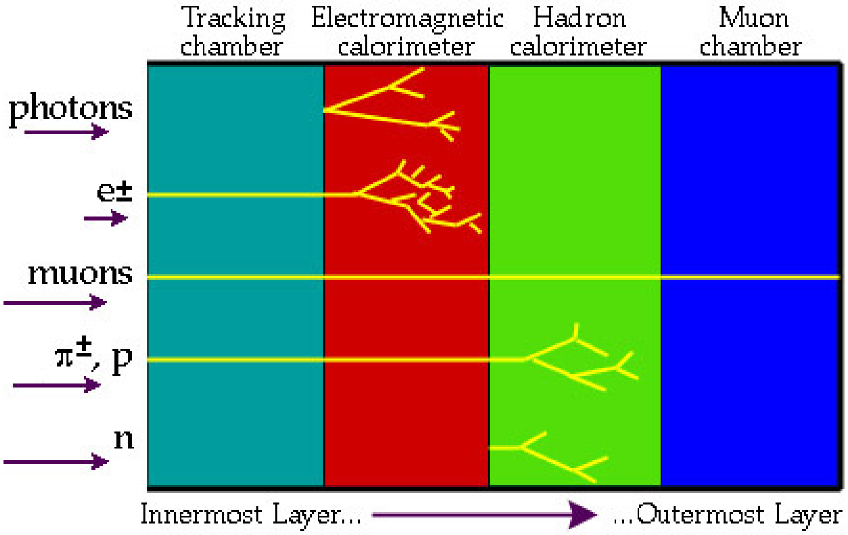

Figure 3.2: Interactions of different types of particles in the various detector subsystems [45]. The momenta of charged particles are measured by the inner detector. Photon and electron energies are measured by the electromagnetic calorimeter, and hadron energies are measured by the hadronic calorimeter. The muon spectrometer measures the momenta of muons.

ters, which use liquid argon (LAr) as active material. They precisely measure the energy and position of photons and electrons. Hadrons are not fully absorbed in the electromagnetic calorimeter and deposit their remaining energy in the hadronic (HAD) calorimeters. The hadronic calorimeter in the central η region (tile calorimeter) uses scintillating tiles as its active material, while the hadronic end-cap calorimeters (HEC) at larger η use liquid argon. A forward calorimeter (FCal), which also uses liquid argon, provides nearly hermetic coverage out to very large η.

Energetic muons are minimum ionizing and penetrate through to the muon system without depositing much energy in the the calorimeters. The muon spectrometer is a tracking detector with multiple layers that measure the position of the muon at different points along the muon's trajectory, which is bent by toroidal magnets outside the calorimeters. The radius of curvature and orientation of the muon allows the muon momentum to be determined. Neutrinos are very weakly interacting and escape the detector without being directly detected, although their presence can be inferred from momentum imbalance in the plane transverse to the beam or “missing transverse momentum”.

During data-taking, the trigger and data acquisition (TDAQ) system is used to evaluate and record data quickly in order to cope with the stringent computational demands of the LHC. It interfaces with the read-out electronics and comprises a set of online algorithms that decide whether to reject events or to store them for offline analysis. Particles interacting in a detector produce signals in that detector’s “front-end” electronics, where the signals are buffered. If the event passes criteria in the level-1 trigger to accept the event, the signals are sent to the “back-end” electronics outside the “cavern”, which is the experimental hall containing the detector. The back-end electronics preprocess and pack the data into data structures, and then transmit them to read-out servers, where they are again buffered. If the event also passes the level-2 trigger “decision”, the information is transmitted to the event builders. These further pack the data, which is then sent to the “event filter” or third level trigger, which performs the final decision whether to accept or reject the event. Accepted events are stored on tape for offline analysis.

Data quality and monitoring checks are performed both online and offline. Data that have been stored on disk are processed offline with appropriate detector conditions, and further requirements are placed to reject bad data.

The detector subsystems, the trigger and data acquisition system, and the detector conditions, data quality, and detector simulation are described in detail in the sections that follow.

3.2 Coordinate System

The ATLAS reference system is a Cartesian right-handed coordinate system, with the nominal collision point at the origin. The counter-clockwise beam direction defines the positive z axis, with the x axis pointing to the center of the LHC ring. The pseudorapidity is defined as $\eta = -\ln\tan(\theta/2)$, where the polar angle, θ, is taken with respect to the positive z direction. The rapidity is defined as $y = \frac{1}{2}\ln[\frac{E+p_{\mathrm{Z}}}{E-p_{\mathrm{Z}}}]$, where E denotes the energy and p_{Z} is the component of the momentum along the beam direction. In the limit of massless particles, $\eta = y$. Since the interacting partons carry an unknown fraction of the momenta of the colliding protons, the physical observables measured in this thesis are jet cross sections that are invariant under Lorentz boosts along the z axis.

3.3 Inner Detector

3.3.1 Overview and Performance

The inner detector is a tracking system that measures the momenta of charged particles. It covers the full range of azimuth and spans the region $|\eta| < 2.5$. It consists of layers of silicon pixel detectors, silicon microstrip detectors, and transition radiation tracking detectors, contained within a solenoid magnet that produces a 2 T field. It is illustrated in Fig. 3.3, with a radial view shown in Fig. 3.4.

Each of its three sub-detectors is divided into barrel and endcap portions. The barrel portion consists of concentric layers of detector modules that cover the central region at small $|\eta|$. The end-cap portion comprises a series of radial disks that cover the forward region at large η.

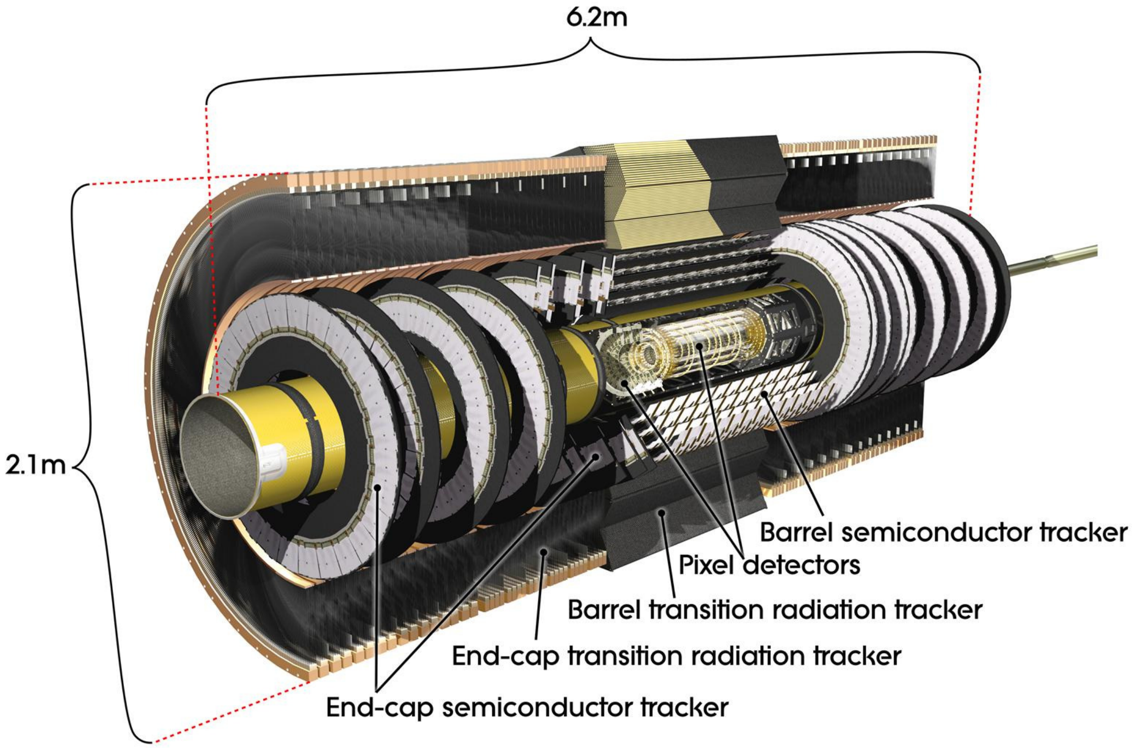

Figure 3.3: Illustration of the subsystems of the inner detector: the pixel detector, semiconductor tracker, and transition radiation tracker [89].

The Pixel and SCT consist of semiconductor detectors, with the Pixel (SCT) using sensors that are segmented into pixels (strips). When a charged particle crosses any of these detectors, it creates electron-hole pairs. An electric field is applied to collect this charge, which is proportional to the energy deposited. Since the size of the signal is related to the velocity of the particle, this signal can be used together with the measured momentum to identify the mass of the particle that traversed the detector. The position of the particle is measured at various points along its trajectory, and these "hits" above the background are combined to form a track.

The TRT uses straw tubes to track charged particles. Particles ionize gas within the

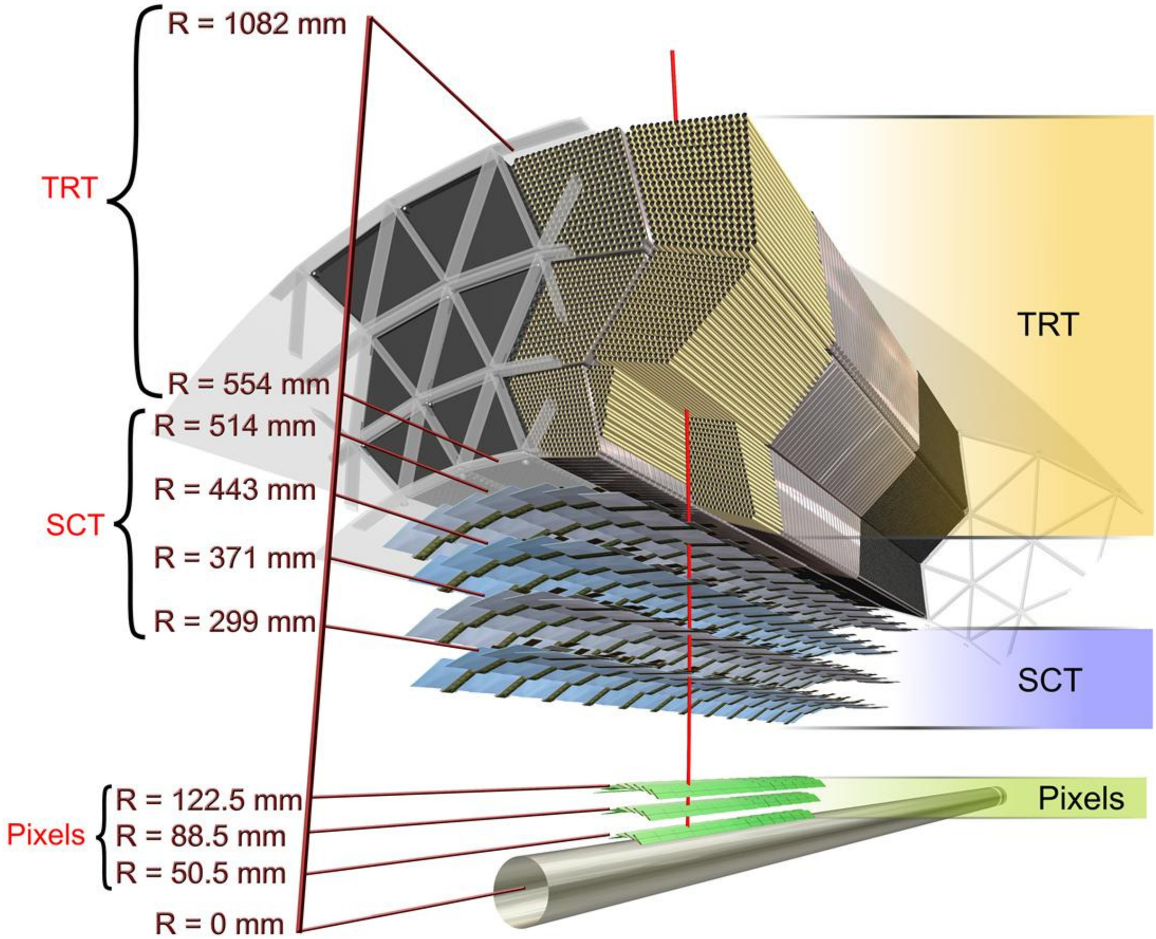

Figure 3.4: Illustration with a radial view of the barrel portions of the detectors that constitute the inner detector [89]. The beampipe is illustrated by the cylinder at radius $R = 0$.

tube, and an electric field is applied between the walls of the tube and the thin wire at the center of the tube. This causes the positive and negative ions to "drift" apart. Their charge is used to measure a hit above the background, whose position can be inferred by the drift time. Because the drift tubes are parallel to the beam axis, they cannot measure the pseudorapidity of the particle's trajectory. In the end-cap disks, the straw tubes are arranged radially so the radius of the particle's trajectory cannot be determined. The TRT typically measures around 30 points, whose large lever arm improves the measurement of the track p_{T}.

The TRT also has the ability to discriminate between electrons and pions. When a particle crosses fibers in the TRT, it radiates low-energy "transition radiation" due to the different index of refraction. Electrons can be identified since they radiate about 250 times more energy than pions.

The 2 T magnetic field allows the ID to measure charged particles with $p_{\mathrm{T}} > 150$ MeV [99]. The track reconstruction efficiency is 78% for tracks with $p_{\mathrm{T}} = 500$ MeV and increases to greater than 85% above 10 GeV [99]. High momentum particles in the central region are measured with a transverse impact parameter resolution of 10 μm [89].

3.3.2 Solenoid

The solenoid is a cylindrical magnet that surrounds the ID with a magnetic field of 2 T. It lies inside the cryostat of the barrel electromagnetic calorimeter (see Sec. 3.4.2), in front of the calorimeters. The magnet is made of superconducting NbTi cables wound around an aluminum cylinder and is designed to minimize the amount of material before the calorimeter. The solenoid, which has an inner radius of about 1.2 m and a length of 5.8 m, is oriented with the beam passing through its axis. It is operated with a current of 7730 A and is cooled using liquid helium to a temperature of 4.5 K. Its magnetic field returns through the steel support structure of the hadronic barrel calorimeter, which resides outside the calorimeter (see Sec. 3.4.3).

3.3.3 Pixel Detector

The Pixel detector [100] has three concentric, cylindrical barrel layers, with the innermost layer at a radius of 5 cm from the interaction point and the outermost layer 12 cm away. It is shown in Fig. 3.4. Three radial endcap disks on each side of the detector span the range 49.5 cm $< |z| <$ 65 cm along the beam axis, extending its coverage to $|\eta| < 2.5$. The detector typically provides three "space point" measurements along the trajectory of a charged particle.

The detector consists of 1,744 modules distributed across the 3 barrel layers and 6 endcap disks, totaling over 80 million pixels. The silicon sensor on each module has an active area of 16.4 mm × 60.8 mm and is segmented into 47,232 pixels, most of which have dimensions of 50 μm × 400 μm. The module is oriented to produce a position resolution of 10 μm in the $r - \phi$ direction and 115 μm in the z direction.

In order to cover the full azimuthal range along ϕ, barrel modules are tilted by 20° from the tangent to the cylinder so that they are staggered with the next module in the $r - \phi$ direction. Similarly, disk modules are situated on two layers on each disk, which are tilted by 3.75° in ϕ with respect to each other.

A module is read out by 16 radiation-hard front-end chips [101]. Each chip has 2,880 read-out channels, which are each interfaced to a sensor pixel through a metal "bump bond". A charge sensitive pre-amplifier converts the charge from each pixel into a pulse with a length proportional to the amount of charge. Hits in a pixel are only collected if the signal exceeds a tunable threshold. To preserve signal integrity, the electrical signals are transformed into optical signals before being transferred.

The detector is cooled using nitrogen gas to an operating temperature between -5°C and -10°C in order to protect its semiconductor sensors from radiation damage. The sensors are operated with a bias voltage between 150–600 V, which is increased with its exposure to radiation. The modules are also cooled using C_3F_8 gas to dissipate heat generated by the readout electronics. The cooling pipes and service cables pass through the endcap disks. The pixel detector and read-out system have an overall length of around 7 m along the beam axis in z.

3.3.4 Semiconductor Tracker

The semiconductor tracker [102] consists of four pairs of concentric, cylindrical barrel layers and nine radial endcap disks (each again with a pair of layers) on each side of the detector. The barrel layers span radii from 29.9 cm $< r <$ 51.4 cm, while the endcaps cover the region 93.4 cm $< |z| <$ 272.0 cm along the beam axis. Together they cover the region $|\eta| < 2.5$. The SCT typically provides eight strip measurements (four space-points) along a charged-particle track with a resolution of 17 μm in the $r-\phi$ direction and 580 μm in the z direction.

In a similar arrangement to that of the Pixel, the SCT contains 4088 modules distributed across the eight barrel layers and 36 endcap layers. Each silicon sensor of a double-sided module is segmented into 768 strips, totaling about 6 million strips in the entire detector. In the barrel modules, the strips have a pitch of about 80 μm and are arranged almost parallel to the solenoid field and beam axis. In the endcap modules, the strips are radial and have a variable pitch. The strips are read out by radiation-hard front-end readout chips [103], each of which contains 128 channels. The readout is similar to that of the Pixel.

The respective strips in each pair of back-to-back layers are tilted by 0.040 radians with respect to each other in order to provide three-dimensional hit information. Full azimuthal coverage in the barrel layers is attained by tilting the modules by about 11° with respect to the tangent to the cylinder and staggering the modules in the $r - \phi$ direction. Disk modules achieve full coverage in an analogous fashion.

The detector operates at the same temperature (between -5°C and -10°C) as the Pixel. The bias voltage applied to the sensors ranges from 150 V up to 450 V as radiation damage increases.

3.3.5 Transition Radiation Tracker

The TRT [104, 105] surrounds the silicon detectors, spanning radii from 56.3 cm $< r <$ 106.6 cm within the region $|\eta| < 2.5$. The barrel portion contains up to 73 layers of 144 cm long straw tubes, arranged longitudinally in three cylindrical layers that each contain 32 ϕ sectors (modules). Each endcap has 160 layers of 37 cm long straws, radially oriented in 18 wheels. Each layer contains 768 straws, for a total of 298,304 straw tubes in the detector.

Each straw tube has a diameter of 4 mm, with straws being spaced apart by an average of 7 mm. The straw tube is filled with a gas mixture of 70% Xe, 27% CO_2, and 3% O_2. Its anode is a gold-coated wire with a diameter of 30 μm that passes through its center and is kept at ground potential. The straw walls serve as the cathode and are operated at about -1500 V.

To ensure full azimuthal coverage in ϕ, each layer is rotated by 3/8 of the straw angular distance. Charged particles with $p_{\mathrm{T}} > 500$ MeV and $|\eta| < 2.0$ typically cross about 30 straws, and their two-dimensional hits can be resolved with a resolution of 130 μm.

For electron identification, the spacing between the barrel (end-cap) layers is filled with fibers (foils) of polypropylene radiator. Electrons passing through this material produce upwards of 6 keV of transition radiation, many times higher than that typically deposited by an ionizing particle.

The TRT is designed to operate at room temperature, but it is cooled with CO_2 to avoid high-voltage discharges and other problems.

3.4 Calorimeters

3.4.1 Overview and Performance

The calorimeters are used to measure the energies of all particles except for muons and neutrinos. Muons are minimum ionizing so they penetrate through to the muon spectrometer, while neutrinos are very weakly interacting and are not directly detected by ATLAS. The various calorimeters are situated outside the ID and cover a total acceptance of $|\eta| < 4.9$, as shown in the diagram of Fig. 3.5. The cells of the calorimeters, with the exception of the forward calorimeter, are arranged in projective towers of η and ϕ that point back towards the interaction point.

Sampling Calorimetry

Each of the calorimeters is a "sampling" calorimeter that contains alternating layers of active material and absorber into which incident particles deposit energy. Only energy in the active material, which results from particle interactions in both the active and absorber materials, is measured. These interactions occur through various processes, which include bremsstrahlung or "braking radiation", electron-positron pair production, and hadron-nucleon scattering. Their relative importance depends on the particle type,

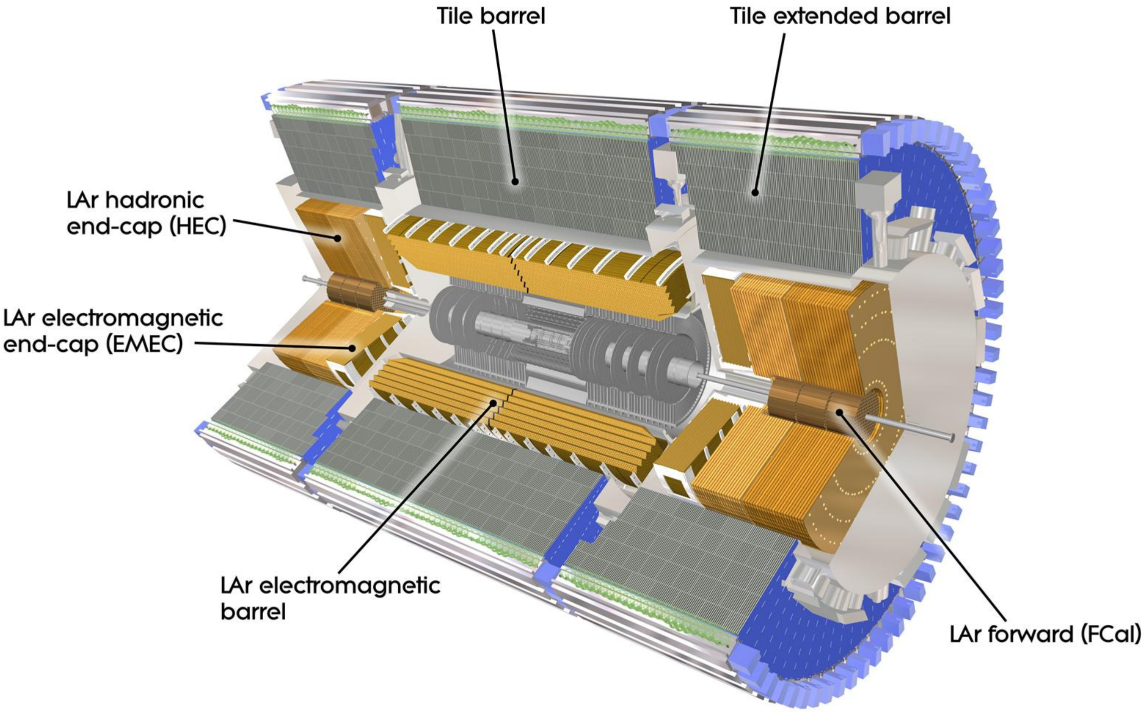

Figure 3.5: Illustration of the calorimeters: the barrel and endcap electromagnetic calorimeters, the barrel (tile) and endcap hadronic calorimeters, and the forward calorimeter [89].

its kinematics, and the absorber material. The ionization or scintillation light produced by the active material is proportional to the energy loss of the particle in the medium. The absorber material is very dense, giving it enough stopping power to prevent incident or secondary particles from penetrating outside the calorimeter at a significant rate.

Charged particles interacting electromagnetically deposit energy in the absorber through bremsstrahlung. The resulting photons produce pairs of electrons and positrons in the calorimeter, which in turn themselves radiate, and so forth. This recursive process produces an exponential cascade of "secondary" particles until the energies of the secondaries are sufficiently low that the energy loss of the electrons and photons in the medium dominates over radiative effects [106]. Since only the energy in the active material is measured, the particular shape of a given shower produces fluctuations in its energy measurement.

Response and Resolution

The performance of each calorimeter is characterized by its energy "response", which is the fraction of the energy of the impinging particle that is measured, and its "resolution", which is the spread in the response. The response depends on the "sampling fraction" $E_{\text{active}}/(E_{\text{active}} + E_{\text{absorber}})$, where E is the energy deposited by the particle. It is also impacted by energy deposited in calorimeter regions without instrumentation, as well as by energy lost in nuclear interactions. The latter causes the calorimeters to have a different response to hadrons than to electrons, an effect referred to as "non-compensation". Calibrations are applied to correct energy measurements for the response, which depends on the type and energy of the impinging particle.

The calorimeter energy resolution is equivalent to the spread in the energy measured for an incident particle of fixed energy, E. It is characterized by the equation:

$$\frac{\sigma_E}{E} = \frac{a}{\sqrt{E}} \oplus \frac{b}{E} \oplus c \tag{3.1}$$

where the symbol "$\oplus$" indicates a sum in quadrature. The first term is a "stochastic" term that reflects statistical fluctuations in the number of particles that are produced in the calorimeter shower and how many times their energies are measured. The impact of these inherent fluctuations generally dominate the resolution of the calorimeter over most of its useful energy range. The second or "noise" term results from noise in the electronics and limits the precision for measuring particles with low energy. The third or "constant" term, which arises from calibration errors and non-uniformities, dominates for very high-energy particles.

The calorimetry spans the region $|\eta| < 4.9$ and comprises both electromagnetic and hadronic calorimeters. The electromagnetic calorimeters are placed in front of the hadronic calorimeters because particles that interact only electromagnetically require less material to be absorbed. The depth of each electromagnetic calorimeter is measured in units of radiation length, X_0, which is the average distance an electron has to travel in the material before its energy is reduced to a fraction, $1/e$, of its initial value. Similarly, the depth of each hadronic calorimeter is quantified in terms of the nuclear interaction length, λ, which is the average length a hadron must travel before it collides inelastically with a nucleus. For lead, which is used as the absorber in the electromagnetic calorimeter, one radiation length is equivalent to 0.033 nuclear interaction lengths [45].

Electromagnetic Calorimetry

The electromagnetic calorimeters are used to identify photons and electrons, as well as to measure their energies. They have a high granularity in η and ϕ, and perform multiple measurements along the direction of the shower. Photons and electrons are identified as particles producing narrow showers that do not penetrate past the electromagnetic calorimeters [107]. The barrel and endcap electromagnetic calorimeters use liquid argon as the active material and lead as the absorber. Liquid argon provides high resistance to radiation and spatial uniformity for energy measurements. The first layer of the forward calorimeter is also designed to measure electromagnetic energy depositions and uses liquid argon as active medium, along with copper absorber. The stochastic term in the electromagnetic calorimeter energy resolution for photons and electrons is approximately 0.1 $\text{GeV}^{-1/2}$, and the constant term is about 0.002.

Hadronic Calorimetry

The hadronic calorimeters are designed to contain and measure the showers of high-energy hadrons. These hadrons deposit much of their energy in the electromagnetic calorimeters but are unlikely to be fully contained there. They are stopped by the hadronic calorimeters, which have a thickness of up to 10 nuclear interaction lengths. The tile calorimeter in the barrel uses polystyrene, a scintillating plastic, as active material and steel as absorber. Both the hadronic endcap calorimeter and the forward calorimeter use liquid argon as active material, which is more radiation tolerant than plastic. The HEC uses copper absorber, while the FCal uses tungsten as absorber material. Together with the electromagnetic calorimeters, they precisely measure jet energies down to 20 GeV, with a linear response at high jet energies. In the barrel and endcaps, the jet energy resolution is characterized by a stochastic term of around 0.5 $\text{GeV}^{-1/2}$ and a constant term of about 0.05. In the forward region, the stochastic and noise terms are a bit larger than those in the barrel and endcaps due to design constraints from limited space and the high radiation environment. Forward jets have a higher energy for a given p_{T} however, so they are measured with a similar performance as those in the central region.

Calibration

The electromagnetic energy scale of the calorimeters is obtained by calibrating the electronic signals from the detector to the energy deposited by electromagnetic showers. This calibration is based on test-beam measurements of electrons in the EMB [108, 109, 110, 111] and EMEC [112, 113] calorimeters.

The hadronic calorimeters are calibrated using “test beams” of electrons, hadrons [114, 115, 116], and muons [115, 117], as well as cosmic ray muons [6]. The invariant mass of the Z boson in decays to electron-positron pairs is measured using proton-proton collision data, and is used to further adjust the calibration in the electromagnetic barrel, electromagnetic end-cap, and forward calorimeters.

3.4.2 Electromagnetic Calorimeter

The electromagnetic calorimeter, which is shown in Fig. 3.5, uses liquid argon as the active medium and lead as absorber. It is used to identify electrons and photons in the region $|\eta| < 3.2$, albeit with lower performance beyond the ID acceptance of $|\eta| < 2.5$. Incident charged particles ionize the liquid argon and the collected charge is used to infer the energy of the incoming particle. Photons produce electron-positron pairs that create an ionization signal. Hadrons also shower within the dense lead absorber, but are not contained by the electromagnetic calorimeter.

The EM calorimeter consists of three components. The electromagnetic barrel (EMB), which extends radially across $1250\text{ mm} < r < 2050\text{ mm}$ and longitudinally within $|z| < 3100\text{ mm}$ along the beam axis, covers the region $|\eta| < 1.475$. The electromagnetic endcaps (EMEC) on each side of the interaction point cover the region $1.375 < |\eta| < 3.2$. Each endcap is situated at $|z| = 3700\text{ mm}$ and is composed of two coaxial "wheels". The outer wheels extend to $|\eta| = 2.5$, while the inner wheels cover the region up to $|\eta| = 3.2$.

The calorimeter is divided along the direction of the shower into three layers for the region $|\eta| < 2.5$ and two layers outside this acceptance. The η direction of the first layer is finely segmented in order to provide a precise measurement of the position of photons. The thickness of the first layer is about four radiation lengths, so most of the energy is deposited in the second layer, which is about 17 X_0 thick. The second layer has a very fine segmentation of $\Delta\eta \times \Delta\phi = 0.025 \times 0.025$. The last layer, which has a thickness between 1–10 X_0 and contains the tails of the electromagnetic shower, has a coarser segmentation.

The total thickness is at least 22 X_0, ranging from 22–30 X_0 in the region $|\eta| < 0.8$ and from 24–33 X_0 in the region $0.8 < |\eta| < 1.3$. This ensures that even high-energy electrons and photons are well-contained within the calorimeter.

In the region $|\eta| < 1.8$, a presampler consisting of a thin layer of instrumented liquid argon serves as the active layer that complements the passive material in front of the calorimeter. The barrel presampler covers the full acceptance $|\eta| < 1.475$ of the barrel portion of the EM calorimeter, being situated inside its cryostat. The end-caps of the presampler are located before the EM endcaps, but only cover the region $1.5 < |\eta| < 1.8$. In this subset of the end-cap acceptance, which has a larger amount of passive material due a gap where services are routed, the presampler provides additional measurements.

Cryostats house each of the barrel and endcap portions. Liquid nitrogen is used to hold the cryostats at a constant temperature of about 89 K, at which argon is a highly pure liquid at ambient pressure. Signal and high-voltage cables carry services from outside the cryostat.

The sampling layers have an "accordion" structure consisting of lead absorber plates clad with stainless steel, arranged in a zig-zag shape radially from the beam. This provides a finely segmented read-out and full ϕ coverage. The geometry of the accordion structure is designed to produce high azimuthal uniformity and constant sampling fraction. The folding angle in the barrel portion of the EM calorimeter decreases with depth, with a similar variation in amplitude in the end-caps. The thickness of the absorber plates is 1.53 mm in the region $|\eta < 0.8$, and decreases to 1.13 mm for $|\eta| > 0.8$ to limit the decrease in sampling fraction. In the end-cap, the thickness is 1.7 mm for $|\eta| < 2.5$ and 2.2 mm beyond this.

Read-out electrodes supported by honeycomb spacers are situated in the gap between absorber plates as shown in Fig. 3.6. In the barrel, the electrodes are 2.1 mm away from

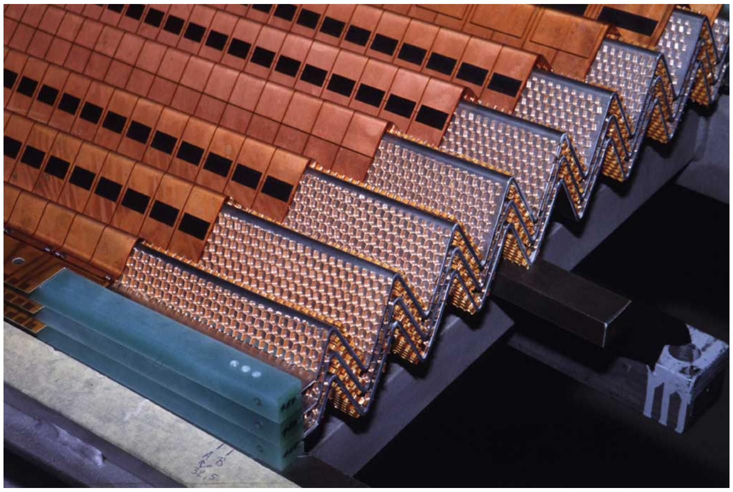

Figure 3.6: Accordion absorbers and electrodes in the barrel of the electromagnetic calorimeter [89].

the absorbers. They are operated at 2000 V to collect the charge ionized from the liquid argon by incident particles, yielding an average drift time of about 450 ns.

Summing boards form cells by combining the signals from electrodes in adjacent gaps. The signals from several summing boards are routed and calibrated by a motherboard. The signals are amplified and shaped by the front-end electronics into a bipolar pulse shape, which is illustrated in Fig. 3.7.

The pulse shape is sampled every 25 ns up to 32 times. The first five samples are used to extract the signal, whose peak height is proportional to the energy deposited by the incident particle. The samples in the tail of the pulse drop below the baseline, canceling the energy contributed by later bunch crossings. By effectively redefining the baseline of the energy measurement, the sensitivity to background from additional proton-proton collisions is reduced. The predicted pulse shapes are validated against the measured pulse shapes using data from cosmic ray muons [118] and in-situ studies.

The digital signals are converted to optical signals for robust transfer between elec-

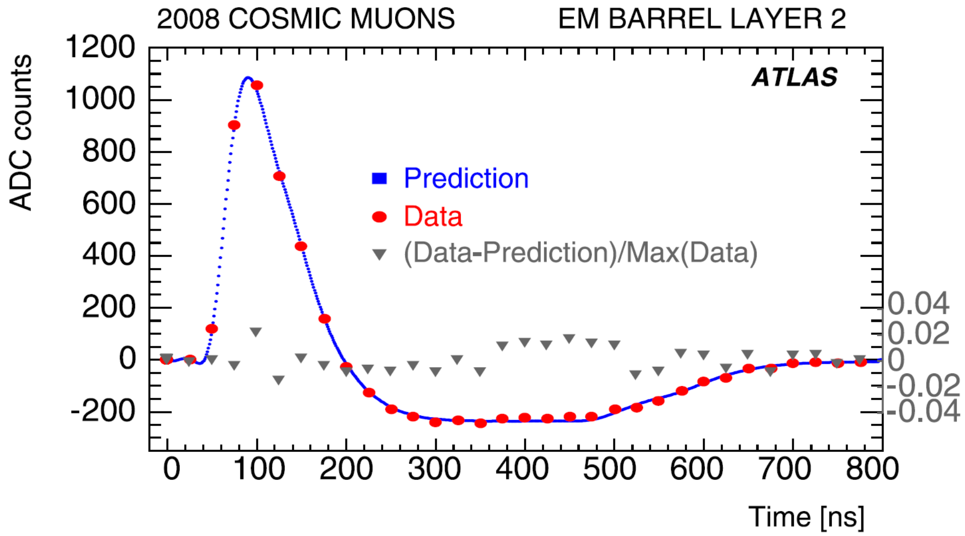

Figure 3.7: Predicted and measured pulse shapes for a signal deposited by a cosmic ray muon in the second layer of the barrel portion of the electromagnetic calorimeter [119]. The pulse shapes are sampled every 25 ns and are shown in units of ADC counts.

tronics. Some of the optical transmitters failed in 2010, so the energies of the affected cells are estimated using measurements from the level-1 calorimeter trigger measurements (see Sec. 3.8). Each signal pulse is calibrated so that its height corresponds to the deposited energy [120], and its timing and shape are computed for use later as quality criteria. The front-end electronics also performs the hardware-level trigger decisions, including the jet triggers (see Secs. 3.7 and 6.2.3).

3.4.3 Hadronic Calorimeters

Tile Calorimeter

The tile calorimeter, which is shown in Fig. 3.5, has polystyrene tiles for its active medium and steel absorber plates. It augments the EM calorimeter by measuring the energies of hadrons with $|\eta| < 1.7$. Its barrel portion covers $|z| < 2.9$ m along the beam axis, while its two extended barrels cover 2.9 m$< |z| <$5.5 m. The barrel portion is situated outside the EM barrel calorimeter, while the extended barrel is located outside the cryostats housing the endcap and forward calorimeters. Scintillating tiles in the gap between the barrel and extended barrel serve as active medium for the non-instrumented material from the services in the gaps.

The tile calorimeter extends radially across 2.28 m $< r <$ 4.25 m. Its outer steel support structure enables the flux return of the solenoidal field and stores the read-out electronics. The tile calorimeter is operated at room temperature, although the read-out electronics are cooled. It is segmented along the shower into three layers that provide measurements of the longitudinal shower shape. The three layers have respective thicknesses of about 1.5, 4.1, and 1.8 λ at $\eta = 0$, as shown in Fig. 3.8. The layers are grouped longitudinally into towers with an angular granularity of $\Delta\eta \times \Delta\phi = 0.1 \times 0.1$ in all layers except for the last one, which has a granularity of 0.2 in η. Sixty-four azimuthal wedges in ϕ referred to as "modules" are each formed from nine towers along η.

The tile calorimeter absorber consists of 5 mm thick steel plates extending from the front to the back of the calorimeter, with smaller 4 mm thick spacer plates staggered radially. Polystyrene tiles with a thickness of 3 mm are inserted between them, spanning the radial distance 97 mm $< r <$ 187 mm. The structure of the tile calorimeter is illustrated in Fig. 3.9. Particles showering in the calorimeter cause the plastic scintillators to produce ultraviolet light, which is converted to visible light by wavelength-shifting fibers. The fibers carry the signals to photomultipliers (PMTs) in the calorimeter support structure, where they are combined.

The photomultiplier converts the light into an electrical signal, which it amplifies through a series of avalanche dynodes. The signal is further amplified in the front-end electronics, which then shapes the pulse into a near-Gaussian waveform such that the peak

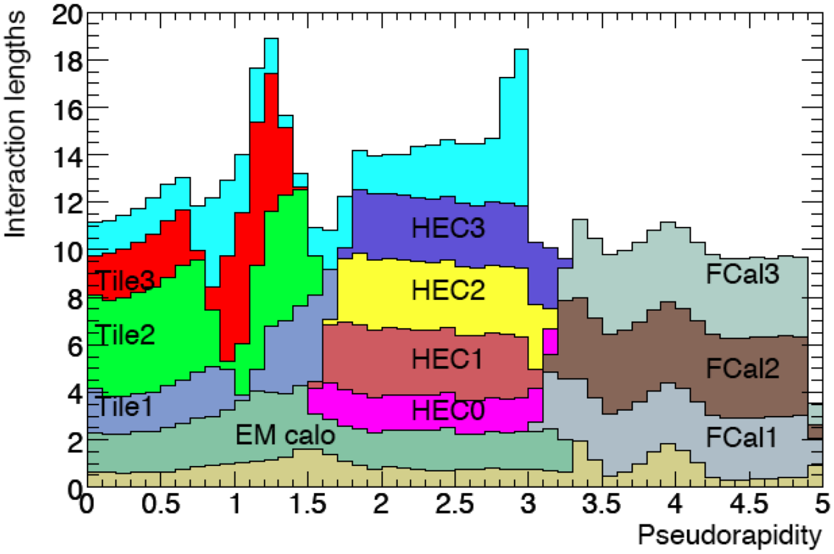

Figure 3.8: Material in units of nuclear interaction lengths in each layer of the barrel (Tile), endcap (HEC), and forward (FCal) hadronic calorimeters, as well as in the electromagnetic (EM) calorimeter, as a function of pseudorapidity [89]. The amount of material before the calorimeters is shown in beige as the first of the stacked histograms, and the material in the support structure before the muon spectrometer is shown in cyan as the last histogram.

height is proportional to the energy deposited. One of two branches in the electronics sums the signals for use in the fast trigger output, while the other branch passes the signal to a digitizer that discretely samples the waveform every 25 ns for the read-out. The digital signals are converted to optical signals and transferred to read-out drivers if the event is accepted by the trigger.

Hadronic Endcap Calorimeter

The hadronic endcap calorimeter, which measures the energies of hadrons within the region $1.5 < |\eta| < 3.2$, uses an active medium of liquid argon and copper as absorber. Liquid argon is used because it is less susceptible to radiation damage than the polystyrene used in the hadronic barrel, which will degrade and become opaque at higher luminosity.

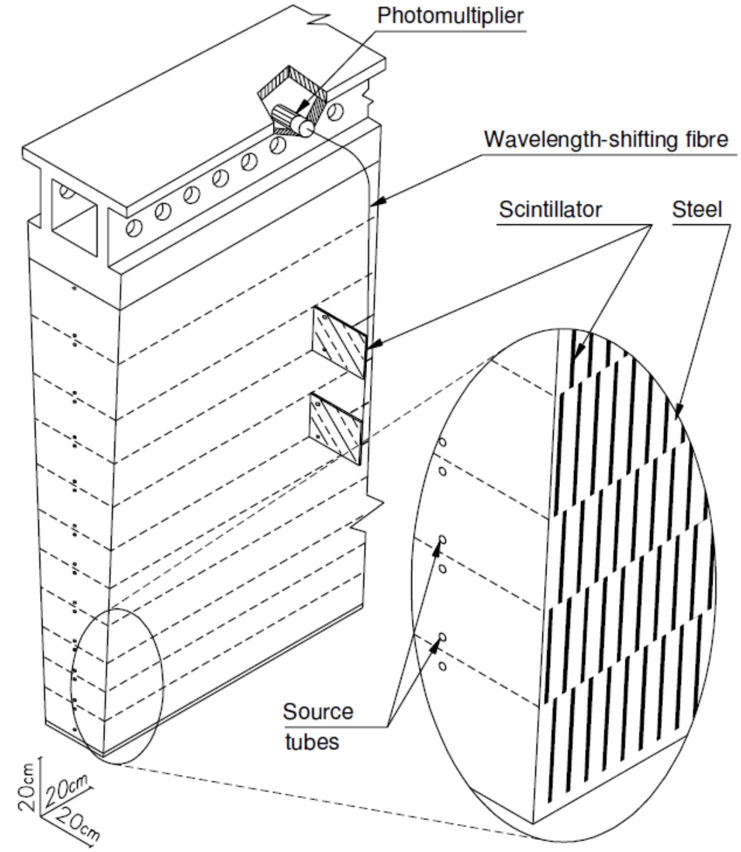

Figure 3.9: Illustration of the tile calorimeter structure showing the staggered steel absorber plates and scintillators [89]. Light from the scintillators is collected by wavelength-shifting fibers, and the signals are read out and amplified by photomultipliers.

The calorimeter consists of two end-caps, each of which is composed of two cylindrical "wheels" along the beam axis with an outer radius of 2030 mm. The two wheels have inner radii of 372 mm and 475 mm, respectively. The end-caps span the approximate region 4.3 m $< |z| <$ 6.1 m along the beam axis.

Unlike the accordion geometry of the EM endcaps, the HEC absorber consists of copper plates that are oriented perpendicular to the beam direction. The front plates are 12.5 mm thick, while the back plates are much thicker at 50 mm. Read-out electrodes operated at a voltage difference of 1800 V are situated in the 8.5 mm gaps between the copper plates, resulting in a drift time of about 400 ns. The read-out has a segmentation of $\Delta\eta \times \Delta\phi = 0.1 \times 0.1$ for $|\eta| < 2.5$ and 0.2×0.2 beyond this. It is also segmented into four layers along the longitudinal direction of the shower, and their thicknesses are shown in Fig. 3.8.

The amplification, shaping, digitization, and electrical-to-optical conversion of the signals is similar to that of the EM calorimeter already described in Sec. 3.4.2. The two calorimeters also share the same environment.

3.4.4 Forward Calorimeter

The forward calorimeter [121] serves as both an electromagnetic and hadronic calorimeter. It measures the energies of all particles, except for muons and neutrinos, within the region $3.1 < |\eta| < 4.9$. It is designed to cope with the high radiation doses sustained at these large pseudorapidities. A high radiation tolerance is achieved by using liquid argon as the active medium, with copper and tungsten absorbers. The calorimeter is constrained to a small form factor because the solid angle corresponding to one unit of pseudorapidity falls steeply with increasing η and because it shares a cryostat with the HEC calorimeters. Its size is minimized by maximizing the amount of absorber compared to active material, at the expense of a lower sampling fraction and response.

The calorimeter consists of two end-caps, one on each side of the interaction point. Each endcap is segmented into three layers along the beam axis. Each layer has a thickness of 45 cm along the beam in $|z|$ and spans a radial distance of 7 cm $< r <$ 45 cm. The first layer, which is situated at approximately $|z| = 470$ cm from the interaction point, measures electromagnetic energy depositions using a copper absorber with a thickness of 27.6 radiation lengths. The second and third layers measure the energies of and fully contain hadrons using a tungsten absorber, which has a thickness of about 3.6 nuclear interaction lengths in each layer. A block of copper alloy is situated behind the third layer to shield the muon system.

The FCal structure consists of a hexagonal array of liquid argon gaps embedded in a matrix of absorber material. Each layer is composed of a stack of absorber plates with holes drilled through the stack. Within each hole, a hollow tube made of copper serves as the cathode, as shown in Fig. 3.10. An anode rod made of the absorber material is positioned concentrically within the cathode, producing a pair of concentric cylindrical electrodes. The annular gap between the two electrodes, which are separated by a distance ranging from 0.269 mm in the first layer to 0.508 mm in the last layer, is filled with liquid argon. A helix of radiation-hard plastic fiber is also placed in the gap to ensure that the outer cathode and inner anode remain electrically isolated. The electrodes are operated at a voltage difference of up to 600 V, resulting in a drift time of 60–120 ns before ionization charge is collected from incident particles.

The FCal environment and read-out chain are similar to those of the EM and HEC calorimeters, which are already described in Sec. 3.4.2.

3.5 Muon Spectrometer

3.5.1 Overview and Performance

The muon spectrometer is an air-toroid system that defines the overall shape of the ATLAS detector and is illustrated in Fig. 3.11. Muons are bent in a plane of constant azimuth by a toroidal magnetic field ranging between 0.5–1 T, which is supplied by eight coils in the barrel and in each endcap. Their curved trajectories are measured by four types of detectors: monitored drift tubes (MDT), cathode strip chambers (CSC), resistive plate

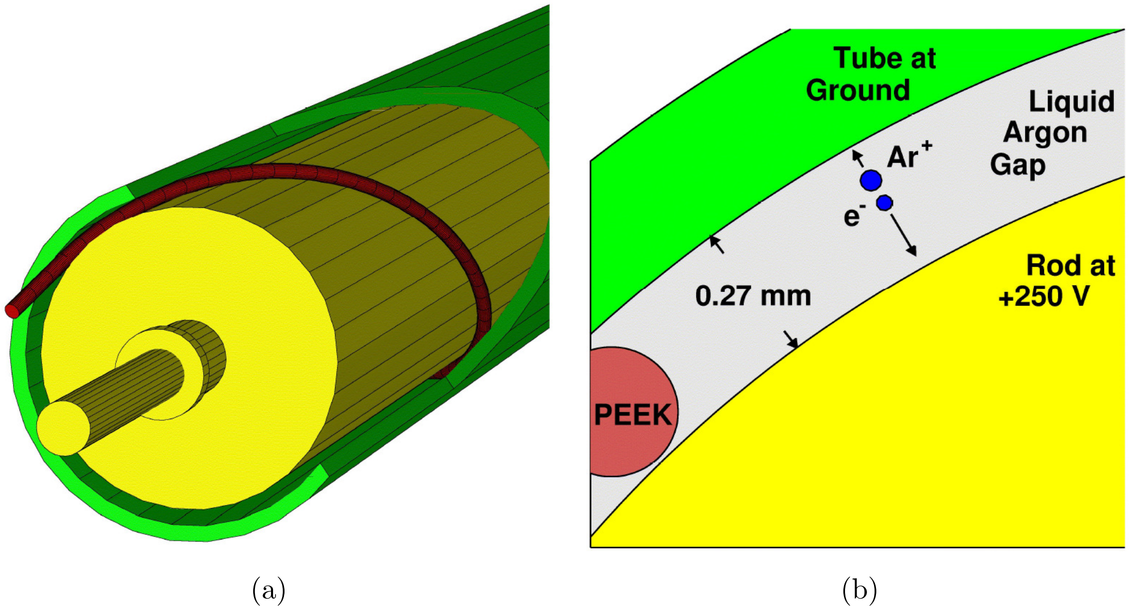

(a) (b)

Figure 3.10: Cut-away drawing of an FCal electrode (a). The green cylinder is the cathode tube, the yellow cylinder is the anode rod, and the red helical structure is the insulating fiber. Liquid argon fills the gap between the two electrodes. A close-up view of the cross-section of the electrode gap in FCal1, the first layer of the FCal, is also shown (b). The insulating ("PEEK") fiber is indicated. [121]

chambers (RPC), and thin gap chambers (TGC). These detectors measure the momenta of muons down to about 5 GeV and can identify the charge up to about 3 TeV.

Precision chambers comprising MDT and CSC detectors are arranged into three layers from the end of the calorimeters, at a radius of about 5 m from the interaction point, to a radius of around 10 m. The chambers span the approximate region 0.15 m $< |z| <$ 23 m along the beam axis, where the gap $|z| <$0.15 m allows services for other detectors to be routed. Thus the chambers cover the range $|\eta| < 2.7$, except for a small region near $\eta = 0$. For the first endcap layer, closest to the interaction point, CSC detectors are used instead of MDT detectors because they can cope with higher fluences. Since the precision chambers have a long charge collection time, trigger chambers comprising RPC and TGC

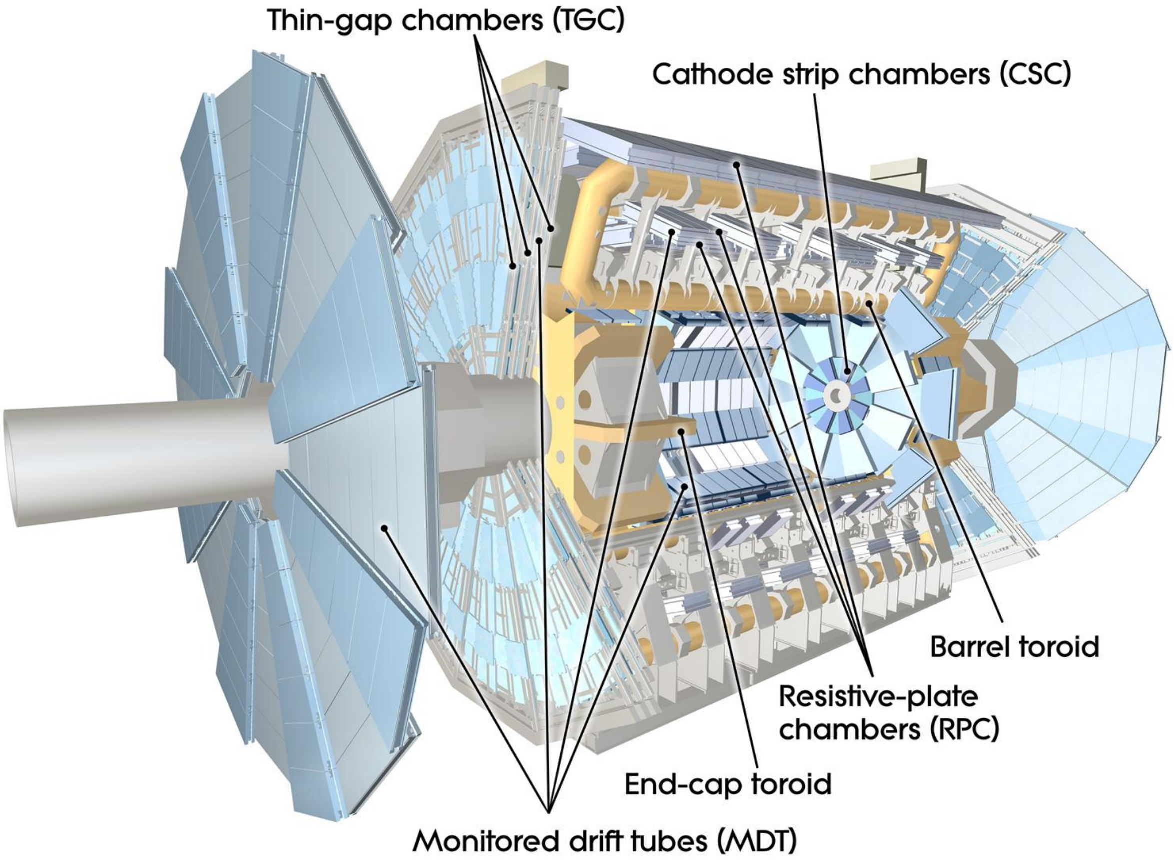

Figure 3.11: Illustration of the subsystems of the muon spectrometer: the monitored drift tubes, thin gap chambers, resistive plate chambers, and cathode strip chambers [89]. The barrel and endcap toroid magnets are also shown.

detectors provide fast measurements for the trigger to decide whether to accept an event. RPC detectors with finer spatial resolution are used in the barrel, while TGC detectors with higher radiation hardness are used in the end-caps.

Cosmic ray data taken during 2008 and 2009 have been used to characterize the muon reconstruction efficiency and tracking performance [122]. The reconstruction efficiency is approximately 97%, excluding the poorly instrumented region near $\eta = 0$ where services exit the detector. Muons in the central region $|\eta| < 1.1$ are measured to have a transverse momentum resolution:

$$\frac{\sigma(p_{\mathrm{T}})}{p_{\mathrm{T}}} = \frac{(0.29 \pm 0.03)\mathrm{GeV}}{p_{\mathrm{T}}} \oplus (0.043 \pm 0.002) \oplus (4.1 \pm 0.4) \times 10^{-4}\,\mathrm{GeV}^{-1} \times p_{\mathrm{T}} \quad (3.2)$$

The first term arises from the uncertainty in the energy loss of the muon as it crosses the detector, so it is inversely proportional to the muon p_{T}. The second term is a "constant term" that represents the uncertainty from multiple scattering. The third term represents the intrinsic resolution of the track to due to measurement error, so it is proportional to the muon p_{T}.

Soft muons at low momenta are measured with a resolution of about 4%, which is dominated by the first term. This is improved to 2% if the muon system and ID measurements are combined. The best stand-alone resolution (3%) is attained for 100 GeV muons and is dominated by the middle term. Energetic muons with momenta of 1 TeV are measured with a stand-alone resolution of 10%, dominated by the last term.

3.5.2 Toroids

Toroid magnets embed the muon chambers in a magnetic field ranging between 0.5–1 T. The magnets consist of eight rectangular coils in the barrel and in each end-cap, housed within cryostats. The barrel coils are more than 10 m wide and about 25 m long. The end-cap coils have a similar width and a length of 5 m, and are situated about 1.65 m from the beam. All of the coils are made of a mixture of aluminum, niobium, titanium and copper. They are cooled using liquid helium to their operating temperature of 4.5 K. They are operated at a current of 20.5 kA and produce a maximum field of about 4 T in the coil windings. Non-uniformity of the toroidal field affects the momenta resolution that can be attained by the muon system.

3.5.3 Precision Chambers

Monitored drift tubes and cathode strip chambers provide three precise measurements for muons within the region $|\eta| = 2.7$ and can resolve the bending coordinate to about 50 μm. The barrel portion consists of three concentric cylinders with radii between 5 m $< r <$ 7.5 m. They have a small gap near $\eta = 0$ to allow service cables for the ID and calorimeters to exit the ATLAS detector. Each end-cap consists of four wheels situated between 7 m $< |z| <$ 21 m along the beam axis, and the last wheel has an outer radius of 12 m.

Each MDT detector has a drift tube of diameter 3 cm that contains a pressurized mixture of argon and CO_2. A tungsten-rhenium wire with a diameter of 50 μm is operated at a voltage of 3 kV and collects charge ionized by muons. The drift time, which is less than 700 ns, is used to infer the muon position. The MDT detectors are organized in 16 sectors following the toroid shape. Long and short chambers in each sector are staggered along the radial direction to provide full azimuthal coverage. Analog electronics amplify, shape, and discriminate the signal from each drift tube. A time-to-digital converter (TDC) performs further signal processing and adds a time stamp.

Each CSC detector is a multi-wire proportional chamber with a mixture of argon and CO_2. Radially oriented wires sandwiched by strip cathodes are operated at a voltage of 1900 V, and the electrodes collect charge ionized by muons. The strip cathodes are 5 mm apart, resulting in a maximum drift time of 40 ns. Each end-cap contains two disks of eight chambers each, where long and small chambers are staggered in z along the beam axis. The readout electronics are similar to those of the MDTs.

3.5.4 Trigger Chambers

Resistive plate chambers and thin gap chambers provide fast position and momentum measurements to trigger on muons within the region $|\eta| < 2.4$. RPCs cover the central region $|\eta| < 1.05$, while TGCs extend the coverage to larger psuedorapidities.

In the barrel, RPCs are arranged in three concentric cylinders with the toroidal shape. Each RPC detector consists of two parallel electrode plates with an electric field applied between them, and is filled with a gas mixture of $C_2H_2F_4$. The plates are 2 mm apart and are operated with a voltage difference of 9.8 kV, resulting in a maximum drift time of about 5 ns. Read-out strips with a width of 25–35 mm are situated along η and ϕ on the outside of each resistive plate.

In each endcap, TGCs are arranged in four layers, each of which consists of two concentric disks within a wheel. Each TGC detector is a multi-wire proportional chamber similar in principle to a CSC, but with a gas mixture of nearly equal parts CO_2 and n-C_5H_{12}. The anode wires are operated at a voltage of 2.9 kV and collect charge from ionization. The strip cathodes are 1.8 mm apart, and the anode wire is 1.4 mm away from the cathode. The anode wire signal determines the bending coordinate of the muon, while the cathode strip signal determines ϕ. The wires are read out in groups to achieve a uniform momentum resolution as a function of η.

The readout electronics for both types of trigger chambers (RPCs and TGCs) are analogous to those of the precision chambers (MDTs and CSCs). They provide amplification, shaping, and discrimination of the signal.

3.6 Forward Detectors

Forward detectors are used, along with the ID, to measure the luminosity delivered by the LHC and recorded by ATLAS. These detectors comprise the minimum bias trigger scintillators (MBTS) [4, 2], the beam condition monitors (BCM) [123], and the luminosity Cerenkov integrating detector (LUCID) [124]. They are used to determine the relative luminosity, which is then absolutely normalized using a beam separation scan [125] (see Sec. 6.5).

3.6.1 Minimum Bias Trigger Scintillators

The MBTS system, illustrated in Fig. 3.12, is designed to trigger on proton-proton collisions with high efficiency and low sampling bias. The MBTS consists of 32 trapezoidal scintillators that are each made of polystyrene and have a thickness of 2 cm. The scintillators are organized into two octagonal disks, one on each side of the interaction point. The disks are situated in front of the endcap electromagnetic calorimeter at $|z| = 3.56$ m, subtending the region $2.09 < |\eta| < 3.84$. Each disk consists of two concentric octagonal rings, where each ring is composed of eight scintillators arranged along ϕ. The scintillators in the inner section are smaller and cover the region $2.09 < |\eta| < 2.82$. The outer scintillators are larger, extending out to a radius of 88 cm and covering the region $2.82 < |\eta| < 3.84$. Each scintillator is read out through wavelength-shifting fibers that carry light to a PMT. Analog electronics designed for the tile calorimeter, but whose gain has been increased by a factor of 64 to process the small signals from the MBTS, provide amplification, shaping, and discrimination of the signal. Each PMT signal exceeding a preset threshold is recorded as a single hit.

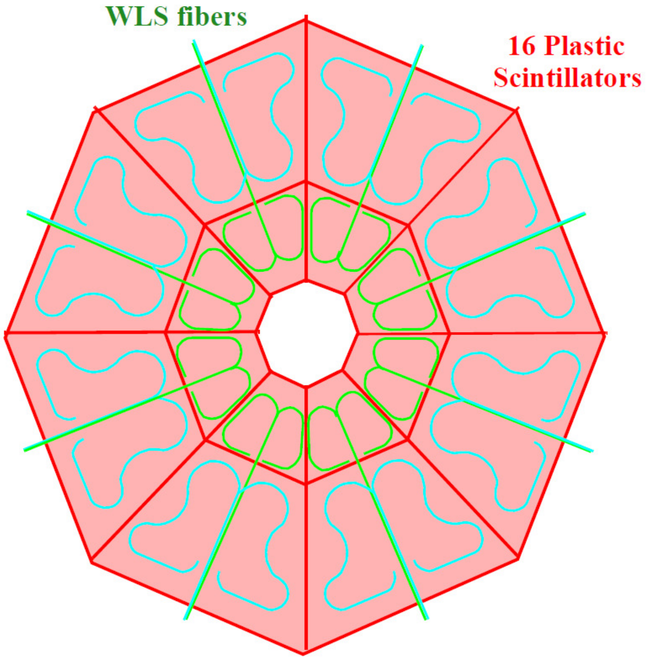

Figure 3.12: Illustration of 16 plastic scintillation counters forming one of the two MBTS disks on each side of the detector [2, 4]. Wavelength-shifting fibers collect light from the scintillators.

3.6.2 Beam Condition Monitors

The BCM system is primarily designed to monitor the proton beams for beam losses that could cause damage to detectors, particularly the pixel detector. If large beam losses are detected, it instructs the LHC to dump the beam in a controlled fashion.

The BCM consists of four small diamond sensors, one pair on each side of the interaction point at $|z| = 1.84$ m. They are arranged around the beampipe in a cross pattern at a radius of 5.5 cm, which corresponds to $|\eta| = 4.2$. The sensors have dimensions of 1 cm×1 cm with a thickness of 500 μm, and are operated at a voltage of 1000 V. They are made of diamond because it is radiation hard, produces a fast signal, and allows the detector to be operated at room temperature without cooling.

3.6.3 Luminosity Cerenkov Integrating Detector

LUCID is a Cerenkov detector specifically designed to monitor the luminosity. It comprises sixteen mechanically polished aluminum tubes, filled with C_4F_{10} gas, on each side of the interaction point at $|z| = 17$ m. The tubes, which are 1.5 m long and 15 mm in diameter, are arranged around the beampipe and cover the region $5.6 < |\eta| < 6.0$. Charged particles create Cerenkov photons that are reflected by the tube walls until they reach PMTs at the end of the tubes. Each PMT signal exceeding a preset threshold is recorded as a hit.

3.7 Trigger and Data Acquisition

The Trigger and Data Acquisition (TDAQ) system selects and records interesting events for offline analysis. The trigger performs online event selection in three sequential stages or "levels": level 1 (L1), level 2 (L2), and Event Filter (EF). The online data flow is illustrated schematically in Fig. 3.13 and is described below.

The L1 stage [126] uses hardware-based algorithms and measurements from the calorimeter and muon systems to decide whether to accept or reject an event. The L2 and EF stages, which are grouped together into the High Level Trigger (HLT) [127, 128], incorporate additional information from the inner detector. The HLT uses software algorithms that run on a farm of massively parallel commercial processors. Because the data bandwidth and CPU time available are tightly constrained at each stage, the online algorithms are optimized for speed and robustness rather than precision. Data satisfying criteria useful for detector calibration or physics analysis are permanently stored on disk.

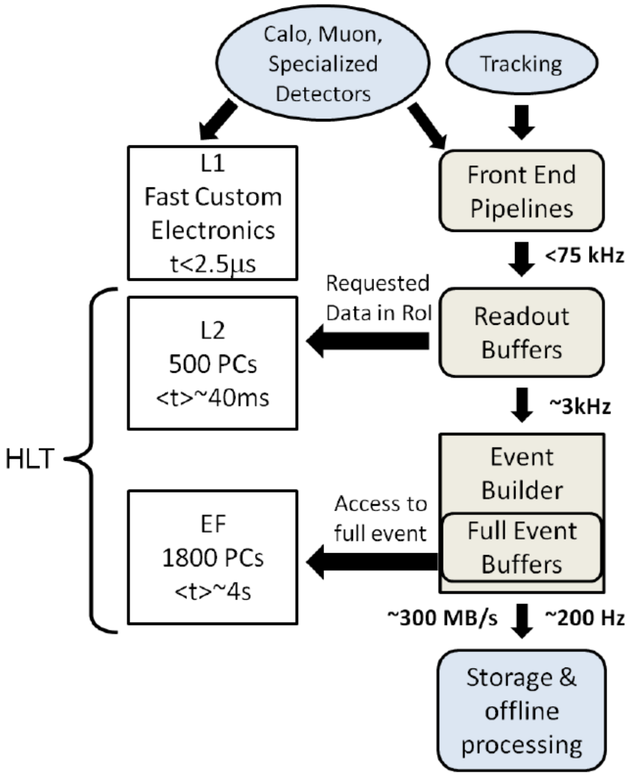

Figure 3.13: Flow chart of the online event selection in the trigger and data acquisition system described in the text [3]. Information of varying granularity from the calorimeters, muon spectrometer, and inner detector are buffered in the read-out system and used at different stages to decide whether to accept an event. Three successive stages – level 1 (L2), level 2 (L2), and event filter (EF) – are used to reduce the final rate of recorded events to approximately 200 Hz.

3.7.1 Level-1 Trigger

The first stage of the trigger system is the level-1 trigger. The L1 trigger can accept up to 75,000 events per second, resulting in a short time window of 4.5 μs within which to decide whether to select or reject an event. It accomplishes this by using information of coarse granularity from the calorimeters and muon trigger chambers, as well as the MBTS; no information from the ID is used. This allows it to select events that may contain electrons, photons, τ leptons, jets, and muons. Events with a large amount of transverse energy or with substantial missing transverse energy can also be selected. The data from each detector is processed by electronics and then sent to the central trigger processor (CTP) [129].

The CTP implements a "menu" that defines the criteria for the trigger decision, which include kinematic thresholds applied to each trigger object or simple combinations of objects. The trigger menu also defines the "prescale", P, that is applied to each trigger. Each trigger only accepts 1 out of every P events, so the prescale controls the rate at which events are accepted. Events that pass the L1 trigger are forwarded by the CTP to the L2 processors.

3.7.2 Level-2 Trigger

The second stage of the trigger system is the level-2 trigger. The L2 trigger has an output bandwidth allocation of 3,500 events per second, but is permitted a substantially larger latency than that for L1. This allows the L2 stage to use information with the full granularity of all the detector subsystems to decide whether to accept an event. These high precision measurements are taken at the L1 "regions of interest" (RoIs) from each detector and are analyzed using more complex algorithms than the hardware-based ones at L1. They include measurements from the inner detector, whose data are used to reconstruct tracks and vertices of charged particles. If an event is accepted, the L2 information is compactified into one data structure by "event building" processors and then forwarded to the EF stage.

3.7.3 Event Filter

The EF is the third and final stage of the trigger system. The EF can accept up to 200 events per second to be recorded to disk for offline analysis. Since its required latency is about 3 seconds, the entire event can be processed with the full detector granularity, instead of only a restricted region as at L2. In addition, the EF processors can run complex and time-consuming algorithms, including those used for offline tracking and jet reconstruction. Events accepted by the EF are divided into a number of inclusive streams, each of which is based on particular trigger requirements that target a specific physics topic. The streams also include a "debug" stream of rare events that take too long to process, as well as a low-rate "express stream" with a broad range of events that are used to calibrate the detector.

3.7.4 Data Acquisition

Data is taken in a series of "runs", which delineate the start and end of each period of data acquisition. A run generally starts at the beginning of an LHC fill and ends when the beam is dumped. Each run is measured in "luminosity blocks", the basic unit of time for data acquisition, where each luminosity block has a typical duration of 2 minutes. The trigger menu can be changed in real time to accommodate hardware problems or changes in beam conditions occurring over the course of a run, for example by changing the trigger prescales.

The efficiency associated with the data acquisition in 2010, which is defined as the fraction of the luminosity delivered by the LHC in 2010 that was recorded by ATLAS, is shown in Fig. 3.14. The luminosity-weighted efficiency integrated over this period is very high at 93.6%.

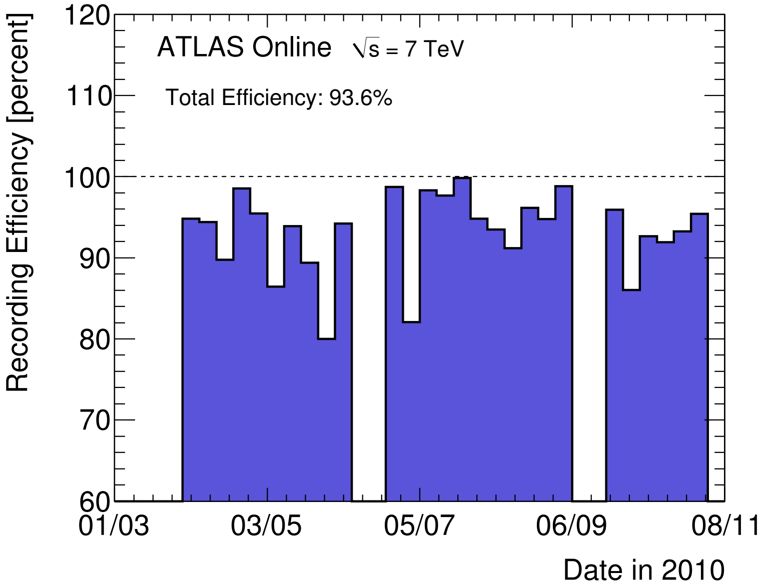

Figure 3.14: Data-taking efficiency in 2010. The denominator is the luminosity delivered between the declaration of stable beams and the LHC request to turn the sensitive detectors off to allow a beam dump or beam studies. The numerator is the luminosity recorded by ATLAS.

3.8 Detector Conditions and Data Quality

All events accepted by the trigger first undergo a “prompt reconstruction” and are written on tape so that the data quality can be assessed. The beam and detector conditions in the reconstruction software are determined using the express stream. The physics streams then undergo “bulk reconstruction”, typically within 36 hours after the end of a run. The reconstructed data is permanently stored on disk for usage in offline analysis. The data is periodically reprocessed offline to reflect increased understanding of the detector conditions and newer versions of the offline software.

The quality of the 2010 data sample is generally very high. The efficiency associated with the data quality, which is defined as the luminosity-weighted fraction of data taken with stable beams that also satisfies criteria for high quality, is shown for each detector

Detector		Data Quality Efficiency
Inner Detector	Pixel	99.1%
	SCT	99.9%
	TRT	100%
Calorimeters	EM	90.7%
	Tile	100%
	HEC	96.6%
	FCal	97.8%
Muon Spectrometer	MDT	99.9%
	RPC	99.8%
	CSC	96.2%
	TGC	99.8%

Table 3.1: Luminosity-weighted relative fraction of good quality data delivered by the various ATLAS subsystems during LHC fills with stable beams in pp collisions at $\sqrt{s} = 7$ TeV, and after switching the tracking detectors on. Runs between March 30 and October 31, 2010, corresponding to a recorded integrated luminosity of 45 pb^{-1}, are included.

in Table 3.1. The efficiency is generally well above 95%, except for the EM calorimeter, which experienced isolated HV trips and noise bursts.

In the high-quality data, there are two problems that slightly degrade the calorimeter measurements. These defects are spread out throughout the calorimeters, only impacting a few percent of the calorimeter cells. In the electromagnetic calorimeter, there are several optical transmitters that failed. The energies in the affected cells are estimated using measurements from the level-1 calorimeter trigger, whose read-out is completely analog. The corrections are only applied for calorimeter towers whose energies measured at the trigger and offline levels differ by more than 2 GeV. This results in a marginally worse calorimeter energy resolution in these regions. In the tile calorimeter, a few of the 256 power supplies failed. This is remedied by estimating their cell energies using the energy deposited in nearby cells that were operational. The energy corrections, which are less than 20% for over 99.9% of jets, are validated using Monte Carlo simulation.

3.9 Detector Simulation

The detector is modeled using a detailed simulation, based on GEANT4 [130], that accurately describes the detector material and geometry [131]. For the calorimeters, the Quark Gluon String model [132] is used to describe the fragmentation of the nucleus, and the Bertini cascade model [133] is used for the description of the interactions of the hadrons in the medium of the nucleus. The parameters in GEANT4 were tuned using data taken where each subdetector was studied with test beams of particles [114, 115, 116]. The test beam energies and particle types are representive of those in proton-proton collisions.

Cosmic ray muons are used to validate the modeling of the ID alignment in the detector simulation [134]. Collision data is also used to validate the modeling of the detector geometry, its material, and interactions of particles in the detector [135, 136, 7, 137, 138]. Detector failures, such as the power supply failures in the tile calorimeter and the optical transmitter failures in the electromagnetic calorimeters (see Sec. 3.8), are modeled by the simulation and validated using in-situ studies. A system of "Hall probes" [139] and nuclear magnetic resonance probes [140] is used to map the solenoidal and toroidal magnetic fields [141] and to validate their modeling in the simulation. The beam conditions, such as the position and intensity of the colliding beams, are also modeled.

In general, the simulation conditions are chosen to be representative of those with which the data in this thesis have been taken. Any residual differences between the simulation and data conditions are quantified using in-situ studies. The impact of the discrepancies are assigned as systematic uncertainties on the corrections applied to the data to correct for detector effects (see Sec. 7.9).

CHAPTER 4

MONTE CARLO SIMULATIONS AND THEORY PREDICTIONS

> *"The mathematical framework of quantum theory has passed countless successful tests and is now universally accepted as a consistent and accurate description of all atomic phenomena."*
>
> — Erwin Schrödinger (Nobel Prize in Physics, 1933)

4.1 Overview

In this thesis, three types of theoretical tools are used: leading-order Monte Carlo simulations, NLO parton-level cross section calculations, and NLO Monte Carlo simulations.

Leading-order (LO) Monte Carlo simulations are used to model and correct for detector effects on the measurements. They are also used to derive "non-perturbative corrections" for the effects of hadronization and underlying event, which must be applied to NLO parton-level calculations in order for those to be compared with data. However, the LO Monte Carlo simulations are not used as theory predictions for measured cross sections. They only include the leading order diagrams for inclusive jet and dijet production, so they result in a large uncertainty arising from the particular choice of renormalization scale.

NLO parton-level calculations are used as the baseline theory predictions for the cross section measurements. Since they are calculated at the parton level, they require the application of separate corrections for the effects of hadronization and the underlying event. These corrections are derived using LO Monte Carlo simulations.

NLO Monte Carlo simulations have recently become available for inclusive jet and dijet production. They are also used as theory predictions that are compared against the measurements.

The three types of tools are described in the following sections. Multiple cross-section calculators, Monte Carlo generators, and tunes are used in order to estimate the systematic uncertainty associated with the modeling of physics effects by the simulation.

4.2 Leading Order Monte Carlo Simulations

4.2.1 Detector Corrections and Systematic Uncertainties

The PYTHIA 6.423 generator [64] is a leading order Monte Carlo simulation. It is used in this thesis as the baseline Monte Carlo simulation to correct the observations for detector effects, but it is not used as a theory prediction to be compared to the measurements. The generator is used with the MRST modified leading order or "LO*" set of parton distribution functions [142] to simulate jet events in proton-proton collisions at a center-of-mass energy of $\sqrt{s} = 7$ TeV. The LO* PDF set is derived from a global fit to experimental data from the Tevatron, HERA, and fixed target experiments that is performed at leading order in the strong coupling constant, α_{S}. However, certain requirements on the PDFs are removed in order to achieve a behavior that more similar to that of NLO PDF sets, such that the LO* PDF set has features that are intermediate to those of a LO PDF set and an NLO one.

PYTHIA utilizes leading-order perturbative QCD matrix elements (ME) for $2 \rightarrow 2$ processes producing jets. It pairs these matrix elements with a p_{T}-ordered parton shower

(PS) that resums the leading logarithms (see Sec. 1.4.3). It models hadronization using the Lund string model and simulates multiple parton interactions in the underlying event in a way that is coupled with radiation from the parton shower.

Samples are generated using the ATLAS Minimum Bias Tune 1 (AMBT1) set of parameters [62], in which the model of non-diffractive scattering has been tuned to ATLAS measurements of charged particle production at $\sqrt{s} = 900$ GeV and $\sqrt{s} = 7$ TeV. Samples are also generated using other PYTHIA tunes, as well as using HERWIG [65]. HERWIG employs LO matrix elements, but differs from PYTHIA in that it uses a parton shower whose successive radiation is sequentially more collinear with the parent parton, hadronization is modeled using the cluster model, and the underlying event is modeled using the JIMMY [143] package. HERWIG is generated with the ATLAS Underlying Event 1 (AUET1) tune [63], in which the generator is tuned to ATLAS measurements of observables such as the leading track p_{T} spectrum that are sensitive to the modeling of the underlying event. The different generators and tunes have different values for the parameters controlling the behavior of the parton shower, hadronization, and the underlying event. Multiple generators and tunes are used to estimate the systematic uncertainties associated with the modeling of these soft physics effects.

After event generation, the particle four-vectors from the generator are passed through a full simulation [131] of the detector and trigger that is based on GEANT4 [130] (see Sec. 3.9). The simulated events are reconstructed, and jets are reconstructed and calibrated, using the same reconstruction chain as the data.

4.2.2 Non-perturbative Corrections

Parton-level calculations (see Sec. 4.3.1) must be corrected for the effects of hadronization and underlying event in order to be compared with data. These effects cannot be calculated with perturbation theory, so they are estimated using leading-logarithmic parton shower generators. The corrections are derived by using PYTHIA 6.425 with the AUET2B CTEQ6L1 tune [61] to evaluate the bin-wise ratio of cross sections with and without hadronization and the underlying event. Each bin of the parton-level cross section is then multiplied by the corresponding correction. The uncertainty is estimated as the maximum spread of the correction factors obtained using PYTHIA 6.425 with the AUET2B LO** [61], AUET2 LO** [60], AMBT2B CTEQ6L1 [61], AMBT1, Perugia 2010 [59], and Perugia 2011 [59] tunes, PYTHIA 8.150 with the 4C tune [61], and HERWIG++ 2.5.1 [144] with the UE7000-2 tune [61]. The AMBT2B CTEQ6L1 and AMBT1 tunes, which are based on observables sensitive to the modeling of minimum bias interactions, are included to provide a systematically different estimate of the underlying event.

The corrections depend strongly on the jet size; therefore separate sets of corrections and uncertainties are derived for jets with $R = 0.4$ and $R = 0.6$. Figure 4.1 shows the non-perturbative corrections for inclusive jets in two representative rapidity regions, for jet clustering parameters $R = 0.4$ and $R = 0.6$. The correction factors become closer to unity as the jet rapidity increases. The correction factors and their uncertainties depend on the interplay of the hadronization and the underlying event for the different jet sizes, and they have a significant influence at low p_{T} and low dijet mass. For $R = 0.4$, the correction factors are dominated by the effect of hadronization and are approximately 0.95 at jet $p_{\mathrm{T}} = 20$ GeV, increasing closer to unity at higher p_{T}. For $R = 0.6$, the correction factors are dominated by the underlying event and are approximately 1.6 at jet $p_{\mathrm{T}} = 20$ GeV, decreasing to between 1.0-1.1 for jets above $p_{\mathrm{T}} = 100$ GeV.

Similarly, non-perturbative corrections are evaluated for the dijet measurement as a function of the dijet mass and the rapidity interval y^*, for each of the two jet sizes. These

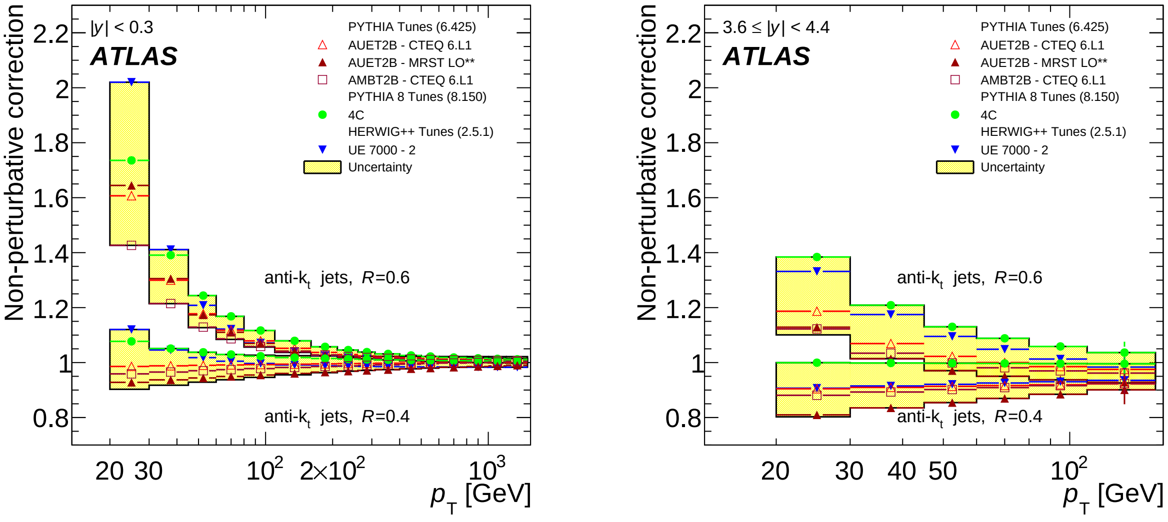

(a) $|y| < 0.3$ (b) $3.6 \leq |y| < 4.4$

Figure 4.1: Non-perturbative correction factors, $c = \sigma_{\text{Had, UE on}}/\sigma_{\text{Parton, UE off}}$, for inclusive jets identified using the anti-k_t algorithm with clustering parameters $R = 0.4$ and $R = 0.6$ in two representative rapidity regions, $|y| < 0.3$ (a) and $3.6 \leq |y| < 4.4$ (b), derived using various Monte Carlo generators. The correction factors for intermediate rapidity regions lie between those shown. The increase in the corrections at low p_{T} for wide jets with $R = 0.6$ is due to the contribution of the underlying event. The corrections derived using PYTHIA 6.425 with the AUET2B CTEQ6L1 tune are used for the fixed-order NLO calculations presented in this analysis.

follow a similar behavior to those for inclusive jets, with the corrections becoming smaller for large invariant masses and rapidity differences.

4.3 Next-to-leading Order Theory Predictions

4.3.1 NLO Fixed-order Predictions

The measured jet cross sections are compared to fixed-order NLO pQCD predictions, with the corrections for non-perturbative effects derived in Sec. 4.2.2 applied. For the hard scattering, both the NLOJET++ 4.1.2 [145] package and the POWHEG generator [146, 147] are used. POWHEG is used in a specific configuration where the parton shower is switched off and calculations are performed using NLO matrix elements. The two programs are used with the CT10 [148] NLO parton distribution functions, which use a global fit to experimental data at the next-to-leading order in $\alpha_{\rm S}$.

They are compared using the same value of renormalization and factorization scale, corresponding to the transverse momentum of the leading jet, $p_{\rm T}^{\rm max}$:

$$\mu = \mu_{\rm R} = \mu_{\rm F} = p_{\rm T}^{\rm max} \tag{4.1}$$

For POWHEG, $p_{\rm T}^{\rm max}$ is evaluated at leading order and is denoted $p_{\rm T}^{\rm Born}$. Using this scale choice, the cross section results of the two NLO codes are compatible at the few percent level for the inclusive jet $p_{\rm T}$ spectrum over the whole rapidity region. They are also consistent for dijet events where both jets are in the central region, while they differ substantially when the two leading jets are widely separated in rapidity ($y^* = |y_1 - y2|/2 \gtrsim 3$).

In the latter case, NLOJET++ produces an unstable and much smaller cross section than POWHEG that is even negative for some rapidity separations. By contrast, POWHEG remains positive over the whole region of phase space. It should be noted that the forward dijet cross section predicted by NLOJET++ in this region has a very strong scale dependence, which however is much reduced for larger values of scale than that of Eq. 4.1.

The forward dijet cross section for NLOJET++ is much more stable if instead of a scale fixed entirely by $p_{\rm T}$, a scale that depends on the rapidity separation between the two jets is used. The values chosen for each y^*-bin follow the formula:

$$\mu = \mu_{\rm R} = \mu_{\rm F} = p_{\rm T}\, e^{0.3y^*} \tag{4.2}$$

and are indicated by the histogram in Fig. 4.2. These values are motivated by the formula (shown by the dot-dashed curve):

$$\mu = \mu_{\mathrm{R}} = \mu_{\mathrm{F}} = \frac{m_{12}}{2\cosh(0.7y^*)} \tag{4.3}$$

that is suggested in Ref. [149], and are in a region where the cross section predictions are more stable as a function of scale (they reach a "plateau"). At small y^*, the scale in Eq. 4.2 reduces to the leading jet p_{T} (dotted line), which is used for the inclusive jet predictions. With this scale choice, NLOJET++ is again in reasonable agreement with POWHEG, which uses the scale from Eq. 4.1. The NLOJET++ predictions are used as a baseline for both inclusive jet and dijet calculations, with the scale choice from Eq. 4.1 for the former and that from Eq. 4.2 for the latter. The POWHEG scale used for both inclusive jets and dijets, $p_{\mathrm{T}}^{\mathrm{Born}}$, is given by Eq. 4.1 but evaluated at leading order. Despite using different scale choices, the dijet theory predictions from NLOJET++ and POWHEG are stable with respect to relatively small scale variations and give consistent results.

The measured jet cross sections are also compared with NLO predictions obtained using the MSTW 2008 [47], NNPDF 2.1 (100) [150, 151] and HERAPDF 1.5 [152] PDF sets. The main uncertainties on the predictions come from the uncertainties on the PDFs, the choice of factorization and renormalization scales, and the uncertainty on the value of the strong coupling constant, α_{S}. To allow for fast and flexible evaluation of PDF and scale uncertainties, the APPLGRID [153] software is interfaced with NLOJET++ in order to calculate the perturbative coefficients once and store them in a look-up table. The PDF uncertainties are defined at 68% CL and evaluated following the prescriptions given for each PDF set. They account for the data uncertainties, tension between input

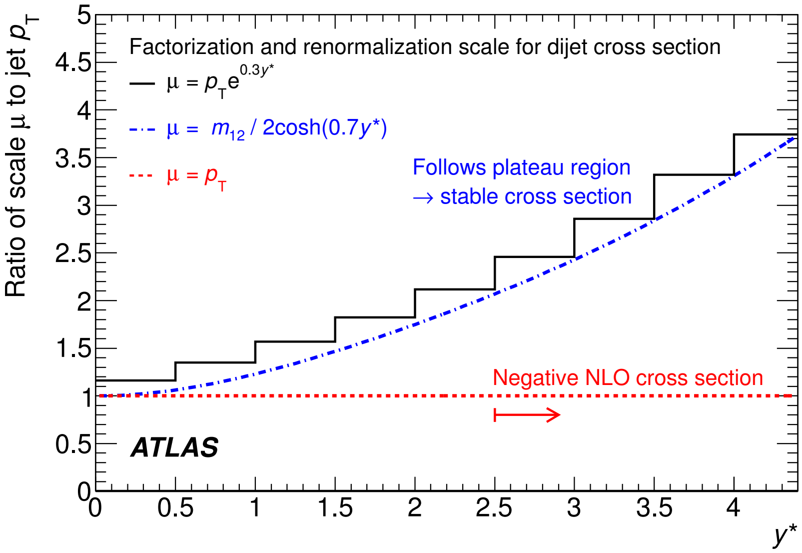

Figure 4.2: The histogram indicates the values of the renormalization and factorization scales (denoted by $\mu = \mu_R = \mu_F$) used for the dijet predictions obtained using NLOJET++, as a function of y^*, half the rapidity separation between the two leading jets. This is motivated by the scale choice suggested in Ref. [149] (dot-dashed line), and is also compared to the scale choice used for the inclusive jet predictions (dotted line).

data sets used for the fits, uncertainties associated with the choice of parametrization of the functional forms to which to fit, and various theoretical uncertainties related to PDF determination.

To estimate the uncertainty on the NLO prediction due to neglected higher-order terms, each observable is recalculated while varying the renormalization scale by a factor of two with respect to the default choice. Similarly, to estimate the sensitivity to the choice of scale where the PDF evolution is separated from the matrix element, the factorization scale is separately varied by a factor of two. Cases where the two scales are simultaneously varied by a factor 2 in opposite directions are not considered due to the presence of logarithmic factors in the theory calculation that become large in these configurations. The envelope of the variation of the observables is taken as a systematic uncertainty. The effect of the uncertainty on the value of the strong coupling constant, $\alpha_{\rm S}$, is evaluated following the recommendation of the CTEQ group [154], in particular by using different PDF sets that are derived using the positive and negative variations of the coupling from its best estimate.

Electro-weak corrections, which may be non-negligible [155], are not included in the theory predictions.

4.3.2 NLO Monte Carlo Simulations

The measured jet cross sections are also compared to POWHEG [146], an NLO parton shower Monte Carlo generator that has recently become available for inclusive jet and dijet production. POWHEG uses the POWHEG BOX package [156, 157, 158] and allows one to use either PYTHIA or HERWIG + JIMMY to shower the partons, hadronize them, and model the underlying event. The ATLAS underlying event tunes, AUET2B for PYTHIA and AUET2 [63] for HERWIG, are derived from the standalone versions of these event generators, with no optimization for the POWHEG predictions. The showering portion of POWHEG uses the PDFs from PYTHIA or HERWIG as part of the specific tune chosen.

In the POWHEG algorithm, each event is built by first producing a QCD 2 → 2 parton scattering. The renormalization and factorization scales are set to be equal to the transverse momentum of the outgoing partons, $p_{\rm T}^{\rm Born}$, before proceeding to generate the hardest parton emission in the event. The CT10 NLO PDF set is used in this step of the simulation. Then the event is evolved to the hadron level using a parton shower event generator, where the radiative emissions in the parton showers are required to be softer than the hardest parton emission generated in the matrix element calculation by POWHEG.

The coherent simulation of the parton showering, hadronization, and the underlying event with the NLO matrix element is expected to produce a more accurate theoretical prediction. In particular, the non-perturbative effects are modeled in the NLO parton shower simulation itself, rather than being derived separately using a LO parton shower Monte Carlo generator as described in Sec. 4.2.2.

CHAPTER 5

JET RECONSTRUCTION AND CALIBRATION

"Measure what is measurable, and make measurable what is not so."

— Galileo Galilei

5.1 Jet Reconstruction

Jets are reconstructed at the electromagnetic (EM) scale[1] using the anti-k_t algorithm. The input objects to the jet algorithm are three-dimensional topological clusters or "topo-clusters" [159] built from calorimeter cells. Each topo-cluster is constructed from a seed calorimeter cell with $|E_{\text{cell}}| > 4\sigma$, where σ is the RMS of the noise of the cell. Adjacent cells are iteratively added to the topo-cluster if they have $|E_{\text{cell}}| > 2\sigma$. Finally, an outer layer of surrounding cells is added. In the jet reconstruction, each such calorimeter cluster is considered as a massless particle with energy $E = \sum E_{\text{cell}}$, with position at the energy-weighted barycenter of the cells in the cluster, and originating from the geometrical center of the detector.

---

[1] The electromagnetic scale is the basic calorimeter signal scale of the calorimeters. It has been established using test-beam measurements for electrons and muons to give the correct response for the energy deposited in electromagnetic showers, while it does not correct for the lower hadron response.

η region	Calorimeter region
$\lvert\eta\rvert < 0.3$	Barrel
$0.3 \leq \lvert\eta\rvert < 0.8$	
$0.8 \leq \lvert\eta\rvert < 1.2$	Barrel-endcap transition
$1.2 \leq \lvert\eta\rvert < 2.1$	
$2.1 \leq \lvert\eta\rvert < 2.8$	Endcap
$2.8 \leq \lvert\eta\rvert < 3.2$	Endcap-forward transition
$3.2 \leq \lvert\eta\rvert < 3.6$	
$3.6 \leq \lvert\eta\rvert < 4.5$	Forward

Table 5.1: Calorimeter regions used for jet calibration.

5.2 Jet Calibration

The response of the calorimeters to jets depends on the jet energy and direction due to instrumental effects. The jets are calibrated to restore the jet energy scale (JES) on average to that of a particle jet entering the calorimeter, ensuring a uniform calorimeter response to jets. Jets are calibrated using an "EM+JES" scheme, which uses detector measurements that are calibrated to electromagnetic showers and scaled to those of hadrons using a p_{T}- and η-dependent factor determined from the Monte Carlo simulation. The Monte Carlo-based corrections applied are validated using in-situ techniques in collision data [14].

The jet calibration scheme consists of three main steps. First, additional energy due to multiple proton-proton interactions within the same bunch crossing or "pile-up" is subtracted. Second, the position of the jet is corrected such that the jet direction points to the primary vertex of the interaction instead of the geometrical center of the detector. Third and last, the energy and the position of the jet are corrected for instrumental effects such as calorimeter non-compensation. Each step is described in the following sections.

The calibration is derived in pseudorapidity bins that divide the calorimeters into the eight η-regions specified in Table 5.1.

5.2.1 Pile-up Correction

An "offset" correction to subtract the average amount of energy contributed by additional proton-proton interactions is derived in minimum bias data. The average additional E_T per calorimeter tower is first measured as a function of the number of reconstructed primary vertices, N_{PV}, the jet pseudorapidity, η, and the bunch spacing [160]. This is translated into a correction to the jet energy based on the average number of towers in a jet, which is measured in-situ.

This correction can be written generically as:

$$E_{\mathrm{T}}^{\mathrm{EM,corr}} = E_{\mathrm{T}}^{\mathrm{EM}} - E^{\mathrm{pile-up}}(\eta, N_{\mathrm{PV}}, \tau_{\mathrm{bunch}}), \tag{5.1}$$

where $E^{\mathrm{pile-up}}(\eta, N_{\mathrm{PV}}, \tau_{\mathrm{bunch}})$ is derived as a function of the pseudorapidity. The amount of in-time pile-up is parameterized by N_{PV}. The spacing between consecutive bunches, τ_{bunch}, parameterizes the amount by which collisions in previous bunch crossings affect the jet energy measurement.

To derive the offset correction for each jet, the tower-based offset at the electromagnetic scale is determined by measuring in a sample of minimum bias events the average tower transverse energy for all towers as a function of N_{PV}. The resulting tower-level offset is shown in Fig. 5.1(a).

The pile-up offset is proportional to the area of a jet. Since each jet is built from dynamically-sized topological clusters, the jet area is described in terms of the equivalent number of constituent towers. The tower-level offset is extrapolated to a jet-level offset:

$$E_{\mathrm{jet}}(\eta, N_{\mathrm{PV}}) = E_{\mathrm{tower}}(\eta, N_{\mathrm{PV}}) \cdot \langle N_{\mathrm{towers}} \rangle, \tag{5.2}$$

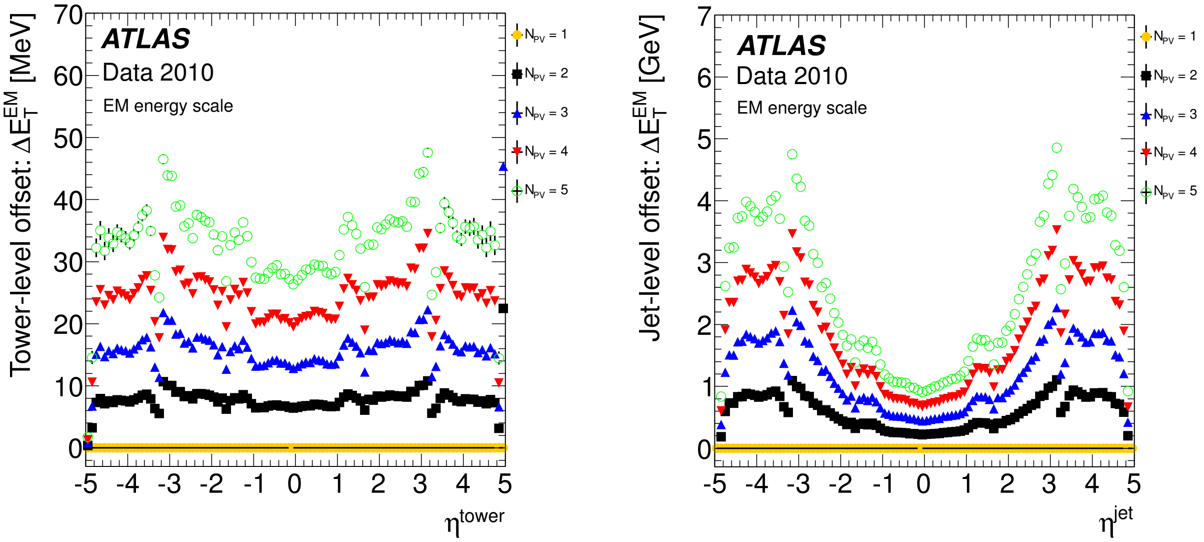

(a) Tower-level (b) Jet-level

Figure 5.1: Offset in energy at the EM scale due to pile-up, shown for calorimeter towers (a) and jets (b) as a function of pseudorapidity in bins of the number of reconstructed primary vertices [14]. The jet-level offset is shown for anti-k_t jets with $R = 0.6$.

where $\langle N_{\text{towers}} \rangle$ is the mean number of towers in a jet. The jet-level offset for jets with $R = 0.6$ is shown in Fig. 5.1(b). The tower-based offset correction is validated by applying a similar procedure using "track jets", which are jets whose input objects are ID tracks rather than calorimeter topo-clusters.

5.2.2 Origin Correction

Calorimeter jets are reconstructed using the geometrical center of the detector as the reference to calculate the direction of jets (see Sec. 5.1). The jet four-momentum is corrected in each event such that the direction of each of its constituent topo-clusters points back to the primary hard-scattering vertex. This correction improves the angular resolution and results in a small improvement ($< 1\%$) in the jet p_T response. The jet energy is unaffected.

5.2.3 Energy Correction

The final step of the jet calibration restores the reconstructed jet energy to the energy of a "truth jet", which is a particle jet but excludes muons and neutrinos. This step corrects for calorimeter non-compensation, energy losses in inactive regions, out-of-cone showering effects, and inefficiencies in the calorimeter clustering and jet reconstruction. This calibration is primarily dependent on energy (since calorimeters respond to energy) and the jet direction, due to the changing calorimeter technology and to the varying amounts of dead material in front of the calorimeters.

The calibration is derived using isolated[2] truth jets that are matched to isolated jets reconstructed in the calorimeter. The correction is calculated by dividing the true particle jet energy by the EM-scale energy of the matching calorimeter jet.

The average jet energy scale correction is shown as a function of calibrated jet transverse momentum for three representative regions of jet η in Fig. 5.2. The calorimeter jet response is shown for various energy- and η_{det}-bins in Fig. 5.3. The values of the jet energy correction factors range from about 2.1 at low jet energies in the central region to less than 1.2 for high energy jets in the most forward region.

5.2.4 Position Correction

Lastly the jet η is further corrected for a bias due to poorly instrumented regions of the calorimeter. In these regions topo-clusters are reconstructed with a lower energy with respect to better instrumented regions, as shown in Fig. 5.3. This causes the jet direction

---

[2] An isolated jet is defined as a jet that has no other jet within $\Delta R = 2.5R$, where R is the clustering parameter of the jet algorithm.

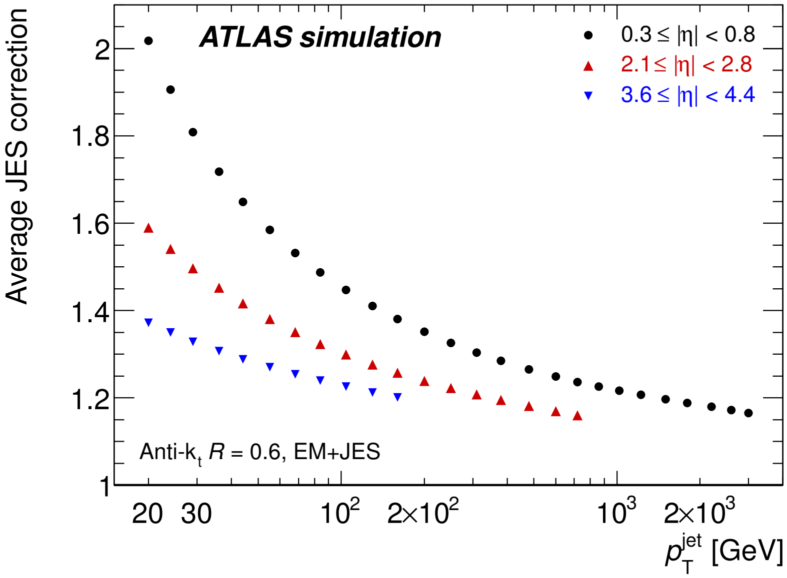

Figure 5.2: Average jet energy scale correction obtained from the Monte Carlo simulation, shown as a function of the calibrated transverse momentum of anti-k_t jets with $R = 0.6$ in three representative η regions [14].

to be biased towards the better instrumented calorimeter regions. The correction for this η bias is shown in Fig. 5.4 and is very small ($\Delta\eta < 0.01$) for most regions of the calorimeter. However it is larger in the crack regions and is up to $\Delta\eta = 0.05$ for low p_{T} jets in the HEC-FCal transition region.

5.2.5 Jet Energy Scale and Resolution

After the jets have been calibrated, the resulting jet energy response and resolution are determined by associating calorimeter jets to truth jets (particle jets, but without muons and neutrinos) in the Monte Carlo simulation using a matching criterion of $\Delta R = 0.3$. No isolation requirement is applied.

The fractional p_{T} response is determined as a function of the truth jet p_{T} as the mean of the ratio of the transverse momentum of its matched, calibrated calorimeter jet and

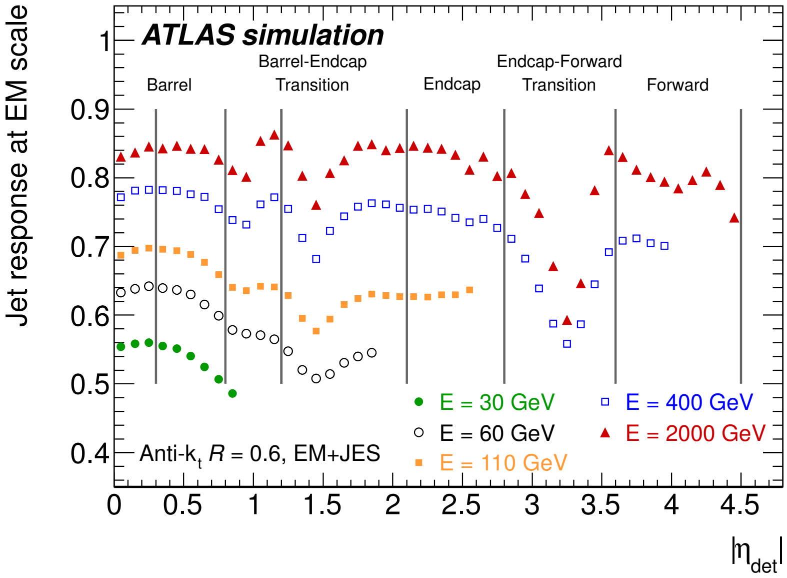

Figure 5.3: Average simulated jet response at the electromagnetic scale as a function of pseudorapidity, shown for different bins of the jet energy calibrated using the EM+JES scheme [14]. The vertical lines illustrate the η regions used to calibrate the jets (see Table 5.1). The average jet energy scale correction in Fig. 5.2 is equal to the inverse of the response in the corresponding bin in this figure.

of the truth jet. The fractional p_{T} resolution is determined similarly by dividing the spread of this ratio by its mean. These are shown for anti-k_t truth jets with $R = 0.6$ in Fig. 5.5. The response is close to unity, and the residual bias is incorporated as a systematic uncertainty on the energy scale (see Sec. 7.6).

5.2.6 Jet Angular Bias and Resolution

The jet angular bias and resolution after calibration are determined from the Monte Carlo simulation using a similar procedure to that used to determine the p_{T} response and resolution (see Sec. 5.2.5). The absolute bias and resolution in jet y are shown as a function of the p_{T} of anti-k_t truth jets with $R = 0.6$ in Fig. 5.6. Similarly, the absolute bias and resolution in jet ϕ are shown in Fig. 5.7. The angular biases in y and ϕ are

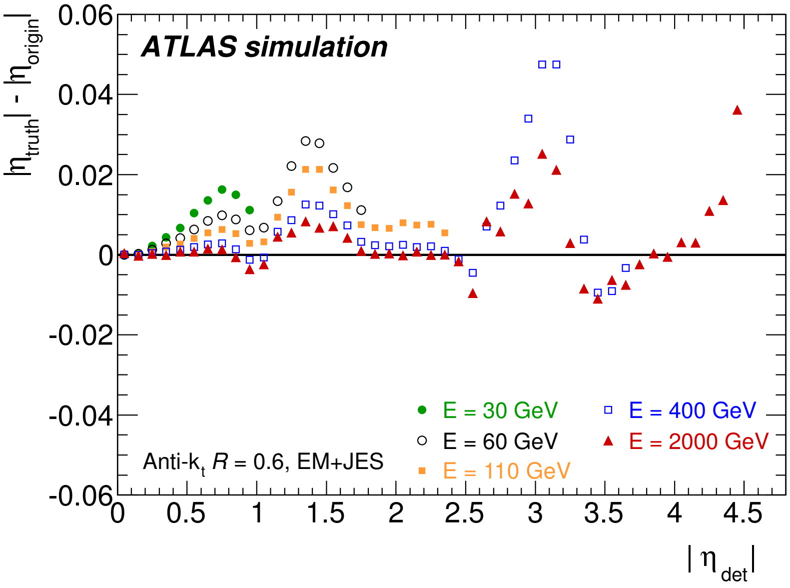

Figure 5.4: Difference between the calorimeter jet pseudorapidity, calculated after a correction has been applied to account for the origin of the jet, and the true jet pseudorapidity. This is shown in bins of the calorimeter jet energy calibrated with the EM+JES scheme and as a function of the detector pseudorapidity, $|\eta_{\rm det}|$ [14].

negligible after the jets have been calibrated.

5.3 Missing Transverse Momentum

The missing transverse momentum vector ($\vec{E}_{\rm T}^{\rm miss}$) is defined as the opposite of the vector sum of the transverse projections of calorimeter energy depositions that are included in topo-clusters. The calorimeter cell energy is computed using the same calibration as that used in the jet calibration scheme.

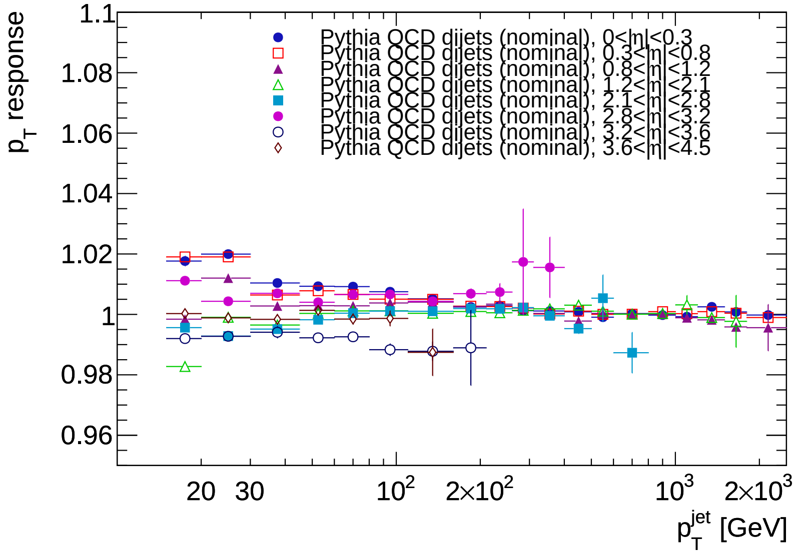

(a) Jet p_{T} response

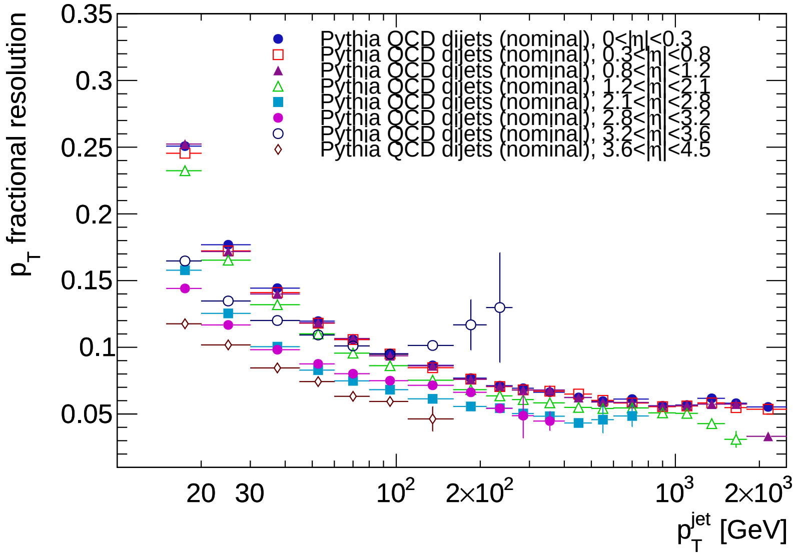

(b) Jet p_{T} resolution

Figure 5.5: The fractional p_{T} response (a) and resolution (b) as a function of the p_{T} of anti-k_t truth jets with $R = 0.6$. These are shown separately for each of the seven rapidity bins used in the measurement, except for the rapidity bin $2.8 < |y| < 3.6$, which has been separated here into $2.8 < |y| < 3.2$ and $3.2 < |y| < 3.6$.

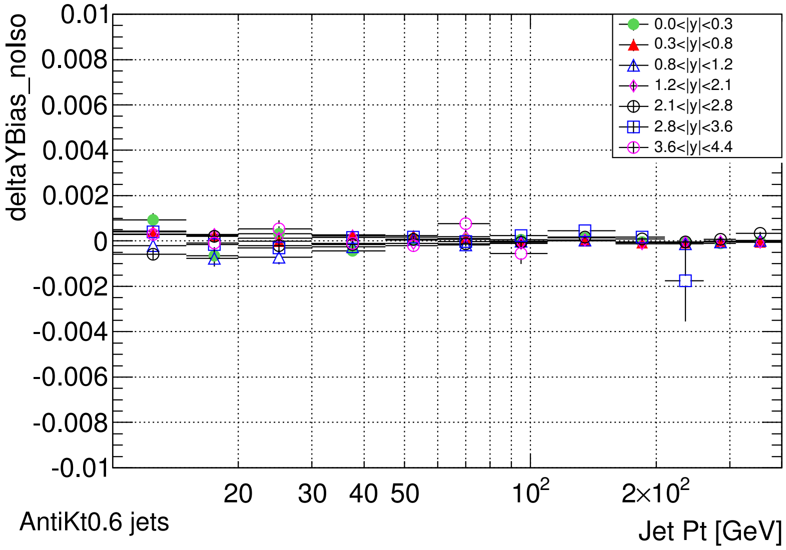

(a) Jet y bias

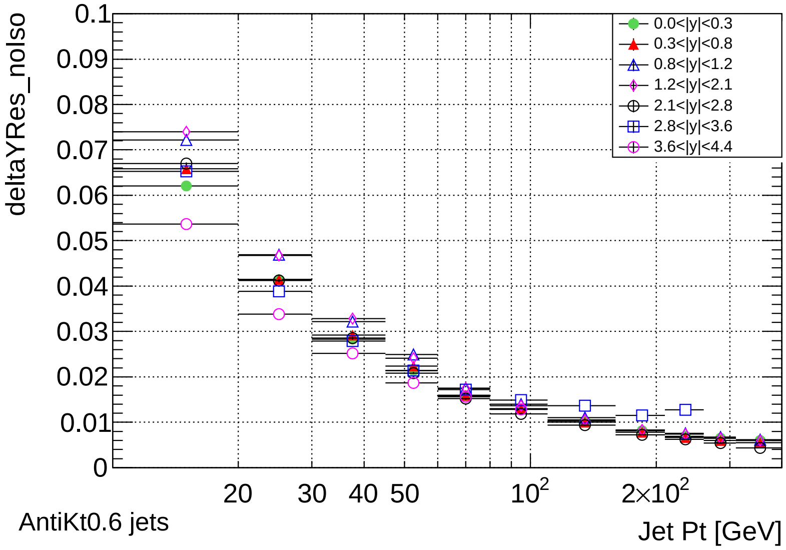

(b) Jet y resolution

Figure 5.6: The absolute bias (a) and resolution (b) in jet y as a function of the p_{T} of anti-k_t truth jets with $R = 0.6$ in each of the seven rapidity bins used in the measurement.

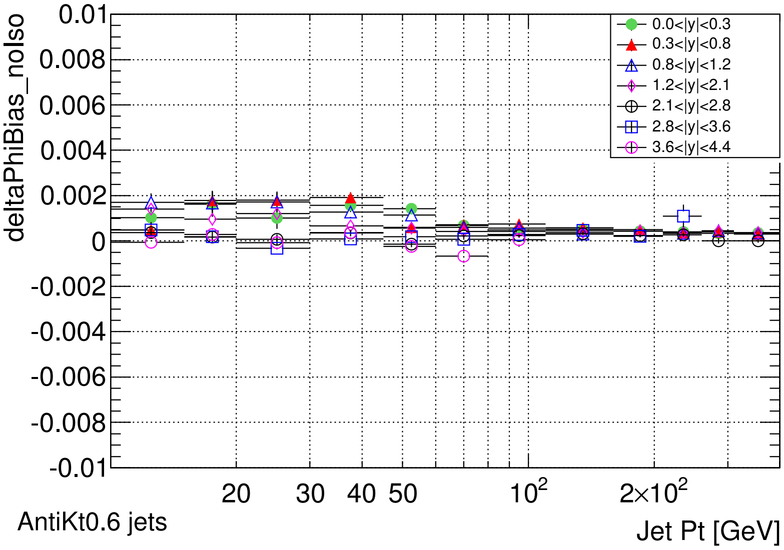

(a) Jet ϕ bias

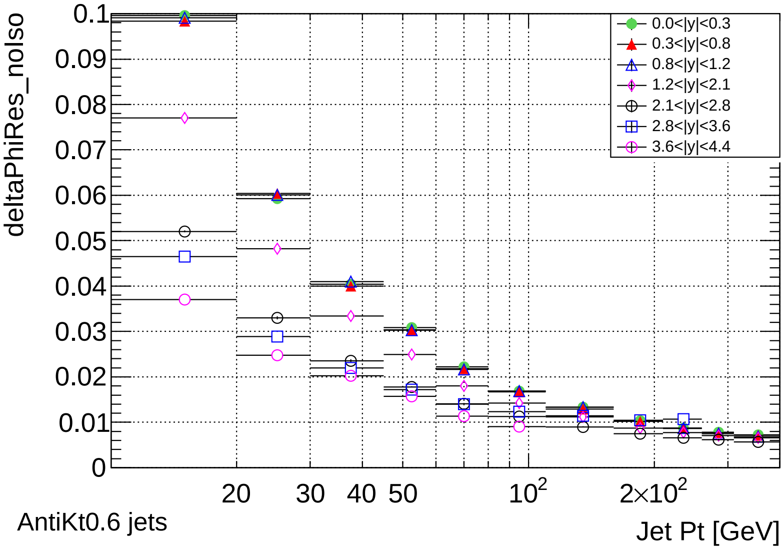

(b) Jet ϕ resolution

Figure 5.7: The absolute bias (a) and resolution (b) in jet ϕ as a function of the p_{T} of anti-k_t truth jets with $R = 0.6$ in each of the seven rapidity bins used in the measurement.

CHAPTER 6

DATA ANALYSIS AND DETECTOR CORRECTIONS

"On two occasions I have been asked [by members of Parliament]: 'Pray, Mr. Babbage, if you put into the machine wrong figures, will the right answers come out?' I am not able rightly to apprehend the kind of confusion of ideas that could provoke such a question."

— Charles Babbage

6.1 Observables Measured

Inclusive jet double-differential cross sections are measured as a function of jet p_{T} in bins of y, in the region $p_{\mathrm{T}} > 20$ GeV and $|y| < 4.4$. The term "inclusive jets" is used in this thesis to indicate that all jets in each event are considered in the cross section measurement. Dijet double-differential cross sections are measured as a function of the invariant mass of the two leading (highest p_{T}) jets, which is given as $m_{12} = \sqrt{(E_1 + E_2)^2 - (\vec{p}_1 + \vec{p}_2)^2}$, where $E_{1,2}$ and $\vec{p}_{1,2}$ are the energies and momenta of the two leading jets. The cross sections are binned in the variable y^*, defined as half the absolute value of the rapidity difference of the two leading jets, $y^* = |y_1 - y_2|/2$. The quantity y^* is the rapidity in the two-parton center-of-mass frame (in the massless particle limit), where it is determined by the polar scattering angle with respect to the beamline, θ^*:

$$y^* = \frac{1}{2} \ln \left(\frac{1 + |\cos \theta^*|}{1 - |\cos \theta^*|} \right) \tag{6.1}$$

For the dijet measurement, the two leading jets are selected to lie in the $|y| < 4.4$ region, where the leading jet is required to have $p_{\mathrm{T}} > 30$ GeV and the sub-leading jet $p_{\mathrm{T}} > 20$ GeV. Restricting the leading jet to higher p_{T} improves the stability of the NLO calculation [161].

The jet cross section measurements are corrected for all experimental effects to the particle level (see Sec. 1.4.8). Theory calculations are used in the same kinematic range as the measurement.

6.2 Data Sample

The inclusive jet and dijet cross section measurements use the full 2010 data sample from proton-proton collisions at $\sqrt{s} = 7$ TeV. This data sample, which was taken between March and November in 2010, comprises an integrated luminosity of 47 pb^{-1}. Data were taken at instantaneous luminosities ranging from 1.0×10^{27} $\mathrm{cm}^{-2}\ \mathrm{s}^{-1}$ to 2.1×10^{32} $\mathrm{cm}^{-2}\ \mathrm{s}^{-1}$. This can be seen in Fig. 6.1(a), which shows the peak instantaneous luminosity per day delivered by the LHC as a function of time in 2010. Figure 6.1(b) shows the cumulative integrated luminosity delivered by the LHC and collected by the ATLAS detector as a function of time. The ATLAS determination of the luminosity is described in Sec. 6.5.

For low-p_{T} jets, only the first 17 nb^{-1} of data taken are considered since the instantaneous luminosity of the accelerator was low enough that a large data sample triggered with a minimum bias trigger (see Sec. 6.2.3) could be recorded. This provides an unbiased sample for reconstructing jets with p_{T} between 20–60 GeV, below the lowest jet trigger threshold. In addition, during this period there were negligible contributions from pile-up events. This can be seen in Fig. 6.2, which shows the maximum average number of pp interactions per beam crossing as a function of time. The early period of data-taking

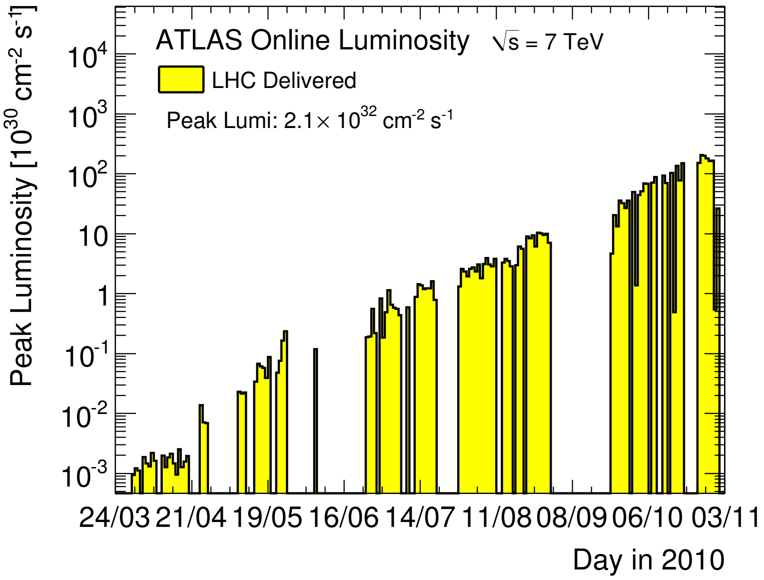

(a) Instantaneous luminosity

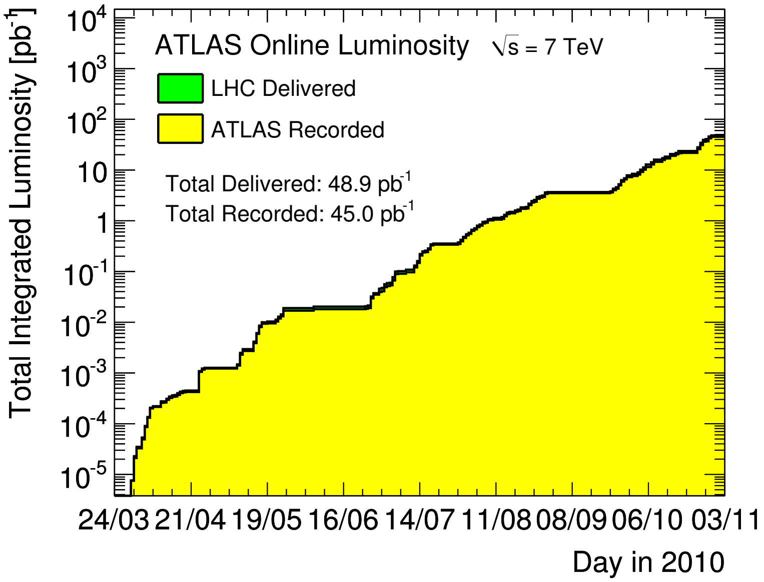

(b) Integrated luminosity

Figure 6.1: Peak instantaneous luminosity per day delivered by the LHC to ATLAS as a function of time during stable beam operation (a). Cumulative integrated luminosity delivered by the LHC and collected by the ATLAS detector as a function of time (b).

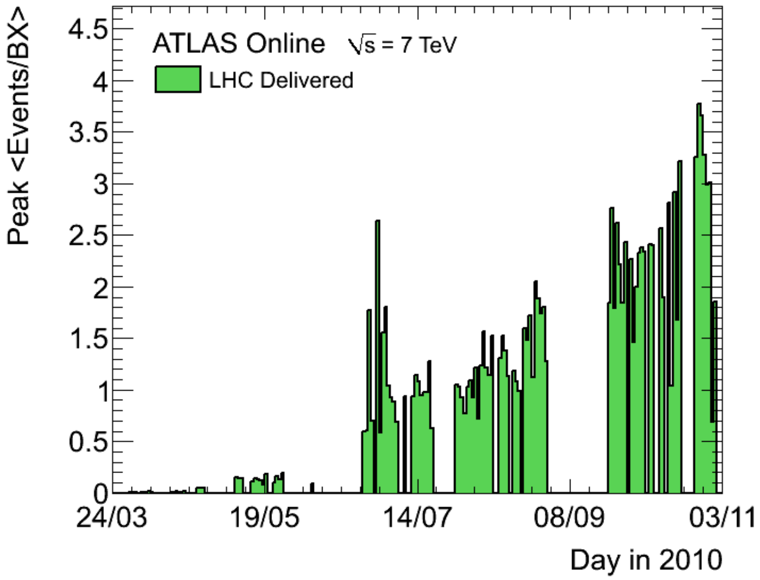

Figure 6.2: The average number of pp interactions per beam crossing at the start of an LHC fill as a function of time.

provides a well-measured sample of low-p_{T} jets. The first data-taking period is not used for forward jets with $|y| > 2.8$ and $p_{\mathrm{T}} > 60$ GeV because the forward jet trigger was not yet commissioned.

6.2.1 Data Quality

For all events considered in this analysis, good operational status is required for the first-level trigger, the solenoid magnet, the inner detector, the calorimeters, and the luminosity detectors, as well as for tracking and jet reconstruction. In addition, stable operation is required for the high-level trigger during the periods when this system was used for event rejection.

6.2.2 Primary Vertex

To reject events due to cosmic-ray muons and other non-collision backgrounds, events are required to have at least one primary vertex that is consistent with the beamspot position and that has at least five tracks with $p_{\mathrm{T}} > 150$ MeV associated to it. The efficiency for collision events to pass these vertex requirements, as measured in a sample of events passing all selections of this analysis, is well over 99%.

6.2.3 Trigger

Three different triggers are used in this measurement: the minimum bias trigger scintillators; the central jet trigger, covering $|\eta| < 3.2$; and the forward jet trigger, spanning $3.1 < |\eta| < 4.9$. The MBTS trigger requires at least one hit in the minimum bias scintillators covering $2.09 < |\eta| < 3.84$. It has been demonstrated to have negligible inefficiency for the events of interest for this analysis [162] and is used to select events with jets having transverse momenta in the range 20–60 GeV. For the jet triggers, only L1 information is used to select events in the first 3 pb^{-1} of data taken, while both the L1 and L2 stages are used for the rest of the data sample. The jet trigger did not reject events at the EF stage in 2010.

The central and forward jet triggers independently select data using several thresholds for the jet transverse energy ($E_{\mathrm{T}} \equiv E \sin\theta$), each of which requires the presence of a jet with sufficient E_{T} at the electromagnetic scale. For each L1 threshold, there is a corresponding L2 threshold that is generally 15 GeV above the L1 value. Each such L1+L2 combination is referred to as an L2 trigger chain. The efficiency of each trigger jet is determined using a "bootstrap" procedure in which the efficiency is measured with respect to a lower threshold trigger that is fully efficient. In the special case of the

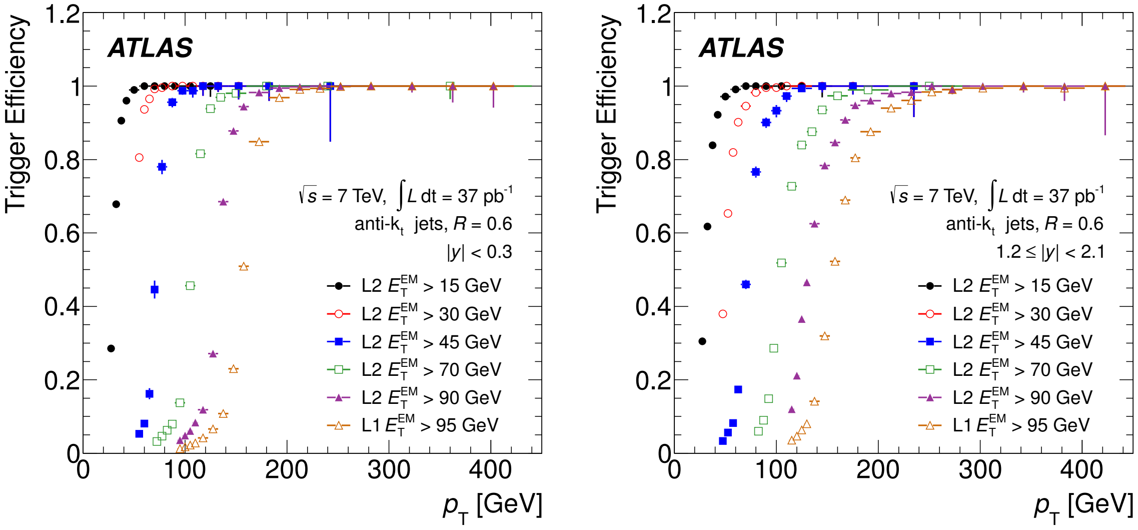

(a) $|y| < 0.3$ (b) $1.2 < |y| < 2.1$

Figure 6.3: Combined L1+L2 jet trigger efficiency as a function of reconstructed jet p_T for anti-k_t jets with $R = 0.6$ in the central region $|y| < 0.3$ (a) and the barrel-endcap transition region $1.2 \leq |y| < 2.1$ (b) for the different L2 trigger thresholds used in the analysis. The trigger thresholds are at the electromagnetic scale, while the jet p_T is at the calibrated scale (see Sec. 5.2). This inefficiency is assigned as a systematic uncertainty on the trigger efficiency in the measurement.

lowest threshold jet trigger, the efficiency is determined using an "orthogonal" method by measuring it with respect to the fully efficient MBTS.

Figure 6.3 shows the combined L1+L2 efficiency for L2 central jet trigger chains with various thresholds as a function of the reconstructed jet p_T for anti-k_t jets with $R = 0.6$ in the central region $|y| < 0.3$ and the barrel-endcap transition region $1.2 \leq |y| < 2.1$. Similar efficiencies are found for jets with $R = 0.4$. The highest trigger chain does not apply a threshold at L2, so its L1 threshold is listed.

As the instantaneous luminosity increased throughout 2010, it was necessary to prescale triggers with lower E_T thresholds, while the central jet trigger with the highest E_T threshold remained unprescaled. As a result, the vast majority of the events where the leading

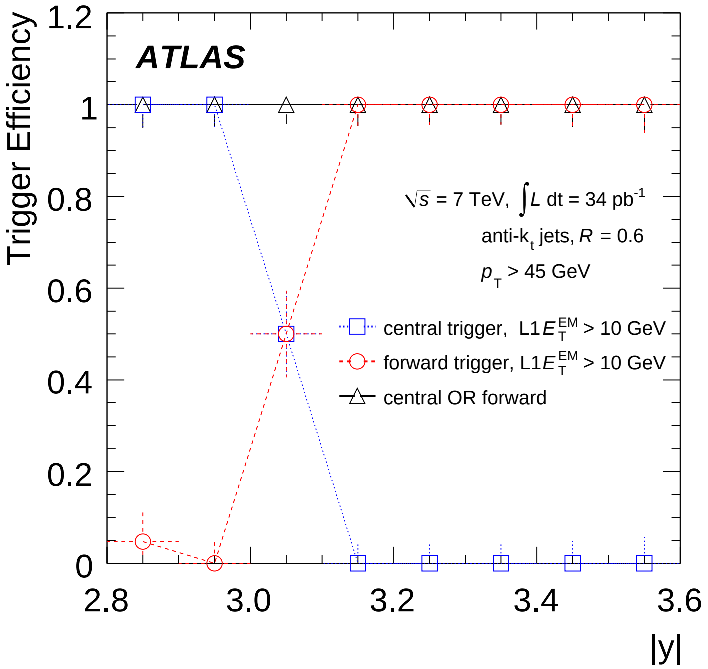

Figure 6.4: Efficiencies for the central and forward jet triggers with a L1 E_{T} threshold of 10 GeV, and for their logical OR, as a function of the rapidity y of the reconstructed jet in the transition region between the two trigger systems. The logical OR is used for the inclusive jet measurement to collect data in the $2.8 \leq |y| < 3.6$ rapidity slice.

jet has transverse momentum smaller than about 100 GeV have been taken in the first period of data-taking, under conditions with a low amount of pile-up, while the majority of the high-p_{T} events have been taken during the second data-taking period, with an average of 2-3 interactions per bunch crossing. For each p_{T}-bin considered in this analysis, a dedicated trigger chain is chosen that is fully efficient ($> 99\%$) while having as small a prescale factor as possible. For inclusive jets fully contained in the central or in the forward trigger region, only events taken by this fully efficient trigger are considered. For inclusive jets in the HEC-FCal transition region $2.8 \leq |y| < 3.6$, neither the central nor the forward trigger is fully efficient. Since the logical OR of the triggers is fully efficient at sufficiently high jet p_{T}, as illustrated in Fig. 6.4, the OR combination is used.

A specific strategy is used to account for the various prescale combinations for inclusive jets in the HEC-FCal transition region, which can be accepted either by the central jet trigger only, by the forward jet trigger only, or by both triggers. A similar strategy is used for dijet events in a given (m_{12}, y^*)-bin, which can be accepted by several jet triggers depending on the transverse momenta and pseudorapidities of the two leading jets. Events that can be accepted by more than one trigger chain have been divided into several categories according to the trigger combination that could have accepted the events. For inclusive jets in the transition region, these correspond to central and forward triggers with a similar threshold; for dijets, the trigger combination depends on the position and transverse momenta of the two leading jets, each of which is matched to a trigger object using angular criteria. Corrections are applied for any trigger inefficiencies, which are generally below 1%. The equivalent luminosity of each of the categories of events is computed based on the prescale values of these triggers throughout the data-taking periods, and all results from the various trigger combinations are combined together according to the prescription given in Ref. [163].

6.3 Jet Selection

6.3.1 Acceptance

For the inclusive jet measurements, jets are required to have $p_{\mathrm{T}} > 20$ GeV and to be within $|y| < 4.4$. They must also pass the specific fully-efficient trigger for each p_{T}- and $|y|$-bin, as described in Sec. 6.2.3. For the dijet measurements, events are selected if they have at least one jet with $p_{\mathrm{T}} > 30$ GeV and another jet with $p_{\mathrm{T}} > 20$ GeV, both within $|y| < 4.4$. Corrections are applied for inefficiencies in jet reconstruction. These inefficiencies are generally negligible except in the lowest jet p_T (dijet mass) bin, where the inefficiency is a few percent.

6.3.2 Jet Quality

Jet quality criteria established with collision data are applied to reject jets reconstructed from calorimeter signals that do not originate from a proton-proton collision, such as those due to noisy calorimeter cells [14]. The main sources of fake jets are noise bursts in the hadronic endcap calorimeter (HEC) electronics, coherent noise from the electromagnetic calorimeter, cosmic rays, and beam-related backgrounds.

Quality selection criteria are developed for each of these categories by studying jet samples classified as real or fake energy depositions. This classification is performed by applying criteria on the magnitude and direction of the missing transverse momentum, $\vec{E}_\mathrm{T}^\mathrm{miss}$. Following this, about a dozen events with $|\vec{E}_\mathrm{T}^\mathrm{miss}| > 500$ GeV pass the standard analysis selection. These events are visually scanned and are generally found to be collision events with mostly low p_T jets and a muon escaping at low scattering angle. The effect of successive criteria applied to remove fake jets is shown for the inclusive jet p_T spectrum in Fig. 6.5. After applying criteria to remove jets produced by noise bursts in the hadronic endcap calorimeter or coherent noise in the EM calorimeter, the data agree well with the predictions for minimum bias interactions.

The efficiency for identifying real jets is measured using a tag-and-probe method. A "probe jet" sample is selected by requiring the presence of a "tag jet" that is within $|\eta| < 2.0$, fulfills the jet quality criteria, and is back-to-back ($\Delta\phi > 2.6$) and well-balanced with a probe jet ($|p_\mathrm{T1} - p_\mathrm{T2}|/p_\mathrm{T}^\mathrm{avg} < 0.4$, with $p_\mathrm{T}^\mathrm{avg} = (p_\mathrm{T1} + p_\mathrm{T2})/2$ and where $p_\mathrm{T1,2}$ are the transverse momenta of the tag and probe jets). The jet quality criteria is then

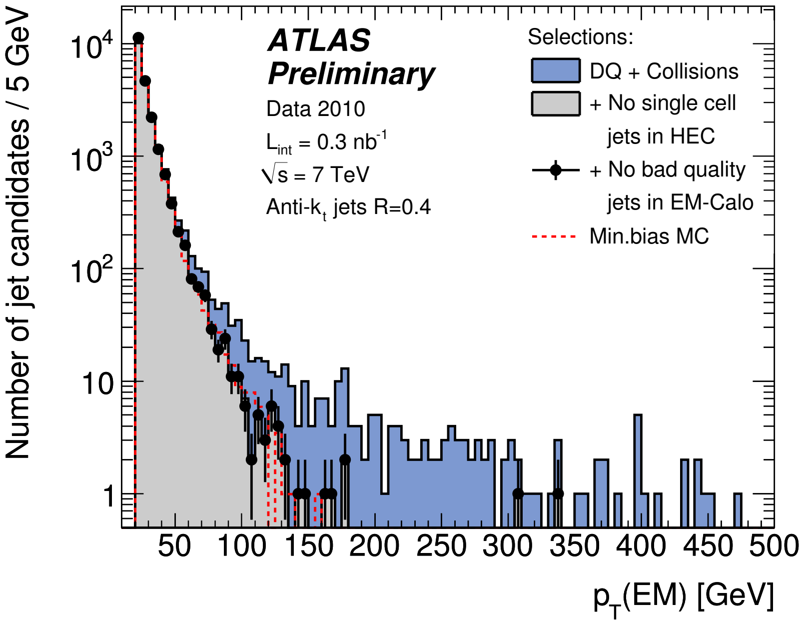

Figure 6.5: Inclusive jet p_T distribution for anti-k_t jets with $R = 0.4$ after successive cleaning criteria are applied [164]. The jet momenta are calibrated at the electromagnetic scale. The expectation from Monte Carlo simulation is superimposed and normalized to the number of jets in the data. The effect of eliminating jets consisting of a single cell in the hadronic endcap calorimeter, which arise from bursts of noise, and jets produced by coherent noise in the electromagnetic calorimeter can be seen. Two remaining outlier jets with transverse momenta greater than 300 GeV are real jets and belong to the same dijet event.

applied to the probe jet, measuring as a function of its $|\eta|$ and p_T the fraction of jets that are not rejected.

The efficiency to select a jet is shown in Fig. 6.6 for the central region $|y| < 0.3$, along with the systematic uncertainty on this efficiency. The jet quality selection efficiency is greater than 96% for jets with $p_T = 20$ GeV and quickly increases with jet p_T. The efficiency is above 99% for jet $p_T > 60$ GeV in all rapidity regions. The inclusive jet and dijet cross sections are corrected for these inefficiencies in regions where the efficiency is less than 99%.

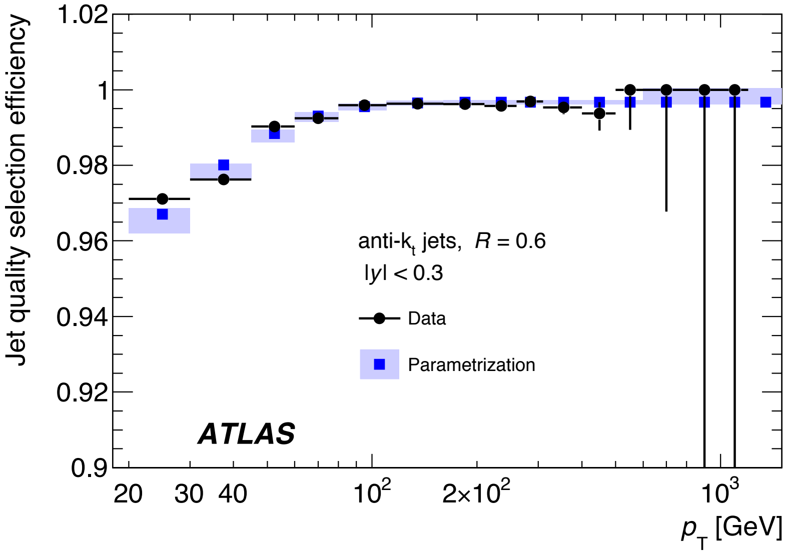

Figure 6.6: Efficiency ϵ for passing the jet quality selection as a function of p_{T} for anti-k_t jets with $R = 0.6$ in the rapidity region $|y| < 0.3$. The circles indicate the efficiency measured in-situ using a tag-probe method. The squares indicate the fit to the parameterization $\epsilon(p_{\mathrm{T}}) = A - e^{-(Bp_{\mathrm{T}}-C)}$ used in this analysis, where A, B, and C are fitted constants, and the shaded band indicates the systematic uncertainty on the efficiency obtained by varying the tag jet selection. The turn-on is due to more stringent jet quality selection at low jet p_{T}.

6.4 Backgrounds

6.4.1 Non-collision Backgrounds

Background contributions from sources other than proton-proton collisions are evaluated using events from cosmic-ray runs, as well as unpaired proton bunches in the accelerator, in which no real collision candidates are expected. Based on the duration of the cosmic-ray runs and the fact that only one event satisfies the selection criteria, the non-collision background rates across the entire data period are found to be negligible.

6.4.2 Pile-up

The p_{T} of each jet is corrected for additional energy from soft pile-up interactions in the event, which is about 0.5 GeV per additional reconstructed primary vertex (see Sec. 5.2.1). The jet measurements are then compared to the Monte Carlo simulation without pile-up. An uncertainty associated to the pile-up offset correction is assigned that is dependent on the number of reconstructed primary vertices (see Sec. 7.6.5).

6.4.3 Physics Backgrounds

The cross sections of other physics processes are generally negligible compared to the very high rate of QCD jet production, which dominates the hard-scattering cross-section at the LHC.

6.5 Luminosity

6.5.1 Overview

The luminosity is derived [165, 166] by counting rates measured by the luminosity detectors. These detectors are calibrated using dedicated beam separation scans, also known as "van der Meer" scans [125], where the two beams are stepped through each other in the horizontal and vertical planes to measure their overlap function.

6.5.2 Absolute Calibration

Visible Cross Section

The observed number of inelastic interactions per crossing μ_{vis} is measured independently with a variety of detectors and using several different algorithms, where $\sigma_{\mathrm{vis}} = \varepsilon\sigma_{\mathrm{inel}}$ is the total inelastic cross-section multiplied by the efficiency ε of a particular detector and algorithm. The visible cross-section σ_{vis} is also measured using each particular detector and algorithm and is used to determine the calibration of the luminosity scale.

The calibration of σ_{vis} is performed using van der Meer scans, where the absolute luminosity can be inferred from direct measurements of machine parameters [166]. The delivered luminosity can be written as:

$$\mathcal{L} = \frac{n_{\mathrm{b}} f_{\mathrm{rev}} n_1 n_2}{2\pi \Sigma_{\mathrm{x}} \Sigma_{\mathrm{y}}} \tag{6.2}$$

where n_1 and n_2 are the bunch populations (protons per bunch) in beam 1 and beam 2 respectively (together forming the bunch charge product), and Σ_{x} and Σ_{y} characterize the horizontal and vertical profiles of the colliding beams. In a van der Meer scan, the beams are separated by steps of a known distance which allows a direct measurement of Σ_x and Σ_y. The bunch charge product $n_1 n_2$ is measured [167, 168] and used to determine the luminosity when the beams are unseparated. By comparing this peak luminosity to the peak interaction rate $\mu_{\mathrm{vis}}^{\mathrm{Max}}$ observed by a given detector and algorithm during the van der Meer scan, σ_{vis} is determined as:

$$\sigma_{\mathrm{vis}} = \mu_{\mathrm{vis}}^{\mathrm{Max}} \frac{2\pi \Sigma_{\mathrm{x}} \Sigma_{\mathrm{y}}}{n_1 n_2}. \tag{6.3}$$

Two classes of algorithms are used to count “events”, which are bunch crossings that satisfy some requirement. Inclusive rates (at least one hit) and coincidence rates (at least one hit on each side) are measured by the LUCID, BCM, and MBTS detectors. In one algorithm with MBTS, a primary vertex is also required. Using Poisson statistics, μ_{vis} is determined from the event counting rate.

Five van der Meer scans were taken between April and October, 2010. Two sets of

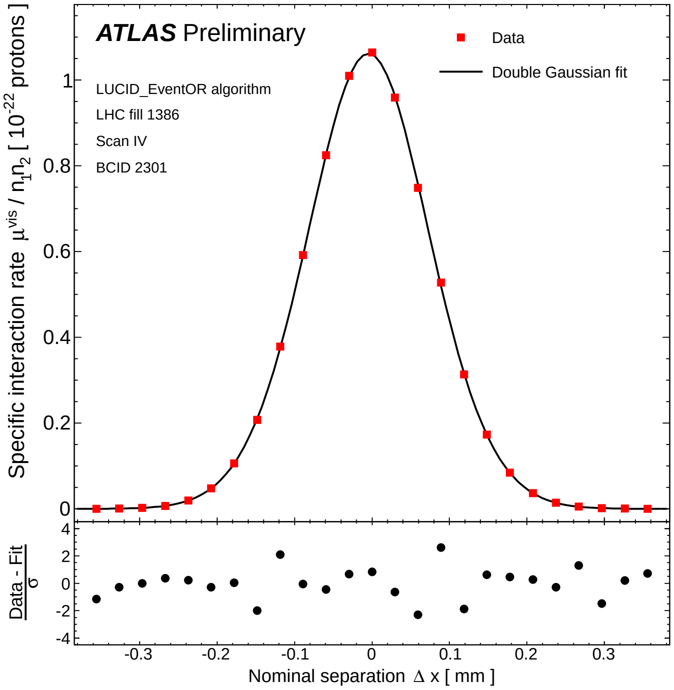

Figure 6.7: Specific interaction rate versus nominal beam separation for the LUCID_EventOR algorithm during van der Meer scan IV in the x plane [165]. The bunch charge product $(n_1 n_2)$ is measured in units of $(1 \times 10^{11}\text{protons})^2$. The residual deviation of the data from the fit assuming statistical errors only is shown in the bottom panel.

scans, each consisting of one horizontal and one vertical scan, were performed in short succession so as to quantify the reproducibility of the optimal relative beam position, convolved beam sizes, and visible cross-sections. An an example, Fig. 6.7 shows the specific visible interaction rate $\mu_{\text{vis}}/(n_1 n_2)$ measured by the LUCID detector with an inclusive algorithm as a function of the beam separation in the x direction.

Each scan for each colliding bunch pair (BCID) independently provides a measurement of $\mu_{\text{vis}}^{\text{Max}}$ and Σ. The average value of $\mu_{\text{vis}}^{\text{Max}}$ from at least one x scan and at least one y scan is used to measure σ_{vis}. Good agreement is observed for the σ_{vis} values determined using the different BCID and scans.

LHC Bunch Currents

The bunch currents in the LHC are measured by eight current transformers. DC current transformers (DCCT) are calibrated using a precise current source and used to measure the total bunch charge in each beam. The DCCT measurement may drift due to instrumental effects such as temperature effects, mechanical vibrations, and electromagnetic pick-up in cables. The baseline corresponding to zero current is calibrated by looking at periods with no beam immediately before and after each fill.

The relative fraction of the total current in each BCID is measured using two fast beam current transformers (FBCT). This is normalized to the overall current scale provided by the DCCT system, allowing the bunch charge product colliding in a particular BCID to be determined.

6.5.3 Results

The individual measurements of σ_{vis} from the five scans are combined to determine the best calibrated $\overline{\sigma}_{\text{vis}}$ value per algorithm. This is done using a Best Linear Unbiased Estimator (BLUE) technique that takes into account both the statistical and systematic uncertainties, as well as their respective correlations [169, 170]. The BLUE technique generalizes the procedure of χ^2 minimization by accounting for non-trivial correlations.

The best estimate of the visible cross section $\overline{\sigma}_{\text{vis}}$ for each luminosity method is shown in Table 6.1 along with the uncertainty and total χ^2. The "LUCID_EventOR" algorithm, wherein the LUCID detector counts inclusive hits, measures the visible cross section to be $\overline{\sigma}_{\text{vis}} = 41.67 \pm 1.40$ mb. This is used to determine the luminosity calibration using Eq. 6.2.

	$\overline{\sigma}_{\text{vis}}$ (mb)	χ^2
LUCID_EventOR	$41.67 \pm 0.02 \pm 1.40$	1.0
LUCID_EventAND	$13.04 \pm 0.01 \pm 0.44$	1.6
MBTS_Timing	$51.13 \pm 0.15 \pm 1.71$	0.6
PrimVtx	$49.28 \pm 0.14 \pm 1.65$	0.6
BCM_EventOR	$4.594 \pm 0.005 \pm 0.147$	0.8

Table 6.1: Best estimate of the visible cross section determined from van der Meer scan data [165]. Errors shown are the statistical component and the total systematic uncertainty taking all correlations into account. For BCM_EventOR, a straight average of the results from scans IV-V has been used.

6.6 Correction for Detector Effects

6.6.1 Unfolding

Aside from the jet energy scale correction, all other corrections for detector biases, inefficiencies, and resolutions are performed using an iterative "unfolding" procedure. This procedure is based on a transfer matrix that relates the true particle-level variable to the observed reconstruction-level variable, using the same binning as the final distribution. The unfolding is performed separately for each bin in rapidity since the migrations across rapidity bins are negligible compared to those across jet p_{T} (dijet mass) bins. A similar procedure is applied for inclusive jets and dijets, with the following description applying specifically to the inclusive jet case.

6.6.2 Iterative Dynamically Stabilized Technique

The Monte Carlo simulation described in Sec. 4.2 is used to derive the unfolding matrices. In the Monte Carlo events, particle-level and reconstructed jets are matched together based on geometrical criteria and used to derive a transfer matrix. For the jet p_{T} variable, this matrix contains the expected number of jets within each bin of particle-level p_{T} (row index) and reconstructed jet p_{T} (column index). A folding matrix is constructed from the transfer matrix by normalizing row-by-row so that the sum of the elements corresponding to a given particle-level jet p_{T} is unity. Similarly, an unfolding matrix is constructed by normalizing column-by-column so that the sum of the elements corresponding to a specific reconstructed jet p_{T} is unity. Thus each element of the unfolding matrix reflects the probability for a reconstructed jet in a particular p_{T} bin to originate from a specific particle-level p_{T} bin, given the assumed input particle-level jet p_{T} spectrum. The spectra of unmatched particle-level and reconstructed jets are also derived from the simulated sample. The ratio between the number of matched jets and the total number of jets provides the matching efficiency both for particle-level jets, $\epsilon^{\mathrm{ptcl},i}$, and for reconstructed jets, $\epsilon_{\mathrm{reco},j}$.

The data are unfolded to particle level using a three-step procedure, with the final results being given by the equation:

$$N^{\mathrm{ptcl},i} = \sum_j N_{\mathrm{reco},j} \times \epsilon_{\mathrm{reco},j} A^{\mathrm{ptcl},i}_{\mathrm{reco},j} / \epsilon^{\mathrm{ptcl,i}} \tag{6.4}$$

where i and j are the particle-level and reconstructed bin indices, respectively, and $A^{\mathrm{ptcl},i}_{\mathrm{reco},j}$ is an unfolding matrix refined through iteration, as discussed below.

The first step is to multiply the reconstructed jet spectrum in data by the matching efficiency $\epsilon_{\mathrm{reco},j}$, such that it can be compared to the matched reconstructed spectrum from the Monte Carlo simulation. In the second step, the iterated unfolding matrix $A^{\mathrm{ptcl},i}_{\mathrm{reco},j}$ is determined using the Iterative, Dynamically Stabilized (IDS) method [171]. This procedure improves the transfer matrix through a series of iterations, where the particle-level distribution is reweighted to the shape of the corrected data spectrum, while leaving the folding matrix unchanged. The main difference with respect to previous iterative unfolding techniques [172] is that, when performing the corrections, regularization is provided by the use of the significance of the data-MC differences in each bin. The third step is to divide the spectrum obtained after the iterative unfolding by the matching efficiency at particle level, thus correcting for the jet reconstruction inefficiency.

The statistical uncertainties on the spectrum are propagated through the unfolding by performing pseudo-experiments. An ensemble of pseudo-experiments is created in which each bin of the transfer matrix is varied according to its statistical uncertainty. A separate set of pseudo-experiments is performed where the data spectrum is varied while respecting correlations between jets produced in the same event. The unfolding is then applied to each pseudo-experiment, and the resulting ensembles are used to calculate the covariance matrix of the corrected spectrum.

CHAPTER 7

SYSTEMATIC UNCERTAINTIES

"If you're doing an experiment, you should report everything that you think might make it invalid — not only what you think is right about it . . . . Details that could throw doubt on your interpretation must be given . . . ."

— Richard Feynman (Nobel Prize in Physics, 1965)

7.1 Overview

7.2 Primary Vertex Position

The primary vertices span the luminous region around the nominal beamspot. To determine the systematic uncertainty due to possibly incorrect modeling of the event vertex position, the jet p_{T} spectrum is studied as a function of the $|z|$ position of the primary vertex with the largest $\sum p_{\mathrm{T}}^2$ of associated tracks. The fraction of events with $|z| > 200$ mm is 0.06%, and the difference in the p_{T} spectrum compared to events with $|z| < 100$ mm is small. Consequently, the uncertainty from mis-modeling of the vertex position is taken to be negligible.

7.3 Trigger Efficiency

The trigger efficiencies are measured in collision data using the bootstrap and orthogonal methods (see Sec. 6.2.3). These methods are validated using closure tests in the Monte Carlo simulation, wherein they reproduce the expected efficiency to within 1%. Cross-checks are also performed that demonstrate that variations in the specific procedure, in particular relating to the matching of reconstructed jets with trigger objects, have an effect of less than 2% on the efficiency. Each jet or MBTS trigger is only used in a region where it is greater than 99% efficient. Together these effects are used to assign a systematic uncertainty on the trigger efficiency of 1% or 2%, depending on the particular rapidity bin.

7.4 Jet Reconstruction Efficiency

The uncertainty on the jet reconstruction efficiency for $|y| < 2.1$ (within the tracking acceptance) is evaluated using track jets, which are used to play the role of truth jets. The efficiency to reconstruct a calorimeter jet given a track jet nearby is studied in both data and the MC simulation. The data versus MC comparison of this efficiency is used to infer the degree to which the calorimeter jet reconstruction efficiency may be mis-modeled in the Monte Carlo simulation.

The disagreement is found to be 2% for calorimeter jets with p_{T} of 20 GeV, and less than 1% for those with $p_{\mathrm{T}} > 30$ GeV. The disagreement for jets with $|y| < 2.1$ is taken as a systematic uncertainty for all jets in the rapidity range $|y| < 4.4$. This is expected to be a conservative estimate in the forward region where the jets have higher energy for a given p_{T}.

7.5 Jet Selection Efficiency

The efficiency for identifying real jets, shown in Fig. 6.6 is measured using a tag-probe method as described in Sec. 6.3.2. The systematic uncertainty on the efficiency is obtained by varying the tag jet selection and is illustrated as the shaded band in the figure. The systematic uncertainty on the efficiency, which is generally below 1%, translates to a correspondingly negligible systematic uncertainty on the cross section.

7.6 Jet Energy Scale

7.6.1 Overview

The uncertainty on the jet energy scale is the dominant uncertainty for the inclusive jet and dijet cross section measurements presented herein. In the central barrel region ($|\eta| < 0.8$), the dominant source of the JES uncertainty is the calorimeter response to hadrons (JES 7-13 in Table 7.3).

The JES systematic uncertainty is derived in the central calorimeter region by combining the uncertainties on the single hadron response measured in-situ and single pion test-beam measurements [173, 137]. The uncertainty is extended to the endcap and forward detector regions by exploiting the transverse momentum balance between a central jet and a forward jet in events where only two jets are produced [174]. Further uncertainties arise from the description of the electronic noise, the amount of material in the detector, and the Monte Carlo modeling used in the event generation. These are evaluated using systematic variations of Monte Carlo simulations [175]. Finally the uncertainty on the pile-up offset correction is also accounted for. Each of the systematic sources are described in the sections that follow.

7.6.2 Calorimeter Response

The response and uncertainties for single particles interacting in the calorimeters are used to derive the corresponding jet energy scale uncertainty in the central calorimeter region [137]. In the Monte Carlo simulation, the true calorimeter energy depositions in each calorimeter cell are traced to the particles generated in the collision. The uncertainty in the response for each of the individual particles constituting the jet is then translated into an uncertainty on the calorimeter response to jets. The in-situ measurement of the single particle response significantly reduces the uncertainty due to the limited knowledge of the exact detector geometry, and in particular due to the presence of additional dead material. It also validates the modeling of the interactions of the particles in the detector.

Two single particle response measurements are used to determine the calorimeter response. The first involves a measurement of the single hadron response, E/p. It is defined as the ratio of the calorimeter energy measured in a cone around an isolated track, divided by the track momentum. This has been measured for tracks with momentum between $0.5 \leq p^{\text{track}} < 20$ GeV using collision data at $\sqrt{s} = 7$ TeV, as shown for the region $0.6 < |\eta| < 1.1$ in Fig. 7.1 [137]. The second measurement involves the response to pions, which has been measured in the 2004 combined test-beam, where a full slice of the ATLAS detector was exposed to pion beams with momenta between 20 GeV and 350 GeV [176].

The uncertainties in the response to charged hadrons are estimated from these measurements and include a number of sources, which can be grouped into three primary classes. The first class of uncertainty concerns the single response measurements themselves. For particles with momentum below 20 GeV, the discrepancy in the E/p response between data and the Monte Carlo simulation is taken as a systematic uncertainty on the response. Similarly, for the pion combined test beam measurements, the discrepancy

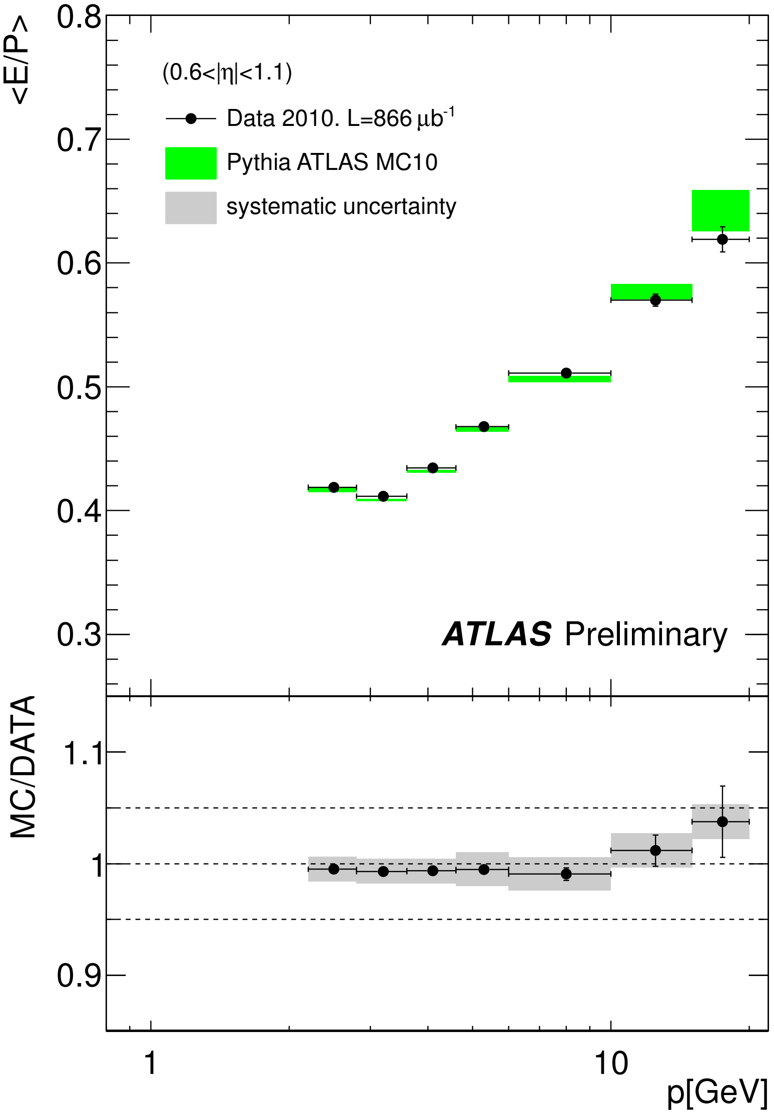

Figure 7.1: Mean E/p response as a function of the track momentum for tracks with $0.6 < |\eta| < 1.1$ [137]. The black dots represent the response measured using collision data, while the green rectangles represent the response predicted by the Monte Carlo simulation. The lower part of the figure shows the ratio between the response from the Monte Carlo simulation and the response measured in collision data. The gray band indicates the systematic uncertainty on the ratio. The dotted lines are placed at ±5% of unity.

between data and the Monte Carlo simulation is assigned as a systematic uncertainty.

The second class of uncertainties deals with particles for which there is no response measurement. Two primary examples are that there are no test beam measurements for neutral hadrons (K^0, Λ^0, etc.) and anti-protons. Therefore uncertainties on their responses are assigned based on the variation in the response with different shower models in GEANT4 [177]. Similarly, there are uncertainties on the baseline absolute electromagnetic scales for the tile and electromagnetic calorimeters for particles not measured in-situ, such as photons from π_0 decays for the EM calorimeter and hadrons with momentum above 20 GeV for Tile. The respective EM scale uncertainties of 3% and 1.5% for the Tile and EM calorimeter are assigned to the response of these particles. The latter figure of 1.5% has been attained after calibrating the EM calorimeter using Z boson decays to electron-positron pairs (see Sec. 3.4.1).

Finally, the last class of uncertainties involves possible errors in the process of translating the response to single particles making up a jet into the response to the overall jet. This translation can be affected by material upstream of the calorimeter or by the topo-cluster threshold. Low-p_{T} particles may not reach the calorimeter or may not be reconstructed in a topo-cluster due to the noise thresholds. And at high p_{T}, the dominant uncertainty arises from the response to particles with $p > 400$ GeV. To account for possible calorimeter non-linearities and longitudinal leakage in this regime, a conservative systematic uncertainty of 10% is assigned.

The response for each of the individual particles constituting a jet is translated into an uncertainty on the calorimeter response to jets, accounting for the systematic uncertainties described above. Figure 7.2 shows the ratio of the resultant calorimeter response to jets in $0.3 < |\eta| < 0.8$, determined from in-situ and test beam response measurements, with respect to the calorimeter jet response predicted by the Monte Carlo simulation. The

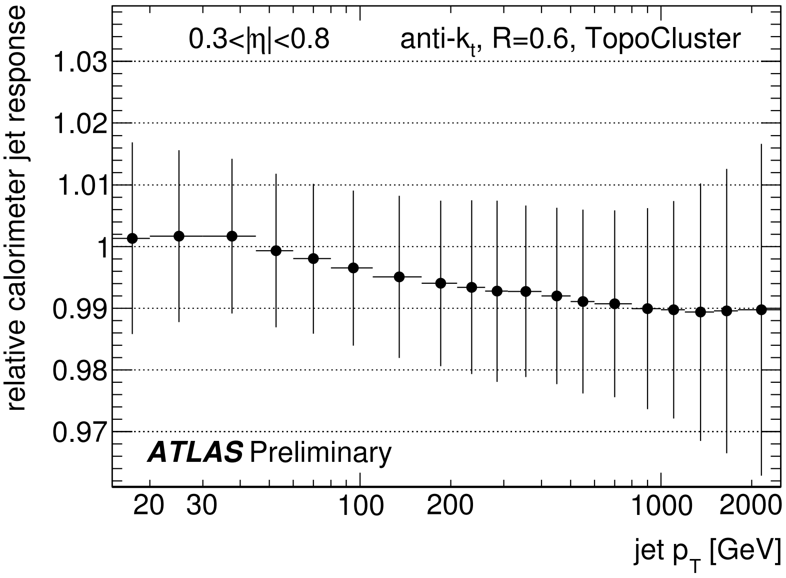

Figure 7.2: Ratio of the calorimeter response, determined from in-situ and test beam response measurements, with respect to the calorimeter jet response predicted by the Monte Carlo simulation [137]. This is shown as a function of the calibrated transverse momentum of jets reconstructed with the anti-k_t jet algorithm with $R = 0.6$ in the region $0.3 < |\eta| < 0.8$. The jet transverse momentum is calibrated to the hadronic scale using the EM+JES calibration scheme (see Sec. 5.2). The error bars indicate the systematic uncertainty on the ratio.

error bars indicate the systematic uncertainty on the ratio. The results for the region $|\eta| < 0.3$ are similar.

In the pseudorapidity range $0 \leq |\eta| < 0.8$, the jet energy scale expected from the single hadron response measurements is shifted by about 1 % with respect to the nominal calibration, with a fractional uncertainty on the shift ranging between 1% to 3%. The total envelope, which is defined as the shift added linearly to the uncertainty, ranges from $1.5 - 4\%$, depending on the jet transverse momentum. The envelope is assigned as the fractional JES uncertainty arising from the calorimeter response.

7.6.3 Detector Simulation

Calorimeter Cell Noise Thresholds

As described in Sec 5.1, topo-clusters are constructed based on the signal-to-noise ratio of calorimeter cells, where the noise is defined as the spread of the measured cell energy distribution in events with no energy depositions from collision events. Discrepancies between the simulated noise and the real noise in data may lead to differences in the cluster shapes and to the presence of fake topo-clusters. For data, the noise can change over time, while the noise RMS used in the simulation is fixed at the time of the production of the simulated data sets. These effects can lead to biases in the jet reconstruction and calibration if the electronic noise injected in the Monte Carlo simulation does not reflect that in data. An uncertainty is assigned based on the change in response for jets reconstructed with modified cell noise thresholds.

The maximal observed change in the jet response is used to estimate the corresponding uncertainty on the jet energy measurement due to the calorimeter cell noise modeling. The uncertainty is below 3% for the whole pseudorapidity range and is negligible for jets with transverse momenta above 45 GeV. It is 2% for $20 \leq p_{\mathrm{T}}^{\mathrm{jet}} < 30$ GeV.

Additional Detector Material

The jet energy scale is affected by possible inaccuracies in the material description, since the calibration is derived to restore energy lost according to the geometry modeled in the Monte Carlo simulation. Systematic variations to the amount of material have been designed based on test-beam measurements [108], in addition to studies of photon conversion at $\sqrt{s} = 900$ GeV [136] and mapping of the ID material using hadronic interactions in collision data at $\sqrt{s} = 7$ TeV [135].

The effects on the jet response of possible additional material can be very important. For example, the quality criteria of the track selection for the single hadron response measurement effectively only allow particles that have not interacted in the Pixel and SCT detectors to be measured. The uncertainty associated with mismodeling the material is evaluated by studying the impact of systematically adding 5% of material to the existing inner detector services [178]. In addition, systematic variations of the material are also performed by adding material at various places around the EM calorimeter: in the cryostat in front of the EM calorimeter, between the presampler and the first layer of the EM calorimeter, in the cryostat after the barrel EM calorimeter, and in the barrel-endcap transition [178].

The contribution to the jet energy scale uncertainty from possible extra detector material is computed by weighting the resulting difference in response for each type of particle when extra material is added by the average energy fraction of that type of particle.

7.6.4 η Intercalibration

Dijet p_{T} Balance

The relative calorimeter response to jets and its uncertainty is studied by comparing the transverse momenta of a well-calibrated central jet and a jet in the forward region in events with only two jets at high transverse momenta [174]. A simple way to perform this is to define a fixed central region of the calorimeters as the reference region. The relative response to jets in other calorimeter regions is then quantified using the p_{T} balance between the reference jet and the probe jet, exploiting the fact that these jets are expected to have equal p_{T} due to transverse momentum conservation.

The p_{T} balance is characterized by the asymmetry $\mathcal{A}$, which is defined as

$$\mathcal{A} = \frac{p_{\mathrm{T}}^{\mathrm{probe}} - p_{\mathrm{T}}^{\mathrm{ref}}}{p_{\mathrm{T}}^{\mathrm{avg}}}, \tag{7.1}$$

with $p_{\mathrm{T}}^{\mathrm{avg}} = (p_{\mathrm{T}}^{\mathrm{probe}} + p_{\mathrm{T}}^{\mathrm{ref}})/2$. The reference region is chosen as the central region of the barrel: $|\eta| < 0.8$. The asymmetry is then used to measure an η-intercalibration factor c for the probe jet, or equivalently its response relative to the reference jet $1/c$, using the relation

$$\frac{p_{\mathrm{T}}^{\mathrm{probe}}}{p_{\mathrm{T}}^{\mathrm{ref}}} = \frac{2+\mathcal{A}}{2-\mathcal{A}} = 1/c. \tag{7.2}$$

One disadvantage with the method outlined above is the requirement that each event have a jet in the central reference region. This causes a significant loss of statistics, especially in the forward region, where the dijet cross section drops steeply as the rapidity interval between the jets increases. In order to use the full event statistics, the default method can be extended by generalizing the method from use of a probe jet and a reference jet to a "left" jet and "right" jet. Then the relative correction factor c_{ik} for a given jet η-bin i and for a fixed $p_{\mathrm{T}}^{\mathrm{avg}}$-bin k is obtained by minimizing a matrix of linear equations.

Uncertainties in the Forward Region

The Monte Carlo simulation predictions for the relative jet response show some disagreement at low values of $p_{\mathrm{T}}^{\mathrm{avg}}$, such that the data lie between the different predictions. Therefore the uncertainty on the relative jet response must reflect this disagreement since it is not known a priori which theoretical prediction is more accurate.

The uncertainty on the relative response is taken to be the RMS deviation of the Monte Carlo predictions from the data. At high p_{T}, where the spread among the Monte

Carlo simulation predictions is small, the uncertainty primarily reflects the true difference between the response in data and simulation. At low p_{T} and large $|\eta|$ however, the uncertainty mostly reflects the physics modeling uncertainty, although the detector-based differences between data and simulation are also accounted for. This uncertainty is added in quadrature to the baseline uncertainty that is taken from the central region $0.3 < |\eta| < 0.8$. Figure 7.3 shows the relative jet response, and the associated intercalibration uncertainty calculated as detailed above, as a function of jet $|\eta|$ for two representative $p_{\mathrm{T}}^{\mathrm{avg}}$-bins.

7.6.5 Pile-up

Offset Correction

The uncertainty on the jet offset correction for pile-up arises from a number of sources. The trigger selection is varied to estimate the resulting impact on the distribution of tower energies. Similarly, the tower multiplicity is studied as a function of $p_{\mathrm{T}}^{\mathrm{jet}}$ and N_{PV} for jets based on topo-clusters. The offset correction derived from track jets is studied as a function of the number of primary vertices for various values of track jet p_{T}. The non-closure of the tower-based offset correction is evaluated by examining the dependence of the corrected calorimeter jet energy for calorimeter jets matched to track jets as a function of the number of primary vertices. The mapping of the tower-based offset correction to the jet-based offset correction also has an uncertainty.

Lastly, the offset correction for jets based on topo-clusters receives an additional uncertainty due to the average tower multiplicity approximation. This contribution is estimated to introduce a 20% uncertainty in the constituent tower multiplicity by comparing jets in events with $1 \leq N_{\mathrm{PV}} \leq 3$ and for the five highest $p_{\mathrm{T}}^{\mathrm{track\ jet}}$-bins. This estimation

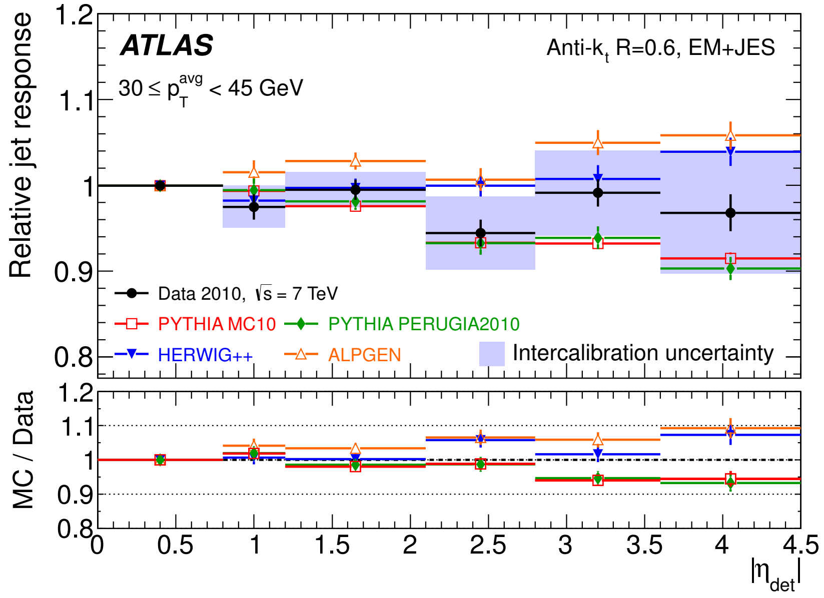

(a) $30 \le p_{\mathrm{T}}^{\mathrm{avg}} < 45$ GeV

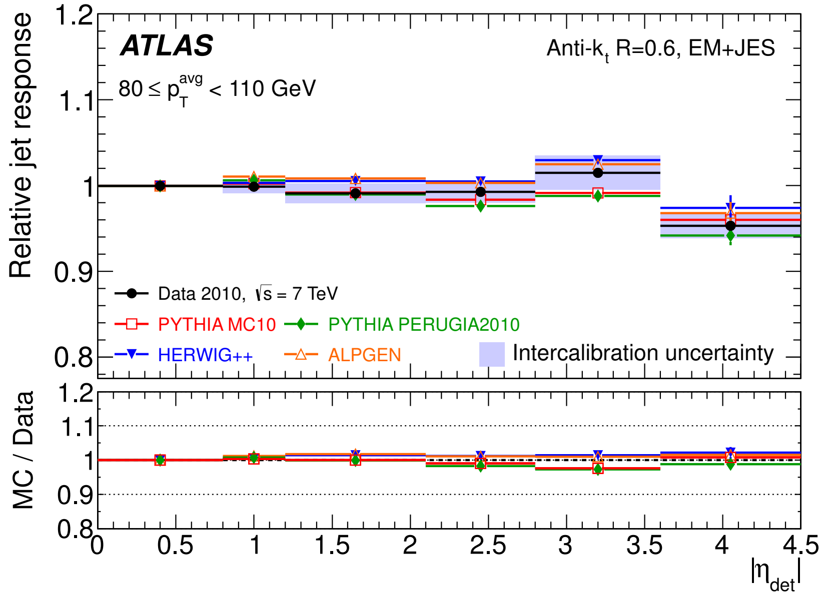

(b) $80 \le p_{\mathrm{T}}^{\mathrm{avg}} < 110$ GeV

Figure 7.3: Average jet response for anti-k_t jets with $R = 0.6$ measured relative to a central reference jet within $|\eta| < 0.8$ using collision data and various Monte Carlo simulations [14]. The response is shown as a function of $|\eta|$ for $p_{\mathrm{T}}^{\mathrm{avg}}$ in the ranges $30 - 45$ GeV (a) and $80 - 110$ GeV (b). The resulting systematic uncertainty is shown as a shaded band around the data points. The data points are only shown with statistical uncertainties.

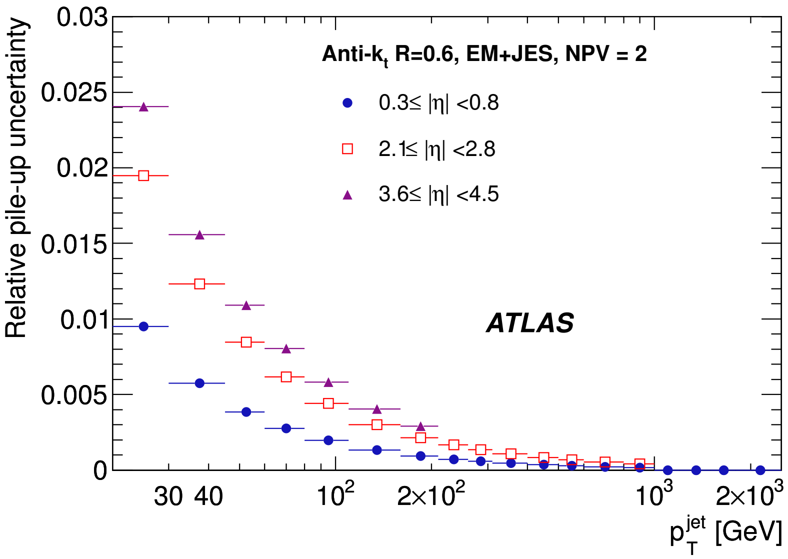

Figure 7.4: Fractional uncertainty in the jet energy scale due to pile-up, shown for anti-k_t jets with $R = 0.6$ for events containing two measured primary vertices, $N_{\mathrm{PV}} = 2$ [14]. The uncertainty is shown separately for jets in the central ($0.3 \leq |\eta| < 0.8$, full circles), endcap ($2.1 \leq |\eta| < 2.8$, open squares), and forward ($3.6 \leq |\eta| < 4.5$, full triangles) regions as a function of jet transverse momentum.

translates directly into a 20% uncertainty on the jet-level offset. The resulting systematic uncertainty on jets corrected by the offset correction is estimated to be about 160 MeV per primary vertex, a factor of three smaller than pile-up correction itself.

Figure 7.4 shows the fractional uncertainty due to pile-up in events with two measured primary vertices. The uncertainty due to pile-up for central jets with $p_{\mathrm{T}} = 20$ GeV and pseudorapidity $|\eta| \leq 0.8$ is about 1%. It is less than 2.5% for all jets with $|\eta| \leq 4.5$.

Out-of-time Pile-up

The effect of additional proton-proton collisions from previous bunch crossings within trains of consecutive bunches, which is referred to as “out-of-time” pile-up, has been studied and found to be negligible in the 2010 data.

7.6.6 Non-closure of the Calibration

After the jets in the nominal jet Monte Carlo simulation sample are calibrated (see Sec. 5.2), the calibrated jet p_{T} shows slight deviations from the true value at low p_{T}, which is termed "non-closure". One of the reasons that this occurs is that the calibration is derived to correct the jet E and η. There is no explicit correction for the jet p_{T}, which exhibits a different response than E since jets have non-zero mass. The deviation from unity is taken as a separate uncertainty.

7.6.7 Summary

The JES uncertainty is estimated by adding all the systematic uncertainties in quadrature. Figures 7.5–7.6 show the total systematic uncertainty on the jet energy scale as a function of $p_{\mathrm{T}}^{\mathrm{jet}}$ for three selected η regions. The individual contributions to the JES uncertainty are indicated.

The fractional JES uncertainty in the central region, excluding the uncertainty from pile-up, is between 2–2.5% for $60 \leq p_{\mathrm{T}}^{\mathrm{jet}} < 800$ GeV. For jets with $p_{\mathrm{T}}^{\mathrm{jet}} > 800$ GeV, the uncertainty ranges from 2.5% to 4%. In the forward region, the JES uncertainty for $p_{\mathrm{T}}^{\mathrm{jet}} =$ 20 GeV is 13%. Here the uncertainty is dominated by the modeling of the soft physics in the forward region, which enters through the η-intercalibration. The contribution to the uncertainty from pile-up is added separately and depends on the number of primary vertices in the event (see Sec. 7.6.5).

7.7 In-situ Validation of JES

The jet energy calibration is tested using three in-situ techniques, each of which uses a well-calibrated object as a reference and compares data to the nominal PYTHIA Monte Carlo

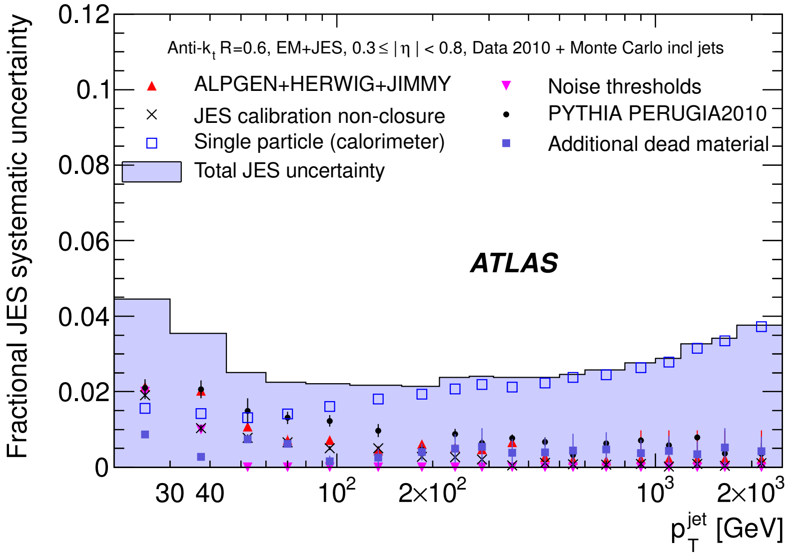

(a) $0.3 \leq |\eta| < 0.8$

Figure 7.5: Fractional uncertainty in the jet energy scale as a function of the transverse momentum of jets in the region $0.3 \leq |\eta| < 0.8$ in the calorimeter barrel [14]. The total uncertainty is shown as the solid light shaded area, and the individual sources of uncertainty are also indicated.

simulation. The first of these involves the comparison of the jet transverse momentum with the transverse momentum carried by tracks associated to the jet [179]. The second method uses the transverse momentum balance between a photon and a jet, with an alternative but similar technique involving the balance of the photon p_{T} against that of the hadronic recoil [15]. The third and last technique involves the transverse momentum balance between a high-p_{T} jet and a system of low-p_{T} jets [180].

To determine the JES uncertainty using each technique, the modeling of physics effects is separated from detector effects by systematically varying the event selection criteria. The ability of the Monte Carlo simulation to describe extreme variations of the selection criteria determines the systematic uncertainty in the in-situ methods, since physics effects can be suppressed or amplified by these variations. The in-situ techniques are used only to assess the systematic uncertainty in the jet energy measurement, not to derive the

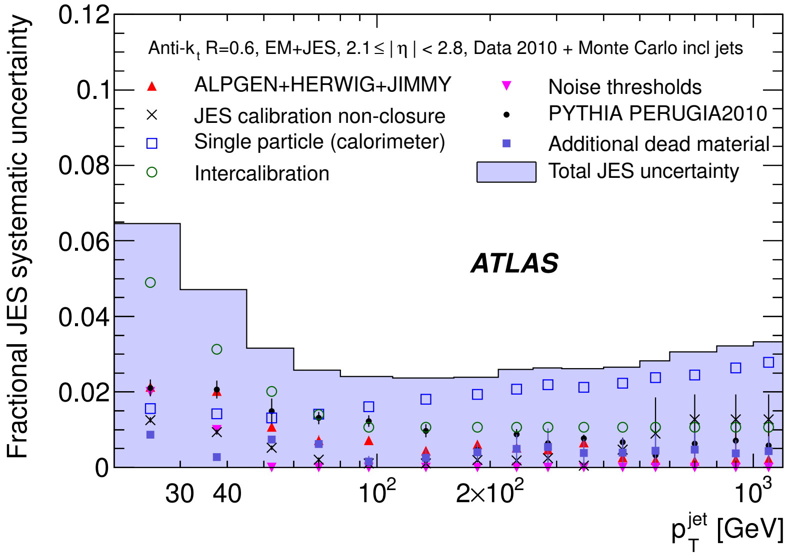

(a) $2.1 \leq |\eta| < 2.8$

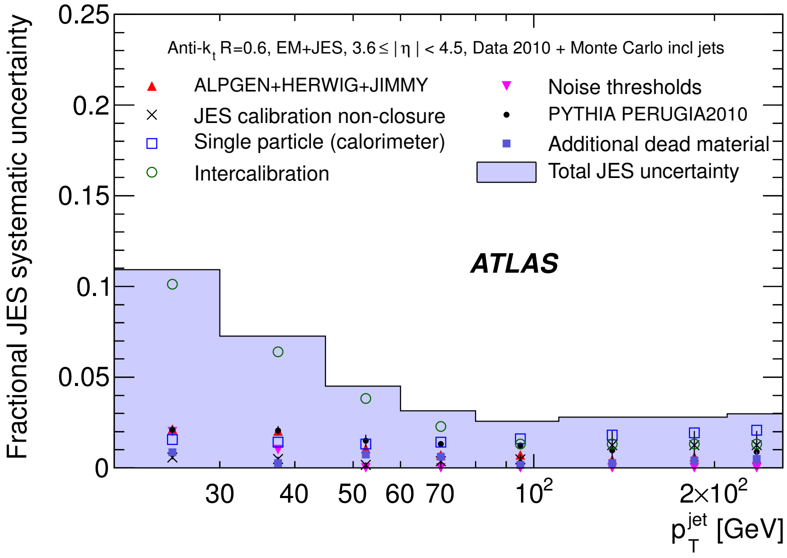

(b) $3.6 \leq |\eta| < 4.5$

Figure 7.6: Fractional uncertainty in the jet energy scale as a function of the transverse momentum of jets in the region $2.1 \leq |\eta| < 2.8$ in the calorimeter endcap (a) and in the forward region $3.6 \leq |\eta| < 4.5$ (b) [14]. The total uncertainty is shown as the solid light shaded area, and the individual sources of uncertainty are also indicated.

calibration itself.

7.7.1 Transverse Momentum Balance of Calorimeter Jets vs. Tracks

Technique

The mean transverse momentum sum of tracks that are within a cone with size R around a jet provides an independent test of the calorimeter energy scale within the tracking acceptance. The transverse momentum of each jet is compared with the total transverse momentum of tracks associated with the jet by means of the charged-to-total-momentum ratio:

$$r_{\mathrm{trk}} = \frac{\sum p_{\mathrm{T}}^{\mathrm{track}}}{p_{\mathrm{T}}^{\mathrm{jet}}} \tag{7.3}$$

The ratio, r_{trk}, is used to determine the calorimeter jet energy scale. This calibration is used for jets with $|\eta| < 2.1$ that are confined within the tracking detector coverage. The ratio is compared between the data and Monte Carlo predictions to evaluate the quality of the simulation.

Event Selection

To ensure that the majority of tracks associated with the jets found in the calorimeter are within the inner detector fiducial volume, jets are required to have $|\eta| < 2.1$. Tracks with $p_{\mathrm{T}}^{\mathrm{track}} > 1$ GeV are selected, in order to select mainly tracks from fragmentation rather than those arising from soft and diffuse interactions. A track is associated to a jet if the distance $\Delta R_{\,\mathrm{track,jet}}$ between the track and the jet is less than the clustering parameter ($R = 0.4$ or $R = 0.6$) of the jet algorithm.

Systematic Uncertainties

There are a number of sources of systematic uncertainty on these measurements. There is a model dependence due to the parameterization of the fragmentation function and of the underlying event, as well as the probability of producing different particles. The charged particle fragmentation function and transverse profile for jets have been measured using collision data and are reasonably described by several Monte Carlo generators and tunes [181]. There is an uncertainty on the reconstruction efficiency for isolated tracks, which is derived from the uncertainty on the modeling of the inner detector material. Moreover the tracking efficiency inside a jet is degraded compared to that for isolated tracks, due to missed hits or shared ID hits. The calorimeter jet transverse momentum resolution and ID alignment also contribute to the uncertainty.

Results

The average charged-to-total momentum ratio, $\langle r_{\rm trk} \rangle$, obtained using collision data and the Monte Carlo simulation, is shown in Fig. 7.7. The ratio is shown as a function of the transverse momentum of anti-k_t jets with $R = 0.6$ that are in the region $|\eta| < 1.2$ and that have been calibrated using the EM+JES scheme [179]. If all particles in jets were pions, isospin symmetry would cause the charged-to-total momentum ratio to be 2/3. However other particles such as kaons, η mesons, and baryons give different charged fractions, and detector effects also influence the ratio. The charged-to-total momentum ratio measured using collision data ranges from about 0.37 for jets with $p_{\rm T} = 20$ GeV to around 0.5 for high-energy jets with $p_{\rm T} = 1$ TeV. It is well-modeled by the Monte Carlo simulation.

The double ratio, $R_{r_{\rm trk}}$, of the charged-to-total momentum ratio obtained using data and the Monte Carlo simulation is shown in Fig. 7.8. It is shown for two representative

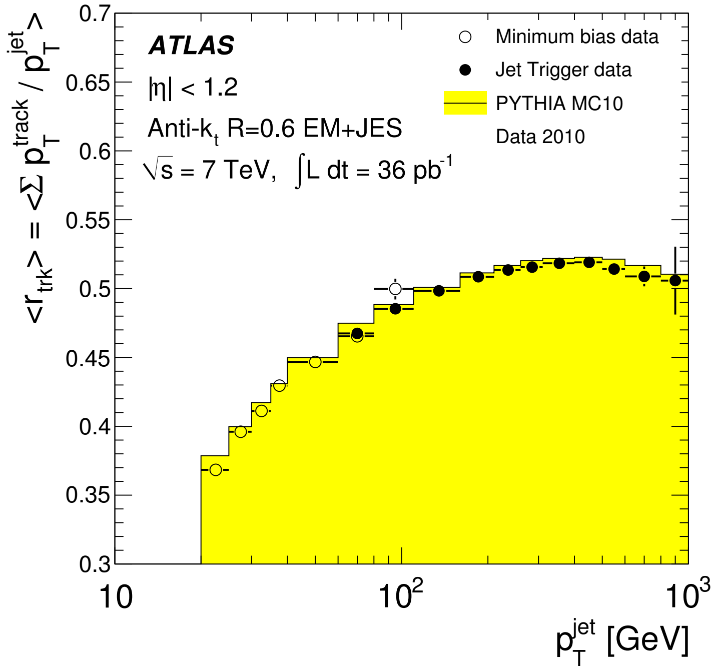

Figure 7.7: The average charged-to-total momentum ratio, $\langle r_{\mathrm{trk}} \rangle$, obtained using collision data and the Monte Carlo simulation, shown as a function of the transverse momentum of anti-k_t jets with $R = 0.6$ that are in the region $|\eta| < 1.2$ and that have been calibrated using the EM+JES scheme [179]. The data measured with the jet (minimum bias) trigger are shown as closed (open) circles. Only statistical uncertainties are shown.

bins in η together with the systematic uncertainties on the double ratio. Averaging all data with $p_{\mathrm{T}}^{\mathrm{jet}} > 25$ GeV and $|\eta| < 1.2$ yields a value of r_{trk} that agrees with the simulation to better than 1%. This small discrepancy is well within the quoted systematic uncertainty, which is highly correlated between bins in $p_{\mathrm{T}}^{\mathrm{jet}}$. No significant variation of $R_{r_{\mathrm{trk}}}$ with $p_{\mathrm{T}}^{\mathrm{jet}}$ is observed. For $1.7 \leq |\eta| < 2.1$, the statistical uncertainties are large for $p_{\mathrm{T}}^{\mathrm{jet}} > 500$ GeV. For $p_{\mathrm{T}}^{\mathrm{jet}} < 500$ GeV, the level of agreement between data and simulation is similar to that obtained at low η.

The systematic uncertainties are below 3% for $0 \leq |\eta| < 1.2$ and rise to about 4% for $1.7 \leq |\eta| < 2.1$ for $40 \leq p_{\mathrm{T}}^{\mathrm{jet}} < 800$ GeV. The results agree within systematic uncertainties

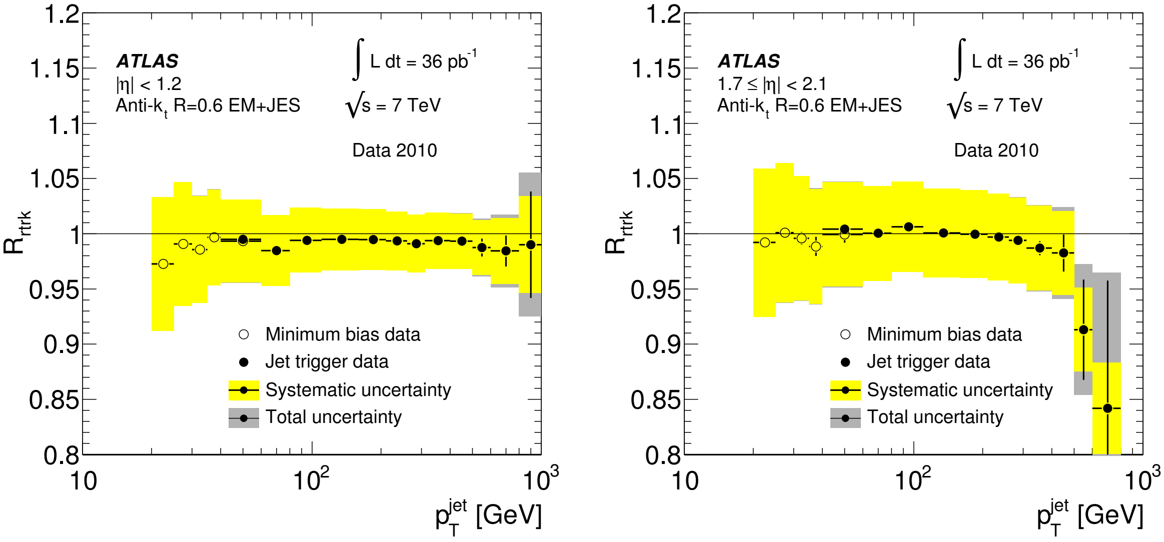

(a) $0 \leq |\eta| < 1.2$

(b) $1.7 \leq |\eta| < 2.1$

Figure 7.8: Double ratio of the mean track to calorimeter response ratio in data and Monte Carlo simulation, $R_{r_{\mathrm{trk}}} = [r_{\mathrm{trk}}]_{\mathrm{Data}}/[r_{\mathrm{trk}}]_{\mathrm{MC}}$, for anti-$k_t$ jets with $R = 0.6$ calibrated with the EM+JES scheme as a function of $p_{\mathrm{T}}^{\mathrm{jet}}$ for two representative η bins [179].

with those predicted using the calorimeter simulation and provide an independent estimate of the overall jet energy scale and its uncertainty.

7.7.2 Photon-jet Transverse Momentum Balance

Techniques

In γ-jet events, a jet recoils against a photon at high transverse momentum. The photon energy, being accurately measured in the electromagnetic calorimeter, is used as a reference. Any discrepancy between data and simulation is taken as an uncertainty on the jet energy calibration. Two methods of balancing the photon and the recoiling jet transverse momenta, with different sensitivities and systematic uncertainties, are used: a direct p_{T}

balance technique and a missing p_{T} projection fraction technique. Both comparisons are done in the jet η range $|\eta| < 1.2$ and for photon transverse momenta $25 \leq p_{\mathrm{T}}^{\gamma} < 250$ GeV.

The "direct p_{T} balance" technique exploits the approximate transverse momentum balance in events with only one photon and one jet with high p_{T}. The ratio of the jet p_{T} to the photon p_{T} ($p_{\mathrm{T}}^{\mathrm{jet}}/p_{\mathrm{T}}^{\gamma}$) is used to estimate the jet response. Since the photon p_{T} is well-measured and well-described by the simulation, the quality of the jet p_{T} calibration can be assessed by comparing data and Monte Carlo simulation using the ratio $p_{\mathrm{T}}^{\mathrm{jet}}/p_{\mathrm{T}}^{\gamma}$.

The "missing p_{T} projection fraction" (MPF) technique exploits the transverse momentum balance of the photon and the hadronic recoil to derive the detector response to hadronic jets. It uses the projection of the missing transverse energy onto the photon direction. The method is based on the assumption that the only missing transverse momentum in a γ-jet event arises from calorimeter non-compensation, signal losses due to noise suppression, and energy losses in the non-active regions of the detector by the hadronic jet. Using transverse momentum balance of the photon and the jet, the calorimeter response can be written as:

$$\mathcal{R}_{\mathrm{MPF}} = 1 + \frac{\vec{p}_{\mathrm{T}}^{\gamma} \cdot \vec{E}_{\mathrm{T}}^{\mathrm{miss}}}{|p_{\mathrm{T}}^{\gamma}|^2}, \tag{7.4}$$

where $\mathcal{R}_{\mathrm{MPF}}$ is defined as the MPF response, $\vec{p}_{\mathrm{T}}^{\gamma}$ is the photon transverse momentum, and $\vec{E}_{\mathrm{T}}^{\mathrm{miss}}$ is the missing transverse momentum. Because it does not use the jet energy directly, the MPF response does not strongly depend on the jet algorithm.

Event Selection

The leading photon in each event must have $p_{\mathrm{T}}^{\gamma} > 25$ GeV and lie in the pseudorapidity range $|\eta^{\gamma}| < 1.37$. In this range the photon is fully contained within the electromagnetic barrel calorimeter. Furthermore, events are rejected if the leading photon is in a calorimeter region where an accurate energy measurement is not possible. The leading photon candidate must satisfy strict photon identification criteria [182], meaning that the pattern of energy deposition in the calorimeter is consistent with the expected photon showering behavior. The photon candidate must be isolated from other activity in the calorimeter using an isolation cone of size $R = 0.4$.

The leading jet must be in the fiducial region $|\eta| < 1.2$. Soft QCD radiation can affect the p_{T} balance between the jet and photon. This effect is suppressed by selecting events where the photon and the leading jet are anti-aligned, and where the third highest-p_{T} jet in the event has small p_{T}.

Systematic Uncertainties

Systematic uncertainties from a number of effects are estimated. The systematic uncertainty from jets which are identified as photons (fakes) are studied using the Monte Carlo simulation. The rate of dijet events faking photons is sensitive to the detailed modeling of the jet fragmentation and the detector simulation, and is therefore subject to large uncertainties. This is estimated by studying distributions of the transverse isolation energy and the photon identification of the photon candidate. The effect of background contamination in the γ-jet sample has been further validated by varying the photon identification criteria. Additional uncertainties arise from in-time pile-up, the choice of criteria to suppress soft QCD radiation, and the photon energy scale.

The direct p_{T} balance and MPF techniques are dominated by different systematic uncertainties, thereby providing a useful cross-check of each other. The total systematic uncertainty on the ratio of the jet response in data to that in the Monte Carlo simulation is smaller than 1% for the MPF method, and smaller than 1.6% for the direct p_{T} balance method.

Results

Figure 7.9 shows the jet response measured in both data and the Monte Carlo simulation using the direct p_{T} balance technique with the anti-k_t jet algorithm with $R = 0.6$ for the EM+JES calibration scheme. The data to Monte Carlo simulation agreement is well within ±5%. Figure 7.10(a) shows the ratio of $(p_{\mathrm{T}}^{\mathrm{jet}}/p_{\mathrm{T}}^{\gamma})$ between data and the Monte Carlo simulation, together with the total uncertainty on the determination of the data to Monte Carlo simulation ratio, for anti-k_t jets with $R = 0.6$. Similarly, Fig. 7.10(b) shows the ratio of calorimeter response in data and the Monte Carlo simulation, as determined using the MPF technique, together with the total uncertainty on the determination of the data to Monte Carlo simulation ratio.

For $p_{\mathrm{T}}^{\gamma} > 45$ GeV, the response in data and Monte Carlo simulation agree to within 3% for both MPF and direct balance techniques. In the range $25 \leq p_{\mathrm{T}}^{\gamma} < 45$ GeV there is an observed shift of 5% for the direct p_{T} balance technique and 3% for the MPF technique. The size of these shifts is consistent with the systematic uncertainty on the EM+JES jet energy calibration (see Sec. 7.6). At high p_{T}^{γ} the dominant uncertainty is statistical while the systematic uncertainty dominates at low p_{T}^{γ}.

Based on the differences in the response observed between the data and the Monte Carlo simulation for the MPF method shown in Fig. 7.10(b), and accounting for the systematic and statistical uncertainties on each response determination, the in-situ JES systematic uncertainty is estimated to be less than 1.6% for $45 \leq p_{\mathrm{T}}^{\gamma} < 240$ GeV.

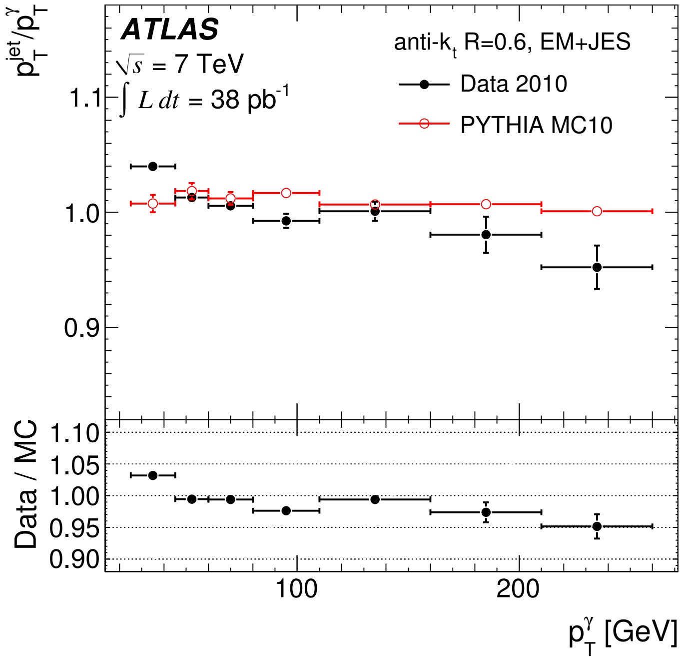

Figure 7.9: Average jet response as determined by the direct p_{T} balance technique for anti-k_t jets with $R = 0.6$ calibrated with the EM+JES scheme as a function of the photon transverse momentum for both data and Monte Carlo simulation [15]. The lower part of the figure shows the data to Monte Carlo simulation ratio. Only statistical uncertainties are shown.

7.7.3 Multijet Transverse Momentum Balance

Technique

The p_{T} reach in the γ-jet transverse momentum balance technique is limited by the available event statistics. If jets at low transverse momentum are well-calibrated, jets at high transverse momentum can be balanced against a recoil system of low transverse momentum jets. This multijet balance technique is used to assess the jet calibration for p_{T} values up to 1 TeV. The η range used for the comparison is $|\eta| < 2.8$.

The method exploits the p_{T} balance in events where the highest p_{T} jet (leading jet)

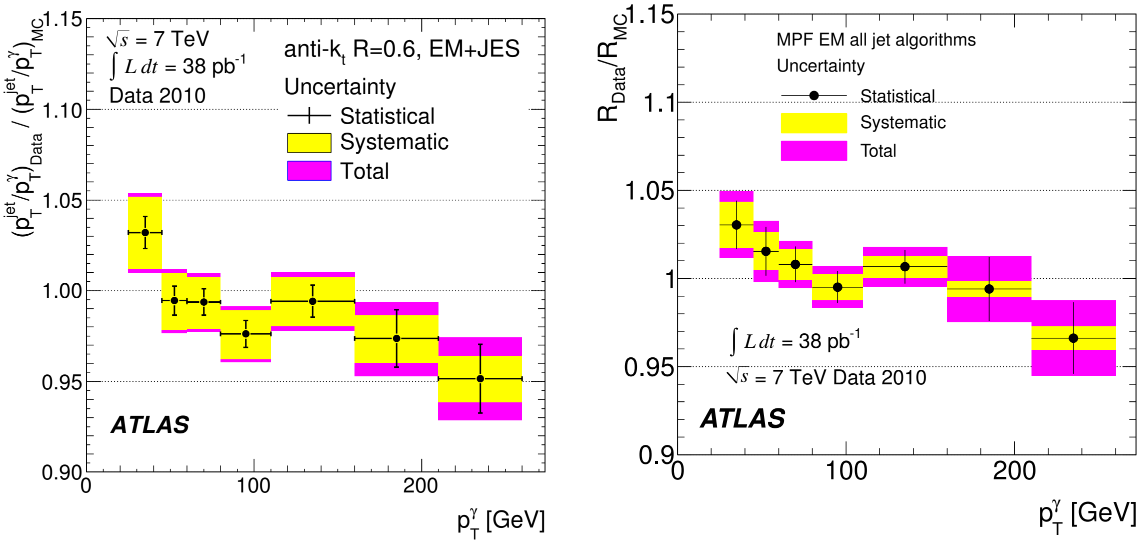

(a) Direct balance

(b) MPF

Figure 7.10: Ratio of the jet response in data and Monte Carlo simulation using the direct p_T balance technique (a) and the MPF method (b) as a function of the photon transverse momentum [15]. Statistical and systematic uncertainties (light band) are included with the total uncertainty shown as the dark band.

is produced back-to-back in ϕ to a multijet recoil system. The vectorial sum of the transverse momenta of all non-leading jets defines the transverse momentum of the recoil system ($p_\mathrm{T}^\mathrm{Recoil}$), which is expected to approximately balance the transverse momentum of the leading jet ($p_\mathrm{T}^\mathrm{Leading}$). Thus a correlation between the momentum scale of the leading jet and the scale of the non-leading jets can be established. If the absolute JES is well-known for all non-leading jets, the JES of the leading jet can be verified by studying the multijet balance (MJB), which is defined as the ratio:

$$\mathrm{MJB} = \frac{|\vec{p}_\mathrm{T}^{\,\mathrm{Leading}}|}{|\vec{p}_\mathrm{T}^{\,\mathrm{Recoil}}|}. \tag{7.5}$$

Event Selection

Events with one jet produced opposite to a well-defined recoil system are selected by requiring that the leading jet be anti-aligned with the next-to-leading jet in the transverse plane, and by requiring any additional jets to be well-separated from the leading jet. The leading jet is also required to have higher energy than the jets in the recoil system.

Systematic Uncertainties

The two main categories of systematic uncertainty involve the reference p_{T} of the recoil system and the variable MJB used to characterize its comparison to the leading jet p_{T}. The systematic uncertainty on the p_{T} of the recoil system has been calculated taking into account the JES uncertainty for isolated jets, as well as additional uncertainties for nearby jets and the uncertainty in the quark or gluon nature of the recoil system. The recoil system often contains nearby jets, and the jet response is dependent on the angular distance to the closest jet. A systematic uncertainty is assigned to account for the possible effect of soft radiation between the jets. Since the JES uncertainty is estimated for the average jet composition of the inclusive jet sample, a discrepancy in the specific flavor composition between data and Monte Carlo simulation results in an additional uncertainty.

The second category of systematic uncertainties includes sources that affect the MJB variable used to probe the jet energy scale at high $p_{\mathrm{T}}^{\mathrm{jet}}$. These include the selection criteria, jet rapidity acceptance, soft physics modeling, and pile-up.

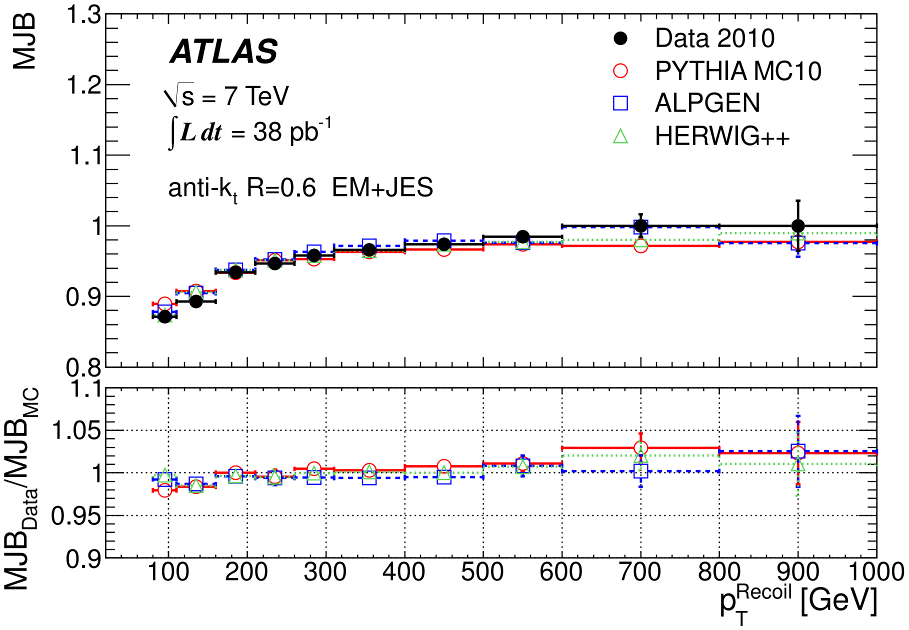

Figure 7.11: Multijet balance MJB as a function of the recoil system $p_{\rm T}$ for data and Monte Carlo simulation for anti-k_t jets with $R = 0.6$ [180]. Only statistical uncertainties are shown.

Results

The multijet balance obtained using collision data and various Monte Carlo simulations are shown in Fig. 7.11 for anti-k_t jets with $R = 0.6$. The transverse momentum of the recoil system ranges from 80 GeV up to 1.0 TeV. The multijet balance at low $p_{\rm T}^{\rm Recoil}$ values shows a bias towards values lower than one, an effect that is correctly reproduced by the Monte Carlo simulation. The ratio of the multijet balance obtained from data and from the Monte Carlo simulation is shown in the lower part of Fig. 7.11. It is within 3% for transverse jet momenta up to the TeV scale.

The systematic uncertainties resulting from the recoil reference system and from the multijet balance variable are added in quadrature and presented in Fig. 7.12 for anti-k_t jets with $R = 0.6$. The total systematic uncertainty amounts to about 4% for jets of

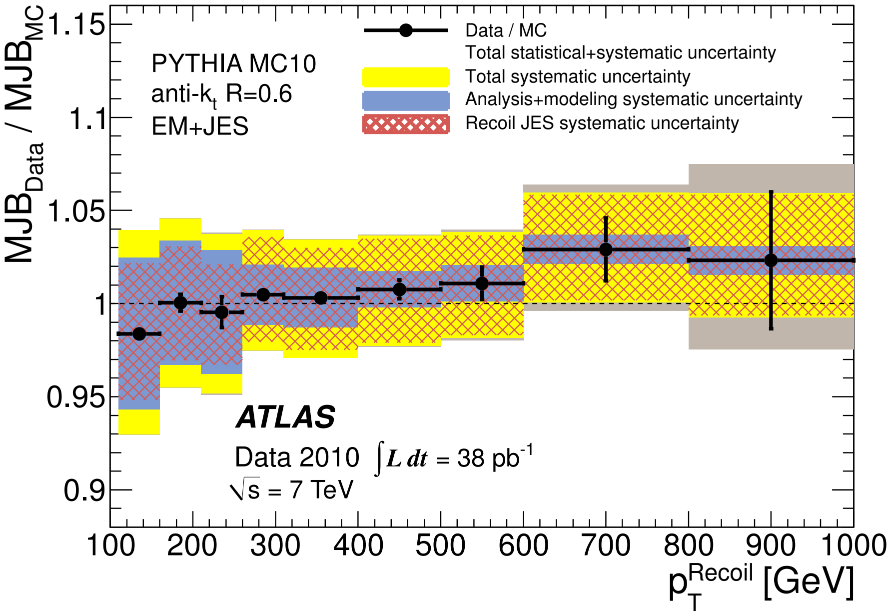

Figure 7.12: Ratio of data to Monte Carlo simulation for the multijet balance (MJB) as a function of the recoil system p_{T} for anti-k_t jets with $R = 0.6$ [180]. The colored regions show the total uncertainty (dark band), which is computed as the squared sum of all total systematic uncertainties (light band) and of the statistical uncertainty (error bars). Also displayed are the contributions to the systematic uncertainty due to the event selection and event modeling (darkest band) and due to the jet energy scale for jets in the recoil system (hatched band).

$p_{\mathrm{T}}^{\mathrm{jet}} = 1$ TeV. At high transverse momentum, the main contribution to the systematic uncertainty is the JES uncertainty. The high-p_{T} jet energy scale is validated to within 5% up to 1 TeV for anti-k_t jets with $R = 0.6$, and the agreement is even better for the range 100–600 GeV.

7.7.4 Summary

The jet energy calibration has been tested in-situ using well-calibrated objects as a reference and comparing data to the Monte Carlo simulation. The in-situ techniques include the comparison of the calorimeter jet transverse energy to the transverse momentum carried by tracks associated to the jet, the direct transverse momentum balance between a jet and a photon, the balance of a photon against the hadronic recoil using the missing transverse momentum projection fraction technique, and the p_T balance of a high-p_T jet recoiling against a system of lower p_T jets.

A summary of the comparisons of data to the Monte Carlo simulation for all in-situ techniques for $|\eta| < 1.2$ is shown in Fig. 7.13. The JES uncertainty as estimated from the single hadron response measurements and systematic variations of the Monte Carlo simulations (see Sec. 7.6) are also illustrated in the shaded band.

The results of the in-situ techniques are consistent with each other within the systematic uncertainties. The discrepancy between the data and the Monte Carlo simulation for the in-situ observables provides an estimate of the JES uncertainty, and is generally at the level of a few percent or less across a wide p_T range from 20 GeV to 1 TeV. The in-situ JES uncertainty is consistent with the JES uncertainty obtained using the independent method that relies on the single particle response.

7.8 Jet Energy Resolution

The jet energy resolution predicted by the Monte Carlo simulation is compared to that obtained in data using two in-situ techniques, one based on dijet balance and the other using a bisector method.

7.8.1 Techniques

The dijet balance method exploits the approximate transverse momentum balance in events with two jets, which implies that the jets have the same mean transverse momentum, $\langle p_{T,1} \rangle = \langle p_{T,2} \rangle \equiv p_T$. By requiring the jets to be in the same rapidity region of

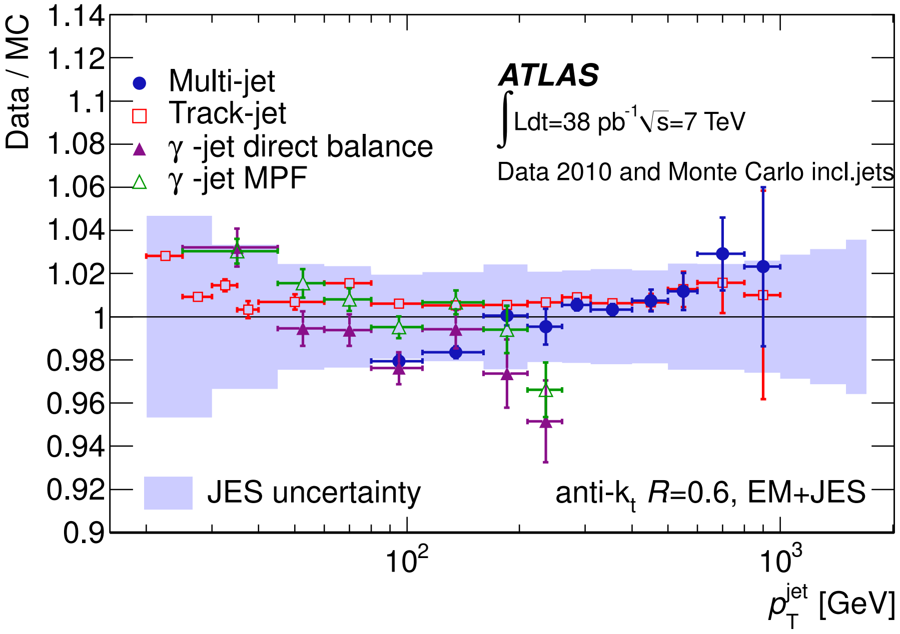

Figure 7.13: Double-ratio of the jet response in data and the Monte Carlo simulation obtained using several in-situ techniques, shown as a function of the transverse momentum of anti-k_t jets with $R = 0.6$ in the region $|\eta| < 1.2$ [14]. Only statistical uncertainties on the in-situ measurements are shown. The discrepancy between the data and the Monte Carlo simulation for the in-situ observables provides an estimate of the jet energy scale uncertainty that is generally a few percent or less for jet transverse momentum from 20 GeV to 1 TeV. The in-situ estimate of the JES uncertainty is consistent with the JES uncertainty for the region $|\eta| < 0.3$ determined using single hadron response measurements and systematic variations of the Monte Carlo simulation (see Sec. 7.6), which is superimposed (light band).

the detector, they also have the same p_{T} resolution: $\sigma_{p_{T,1}} = \sigma_{p_{T,2}} = \sigma_{p_T}$. Consequently the fractional p_{T} resolution for each jet can be written:

$$\frac{\sigma_{p_{\mathrm{T}}}}{p_{\mathrm{T}}} \simeq \sqrt{2}\sigma_A = \frac{\sqrt{2\left[(\sigma(p_{\mathrm{T},1}))^2 + (\sigma(p_{\mathrm{T},2}))^2\right]}}{\langle p_{\mathrm{T},1} + p_{\mathrm{T},2}\rangle} \tag{7.6}$$

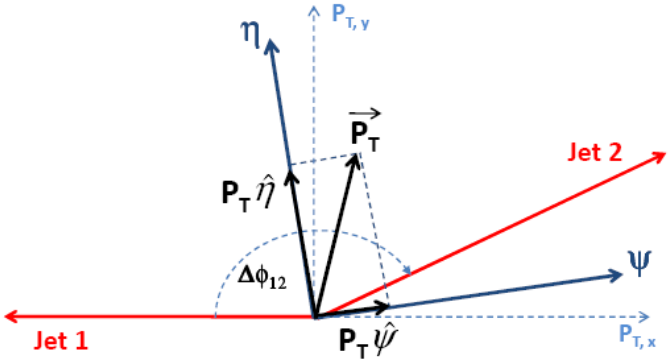

Figure 7.14: Schematic diagram defining the variables used in the bisector technique [183]. The η-axis corresponds to the azimuthal angular bi-sector of the di-jet system while the ψ-axis is defined as the one orthogonal to the η-axis; all in the plane transverse to the beam axis.

where σ_A is the p_T asymmetry of the two jets, and is given by:

$$A(p_{T,1}, p_{T,2}) \equiv \frac{p_{T,1} - p_{T,2}}{p_{T,1} + p_{T,2}}. \tag{7.7}$$

The spread in the p_T asymmetry thus provides an estimate of the fractional jet p_T resolution.

The bi-sector method utilizes the definition of an imbalance (transverse) vector, $\vec{P}_T$, which is defined as the vector sum of the two leading jets in the dijet event. This vector is projected along an orthogonal coordinate system in the transverse plane, (ψ, η), where η is chosen to lie in the direction that bisects $\Delta\phi_{12} = \phi_1 - \phi_2$, the angle formed by $\vec{P}_T^{\mathrm{jet},1}$ and $\vec{P}_T^{\mathrm{jet},2}$. This is illustrated in Fig. 7.14.

If the two leading jets belong to the same y region and thus have the same average jet energy resolution, the fractional jet energy resolution can be written:

$$\frac{\sigma(P_{\mathrm{T}})}{\langle P_{\mathrm{T}}\rangle} = \frac{\sqrt{\sigma_{\psi}^{2} - \sigma_{\eta}^{2}}}{\sqrt{2}\,\langle P_{\mathrm{T}}\rangle\,|\cos\Delta\phi_{12}|}. \tag{7.8}$$

where σ_{ψ}^{2} and σ_{η}^{2} denote the variances of $\vec{P}_{T}$ along the ψ and η directions, and $\Delta\phi_{12}$ is the azimuthal separation between the two leading jets. The effect of initial state radiation and other soft effects, which are approximately isotropic, are removed by subtracting in quadrature σ_{η} from σ_{ψ}.

7.8.2 Event Selection

For the dijet balance method, two leading jets anti-aligned in ϕ are selected by requiring them to be separated by at least $\Delta\phi \geq 2.8$. Both jets are required to be in the same y region in order for them to have the same jet energy resolution. The fractional jet p_{T} resolution is extracted from the dijet asymmetry in events where the transverse momentum of the third leading jet, $p_{\mathrm{T},3}$, is required to be small compared to the p_{T} of the leading jets. A correction for soft radiative effects is applied by extrapolating the resolution to a requirement of $p_{\mathrm{T},3} = 0$.

For the bisector method, no requirement on $\Delta\phi$ is applied. The two leading jets are required to be in the same rapidity region. As with the dijet balance method, the third leading jet is required to have low transverse momentum compared to the leading jets.

7.8.3 Systematic Uncertainties

For the dijet balance method, a systematic uncertainty is assigned to account for the dependence of the results on the particular requirements placed on the angular separation between the two leading jets, $\Delta\phi$, and the transverse momentum of the third leading jet,

$p_{\mathrm{T},3}$. An uncertainty associated with the determination of the soft radiation correction is also included.

For the bisector method, the dominant systematic uncertainty is due to the assumption that the soft radiation is isotropic and that its effect on the jet energy resolution is cancelled when the quadratic difference $\sigma_\psi^2 - \sigma_\eta^2$ is taken in Eq. 7.8. The precision with which the expected cancellation at particle level can be determined is assigned as the systematic uncertainty.

7.8.4 Results

The fractional jet p_T resolution obtained using the dijet balance and bisector methods in collision data and in the Monte Carlo simulation are shown as a function of jet p_T in the central region $|y| < 0.8$ in Fig. 7.15. The energies of the reconstructed jets in the Monte Carlo simulation are smeared so that the jet energy resolution in the simulation matches on average that measured in data for jets with transverse momenta between 30 GeV and 350 GeV. The spread in the resulting fractional difference between the jet energy resolution determined in data and in the smeared Monte Carlo simulation provides an estimate of the uncertainty on the jet energy resolution. The JER uncertainty estimated is 4% for the central region of the calorimeter shown, and is generally within 14% in more forward regions.

7.9 Unfolding

7.9.1 Data-driven Closure Test

The systematic uncertainty in the unfolding procedure has been evaluated using a data-driven closure test [171]. In this test the particle-level p_T (or dijet mass) spectrum in

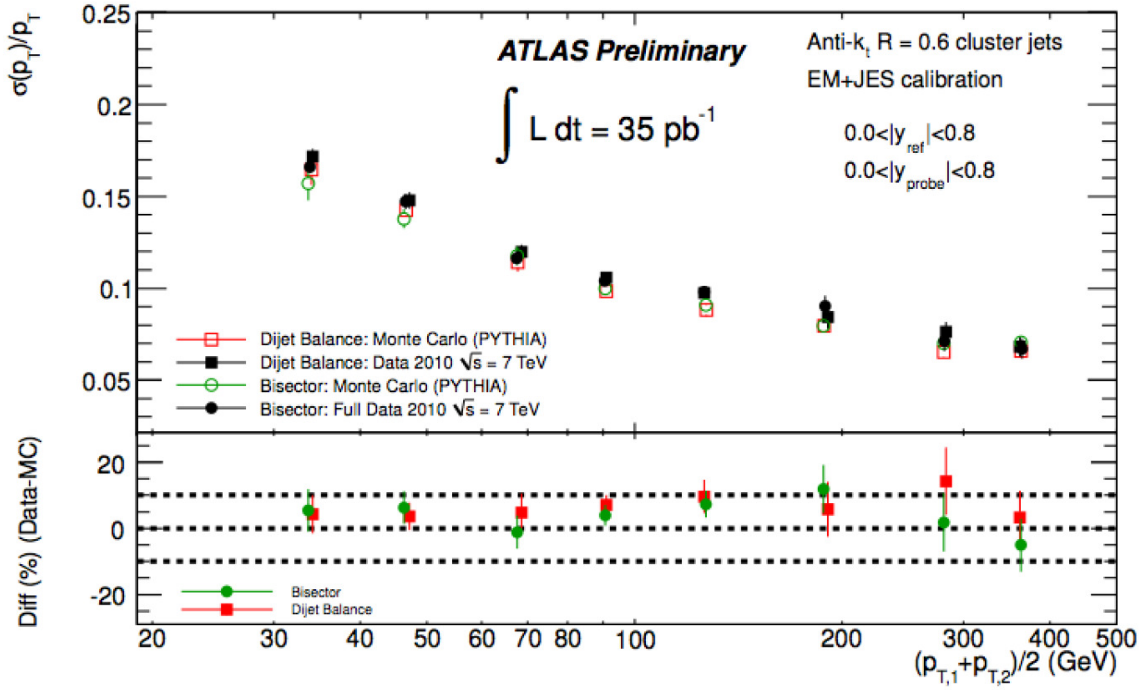

Figure 7.15: Jet energy resolution determined using the dijet balance and bisector techniques as a function of the jet transverse momentum of anti-k_t jets with $R = 0.6$ that have been calibrated using the EM+JES scheme [183]. The lower part of the figure shows the fractional difference between the resolution determined from the data and the Monte Carlo simulation.

the Monte Carlo simulation is reweighted such that after it is convolved through the folding matrix, a significantly improved agreement between the data and the reconstructed spectrum from the Monte Carlo simulation is attained. The reweighted, reconstructed spectrum from the Monte Carlo simulation is then unfolded using the same procedure as for the data. The comparison of the result with the reweighted particle-level spectrum from the Monte Carlo simulation provides the estimation of the bias in the unfolding technique.

7.9.2 Cross-check with Bin-by-bin Method

As a cross-check, the results obtained from the iterative unfolding (see Sec. 6.6) have been compared to those using a simpler bin-by-bin correction procedure, as well as the "singular value decomposition" (SVD) method implemented in the `TSVDUnfold` software [184, 185]. These methods use different regularization procedures and rely to different degrees on the Monte Carlo simulation modeling of the shape of the spectrum.

The bin-by-bin method gives results consistent with those obtained using the iterative unfolding technique, but requires the application of an explicit correction for the NLO k-factor to obtain good agreement. A somewhat larger bias is observed for the SVD method.

7.9.3 Cross-check with Jet Shapes

The use of Monte Carlo simulation to derive the transfer matrix in the unfolding procedure requires that the simulation models the jet properties well. The modeling of the energy flow around the jet core provides a useful test of this. The energy and momentum flow within a jet can be expressed in terms of the differential jet shape, defined for a jet with radius parameter R, as the fraction $\rho(r) = \frac{1}{\Delta r}\frac{p_{\mathrm{T}}^{r}}{p_{\mathrm{T}}^{R}}$, where p_{T}^{R} is the transverse momentum within a radius R of the jet axis, and p_{T}^{r} is the transverse momentum contained within a ring of thickness $\Delta r = 0.1$ at a mean radius $r = \sqrt{(\Delta y)^2 + (\Delta\phi)^2}$ from the jet axis.

Jet shape measurements using calorimeter energy clusters and tracks have been performed with 3 pb^{-1} of data [186], and show good agreement with the PYTHIA and HERWIG + JIMMY Monte Carlo simulations in the kinematic region 30 GeV $< p_{\mathrm{T}} <$ 600 GeV and rapidity $|y| < 2.8$. Using the same technique, the uncorrected jet shapes in the forward rapidity region $2.8 \leq |y| < 4.4$ have been studied in the context of the present analysis and are shown in Fig. 7.16. The maximum disagreement in shape between data and the Monte Carlo simulation is approximately 20%, demonstrating that the distribution of energy within the jets is reasonably well-modeled even in this worst case. Any bias from mis-modeling of the jet shape is included in the unfolding uncertainties described below, so this jet shape study serves only as a cross-check.

7.10 Uncertainty Propagation

Each individual source of uncertainty in the analysis is translated into a corresponding uncertainty on the inclusive jet p_{T} and dijet mass cross section measurements. This is done by repeating the analysis after systematically varying each effect. The total uncertainty on each cross section measurement is defined as the sum in quadrature of the individual uncertainties.

The uncertainties from the efficiencies for jet reconstruction, the selection of good-quality jets, and trigger requirements, are estimated by varying each efficiency up and down by its systematic uncertainty in the Monte Carlo simulation. Similarly, the jet energy scale applied to the reconstructed jets in the Monte Carlo simulation is varied up and down by one standard deviation. The resulting p_{T} or dijet mass spectra are unfolded using the nominal unfolding matrix, and the relative shifts with respect to the nominal unfolded spectra are taken as uncertainties on the cross section.

The effects of the jet energy and angular resolutions are studied by smearing the reconstructed jets in the Monte Carlo simulation such that these resolutions are increased by one standard deviation of their respective uncertainties. For each such variation, a new transfer matrix is constructed, which is used to unfold the reconstructed jet spectrum of the nominal MC sample. The relative shift of this spectrum with respect to the nominal unfolded spectra is taken as the uncertainty on the cross section.

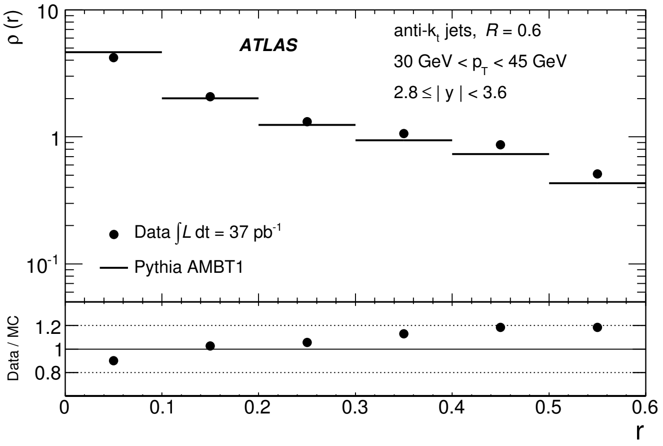

(a) $2.8 \leq |y| < 3.6$

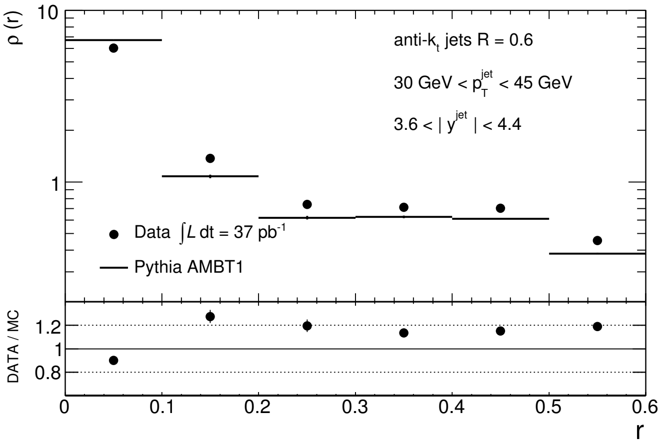

(b) $3.6 \leq |y| < 4.4$

Figure 7.16: The jet shape $\rho(r) = \frac{1}{\Delta r}\frac{p_{\mathrm{T}}^r}{p_{\mathrm{T}}^R}$, where p_{T}^R is the transverse momentum within a radius R of the jet axis, and p_{T}^r is the transverse momentum contained within a ring of thickness $\Delta r = 0.1$ at a mean radius $r = \sqrt{(\Delta y)^2 + (\Delta\phi)^2}$ from the jet axis. It is measured using calorimeter energy clusters, and is shown for anti-k_t jets with $R = 0.6$ in the rapidity intervals $2.8 \leq |y| < 3.6$ and $3.6 \leq |y| < 4.4$ and having transverse momenta in the range $30 < p_{\mathrm{T}} < 45$ GeV. The measurements are compared to PYTHIA with the AMBT1 tune, which is used to correct for detector effects (see Sec. 4.2.1). The statistical error bars are smaller than the size of the markers, while systematic errors are not shown.

The impact of possible mis-modeling of the cross section shape in the Monte Carlo simulation is assessed by shape variations of the particle-level jet spectra introduced to produce reconstructed-level spectra in agreement with data as discussed in Sec. 6.6.

7.11 Magnitude of Systematic Uncertainties

The largest systematic uncertainty for this measurement arises from the jet energy scale. The very steeply falling jet p_{T} spectrum, especially for large rapidities, translates even relatively modest uncertainties on the transverse momentum into large changes for the measured cross section.

As described in Sec. 7.12, the luminosity uncertainty is 3.4%. The detector unfolding uncertainties have been discussed in the previous subsection. Various other sources of systematic uncertainties have been considered and found to have a small impact on the results. The jet energy and angular resolutions, as well as the jet reconstruction efficiency, also contribute to the total uncertainty through the unfolding corrections.

The dominant systematic uncertainties for the measurement of the inclusive jet p_{T} spectrum in representative p_{T} and y regions for anti-k_t jets with $R = 0.6$ are shown in Table 7.1. Similarly, the largest systematic uncertainties for the dijet mass measurement are given for a few representative m_{12} and y^* regions in Table 7.2. The systematic uncertainties on the measurements using anti-k_t jets with $R = 0.4$ are similar to the uncertainties using $R = 0.6$.

The breakdown of the systematic uncertainties as a function of the jet transverse momentum for a few representative rapidity bins used in the inclusive jet measurement is shown in Figs. 7.17–7.19.

p_{T} [GeV]	$\lvert y\rvert$	JES	JER	Trigger	Jet Rec.
80–110	< 0.3	10%	1%	1%	1%
1000–1200	< 0.3	$^{+22\%}_{-20\%}$	1%	1%	1%
20–30	2.1–2.8	$^{+35\%}_{-30\%}$	17%	1%	2%
20–30	3.6–4.4	$^{+65\%}_{-50\%}$	13%	1%	2%

Table 7.1: The effect of the dominant systematic uncertainty sources on the inclusive jet cross section measurement, for representative p_{T} and y regions for anti-k_t jets with $R = 0.6$. There is an additional overall uncertainty of 3.4% due to the luminosity measurement that is not shown.

m_{12} [TeV]	y^*	JES	JER	Trigger	Jet Rec.
0.21–0.26	< 0.5	10%	1%	1%	2%
1.60–1.94	< 0.5	$^{+19\%}_{-17\%}$	0.3%	1%	2%
0.37–0.44	2.0–2.5	$^{+46\%}_{-27\%}$	7%	1%	2%
2.55–3.04	4.0–4.4	$^{+110\%}_{-50\%}$	8%	2%	2%

Table 7.2: The effect of the dominant systematic uncertainty sources on the dijet cross section measurement, for representative m_{12} and y^* regions for anti-k_t jets with $R = 0.6$. There is an additional overall uncertainty of 3.4% due to the luminosity measurement that is not shown.

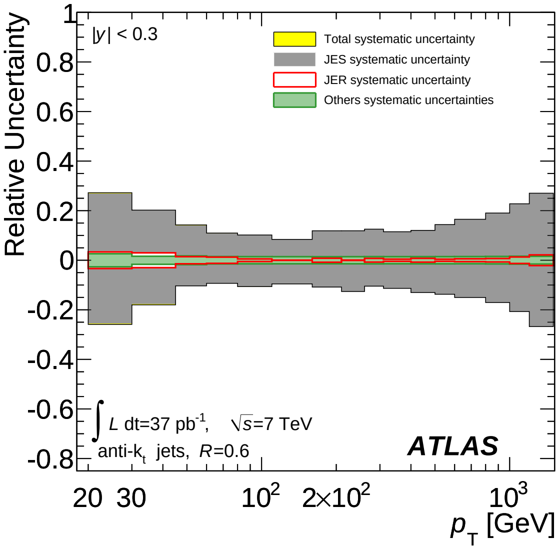

(a) Magnitude, $|y| < 0.3$

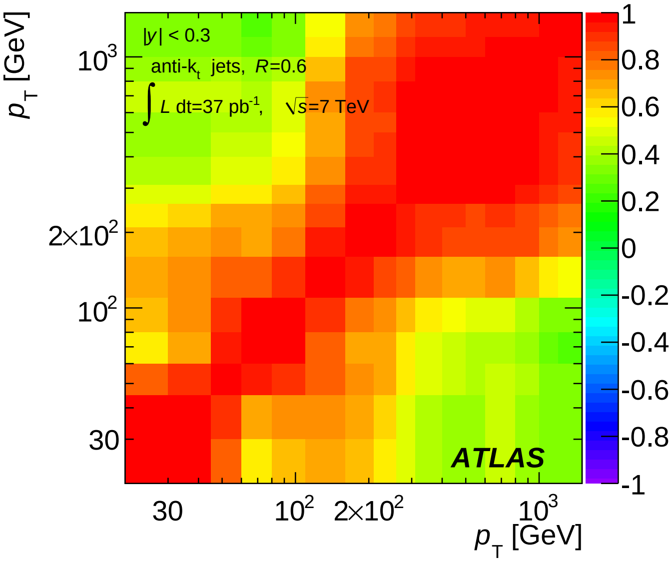

(b) Correlation, $|y| < 0.3$

Figure 7.17: The magnitude (a) and correlation between p_{T}-bins (b) of the total systematic uncertainty on the inclusive jet cross section measurement for anti-k_t jets with $R = 0.6$ in the bin $|y| < 0.3$. The magnitudes of the uncertainties from the jet energy scale (JES), the jet energy resolution (JER), and other sources are shown separately. The correlation matrix is calculated after symmetrizing the uncertainties. The statistical uncertainty and the 3.4% uncertainty of the integrated luminosity are not shown here.

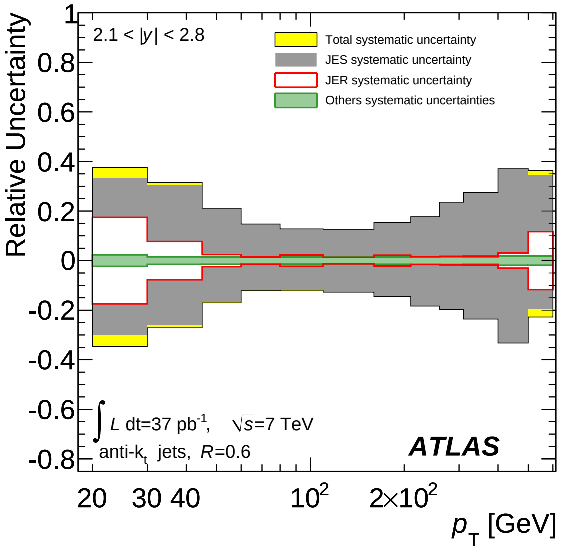

(a) Magnitude, $2.1 < |y| < 2.8$

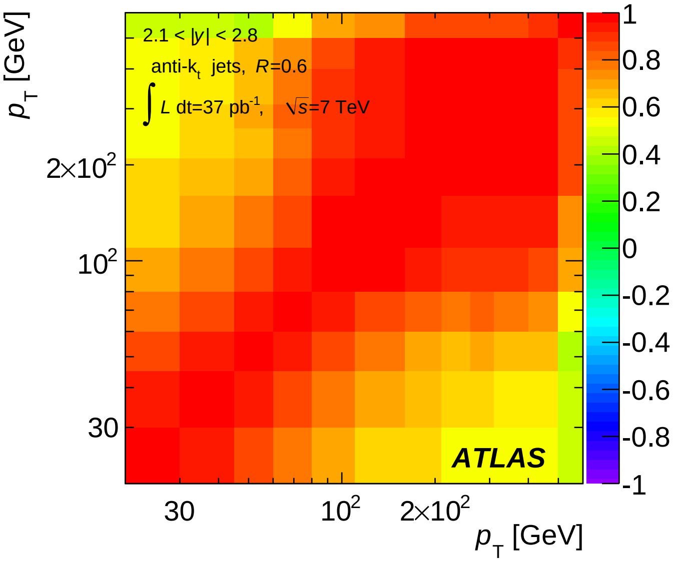

(b) Correlation, $2.1 < |y| < 2.8$

Figure 7.18: The magnitude (left) and correlation between p_{T}-bins (right) of the total systematic uncertainty on the inclusive jet cross section measurement for anti-k_t jets with $R = 0.6$ in the bin $2.1 < |y| < 2.8$. The magnitudes of the uncertainties from the jet energy scale (JES), the jet energy resolution (JER), and other sources are shown separately. The correlation matrix is calculated after symmetrizing the uncertainties. The statistical uncertainty and the 3.4% uncertainty of the integrated luminosity are not shown here.

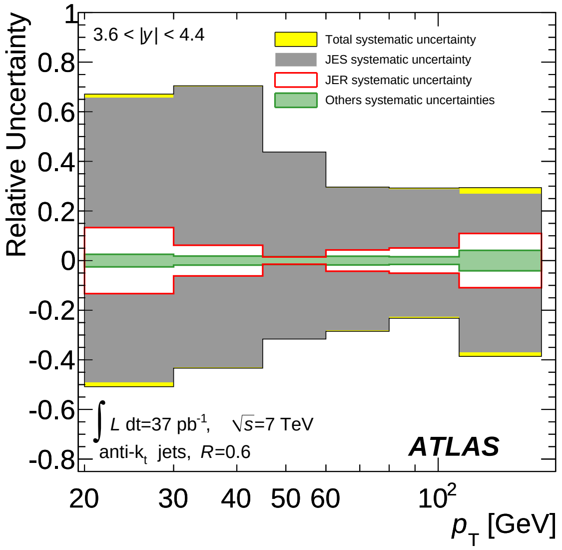

(a) Magnitude, $3.6 < |y| < 4.4$

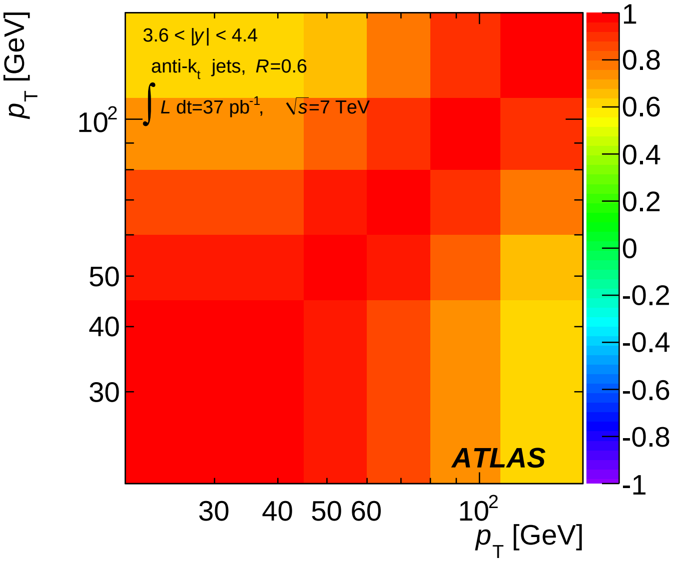

(b) Correlation, $3.6 < |y| < 4.4$

Figure 7.19: The magnitude (left) and correlation between p_{T}-bins (right) of the total systematic uncertainty on the inclusive jet cross section measurement for anti-k_t jets with $R = 0.6$ in the bin $3.6 < |y| < 4.4$. The magnitudes of the uncertainties from the jet energy scale (JES), the jet energy resolution (JER), and other sources are shown separately. The correlation matrix is calculated after symmetrizing the uncertainties. The statistical uncertainty and the 3.4% uncertainty of the integrated luminosity are not shown here.

7.12 Luminosity

The determination of the luminosity is described in Sec. 6.5. The LUCID detector is used to count inclusive hit rates, which are absolutely normalized using a van der Meer scan and measurement of the LHC bunch currents. The visible cross section measured for LUCID is $\overline{\sigma}_{\mathrm{vis}} = 41.67 \pm 1.40$ mb, which corresponds to a luminosity uncertainty of 3.4% [166]. The sources of systematic uncertainty for the luminosity determination are described below. The dominant uncertainty is due to imprecise knowledge of the LHC bunch currents and is 3.1%.

The results for σ_{vis} measured by different detectors and algorithms and across different scans are generally consistent within about 5–10%, reflecting typical bunch-to-bunch differences in transverse emittance. The variation across the scans can be seen in Fig. 7.20(a), which shows the residual variation of each measurement from the combined result for each luminosity method. Only uncorrelated uncertainties between each set of scans in a given fill are shown. The $\overline{\sigma}_{\mathrm{vis}}$ result determined for each algorithm is consistent across all scan data. The fact that the σ_{vis} values are consistent across the scans demonstrates that to first order the emittance growth factors out of the measured luminosity calibration factors.

Meanwhile, Fig. 7.20(b) shows the residual of the ratio of σ_{vis} derived with different detector requirements, $\sigma_{\mathrm{vis}}/\sigma_{\mathrm{vis}}$(LUCID_EventOR), with respect to the ratio of the mean values, $\overline{\sigma}_{\mathrm{vis}}/\overline{\sigma}_{\mathrm{vis}}$(LUCID_EventOR). Any variation between scans related to the bunch charge product $n_1 n_2$ cancels out in the ratio, so the remaining scatter reflects the variation between algorithms in measuring $\mu_{\mathrm{vis}}^{\mathrm{Max}} \Sigma_{\mathrm{x}} \Sigma_{\mathrm{y}}$. This observed variation is consistent with zero within the systematic uncertainty assigned for μ dependence, demonstrating that the results from the different algorithms agree well for each scan. The agreement in the

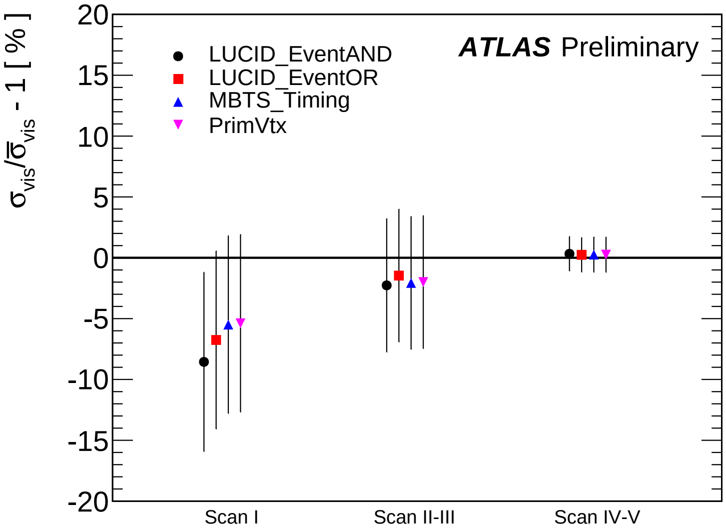

(a) Deviation of each scan.

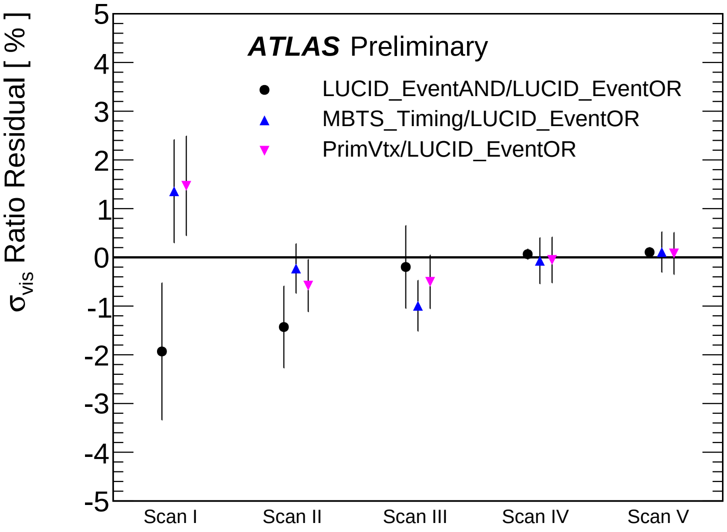

(b) Deviation of each algorithm.

Figure 7.20: Deviation of each set of van der Meer scans from the combined average, where only uncorrelated errors between each set of scans are shown (a). Residuals of the σ_{vis} ratios between algorithms for each van der Meer scan as a relative deviation from the mean ratio based on $\overline{\sigma}_{\text{vis}}$, where error bars represent statistical errors only (b). [165]

visible cross section measured by different methods and in different scans validates the van der Meer scan results.

Systematic uncertainties on the measurement of the beam separation, which impact the extraction of $\Sigma_{\mathrm{x/y}}$, are estimated by determining the actual position of the luminous region using the primary vertex position reconstructed by the (ATLAS) inner detector for several different positions of the beams, as set by the LHC. The uncertainty on the absolute length scale of the Inner Detector is evaluated by analyzing Monte Carlo events simulated using several different misaligned Inner Detector geometries and displaced interaction points. The impact of a possible offset in the beam centering, as well as "jitter", namely random deviations of the beam positions from their nominal setting, is also accounted for.

Additional systematic sources include emittance growth, since it is assumed that the luminosity and the convolved beam sizes $\Sigma_{\mathrm{x/y}}$ are constants. In particular the transverse emittances of the two beams are assumed not to vary significantly either in the interval between the horizontal and the associated vertical scan, nor within a single x or y scan. The systematic uncertainty due to emittance growth between scans is assigned by comparing the slight increase of $\Sigma_{\mathrm{x/y}}$ and the corresponding decrease of the peak specific luminosity in these scans.

Other systematic sources include fit models used in the van der Meer scan data as a function of beam separation, correlations of the transverse profile of the luminous region along the horizontal and vertical axes, and μ dependence. Since the LUCID_EventOR algorithm is used to calibrate the luminosity, an uncertainty is assigned on the long-term stability of the LUCID detector over the 2010 run. Figure 7.21 shows the fractional bias in μ measured by different algorithms with respect to the baseline algorithm. No significant long-term variations are observed.

Systematic uncertainties on the LHC measurement of the DC current transformer

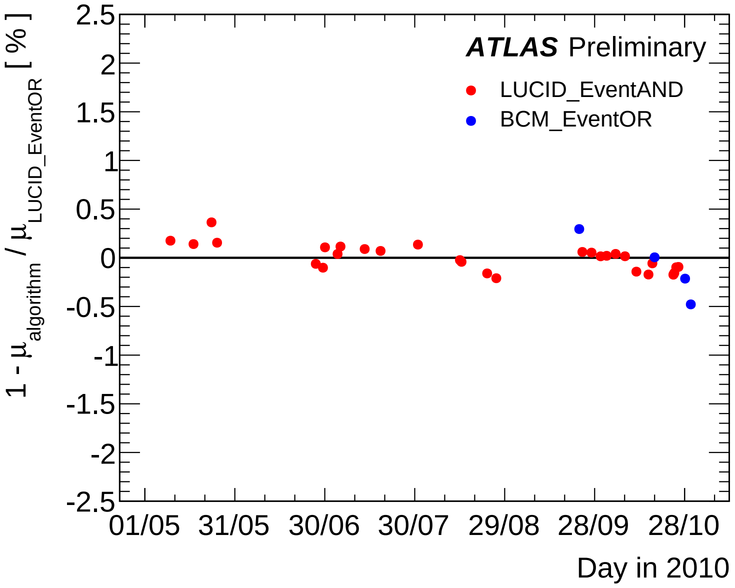

Figure 7.21: Fractional deviation in the average value of μ obtained using different algorithms with respect to the LUCID_EventOR value as a function of time [165]. Each point shows the average deviation for a single ATLAS run. Statistical uncertainties per point are negligible.

arising from the calibration and baseline correction, non-linearities, dependence on accelerator configuration, and variation with time are assigned. The uncertainty on the bunch-current product is determined to be ±2.7%. The systematic uncertainty on the bunch-to-bunch determination is estimated by comparing the fast beam current transformer values against those of the beam position monitors. A variety of measurements from ATLAS, CMS, and LHCb are used to estimate the impact of "ghost" and satellite bunches, where charge is captured by the accelerator. The relative uncertainty on the bunch charge product ($n_1 n_2$) is between 3-5% for each van der Meer scan fill.

In summary, the relative uncertainty on the luminosity for the 2010 pp data is found to be ±3.4%.

7.13 Systematic Correlations

The behavior of various sources of systematic uncertainty in different parts of the detector has been studied to understand their correlations across p_{T}, m_{12}, and rapidity bins. As shown in Tables 7.3–7.4, 22 independent sources of systematic uncertainty have been identified, including luminosity, jet energy scale and resolution, and theory effects such as the modeling of the underlying event and the QCD showering. For example, the sources labeled "JES 7–13" in these tables correspond to the calorimeter response to hadrons, which dominates the JES uncertainty in the central region. The JES uncertainties for jets with $|y| \geq 0.8$ are determined relative to the JES of jets with $|y| < 0.8$. As a consequence, several of the uncertainties that are determined using jets with $|y| < 0.8$ are also propagated to the more forward rapidities (such as the E/p uncertainties).

After examining the rapidity dependence of all 22 sources, it has been found that 87 independent nuisance parameters are necessary to describe the correlations over the whole phase space. The systematic effect on the cross section measurement associated with each nuisance parameter in its range of use is completely correlated in p_{T} and y (dijet mass and y^{*}). These parameters represent correlations between the uncertainties of the various bins.

Since many of the systematic effects are not symmetric, it is not possible to provide a covariance matrix containing the full information. For symmetric uncertainties corresponding to independent sources, the total covariance matrix is given by:

$$\mathrm{cov}(i,j) = \sum_{\lambda} \Gamma_{\lambda i} \Gamma_{\lambda j}, \tag{7.9}$$

where λ is an index running over the nuisance parameters, and $\Gamma_{\lambda i}$ is the one-standard-deviation amplitude of the systematic effect due to source λ in bin i.

				$\lvert y\rvert$-bins			
Uncertainty Source	0-0.3	0.3-0.8	0.8-1.2	1.2-2.1	2.1-2.8	2.8-3.6	3.6-4.4
JES 1: Noise threshold	1	1	2	3	4	5	6
JES 2: Theory UE	7	7	8	9	10	11	12
JES 3: Theory showering	13	13	14	15	16	17	18
JES 4: Non-closure	19	19	20	21	22	23	24
JES 5: Dead material	25	25	26	27	28	29	30
JES 6: Forward JES	31	31	31	31	31	31	31
JES 7: E/p response	32	32	33	34	35	36	37
JES 8: E/p selection	38	38	39	40	41	42	43
JES 9: EM + neutrals	44	44	45	46	47	48	49
JES 10: HAD E-scale	50	50	51	52	53	54	55
JES 11: High p_{T}	56	56	57	58	59	60	61
JES 12: E/p bias	62	62	63	64	65	66	67
JES 13: Test-beam bias	68	68	69	70	71	72	73
Unfolding	74	74	74	74	74	74	74
Jet matching	75	75	75	75	75	75	75
Jet energy resolution	76	76	77	78	79	80	81
y-resolution	82	82	82	82	82	82	82
Jet reconstruction eff.	83	83	83	83	84	85	86
Luminosity	87	87	87	87	87	87	87
JES 14: Pile-up (u_1)	u	u	u	u	u	u	u
Trigger (u_2)	u	u	u	u	u	u	u
Jet selection (u_3)	u	u	u	u	u	u	u

Table 7.3: Description of bin-to-bin uncertainty correlations for the inclusive jet measurement. Each number corresponds to a nuisance parameter for which the corresponding uncertainty is fully correlated versus p_{T}. Bins with the same nuisance parameter are treated as fully correlated, while bins with different nuisance parameters are uncorrelated. The sources indicated by the letter "u" are uncorrelated both between p_{T}- and $\lvert y\rvert$-bins. The 1σ amplitude of the systematic effect associated with each nuisance parameter is detailed in Tables B.1–B.14 in Appendix B.1. The JES uncertainty sources are described in Refs. [14] and [137]. This table is available on HEPDATA [187].

	y^*-bins								
Uncertainty Source	0.0-0.5	0.5-1.0	1.0-1.5	1.5-2.0	2.0-2.5	2.5-3.0	3.0-3.5	3.5-4.0	4.0-4.4
JES 1: Noise threshold	1	1	2	3	4	4	5	6	6
JES 2: Theory UE	7	7	8	9	10	10	11	12	12
JES 3: Theory Showering	13	13	14	15	16	16	17	18	18
JES 4: Non-closure	19	19	20	21	22	22	23	24	24
JES 5: Dead material	25	25	26	27	28	28	29	30	30
JES 6: Forward JES	31	31	31	31	31	31	31	31	31
JES 7: E/p response	32	32	33	34	35	35	36	37	37
JES 8: E/p selection	38	38	39	40	41	41	42	43	43
JES 9: EM + neutrals	44	44	45	46	47	47	48	49	49
JES 10: HAD E-scale	50	50	51	52	53	53	54	55	55
JES 11: High p_{T}	56	56	57	58	59	59	60	61	61
JES 12: E/p bias	62	62	63	64	65	65	66	67	67
JES 13: Test-beam bias	68	68	69	70	71	71	72	73	73
Unfolding	74	74	74	74	74	74	74	74	74
Jet matching	75	75	75	75	75	75	75	75	75
Jet energy resolution	76	76	77	78	79	79	80	81	81
y-resolution	82	82	82	82	82	82	82	82	82
Jet reconstruction eff.	83	83	83	83	84	84	85	86	86
Luminosity	87	87	87	87	87	87	87	87	87
JES 14: Pile-up (u_1)	u	u	u	u	u	u	u	u	u
Trigger (u_2)	u	u	u	u	u	u	u	u	u
Jet selection (u_3)	u	u	u	u	u	u	u	u	u

Table 7.4: Description of bin-to-bin uncertainty correlations for the dijet measurement. Each number corresponds to a nuisance parameter for which the corresponding uncertainty is fully correlated versus dijet mass, m_{12}. Bins with the same nuisance parameter are treated as fully correlated, while bins with different nuisance parameters are uncorrelated. The sources indicated by the letter "u" are uncorrelated both between m_{12}- and y^*-bins. The 1σ amplitude of the systematic effect associated with each nuisance parameter is detailed in Tables B.15–B.32 in Appendix B.2. The JES uncertainty sources are described in Refs. [14] and [137]. This table is available on HEPDATA [187].

The full list of relative uncertainties, γ_λ, where each uncertainty may be asymmetric, is given for all sources λ and bins of this analysis in Tables B.1–B.14 and B.15–B.32. Figures 7.17–7.19 show the magnitude and approximate bin-to-bin correlations of the total systematic uncertainty for a few representative bins of the inclusive jet cross section measurement. The correlation matrix here is converted from the covariance matrix, which is obtained using Eq. 7.9, after symmetrizing the uncertainties: $\Gamma_{\lambda i} = (\Gamma^{+}_{\lambda i} + \Gamma^{-}_{\lambda i})/2$. The inclusive jet and dijet data should not be used simultaneously for PDF fits due to significant correlations between the two measurements.

CHAPTER 8

RESULTS

“There are two possible outcomes: if the result confirms the hypothesis, then you’ve made a measurement. If the result is contrary to the hypothesis, then you’ve made a discovery.”

— Enrico Fermi (Nobel Prize in Physics, 1938)

8.1 Inclusive Jet Cross Sections

The inclusive jet double-differential cross section is shown in Figs. 8.1–8.2 and Tables B.1–B.14 in Appendix B.1 for jets reconstructed with the anti-k_t algorithm with $R = 0.4$ and $R = 0.6$. The measurement extends from jet transverse momentum of 20 GeV to 1.5 TeV, spanning two orders of magnitude in p_{T} and ten orders of magnitude in the value of the cross section. The measured cross sections have been corrected for all detector effects using the unfolding procedure described in Sec. 6.6. The results are compared to NLOJET++ predictions (using the CT10 PDF set) corrected for non-perturbative effects, where the theoretical uncertainties from scale variations, parton distribution functions, and non-perturbative corrections have been accounted for.

In Figs. 8.3–8.11, the inclusive jet results are presented in terms of the ratio with respect to the NLOJET++ predictions using the CT10 PDF set. Figure 8.3 compares the current results to the previous measurements published by ATLAS [21], for jets reconstructed with the anti-k_t algorithm with parameter $R = 0.6$. This figure is limited to the

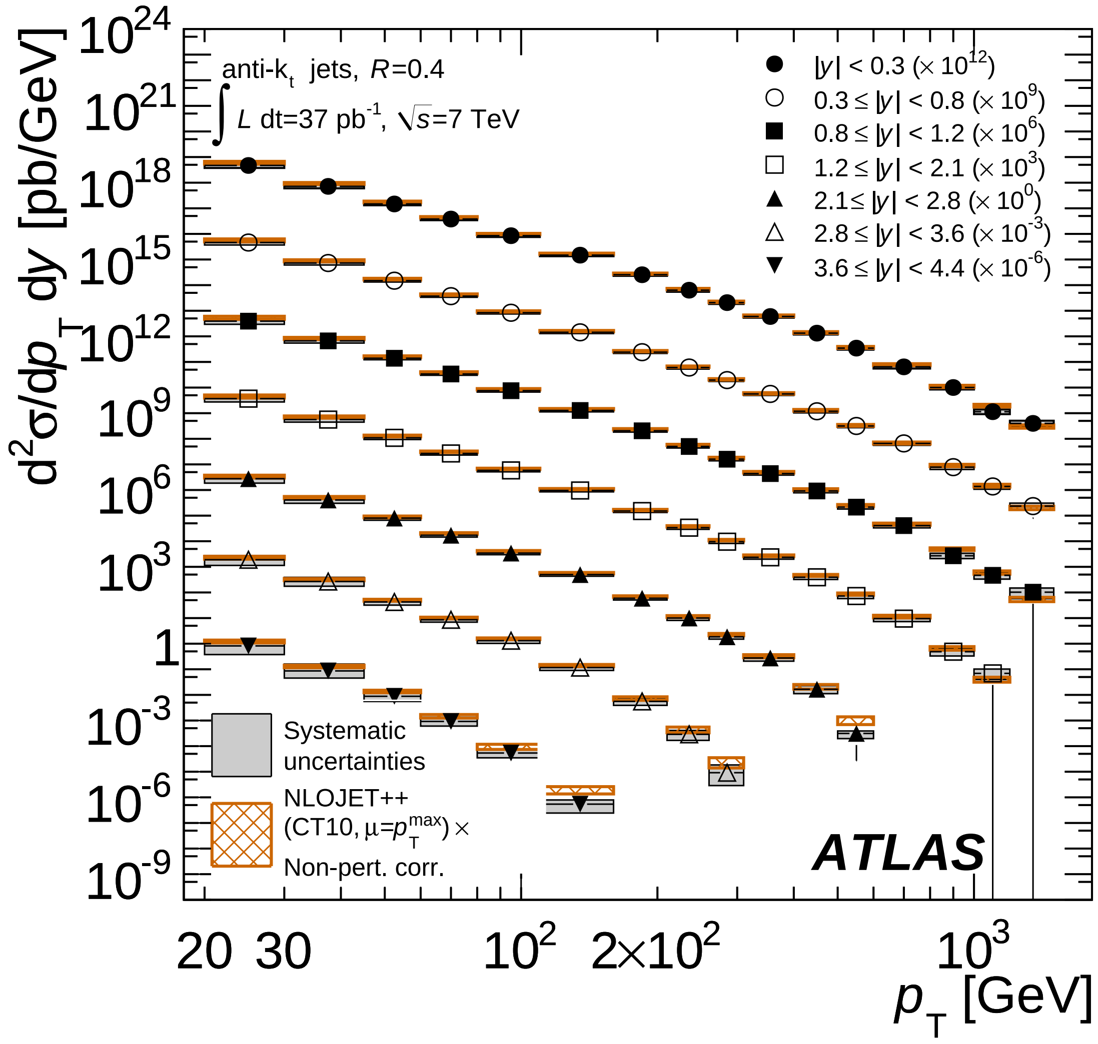

Figure 8.1: Inclusive jet double-differential cross section as a function of jet p_{T} in different regions of $|y|$ for jets identified using the anti-k_t algorithm with $R = 0.4$. For convenience, the cross sections are multiplied by the factors indicated in the legend. The data are compared to NLO pQCD calculations using NLOJET++ to which non-perturbative corrections have been applied. The error bars, which are usually smaller than the symbols, indicate the statistical uncertainty on the measurement. The dark-shaded band indicates the quadratic sum of the experimental systematic uncertainties, dominated by the jet energy scale uncertainty. There is an additional overall uncertainty of 3.4% due to the luminosity measurement that is not shown. The theory uncertainty, shown as the light, hatched band, is the quadratic sum of uncertainties from the choice of the renormalization and factorization scales, parton distribution functions, $\alpha_s(M_Z)$, and the modeling of non-perturbative effects, as described in the text.

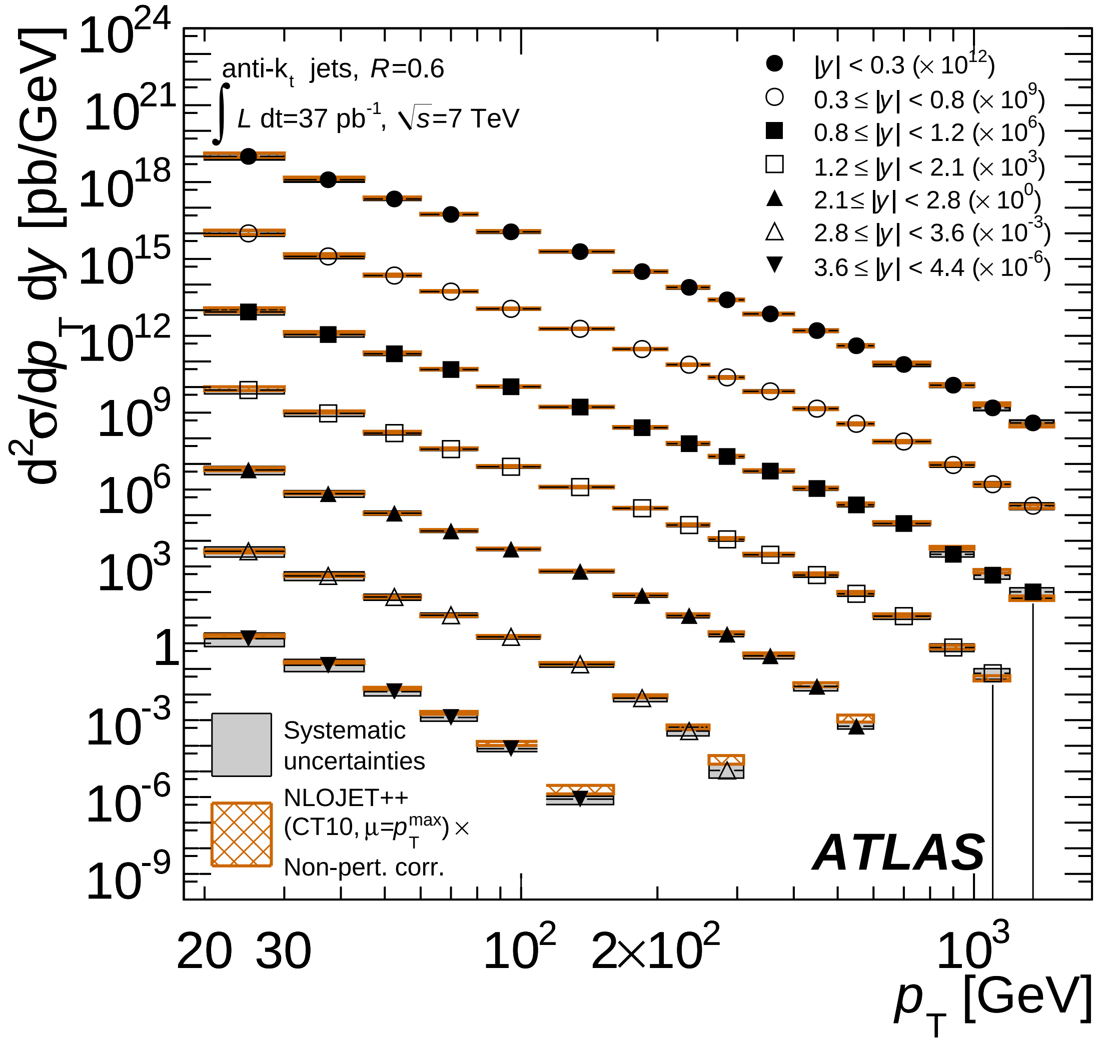

Figure 8.2: Inclusive jet double-differential cross section as a function of jet p_T in different regions of $|y|$ for jets identified using the anti-k_t algorithm with $R = 0.6$. For convenience, the cross sections are multiplied by the factors indicated in the legend. The data are compared to NLO pQCD calculations using NLOJET++ to which non-perturbative corrections have been applied. The theoretical and experimental uncertainties indicated are calculated as described in Fig. 8.1.

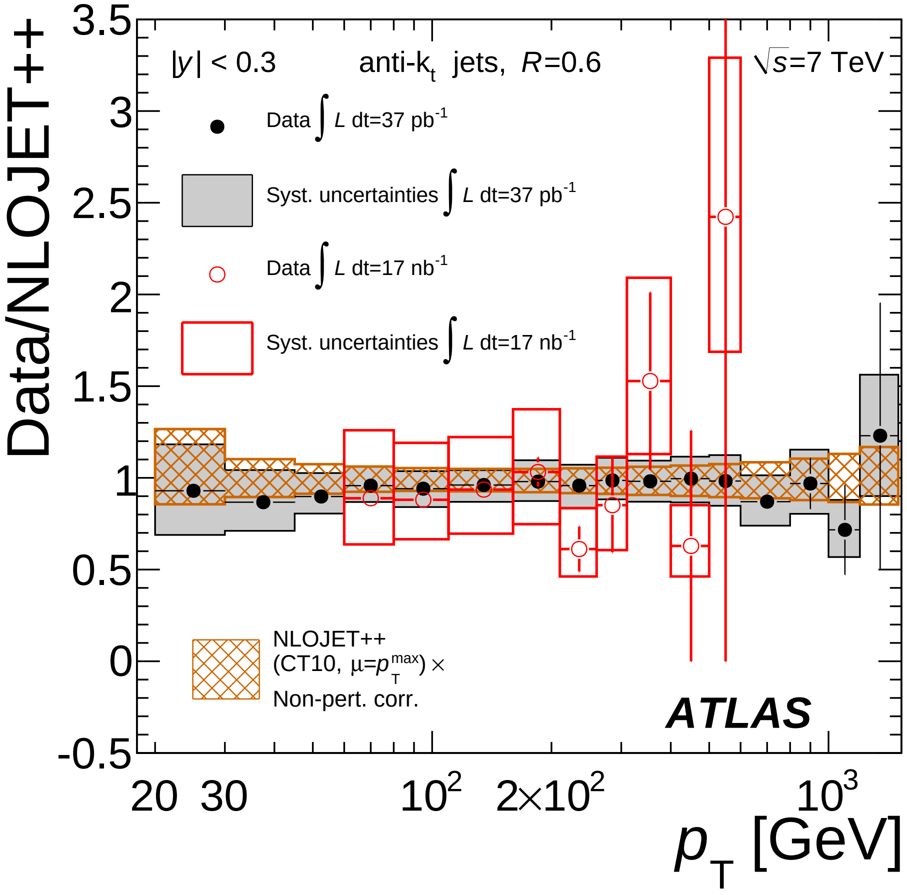

Figure 8.3: Ratio of inclusive jet cross section to the theoretical prediction obtained using NLOJET++ with the CT10 PDF set. The ratio is shown as a function of jet p_T in the rapidity region $|y| < 0.3$, for jets identified using the anti-k_t algorithm with $R = 0.6$. The current result is compared to that published in Ref. [21].

central region, but similar conclusions can be drawn in all rapidity bins. In particular the two measurements are in good agreement, although the new results cover a much larger kinematic range with much reduced statistical and systematic uncertainties.

Figures 8.4–8.5 and 8.6–8.7 show the ratio of the measured cross sections to the NLOJET++ theoretical predictions for various PDF sets, using anti-k_t jets with $R = 0.4$ and $R = 0.6$. Predictions obtained using CT10, MTSW 2008, NNPDF 2.1, and HERAPDF 1.5, including uncertainty bands, are compared to the measured cross sections, where data and theoretical predictions are normalized to the prediction from the CT10 PDF set. The data show a marginally smaller cross section than the predictions from each of the PDF sets. This trend is more pronounced for the measurements with parameter $R = 0.4$ compared to those with $R = 0.6$.

The description becomes worse for large jet transverse momenta and rapidities, where the MSTW 2008 PDF set follows the measured trend better. However, the differences between the measured cross section and the prediction of each PDF set are of the same order of magnitude as the total systematic uncertainty on the measurement, including both experimental and theoretical uncertainty sources. A χ^2 test of the compatibility between data and the PDF curves, accounting for correlations between bins, produces a χ^2/N_{DOF} statistic close to 1, where the number of degrees of freedom, N_{DOF}, is 90. A reasonable probability is observed for each of the PDF sets, with the differences between them being relatively insignificant.[1]

The comparison of the data with the POWHEG prediction, using the CT10 NLO PDF set, is shown for anti-k_t jets with $R = 0.4$ and $R = 0.6$ in different rapidity regions in Figs. 8.8–8.9 and 8.10–8.11. The data are compared with four theory curves, all of which

---

[1] Comparisons to HERAPDF 1.0, CTEQ 6.6 and NNPDF 2.0 were also performed, but they are not shown as they are very similar to those for HERAPDF 1.5, CT10, and NNPDF 2.1, respectively.

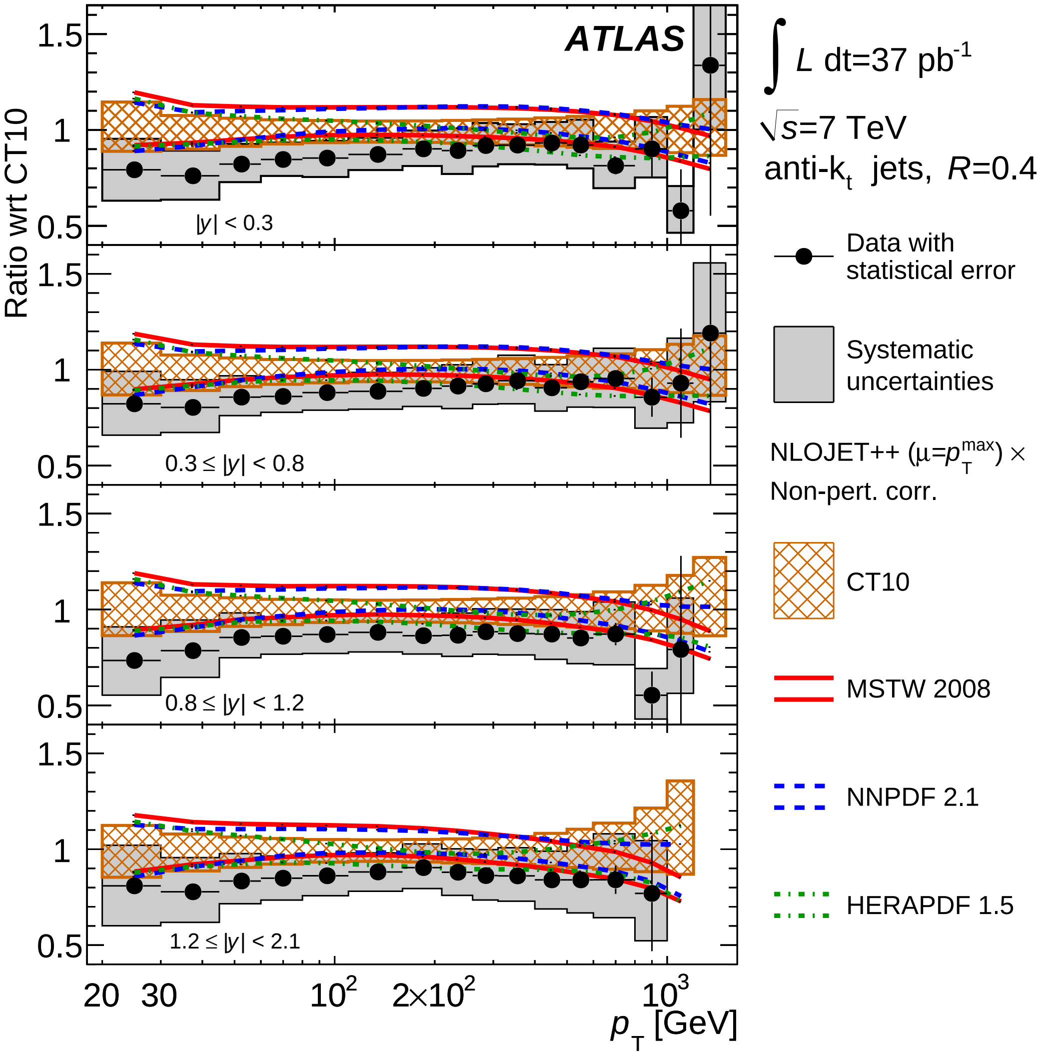

Figure 8.4: Ratios of inclusive jet double-differential cross section to the theoretical prediction obtained using NLOJET++ with the CT10 PDF set. The ratios are shown as a function of jet p_{T} in central regions of $|y|$ for jets identified using the anti-k_t algorithm with $R = 0.4$. The theoretical error bands obtained by using NLOJET++ with different PDF sets (CT10, MSTW 2008, NNPDF 2.1, HERAPDF 1.5) are shown. Statistically insignificant data points at large p_{T} are omitted in the ratio.

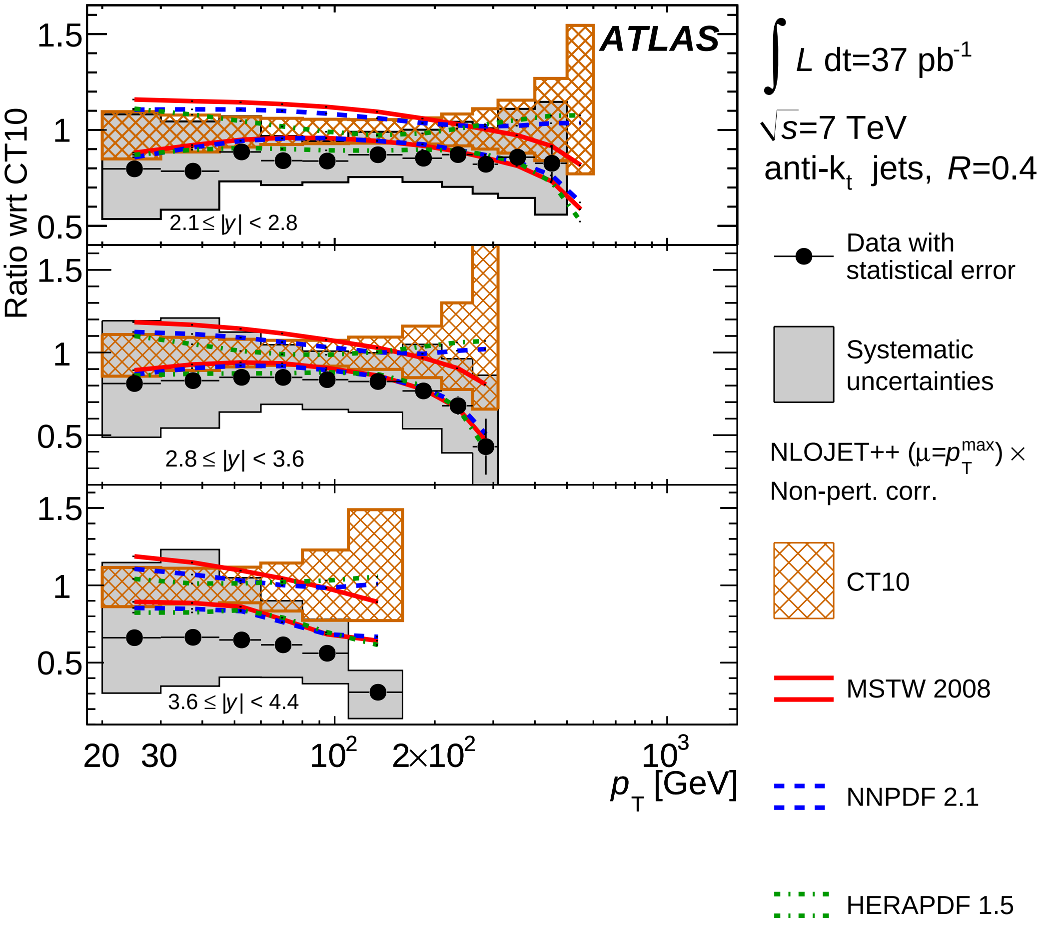

Figure 8.5: Ratios of inclusive jet double-differential cross section to the theoretical prediction obtained using NLOJET++ with the CT10 PDF set. The ratios are shown as a function of jet p_{T} in forward regions of $|y|$ for jets identified using the anti-k_t algorithm with $R = 0.4$. The theoretical error bands obtained by using NLOJET++ with different PDF sets (CT10, MSTW 2008, NNPDF 2.1, HERAPDF 1.5) are shown. Statistically insignificant data points at large p_{T} are omitted in the ratio.

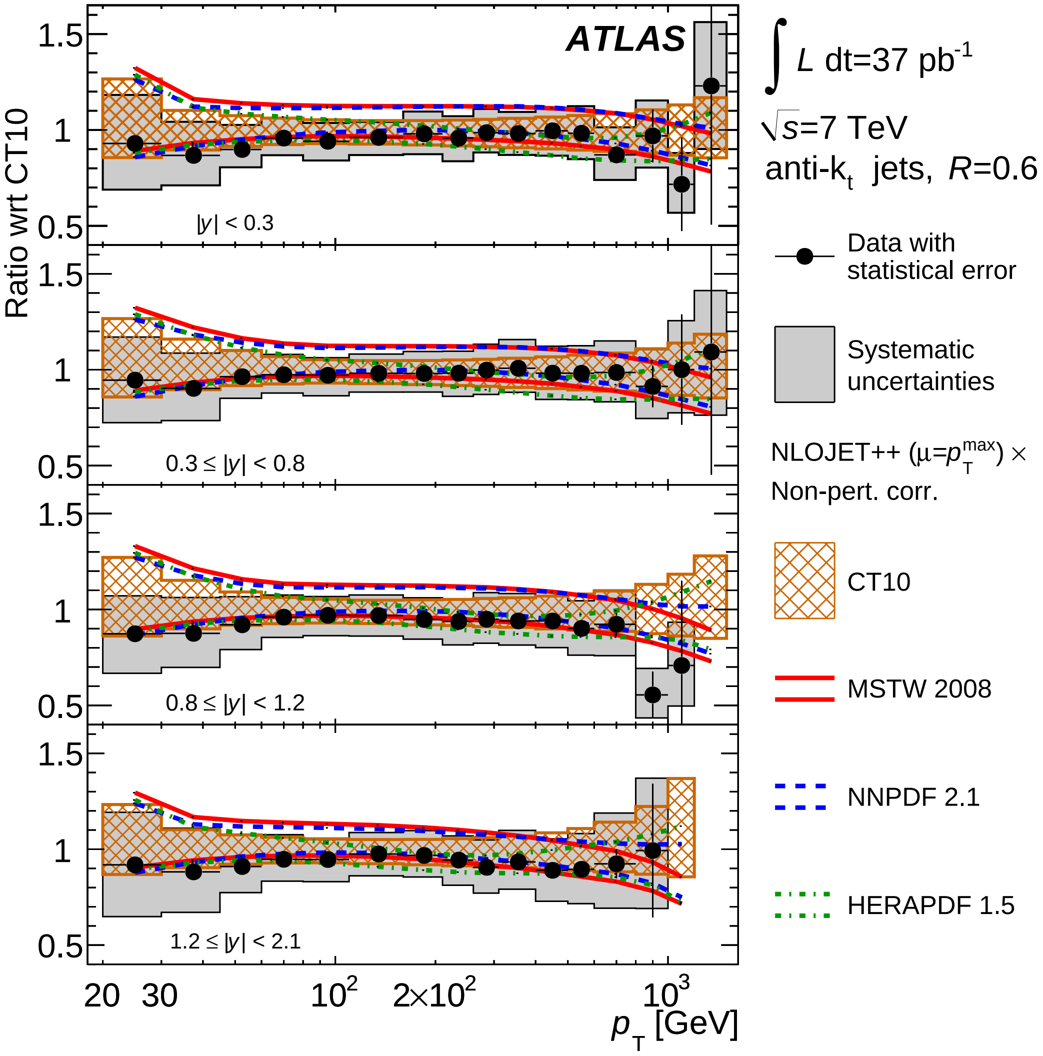

Figure 8.6: Ratios of inclusive jet double-differential cross section to the theoretical prediction obtained using NLOJET++ with the CT10 PDF set. The ratios are shown as a function of jet p_{T} in central regions of $|y|$ for jets identified using the anti-k_t algorithm with $R = 0.6$. The theoretical error bands obtained by using NLOJET++ with different PDF sets (CT10, MSTW 2008, NNPDF 2.1, HERAPDF 1.5) are shown. Statistically insignificant data points at large p_{T} are omitted in the ratio.

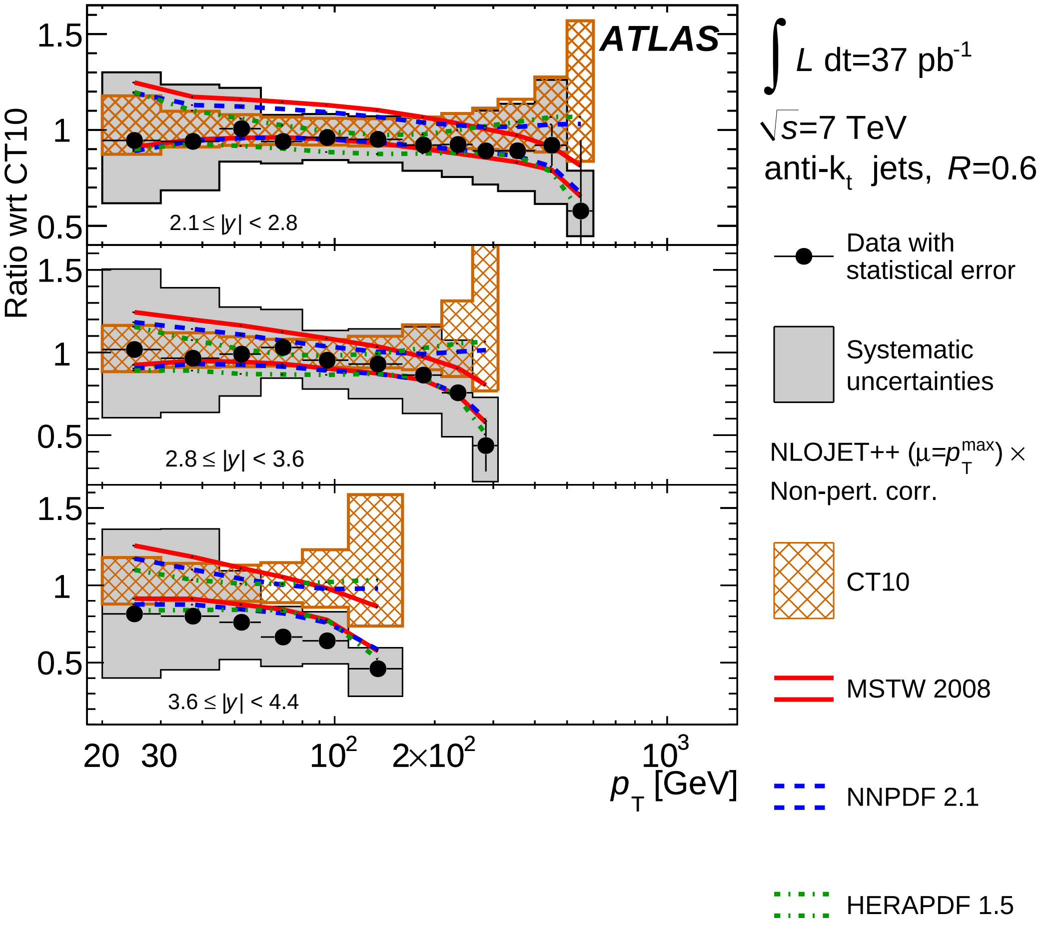

Figure 8.7: Ratios of inclusive jet double-differential cross section to the theoretical prediction obtained using NLOJET++ with the CT10 PDF set. The ratios are shown as a function of jet p_{T} in forward regions of $|y|$ for jets identified using the anti-k_t algorithm with $R = 0.6$. The theoretical error bands obtained by using NLOJET++ with different PDF sets (CT10, MSTW 2008, NNPDF 2.1, HERAPDF 1.5) are shown. Statistically insignificant data points at large p_{T} are omitted in the ratio.

are normalized to the same common denominator of the NLOJET++ prediction corrected for non-perturbative effects: POWHEG showered with PYTHIA with the default AUET2B tune; the same with the Perugia 2011 tune; POWHEG showered with HERWIG; and POWHEG run in “pure NLO” mode (fixed-order calculation), without matching to parton shower, after application of soft corrections calculated using PYTHIA and the AUET2B tune. Scale uncertainties are not shown for the POWHEG curves, but they have been found to be similar to those obtained with NLOJET++.

Good agreement at the level of a few percent is observed between NLO fixed-order calculations based on NLOJET++ and POWHEG, as described in Sec. 4.3.1. However, significant differences reaching $O(30\%)$ are observed if POWHEG is interfaced to different showering and soft physics models, particularly at low p_{T} and forward rapidity, but also at high p_{T}. These differences exceed the uncertainties on the non-perturbative corrections, which are not larger than 10% for the inclusive jet measurements with $R = 0.4$, thus indicating a significant impact of the parton shower. The Perugia 2011 tune tends to produce a consistently larger cross section than the standard AUET2B tune over the full rapidity range. The technique of correcting fixed-order calculations for non-perturbative effects remains the convention to define the baseline theory prediction until NLO parton shower generators become sufficiently mature to describe data well. The corrected NLO result predicts a consistently larger cross section than that seen in the data. Good agreement in normalization is found between the data and the prediction from POWHEG showered with the default tune of PYTHIA. These results are confirmed by a χ^2 test of the compatibility of the POWHEG results with the data, where the curve obtained using the HERWIG shower results in a much worse χ^2/N_{DOF} value after all error correlations have been accounted for.

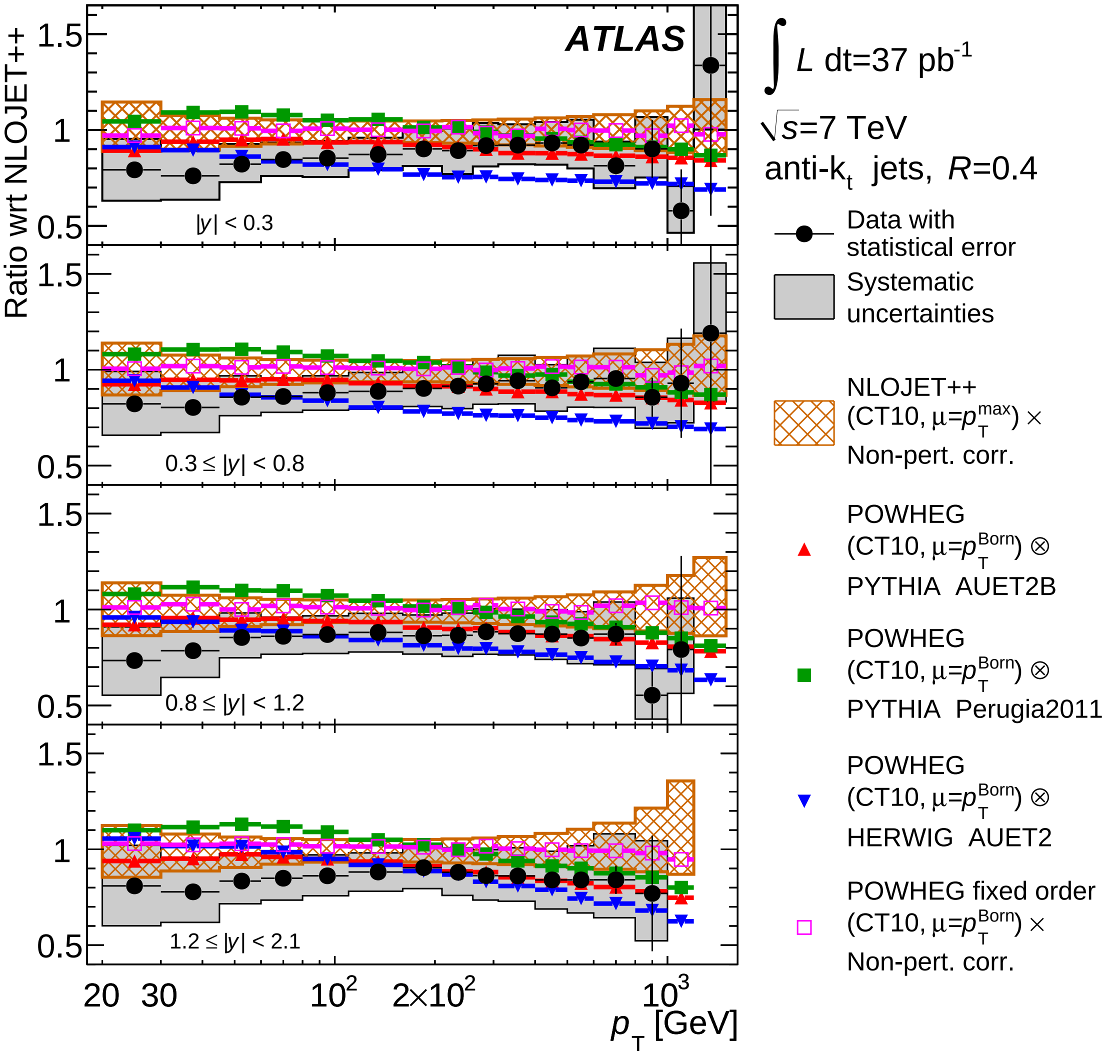

Figure 8.8: Ratios of inclusive jet double-differential cross section to the theoretical prediction obtained using NLOJET++ with the CT10 PDF set. The ratios are shown as a function of jet p_{T} in central regions of $|y|$ for jets identified using the anti-k_t algorithm with $R = 0.4$. The ratios of POWHEG predictions showered using either PYTHIA or HERWIG to the NLOJET++ predictions corrected for non-perturbative effects are shown and can be compared to the corresponding ratios for data. Only the statistical uncertainty on the POWHEG predictions is shown. The total systematic uncertainties on the theory and the measurement are indicated. The NLOJET++ prediction and the POWHEG ME calculations use the CT10 PDF set. Statistically insignificant data points at large p_{T} are omitted in the ratio.

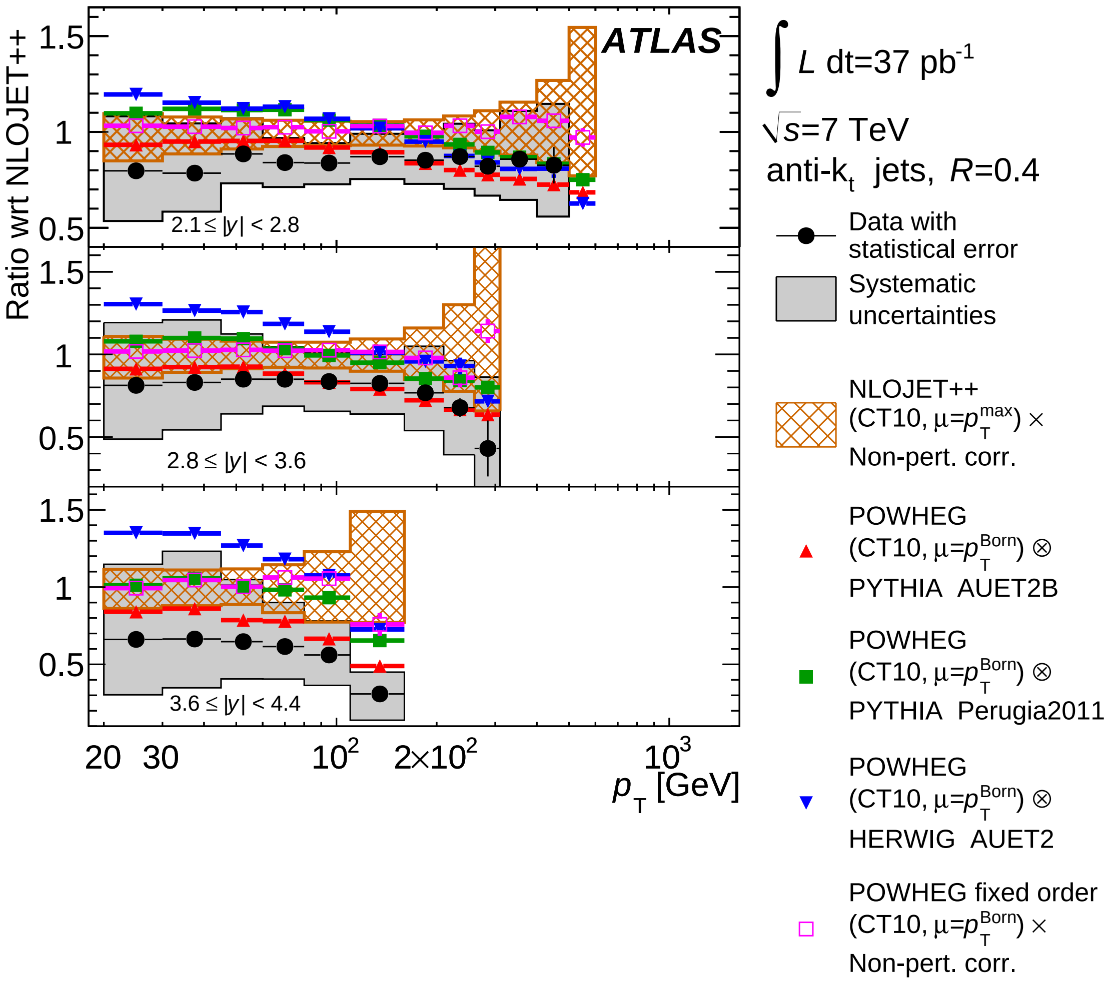

Figure 8.9: Ratios of inclusive jet double-differential cross section to the theoretical prediction obtained using NLOJET++ with the CT10 PDF set. The ratios are shown as a function of jet p_{T} in forward regions of $|y|$ for jets identified using the anti-k_t algorithm with $R = 0.4$. The ratios of POWHEG predictions showered using either PYTHIA or HERWIG to the NLOJET++ predictions corrected for non-perturbative effects are shown and can be compared to the corresponding ratios for data. Only the statistical uncertainty on the POWHEG predictions is shown. The total systematic uncertainties on the theory and the measurement are indicated. The NLOJET++ prediction and the POWHEG ME calculations use the CT10 PDF set. Statistically insignificant data points at large p_{T} are omitted in the ratio.

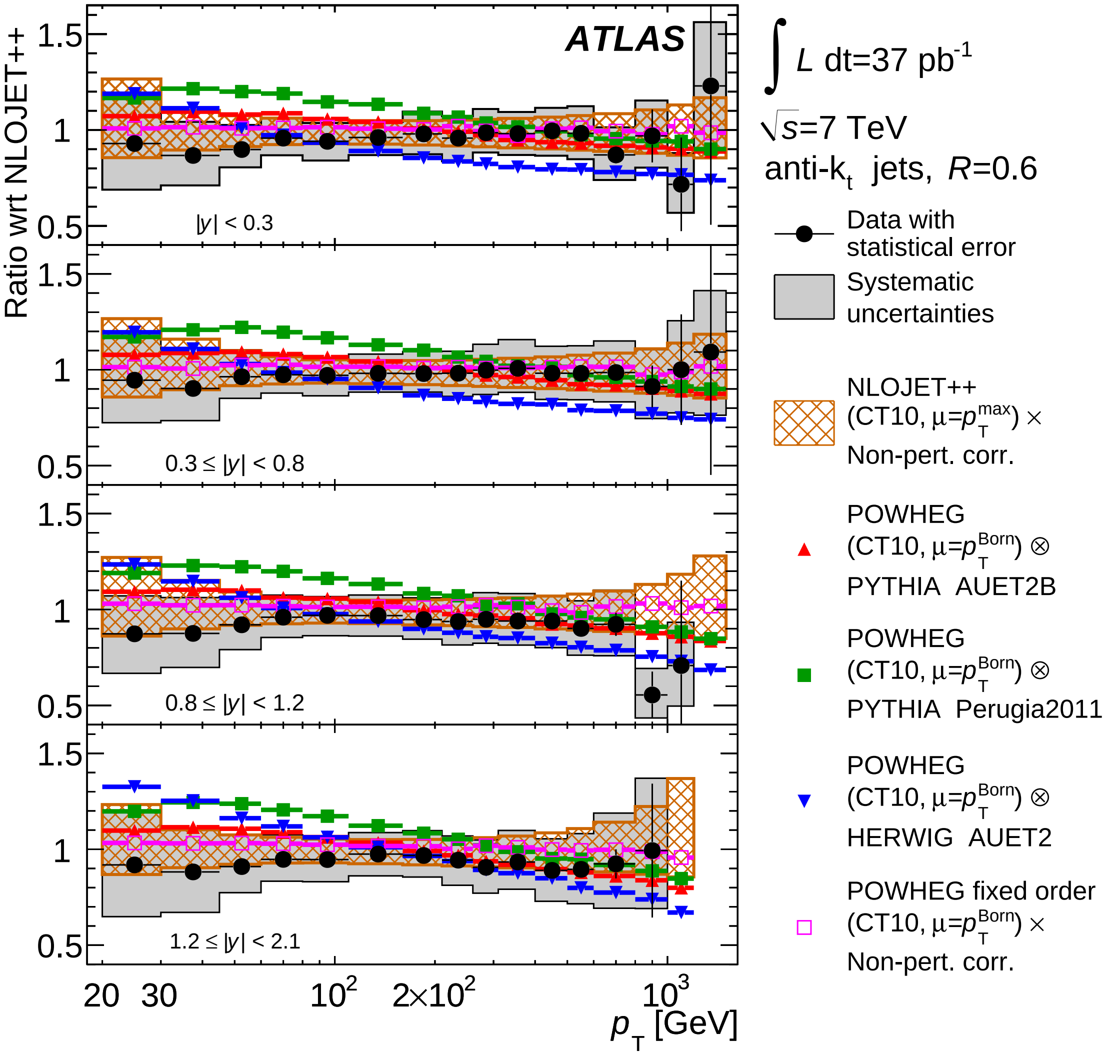

Figure 8.10: Ratios of inclusive jet double-differential cross section to the theoretical prediction obtained using NLOJET++ with the CT10 PDF set. The ratios are shown as a function of jet p_T in central regions of $|y|$ for jets identified using the anti-k_t algorithm with $R = 0.6$. The ratios of POWHEG predictions showered using either PYTHIA or HERWIG to the NLOJET++ predictions corrected for non-perturbative effects are shown and can be compared to the corresponding ratios for data. Only the statistical uncertainty on the POWHEG predictions is shown. The total systematic uncertainties on the theory and the measurement are indicated. The NLOJET++ prediction and the POWHEG ME calculations use the CT10 PDF set. Statistically insignificant data points at large p_T are omitted in the ratio.

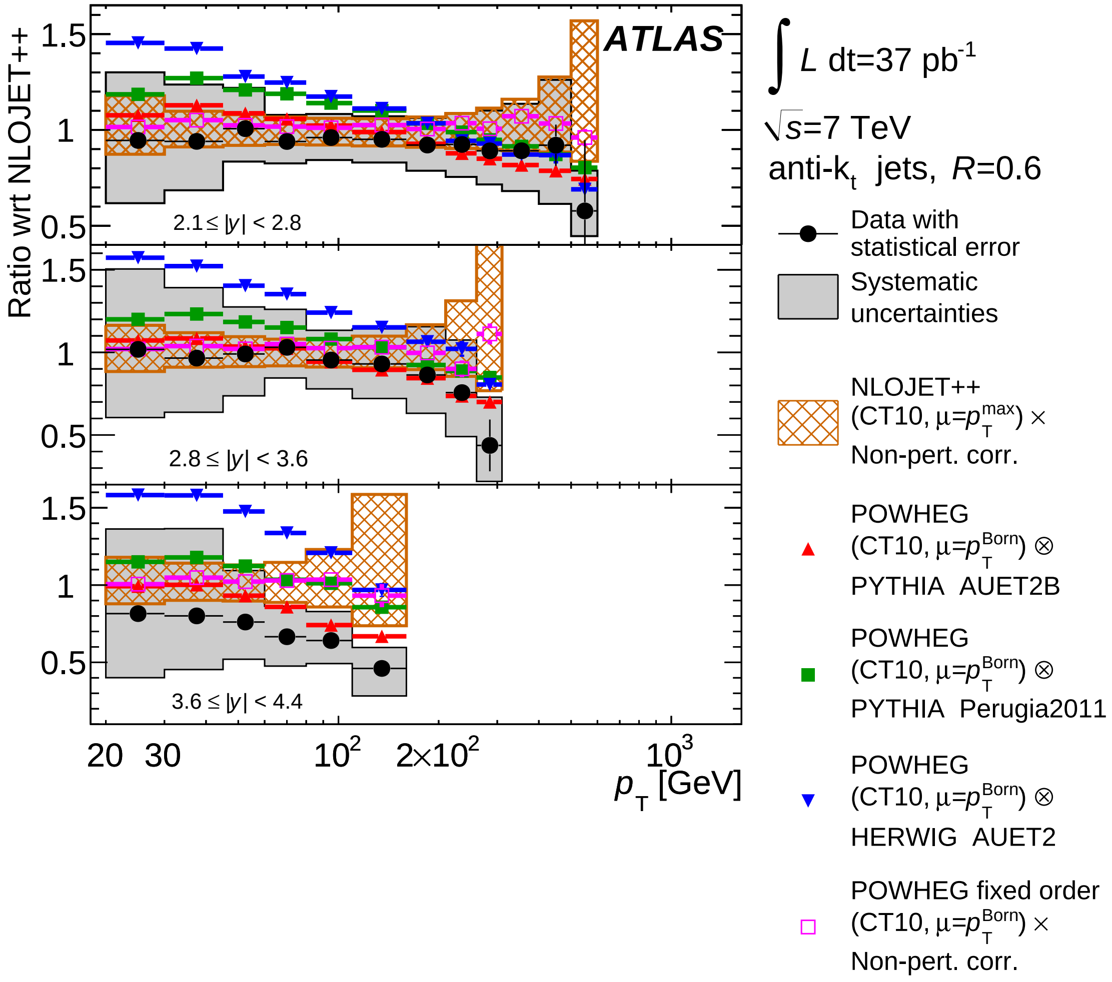

Figure 8.11: Ratios of inclusive jet double-differential cross section to the theoretical prediction obtained using NLOJET++ with the CT10 PDF set. The ratios are shown as a function of jet p_{T} in forward regions of $|y|$ for jets identified using the anti-k_t algorithm with $R = 0.6$. The ratios of POWHEG predictions showered using either PYTHIA or HERWIG to the NLOJET++ predictions corrected for non-perturbative effects are shown and can be compared to the corresponding ratios for data. Only the statistical uncertainty on the POWHEG predictions is shown. The total systematic uncertainties on the theory and the measurement are indicated. The NLOJET++ prediction and the POWHEG ME calculations use the CT10 PDF set. Statistically insignificant data points at large p_{T} are omitted in the ratio.

8.2 Dijet Cross Sections

The dijet double-differential cross section has been measured as a function of the dijet invariant mass for various bins of the variable y^*, which is the rapidity in the two-parton center-of-mass frame. The quantity y^* is calculated as half the absolute value of the rapidity difference of the two leading jets, ranging from 0 to 4.4. The results are shown in Figs. 8.12–8.13 and Tables B.15–B.32 in Appendix B.2 for anti-k_t jets with $R = 0.4$ and $R = 0.6$. The cross section measurements extend from dijet masses of 70 GeV to 5 TeV, covering two orders of magnitude in invariant mass and nine orders of magnitude in the cross section. The dijet measurements are fully corrected for detector effects and are compared to NLOJET++ predictions calculated using the scale defined in Eq. 4.2 (see Sec. 4.3.1) and the CT10 PDF set, with non-perturbative corrections applied to the theory prediction. The theoretical uncertainties have been assessed as described for the inclusive jet measurements in Sec. 8.1.

The dijet data are also compared with NLOJET++ predictions obtained using the MSTW 2008, NNPDF 2.1, and HERAPDF 1.5 PDF sets. Figures 8.14–8.15 and 8.16–8.17 show the dijet mass spectra for anti-k_t jets with $R = 0.4$ and $R = 0.6$ respectively, where both the data and the predictions from the above-mentioned PDF sets have been normalized to the CT10 prediction. The data for $R = 0.6$ exhibit a slight falling slope with respect to the CT10 prediction and appear to be described better by other PDF sets, a similar behavior to that observed in the inclusive jet data. However, in all cases, the differences between the data and each PDF set lie well within the systematic and theory uncertainties, indicating a reasonable agreement with the dijet data, particularly in the kinematic region at low y^*.

The data are also compared with POWHEG predictions produced using the CT10 PDF set and showered with different tunes of the PYTHIA or HERWIG generator. These com-

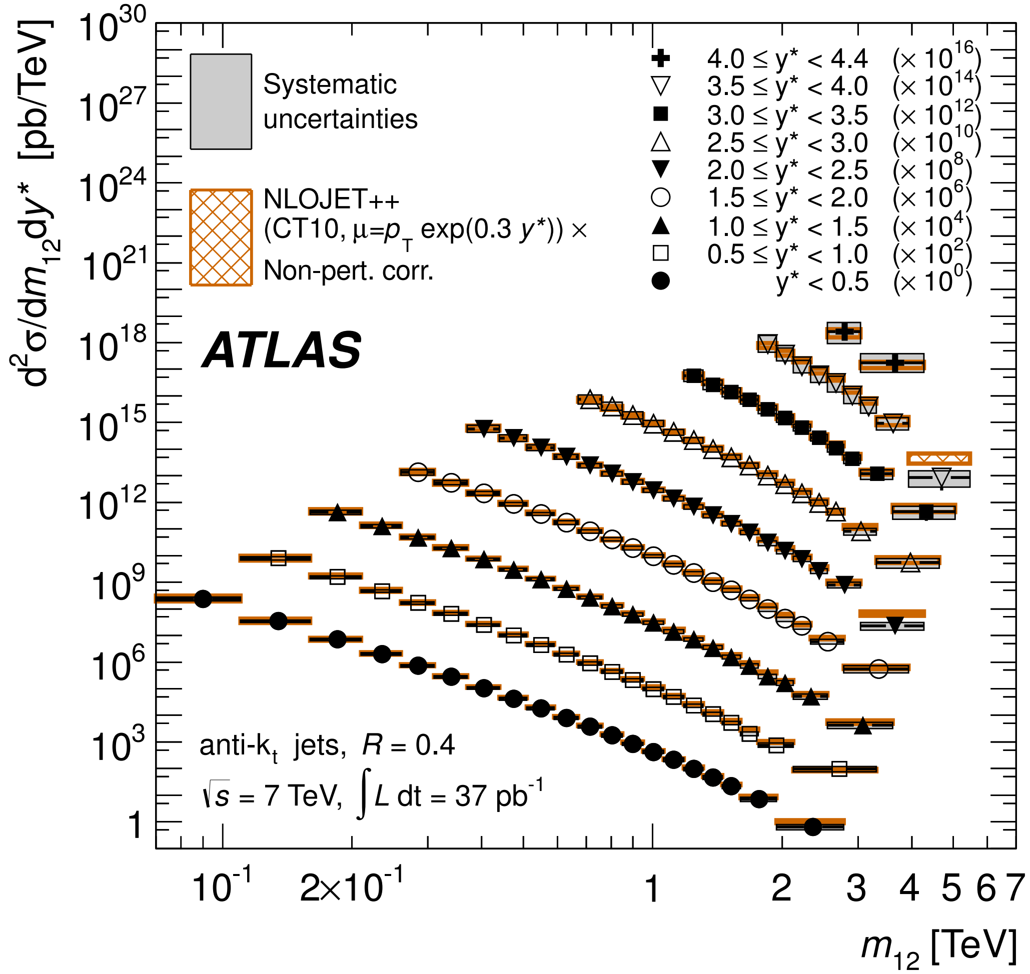

Figure 8.12: Dijet double-differential cross section as a function of dijet mass, binned in half the rapidity separation between the two leading jets, $y^* = |y_1 - y_2|/2$. The results are shown for jets identified using the anti-k_t algorithm with $R = 0.4$. For convenience, the cross sections are multiplied by the factors indicated in the legend. The data are compared to NLO pQCD calculations using NLOJET++ to which non-perturbative corrections have been applied. The error bars, which are usually smaller than the symbols, indicate the statistical uncertainty on the measurement. The dark-shaded band indicates the quadratic sum of the experimental systematic uncertainties, dominated by the jet energy scale uncertainty. There is an additional overall uncertainty of 3.4% due to the luminosity measurement that is not shown. The theory uncertainty, shown as the light, hatched band, is the quadratic sum of uncertainties from the choice of the renormalization and factorization scales, parton distribution functions, $\alpha_s(M_Z)$, and the modeling of non-perturbative effects, as described in the text.

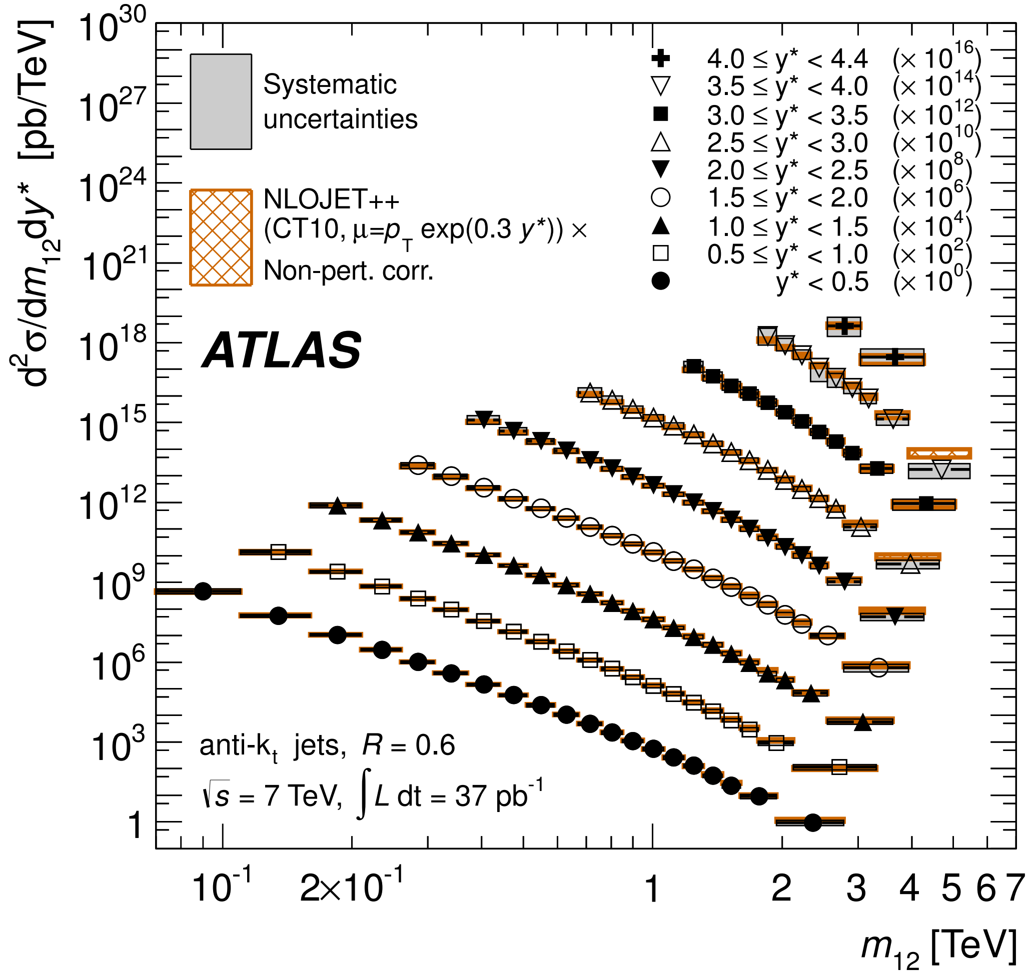

Figure 8.13: Dijet double-differential cross section as a function of dijet mass, binned in half the rapidity separation between the two leading jets, $y^* = |y_1 - y_2|/2$. The results are shown for jets identified using the anti-k_t algorithm with $R = 0.6$. For convenience, the cross sections are multiplied by the factors indicated in the legend. The data are compared to NLO pQCD calculations using NLOJET++ to which non-perturbative corrections have been applied. The theoretical and experimental uncertainties indicated are calculated as described in Fig. 8.12.

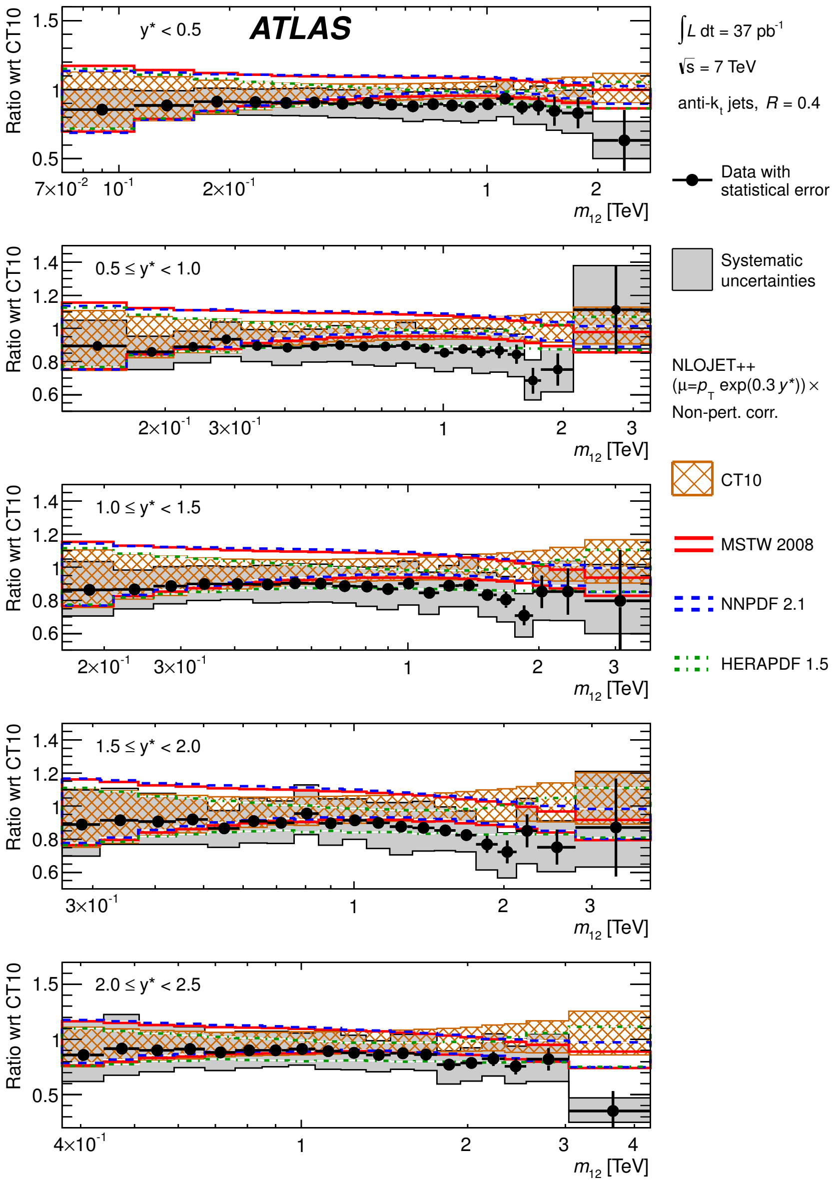

Figure 8.14: Ratios of dijet double-differential cross section to the theoretical prediction obtained using NLOJET++ with the CT10 PDF set. The ratios are shown as a function of dijet mass, binned in half the rapidity separation between the two leading jets, $y^* = |y_1 - y_2|/2$. The results are shown for jets identified using the anti-k_t algorithm with $R = 0.4$ that are in the region $y^* < 2.5$. The theoretical error bands obtained by using NLOJET++ with different PDF sets (CT10, MSTW 2008, NNPDF 2.1, HERAPDF 1.5) are shown. The systematic and theoretical uncertainties are calculated as described in Fig. 8.12.

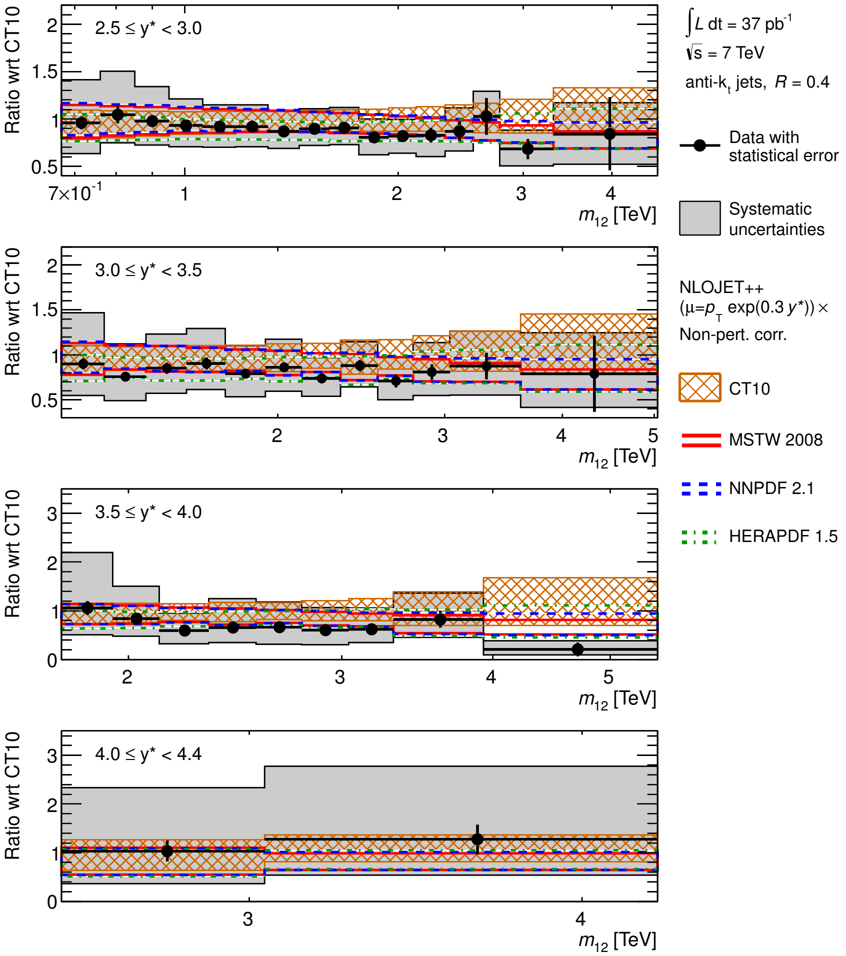

Figure 8.15: Ratios of dijet double-differential cross section to the theoretical prediction obtained using NLOJET++ with the CT10 PDF set. The ratios are shown as a function of dijet mass, binned in half the rapidity separation between the two leading jets, $y^* = |y_1 - y_2|/2$. The results are shown for jets identified using the anti-k_t algorithm with $R = 0.4$ that are in the region $2.5 \leq y^* < 4.4$. The theoretical error bands obtained by using NLOJET++ with different PDF sets (CT10, MSTW 2008, NNPDF 2.1, HERAPDF 1.5) are shown. The systematic and theoretical uncertainties are calculated as described in Fig. 8.12.

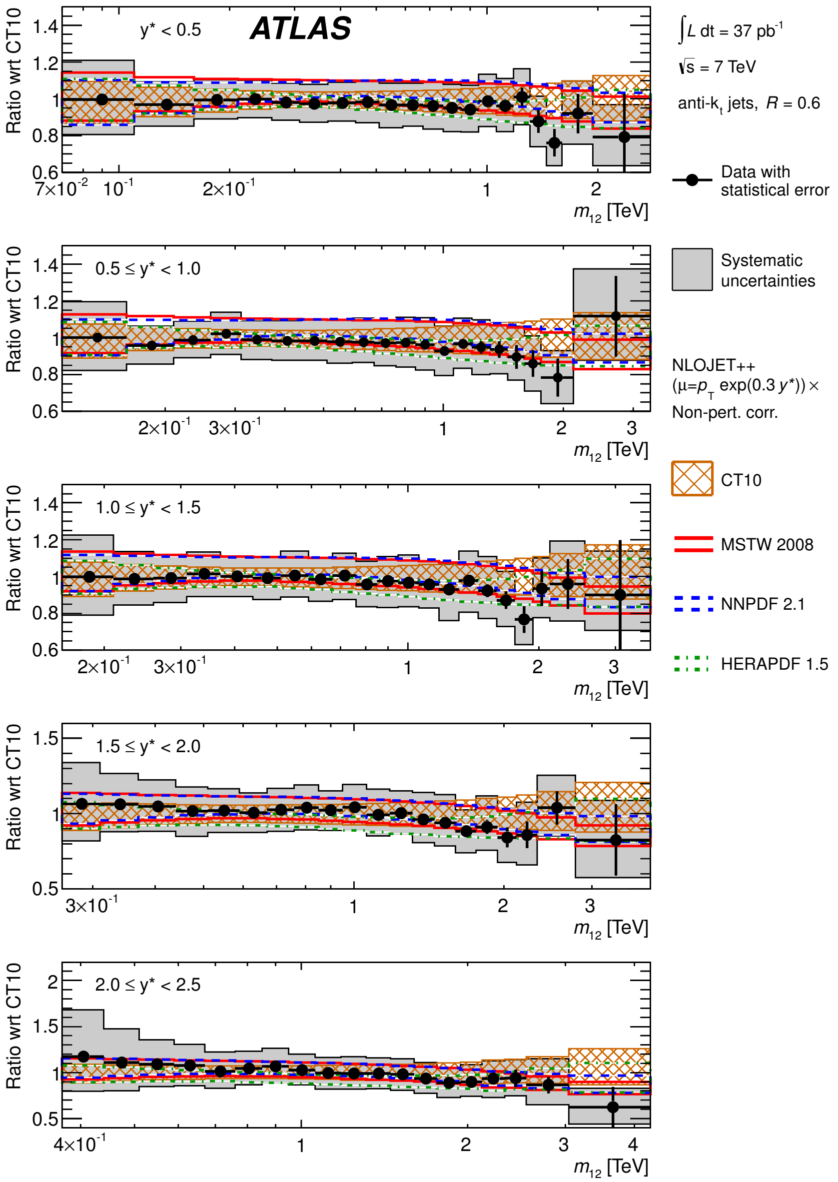

Figure 8.16: Ratios of dijet double-differential cross section to the theoretical prediction obtained using NLOJET++ with the CT10 PDF set. The ratios are shown as a function of dijet mass, binned in half the rapidity separation between the two leading jets, $y^* = |y_1 - y_2|/2$. The results are shown for jets identified using the anti-k_t algorithm with $R = 0.6$ that are in the region $y^* < 2.5$. The theoretical error bands obtained by using NLOJET++ with different PDF sets (CT10, MSTW 2008, NNPDF 2.1, HERAPDF 1.5) are shown. The systematic and theoretical uncertainties are calculated as described in Fig. 8.12.

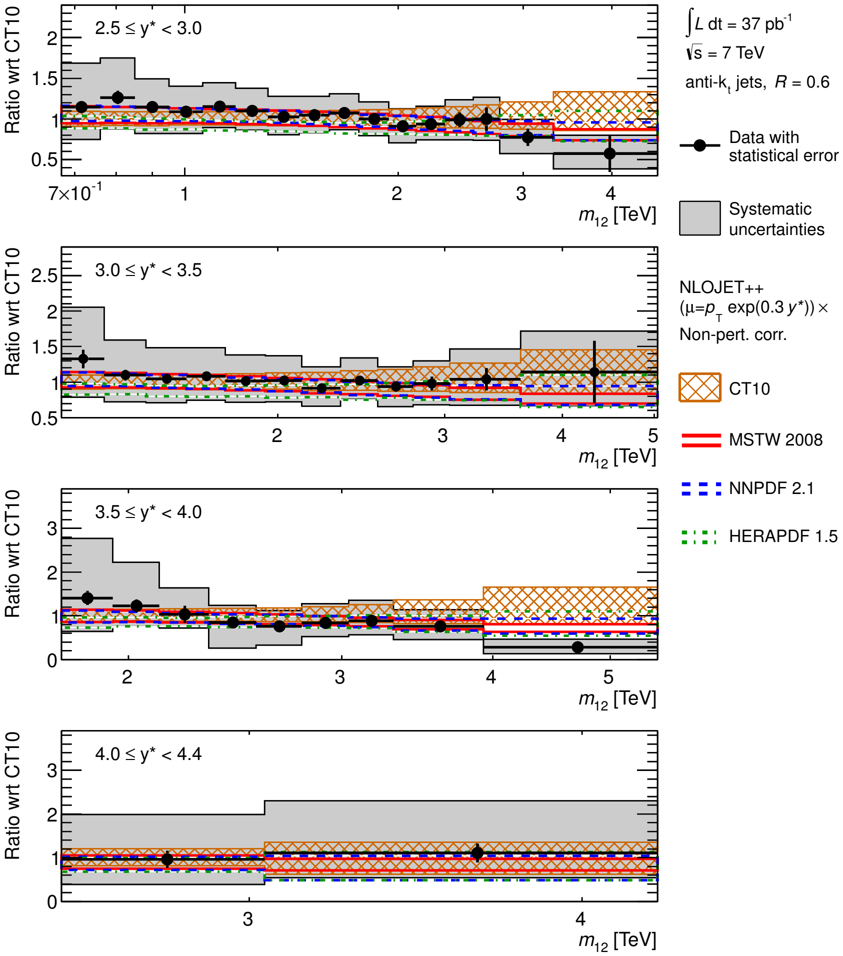

Figure 8.17: Ratios of dijet double-differential cross section to the theoretical prediction obtained using NLOJET++ with the CT10 PDF set. The ratios are shown as a function of dijet mass, binned in half the rapidity separation between the two leading jets, $y^* = |y_1 - y_2|/2$. The results are shown for jets identified using the anti-k_t algorithm with $R = 0.6$ that are in the region $2.5 \leq y^* < 4.4$. The theoretical error bands obtained by using NLOJET++ with different PDF sets (CT10, MSTW 2008, NNPDF 2.1, HERAPDF 1.5) are shown. The systematic and theoretical uncertainties are calculated as described in Fig. 8.12.

parisons are shown for $R = 0.4$ and $R = 0.6$ respectively in Figs. 8.18–8.19 and 8.20–8.21, where the data and all theory predictions have been normalized to the NLOJET++ prediction with CT10. The NLOJET++ prediction has been corrected for non-perturbative effects calculated using the PYTHIA Monte Carlo simulation with the AUET2B tune. The POWHEG predictions shown are interfaced to the PYTHIA parton shower with the AUET2B or Perugia2011 tune, and to the HERWIG parton shower using the AUET2 tune. The data are also compared to the POWHEG fixed-order NLO prediction (corrected for non-perturbative effects), where the POWHEG prediction has been calculated using a scale choice of $\mu_{\mathrm{R}} = \mu_{\mathrm{F}} = p_{\mathrm{T}}^{\mathrm{Born}}$.

The data are in best agreement with the POWHEG prediction showered with PYTHIA using the AUET2B tune. The other POWHEG showered predictions exhibit discrepancies at low dijet mass in all y^* slices, where they predict larger cross sections than are observed in the data.

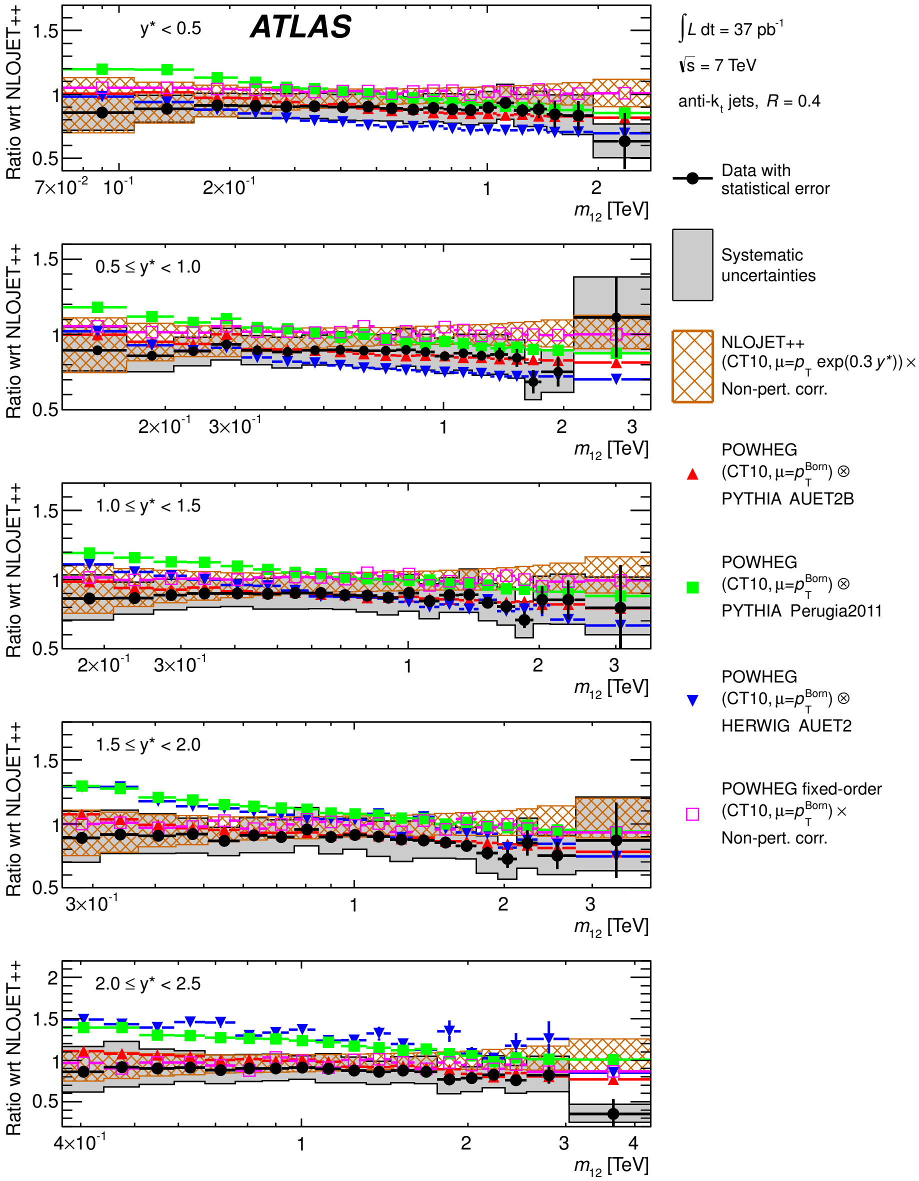

Figure 8.18: Ratios of dijet double-differential cross section to the theoretical prediction obtained using NLOJET++ with the CT10 PDF set. The ratios are shown as a function of dijet mass, binned in half the rapidity separation between the two leading jets, $y^* = |y_1 - y_2|/2$. The results are shown for jets identified using the anti-k_t algorithm with $R = 0.4$ that are in the region $y^* < 2.5$. The ratios of POWHEG predictions showered using either PYTHIA or HERWIG to the NLOJET++ predictions corrected for non-perturbative effects are shown and can be compared to the corresponding ratios for data. Only the statistical uncertainty on the POWHEG predictions is shown. The total systematic uncertainties on the theory and the measurement are indicated. The NLOJET++ prediction and the POWHEG ME calculations use the CT10 PDF set.

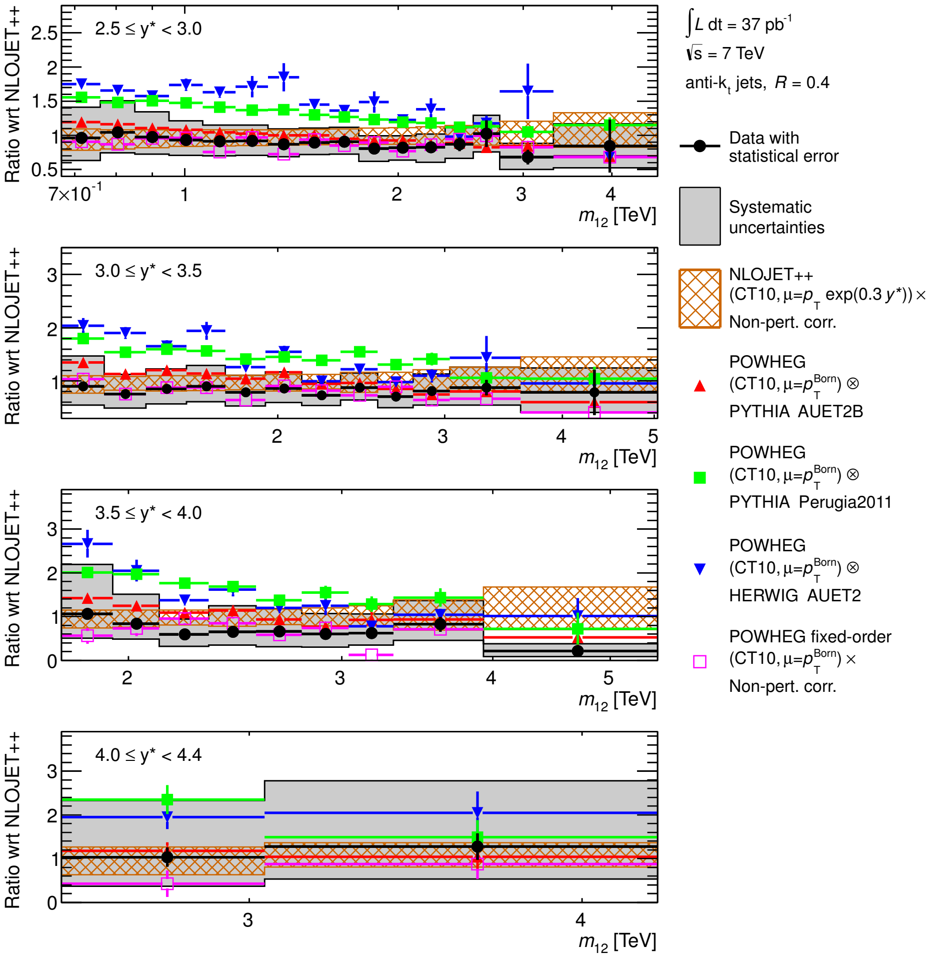

Figure 8.19: Ratios of dijet double-differential cross section to the theoretical prediction obtained using NLOJET++ with the CT10 PDF set. The ratios are shown as a function of dijet mass, binned in half the rapidity separation between the two leading jets, $y^* = |y_1 - y_2|/2$. The results are shown for jets identified using the anti-k_t algorithm with $R = 0.4$ that are in the region $2.5 \leq y^* < 4.4$. The ratios of POWHEG predictions showered using either PYTHIA or HERWIG to the NLOJET++ predictions corrected for non-perturbative effects are shown and can be compared to the corresponding ratios for data. Only the statistical uncertainty on the POWHEG predictions is shown. The total systematic uncertainties on the theory and the measurement are indicated. The NLOJET++ prediction and the POWHEG ME calculations use the CT10 PDF set.

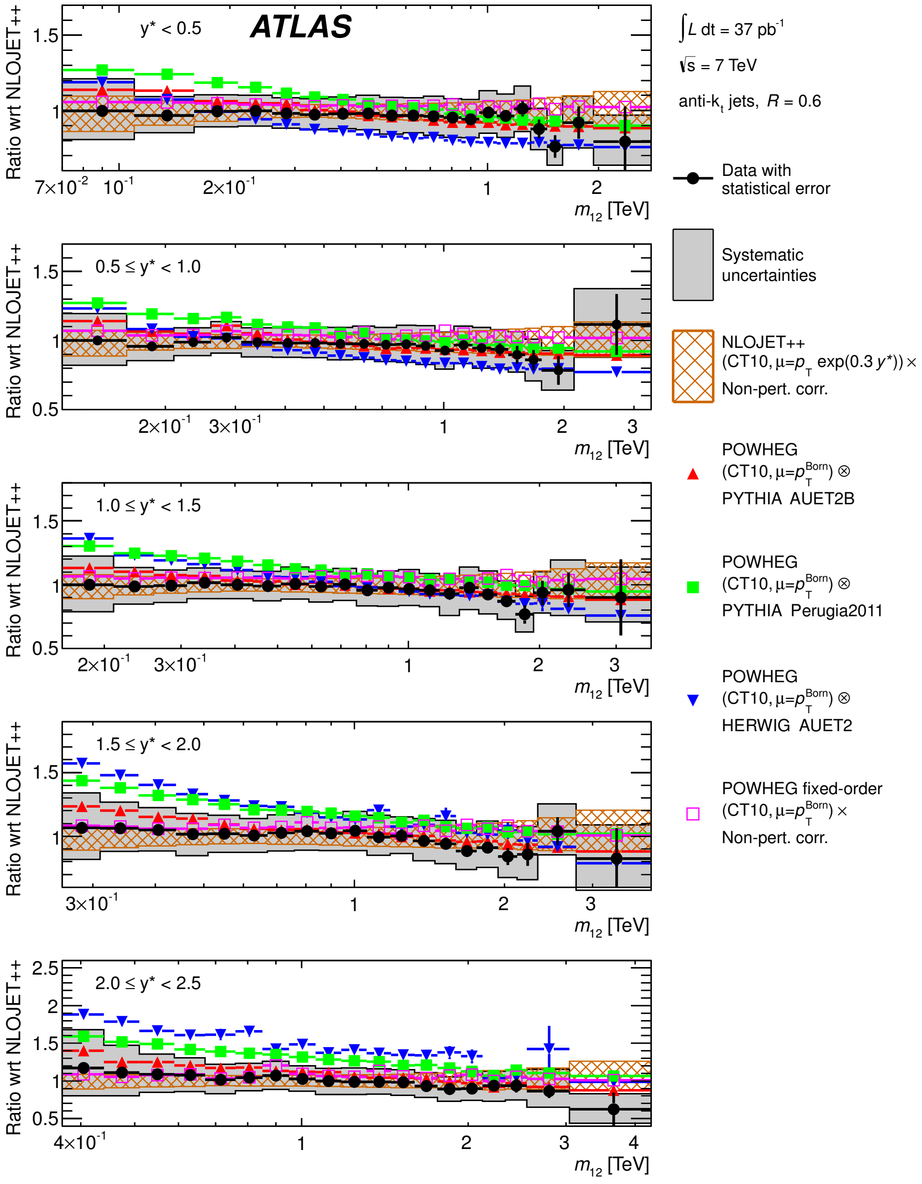

Figure 8.20: Ratios of dijet double-differential cross section to the theoretical prediction obtained using NLOJET++ with the CT10 PDF set. The ratios are shown as a function of dijet mass, binned in half the rapidity separation between the two leading jets, $y^* = |y_1 - y_2|/2$. The results are shown for jets identified using the anti-k_t algorithm with $R = 0.6$ that are in the region $y^* < 2.5$. The ratios of POWHEG predictions showered using either PYTHIA or HERWIG to the NLOJET++ predictions corrected for non-perturbative effects are shown and can be compared to the corresponding ratios for data. Only the statistical uncertainty on the POWHEG predictions is shown. The total systematic uncertainties on the theory and the measurement are indicated. The NLOJET++ prediction and the POWHEG ME calculations use the CT10 PDF set.

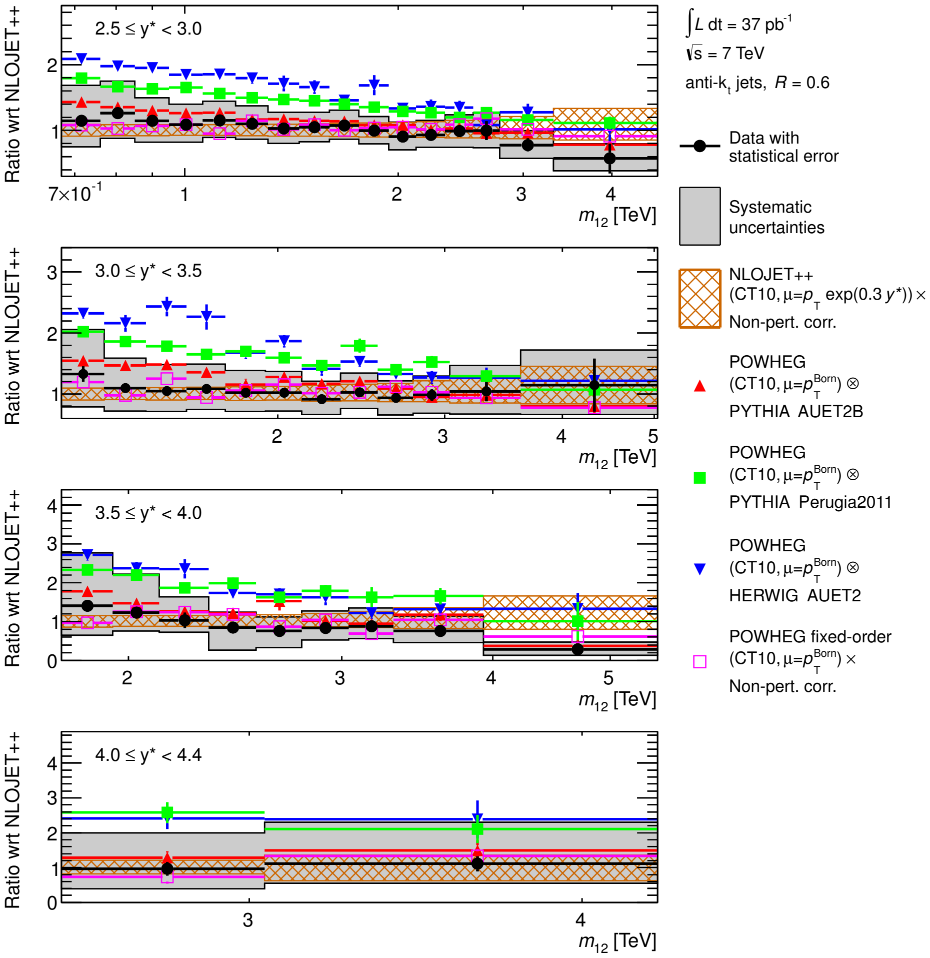

Figure 8.21: Ratios of dijet double-differential cross section to the theoretical prediction obtained using NLOJET++ with the CT10 PDF set. The ratios are shown as a function of dijet mass, binned in half the rapidity separation between the two leading jets, $y^* = |y_1 - y_2|/2$. The results are shown for jets identified using the anti-k_t algorithm with $R = 0.6$ that are in the region $2.5 \leq y^* < 4.4$. The ratios of POWHEG predictions showered using either PYTHIA or HERWIG to the NLOJET++ predictions corrected for non-perturbative effects are shown and can be compared to the corresponding ratios for data. Only the statistical uncertainty on the POWHEG predictions is shown. The total systematic uncertainties on the theory and the measurement are indicated. The NLOJET++ prediction and the POWHEG ME calculations use the CT10 PDF set.

CHAPTER 9

CONCLUSIONS

"The whole structure of science gradually grows, but only as it is built upon a firm foundation of past research."

— Owen Chamberlain (Nobel Prize in Physics, 1959)

Cross section measurements have been presented for inclusive jets and dijets reconstructed with the anti-k_t algorithm using two values of the clustering parameter ($R = 0.4$ and $R = 0.6$). Inclusive jet production has been measured as a function of jet transverse momentum, in bins of jet rapidity. Dijet production has been measured as a function of the invariant mass of the two leading jets, in bins of half their rapidity difference. These results are based on the data sample collected with the ATLAS detector during 2010, which corresponds to (37.3 ± 1.2) pb^{-1} of integrated luminosity.

Two different sizes of the jet clustering parameter have been used in order to probe the relative effects of the parton shower, hadronization, and the underlying event. The measurements have been corrected for all detector effects to the particle level so that they can be compared to any theoretical calculation. In this thesis, they have been compared to NLOJET++ and POWHEG fixed-order NLO pQCD calculations, each of which has been corrected for non-perturbative effects. The data have also been compared to POWHEG parton shower Monte Carlo simulations with NLO matrix elements. The latter predictions have only recently become available for inclusive jet and dijet production.

The current results reflect a number of significant experimental accomplishments:

- The cross section measurements extend to 1.5 TeV in jet transverse momentum and 5 TeV in dijet invariant mass, the highest ever measured. These results probe NLO pQCD in a large, new kinematic regime.
- Using data taken with minimum bias and forward jet triggers, these measurements extend to both the low-p_{T} region (down to jet transverse momentum of 20 GeV and dijet invariant mass of 70 GeV) and to the forward region (out to rapidities of $|y| = 4.4$). The forward region, in particular, has never been explored before with such precision at a hadron-hadron collider.
- High-precision measurements of the data collected during LHC beam position scans have determined the uncertainty on the collected luminosity to 3.4%.
- Detailed understanding of the detector performance has precisely determined systematic uncertainties, in particular those arising from the jet energy scale. In the central region ($|\eta| < 0.8$) the JES uncertainty is lower than 4.6% for all jets with $p_{\mathrm{T}} > 20$ GeV, while for jet transverse momenta between 60 and 800 GeV the JES uncertainty is below 2.5%.
- The correlations of the cross section measurement across various p_{T}, m_{12}, and rapidity bins have been studied for 22 independent sources of systematic uncertainty. These have been provided in the form of 87 nuisance parameters, each of which is fully correlated in p_{T} and y (dijet mass and y^*), for use in PDF fits.

The experimental uncertainties achieved are similar in size to the theoretical uncertainties in some regions of phase space, thereby providing some sensitivity to different theoretical predictions.

The measurements are compared to fixed-order NLO pQCD calculations, as well as to new calculations in which NLO pQCD matrix elements are matched to leading-logarithmic parton showers. Overall, both sets of calculations agree with the data over many orders of magnitude, although the cross sections predicted by the theory tend to be larger than the measured values at large jet transverse momentum and dijet invariant mass. The matched NLO parton shower calculations predict significant effects of the parton shower in some regions of phase space, in some cases improving and in others degrading the agreement with data with respect to the fixed-order calculations.

The results reported here constitute a comprehensive test of QCD across a large kinematic regime. These measurements probe and constrain the largely unexplored area of parton distribution functions at large x and high momentum transfer. The data are also important for tuning the parton shower in NLO Monte Carlo simulations, which have only recently been introduced for inclusive jet and dijet production. No significant deviations of the data from the NLO pQCD predictions, which could arise from new physical phenomena such as heavy resonances or quark contact interactions, are observed.

Future jet analyses using more data may extend the double-differential inclusive jet and dijet observables measured in this analysis. For example, the triple-differential dijet cross section in dijet mass, y^*, and $y_B = |y_1 + y_2|/2$, would provide a full parameterization of the dijet final state. This would produce more finely grained tests of QCD as well as searches for exotic phenomena. These more complex observables will require use of the significantly larger integrated luminosity of ~ 5 fb^{-1} that is available in the 2011 data sample.

APPENDIX A

DISPLAYS OF INTERESTING EVENTS

> *"If I can't picture it, I can't understand it."*
>
> — Albert Einstein (Nobel Prize in Physics, 1921)

The highest-p_T jets collected during 2010 are in the central region and have transverse momenta of about 1.5 TeV. The display for Run 167607, Event 63115223 is shown in Fig. A.1. This event contains a central jet with p_T of 1.5 TeV and $y = -0.6$. The highest-energy jets are in the forward region and approach the kinematically allowed limit of 3.5 TeV. The display of Run 167607, Event 36526763 in Fig. A.2 shows a forward jet with an energy of 3.4 TeV, p_T of 120 GeV, and $y = -4.0$.

Events with large dijet invariant masses can also be categorized as having central or forward dijet systems. Figure A.3 shows a display of Run 167607, Event 40296085. This is one of the highest-mass central dijet events, where the two leading jets have $|y| < 0.8$. The jets have p_T of 1.3 TeV and 1.2 TeV, respectively, and form a dijet invariant mass of 3.1 TeV with $y^* = 0.6$.

One of the highest-mass forward dijet systems, where the two leading jets are within $|y| < 2.8$, is shown in the display of Run 167607, Event 9435121 in Fig. A.4. In this event, the two leading jets each have p_T of 510 GeV and form a dijet invariant mass of 4.0 TeV with $y^* = 2.1$. The largest dijet masses measured in 2010 are about 5 TeV and are attained with relatively low-p_T jets at forward rapidities.

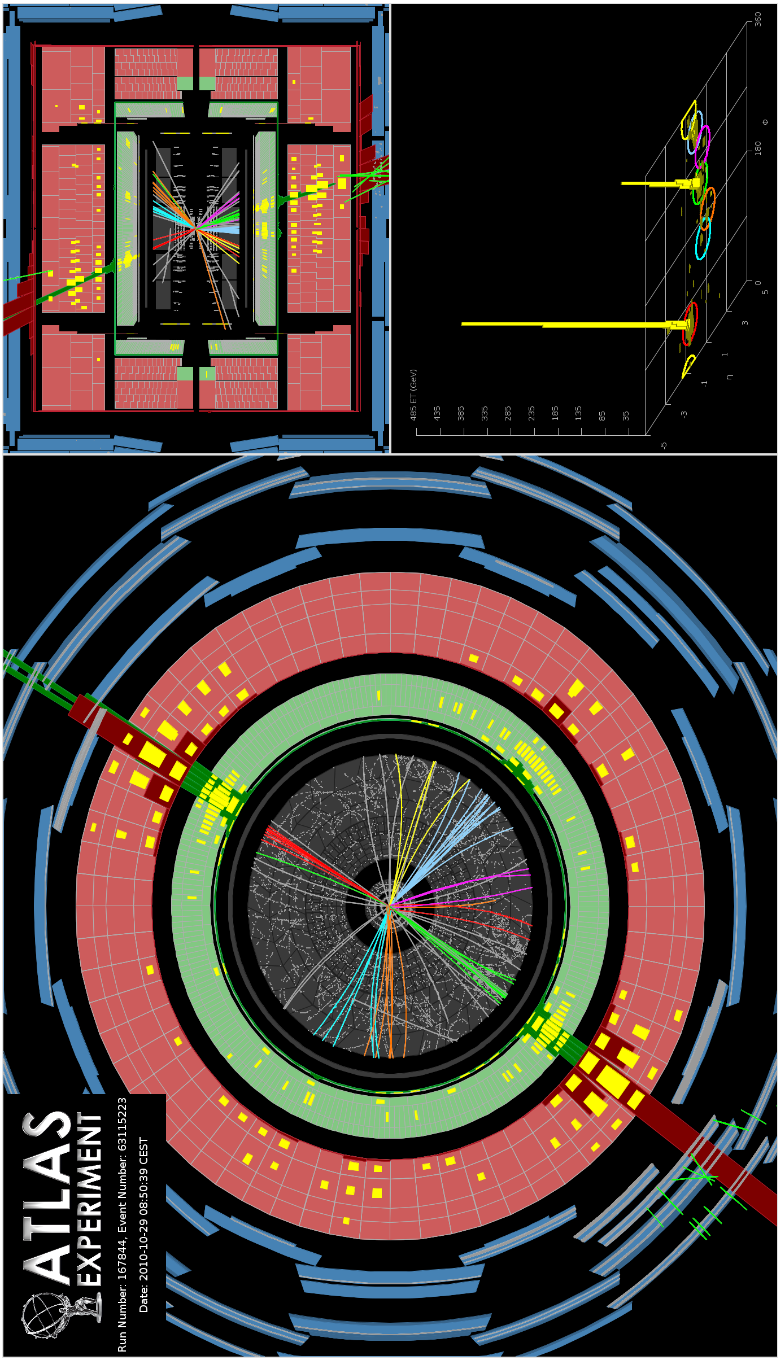

Figure A.1: Display of Run 167607, Event 63115223. This shows one of the highest-p_{T} jets collected during 2010, which has p_{T} of 1.5 TeV. The two leading jets are central high-p_{T} jets with an invariant mass of 2.8 TeV. They have (p_{T}, y) of (1.5 TeV, -0.6) and (1.0 TeV, 0.4), respectively. The missing E_{T} in the event is 310 GeV.

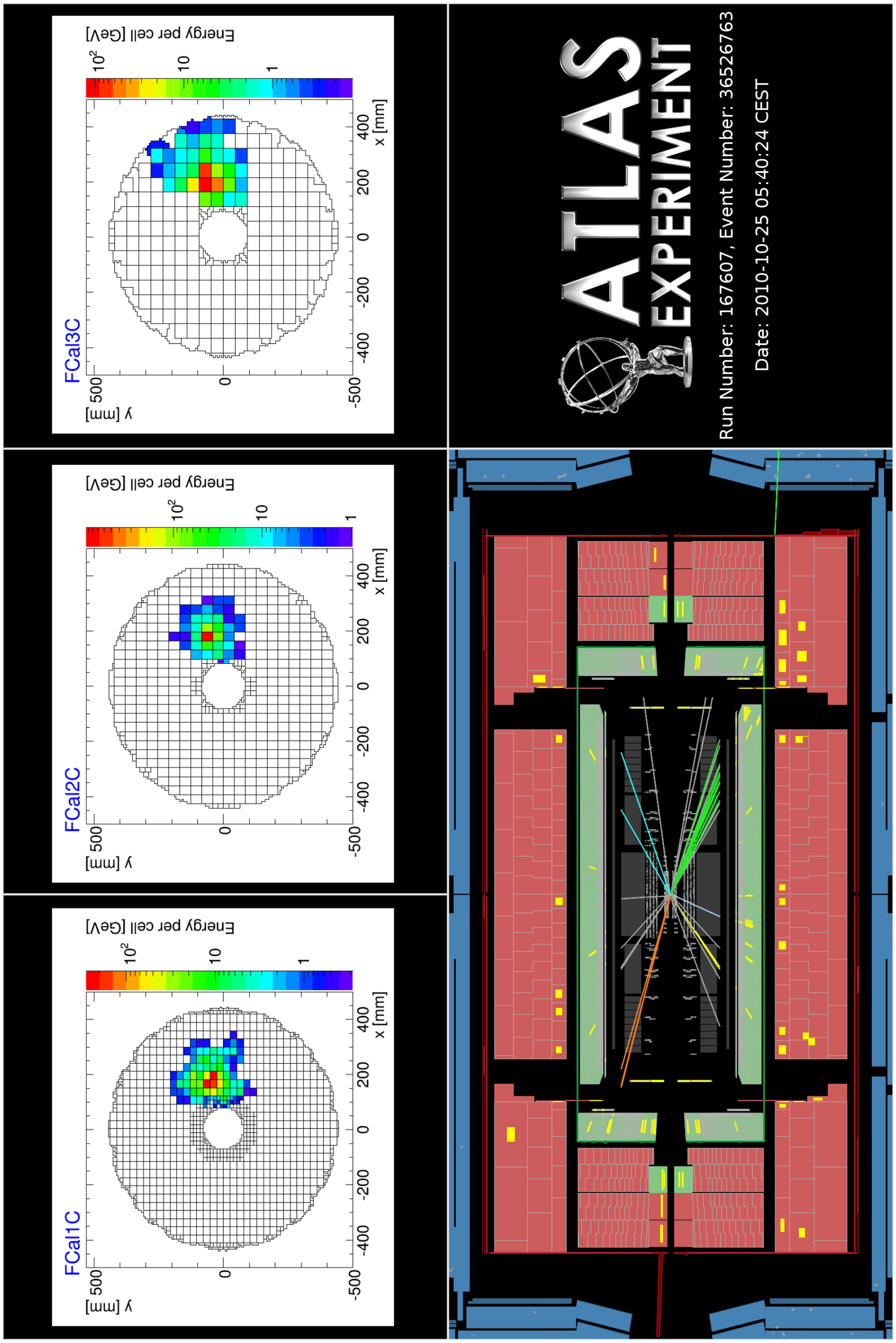

Figure A.2: Display of Run 167607, Event 36526763. This shows one of the highest-energy jets collected during 2010, which is in the FCal and has an energy of 3.4 TeV. This jet has p_{T} of 120 GeV and $y = -4.0$. The energy that its constituent clusters deposit into each of the three FCal layers is shown at the top of the figure. The boundaries of the FCal at approximately ±450 mm and ±100 mm correspond to $|\eta| = 3.1$ and $|\eta| = 4.9$, respectively.

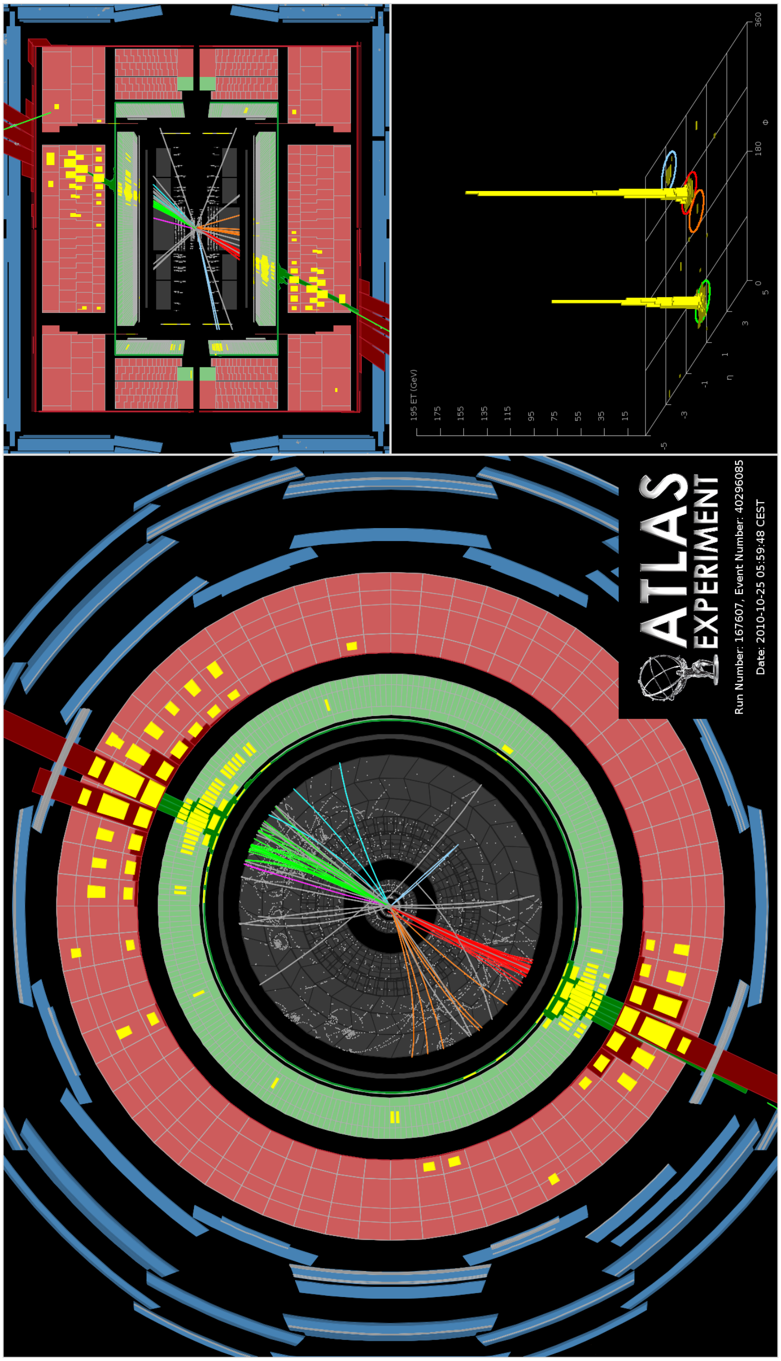

Figure A.3: Display of Run 167607, Event 40296085. This shows one of the highest-mass central dijet events, with two leading jets within $|y| < 0.8$, that was collected during 2010. The dijet system has an invariant mass of 3.1 TeV and $y^* = 0.6$. The two leading jets have ($p_{\rm T}$, y) of (1.3 TeV, -0.6) and (1.2 TeV, 0.6), respectively. The missing $E_{\rm T}$ in the event is 50 GeV.

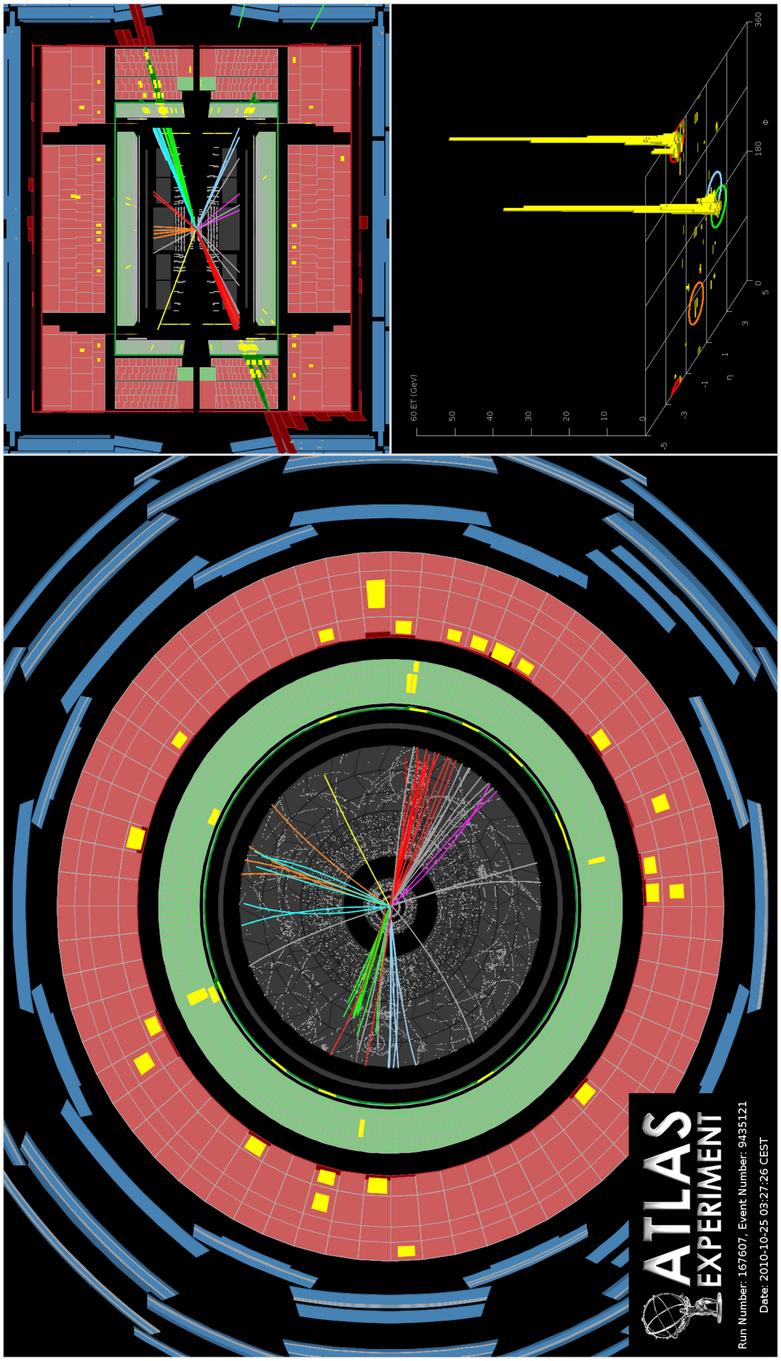

Figure A.4: Display of Run 167607, Event 9435121. This shows one of the highest-mass forward dijet events, with two leading jets within $|y| < 2.8$, that was collected during 2010. The dijet system has an invariant mass of 4.0 TeV and $y^* = 2.1$. The two leading jets have (p_T, y) of (510 GeV, -2.0) and (510 GeV, 2.2), respectively. The missing E_T in the event is 30 GeV.

APPENDIX B

TABLES

"The idea is to try to give all the information to help others to judge the value of your contribution; not just the information that leads to judgment in one particular direction or another."

— Richard Feynman (Nobel Prize in Physics, 1965)

B.1 Inclusive Jet Tables

p_T-bin [GeV]	σ [pb/GeV]	δ_stat %	γ_1	γ_7	γ_{13}	γ_{19}	γ_{25}	γ_{31}	γ_{32}	γ_{38}	γ_{44}	γ_{50}	γ_{56}	γ_{62}	γ_{68}	γ_{74}	γ_{75}	γ_{76}	γ_{82}	γ_{83}	u_1	u_2	u_3
20-30	$4.70 \cdot 10^{6}$	0.86	$^{+10}_{-9.6}$	$^{+10}_{-9.9}$	$^{+7.0}_{-7.1}$	$^{+8.3}_{-8.6}$	$^{+3.7}_{-4.0}$	0.0	$^{+2.0}_{-2.2}$	$^{+4.9}_{-5.0}$	$^{+4.1}_{-4.7}$	0.0	0.0	$^{+1.8}_{-2.0}$	0.0	0.0	±1.5	±4.2	±0.2	±2.0	0.70	1.00	0.33
30-45	$7.17 \cdot 10^{5}$	1.33	$^{+4.7}_{-4.8}$	$^{+8.9}_{-8.3}$	$^{+5.9}_{-6.0}$	$^{+10}_{-9.0}$	$^{+1.4}_{-1.7}$	0.0	$^{+2.3}_{-2.4}$	$^{+4.0}_{-3.8}$	$^{+4.1}_{-4.4}$	0.0	0.0	$^{+3.3}_{-3.5}$	0.0	0.0	±1.1	±0.9	0.0	±1.0	0.41	1.00	0.22
45-60	$1.48 \cdot 10^{5}$	3.03	$^{+1.8}_{-1.7}$	$^{+7.8}_{-6.8}$	$^{+4.1}_{-3.5}$	$^{+5.3}_{-4.7}$	$^{+0.4}_{-0.1}$	0.0	$^{+2.9}_{-2.8}$	$^{+2.4}_{-2.3}$	$^{+4.0}_{-3.7}$	$^{+0.2}_{+0.2}$	$^{+0.3}_{+0.0}$	$^{+4.6}_{-4.4}$	0.0	0.0	±0.7	±0.7	0.0	±1.0	0.27	1.00	0.19
60-80	$3.81 \cdot 10^{4}$	1.10	∓0.6	$^{+6.2}_{-6.0}$	$^{+2.5}_{-2.4}$	$^{+3.3}_{-3.4}$	$^{+0.9}_{-1.0}$	0.0	±3.2	$^{+1.5}_{-1.6}$	$^{+4.1}_{-3.9}$	$^{+0.4}_{-0.3}$	0.0	$^{+4.6}_{-4.2}$	∓0.1	0.0	±0.4	0.0	0.0	±1.0	0.27	1.00	0.15
80-110	$8.52 \cdot 10^{3}$	0.68	∓0.4	$^{+6.4}_{-6.8}$	$^{+3.6}_{-4.1}$	$^{+3.2}_{-3.3}$	$^{+1.7}_{-2.2}$	0.0	$^{+2.7}_{-3.1}$	$^{+1.1}_{-1.6}$	$^{+4.2}_{-4.9}$	$^{+0.5}_{-1.0}$	0.0	±2.4	$^{-0.6}_{+0.2}$	0.0	±2.0	±2.3	0.0	±1.0	0.40	1.00	0.10
110-160	$1.48 \cdot 10^{3}$	0.62	0.0	$^{+5.4}_{-4.9}$	$^{+3.5}_{-3.3}$	$^{+3.3}_{-3.4}$	±0.7	0.0	$^{+3.2}_{-2.9}$	$^{+1.2}_{-1.0}$	$^{+5.3}_{-4.9}$	$^{+1.7}_{-1.6}$	0.0	0.0	$^{+1.3}_{-1.1}$	0.0	0.0	±0.8	0.0	±1.0	0.35	1.00	0.07
160-210	$2.54 \cdot 10^{2}$	0.69	0.0	$^{+3.8}_{-3.5}$	$^{+3.8}_{-3.9}$	$^{+3.0}_{-2.6}$	$^{+1.4}_{-0.9}$	0.0	$^{+2.5}_{-2.6}$	$^{+0.8}_{-0.4}$	$^{+6.1}_{-5.5}$	$^{+2.5}_{-1.9}$	$^{+0.3}_{+0.2}$	∓0.3	±4.5	±0.1	±0.1	±0.4	0.0	±1.0	0.34	1.00	0.06
210-260	$6.34 \cdot 10^{1}$	0.91	0.0	$^{+5.4}_{-5.6}$	$^{+5.7}_{-5.9}$	$^{+2.1}_{-2.7}$	$^{+1.1}_{-1.7}$	0.0	$^{+2.8}_{-2.9}$	$^{+0.5}_{-0.8}$	$^{+6.1}_{-6.5}$	$^{+3.2}_{-3.8}$	$^{+0.2}_{-0.5}$	0.0	$^{+6.2}_{-6.6}$	±0.2	0.0	±0.4	±0.1	±1.0	0.37	1.00	0.05
260-310	$2.07 \cdot 10^{1}$	0.86	0.0	$^{+5.4}_{-4.9}$	$^{+4.0}_{-3.7}$	$^{+2.1}_{-1.9}$	$^{+1.8}_{-1.5}$	0.0	$^{+2.4}_{-2.0}$	$^{+0.6}_{-0.3}$	$^{+6.1}_{-5.7}$	$^{+4.1}_{-3.8}$	$^{+0.6}_{-0.4}$	0.0	$^{+6.9}_{-6.4}$	±0.2	0.0	±0.7	0.0	±1.0	0.28	1.00	0.05
310-400	$5.96 \cdot 10^{0}$	1.03	0.0	$^{+3.7}_{-3.2}$	$^{+2.3}_{-1.9}$	$^{+1.1}_{-0.5}$	$^{+1.9}_{-1.8}$	0.0	$^{+2.0}_{-1.9}$	$^{+0.7}_{-0.1}$	$^{+6.3}_{-6.1}$	$^{+4.5}_{-3.8}$	$^{+0.7}_{-0.2}$	0.0	$^{+7.0}_{-6.5}$	±0.1	0.0	±0.8	0.0	±1.0	0.26	1.00	0.05
400-500	$1.33 \cdot 10^{0}$	2.02	0.0	$^{+0.4}_{-0.8}$	0.0	$^{+1.6}_{-2.0}$	$^{+1.8}_{-2.2}$	0.0	$^{+1.1}_{-1.5}$	$^{+0.3}_{-0.7}$	$^{+6.7}_{-6.6}$	$^{+5.0}_{-5.3}$	$^{+0.1}_{-0.6}$	0.0	$^{+7.7}_{-7.8}$	±0.2	0.0	±0.4	0.0	±1.0	0.21	1.00	0.05
500-600	$3.47 \cdot 10^{-1}$	3.22	0.0	±2.3	$^{+1.0}_{-0.8}$	$^{+1.9}_{-1.8}$	$^{+3.0}_{-2.7}$	0.0	$^{+1.6}_{-1.3}$	$^{+0.3}_{-0.4}$	$^{+7.2}_{-6.7}$	$^{+6.2}_{-5.5}$	$^{+0.5}_{-0.6}$	0.0	$^{+9.6}_{-8.8}$	±0.3	0.0	±0.7	0.0	±1.0	0.19	1.00	0.05
600-800	$6.44 \cdot 10^{-2}$	5.73	0.0	±4.2	$^{+3.3}_{-3.4}$	$^{+0.8}_{-0.6}$	$^{+1.8}_{-2.1}$	0.0	$^{+1.2}_{-1.5}$	$^{+0.5}_{-0.4}$	$^{+7.7}_{-6.8}$	$^{+6.0}_{-5.8}$	$^{+1.0}_{-0.9}$	0.0	$^{+10}_{-9.4}$	±0.3	0.0	±0.7	0.0	±1.0	0.17	1.00	0.21
800-1000	$1.01 \cdot 10^{-2}$	16.7	0.0	$^{+3.0}_{-2.6}$	$^{+5.4}_{-4.9}$	$^{+1.1}_{-0.9}$	$^{+1.7}_{-1.5}$	0.0	$^{+1.1}_{-1.0}$	$^{+0.3}_{+0.1}$	$^{+8.4}_{-7.8}$	$^{+7.9}_{-6.8}$	$^{+1.8}_{-2.1}$	0.0	$^{+12}_{-11}$	±0.5	0.0	±0.9	0.0	±1.0	0.11	1.00	0.21
1000-1200	$1.14 \cdot 10^{-3}$	37.3	0.0	$^{+2.4}_{-2.5}$	$^{+5.6}_{-5.3}$	$^{+0.9}_{-0.7}$	±3.1	0.0	$^{+1.0}_{-0.6}$	$^{+0.5}_{-0.3}$	$^{+8.8}_{-7.9}$	$^{+8.8}_{-8.4}$	±4.9	0.0	$^{+16}_{-14}$	±0.7	0.0	±0.4	0.0	±1.0	0.12	1.00	0.21
1200-1500	$4.00 \cdot 10^{-4}$	58.6	0.0	$^{+2.3}_{-2.5}$	$^{+6.3}_{-6.4}$	$^{+1.0}_{-0.8}$	$^{+2.4}_{-2.7}$	0.0	$^{+0.5}_{-0.8}$	$^{+0.6}_{-0.5}$	$^{+9.7}_{-8.9}$	$^{+10}_{-9.5}$	$^{+9.3}_{-8.6}$	0.0	$^{+20}_{-18}$	±0.5	0.0	±3.0	±0.1	±1.0	0.08	1.00	0.21

Table B.1: Measured jet cross section for $R = 0.4$ and $|y| < 0.3$. σ is the measured cross section. δ_stat is the statistical uncertainty. γ_i and u_i are the correlated and uncorrelated systematic uncertainties, as described in Sec. 7.13 and Table 7.3. All uncertainties are given in %. An overall luminosity uncertainty of 3.4%, which is applicable to all ATLAS data samples based on 2010 data, is not shown. This table is available on HEPDATA [187].

p_{T}-bin [GeV]	σ [pb/GeV]	δ_{stat} %	γ_1	γ_7	γ_{13}	γ_{19}	γ_{25}	γ_{31}	γ_{32}	γ_{38}	γ_{44}	γ_{50}	γ_{56}	γ_{62}	γ_{68}	γ_{74}	γ_{75}	γ_{76}	γ_{82}	γ_{83}	u_1	u_2	u_3
20-30	$4.61 \cdot 10^{6}$	0.61	$^{+10}_{-9.5}$	$^{+8.1}_{-8.3}$	$^{+10}_{-9.6}$	±7.3	±4.2	0.0	±2.1	±4.3	$^{+4.6}_{-4.5}$	0.0	0.0	±2.9	0.0	0.0	±1.3	±3.9	±0.2	±2.0	0.70	1.00	0.30
30-45	$7.30 \cdot 10^{5}$	1.19	$^{+4.9}_{-4.7}$	$^{+11}_{-9.5}$	$^{+6.8}_{-6.3}$	$^{+8.8}_{-7.5}$	$^{+2.4}_{-2.1}$	0.0	±2.4	±3.2	$^{+4.6}_{-4.4}$	0.0	0.0	±3.2	$^{-0.2}_{+0.1}$	0.0	±1.0	±1.7	0.0	±1.0	0.43	1.00	0.20
45-60	$1.49 \cdot 10^{5}$	2.15	$^{+2.0}_{-1.5}$	$^{+7.5}_{-6.7}$	$^{+6.0}_{-5.3}$	$^{+4.9}_{-4.2}$	$^{+1.7}_{-1.1}$	0.0	$^{+3.2}_{-2.6}$	$^{+1.9}_{-1.3}$	$^{+4.4}_{-3.8}$	$^{+0.1}_{+0.2}$	$^{+0.3}_{+0.0}$	$^{+2.7}_{-2.3}$	$^{+0.3}_{+0.1}$	±0.1	±0.5	±1.2	0.0	±1.0	0.28	1.00	0.19
60-80	$3.71 \cdot 10^{4}$	0.83	∓0.6	$^{+6.2}_{-5.3}$	$^{+5.1}_{-4.4}$	$^{+3.9}_{-3.4}$	$^{+2.4}_{-2.1}$	0.0	$^{+3.2}_{-2.7}$	$^{+1.5}_{-1.2}$	$^{+4.6}_{-3.9}$	$^{+0.5}_{-0.2}$	0.0	$^{+0.9}_{-0.7}$	$^{+1.6}_{-1.3}$	0.0	0.0	±0.6	0.0	±1.0	0.30	1.00	0.16
80-110	$8.35 \cdot 10^{3}$	0.56	∓0.4	±5.8	$^{+3.6}_{-3.8}$	$^{+2.7}_{-3.0}$	$^{+0.5}_{-0.9}$	0.0	$^{+2.5}_{-2.8}$	$^{+0.8}_{-1.3}$	$^{+4.6}_{-4.8}$	$^{+0.8}_{-1.2}$	0.0	∓0.3	$^{+3.6}_{-3.7}$	0.0	±0.3	±0.7	0.0	±1.0	0.38	1.00	0.11
110-160	$1.44 \cdot 10^{3}$	0.44	0.0	$^{+5.6}_{-5.4}$	$^{+3.8}_{-3.5}$	$^{+3.4}_{-3.2}$	±0.8	0.0	$^{+2.5}_{-2.4}$	$^{+0.8}_{-0.7}$	$^{+5.2}_{-4.7}$	$^{+1.6}_{-1.5}$	0.0	∓0.1	$^{+5.0}_{-4.9}$	0.0	0.0	±1.3	0.0	±1.0	0.35	1.00	0.08
160-210	$2.41 \cdot 10^{2}$	0.58	0.0	$^{+4.6}_{-4.0}$	$^{+3.8}_{-3.4}$	$^{+3.0}_{-2.6}$	$^{+1.7}_{-1.1}$	0.0	$^{+2.4}_{-1.9}$	$^{+1.1}_{-0.4}$	$^{+5.7}_{-5.4}$	$^{+2.5}_{-1.9}$	$^{+0.4}_{+0.1}$	0.0	$^{+6.7}_{-5.9}$	±0.1	0.0	±0.7	0.0	±1.0	0.39	1.00	0.07
210-260	$6.06 \cdot 10^{1}$	0.72	0.0	$^{+4.0}_{-4.6}$	$^{+3.3}_{-3.9}$	$^{+2.2}_{-2.3}$	$^{+1.5}_{-2.1}$	0.0	$^{+1.8}_{-2.0}$	0.0	$^{+6.2}_{-6.4}$	$^{+3.0}_{-3.5}$	0.0	0.0	$^{+7.8}_{-7.6}$	±0.1	0.0	±0.4	0.0	±1.0	0.30	1.00	0.07
260-310	$1.96 \cdot 10^{1}$	0.68	0.0	$^{+4.1}_{-3.2}$	$^{+3.1}_{-2.1}$	$^{+2.0}_{-1.2}$	$^{+3.0}_{-2.2}$	0.0	$^{+2.1}_{-1.4}$	$^{+0.7}_{-0.2}$	$^{+6.9}_{-6.2}$	$^{+3.9}_{-3.3}$	$^{+0.3}_{0.0}$	0.0	$^{+8.8}_{-7.6}$	±0.2	0.0	±0.7	0.0	±1.0	0.25	1.00	0.07
310-400	$5.64 \cdot 10^{0}$	0.92	0.0	$^{+3.6}_{-3.0}$	$^{+2.6}_{-2.4}$	$^{+1.8}_{-1.6}$	$^{+3.3}_{-2.7}$	0.0	$^{+1.9}_{-1.3}$	$^{+0.4}_{-0.3}$	$^{+7.1}_{-6.3}$	$^{+4.3}_{-4.2}$	$^{+0.5}_{+0.1}$	0.0	$^{+9.4}_{-8.8}$	±0.1	0.0	±0.7	0.0	±1.0	0.30	1.00	0.07
400-500	$1.19 \cdot 10^{0}$	1.76	0.0	$^{+3.5}_{-3.6}$	$^{+2.5}_{-2.9}$	$^{+1.0}_{-1.5}$	$^{+2.5}_{-2.9}$	0.0	$^{+0.9}_{-1.4}$	±0.3	±6.4	$^{+4.3}_{-4.5}$	0.0	0.0	$^{+9.4}_{-9.0}$	±0.3	0.0	±0.4	0.0	±1.0	0.24	1.00	0.07
500-600	$3.16 \cdot 10^{-1}$	3.23	0.0	$^{+3.3}_{-2.9}$	$^{+2.4}_{-2.2}$	±0.6	$^{+2.0}_{-1.9}$	0.0	$^{+1.1}_{-0.9}$	$^{+0.4}_{-0.3}$	$^{+6.7}_{-6.9}$	$^{+5.2}_{-4.9}$	$^{+0.5}_{-0.3}$	0.0	$^{+11}_{-10}$	±0.2	0.0	±0.4	0.0	±1.0	0.21	1.00	0.25
600-800	$6.60 \cdot 10^{-2}$	4.20	0.0	$^{+3.1}_{-3.6}$	$^{+0.7}_{-1.2}$	$^{+0.7}_{-0.6}$	$^{+2.1}_{-2.0}$	0.0	$^{+0.7}_{-1.2}$	±0.4	$^{+7.4}_{-7.3}$	$^{+6.3}_{-5.9}$	$^{+0.9}_{-1.3}$	0.0	$^{+13}_{-12}$	±0.2	0.0	±0.2	0.0	±1.0	0.14	1.00	0.25
800-1000	$7.80 \cdot 10^{-3}$	11.9	0.0	$^{+5.5}_{-5.2}$	$^{+3.6}_{-2.7}$	$^{+1.4}_{-0.9}$	$^{+3.0}_{-2.9}$	0.0	$^{+0.9}_{-0.2}$	$^{+0.4}_{+0.1}$	$^{+9.0}_{-8.0}$	$^{+7.1}_{-6.7}$	$^{+3.2}_{-2.9}$	0.0	$^{+16}_{-14}$	±0.5	0.0	±1.0	0.0	±1.0	0.13	1.00	0.25
1000-1200	$1.38 \cdot 10^{-3}$	30.6	0.0	$^{+5.7}_{-5.2}$	$^{+3.5}_{-3.7}$	$^{+0.5}_{-0.4}$	$^{+3.6}_{-3.4}$	0.0	$^{+0.5}_{-0.9}$	$^{+0.6}_{-0.5}$	$^{+10}_{-8.5}$	$^{+8.4}_{-7.7}$	$^{+6.5}_{-6.1}$	0.0	$^{+19}_{-16}$	±0.6	0.0	±2.2	0.0	±1.0	0.14	1.00	0.25
1200-1500	$2.35 \cdot 10^{-4}$	66.6	0.0	$^{+6.8}_{-7.1}$	$^{+4.4}_{-5.6}$	$^{+0.4}_{-1.2}$	$^{+3.3}_{-3.5}$	0.0	$^{+0.4}_{-1.3}$	0.0	±11	$^{+9.4}_{-9.7}$	$^{+11}_{-12}$	0.0	$^{+23}_{-21}$	±0.5	0.0	±2.4	±0.1	±1.0	0.15	1.00	0.25

Table B.2: Measured jet cross section for $R = 0.4$ and $0.3 < |y| < 0.8$. See Table B.1 for a description of the columns. This table is available on HEPDATA [187].

p_{T}-bin [GeV]	σ [pb/GeV]	δ_{stat} %	γ_2	γ_8	γ_{14}	γ_{20}	γ_{26}	γ_{31}	γ_{33}	γ_{39}	γ_{45}	γ_{51}	γ_{57}	γ_{63}	γ_{69}	γ_{74}	γ_{75}	γ_{77}	γ_{82}	γ_{83}	u_1	u_2	u_3
20-30	$3.92 \cdot 10^{6}$	0.68	± 9.1	$^{+7.0}_{-8.0}$	$^{+8.9}_{-9.3}$	± 13	$^{+3.7}_{-3.9}$	$^{+7.0}_{-7.5}$	$^{+1.8}_{-1.9}$	$^{+3.9}_{-4.1}$	$^{+4.1}_{-4.4}$	0.0	0.0	$^{+2.5}_{-2.8}$	0.0	0.0	± 1.0	± 9.4	± 1.2	± 2.0	1.02	1.00	0.25
30-45	$6.66 \cdot 10^{5}$	1.51	$^{+5.0}_{-4.5}$	$^{+11}_{-9.4}$	$^{+7.2}_{-6.2}$	$^{+5.7}_{-4.8}$	$^{+2.5}_{-1.9}$	$^{+8.7}_{-7.4}$	$^{+2.6}_{-2.3}$	$^{+3.4}_{-3.0}$	$^{+4.9}_{-4.3}$	0.0	0.0	$^{+3.4}_{-3.0}$	$^{-0.2}_{+0.1}$	0.0	± 0.7	± 6.5	± 0.2	± 1.0	0.72	1.00	0.20
45-60	$1.39 \cdot 10^{5}$	2.59	$^{+1.9}_{-1.4}$	$^{+8.2}_{-6.7}$	$^{+6.3}_{-5.3}$	$^{+2.0}_{-1.2}$	$^{+1.8}_{-1.2}$	$^{+7.2}_{-6.0}$	$^{+3.2}_{-2.6}$	$^{+1.9}_{-1.4}$	$^{+4.7}_{-3.8}$	$^{+0.2}_{+0.2}$	$^{+0.3}_{+0.0}$	$^{+2.7}_{-2.2}$	$^{+0.2}_{+0.1}$	0.0	± 0.5	± 3.1	± 0.3	± 1.0	0.46	1.00	0.21
60-80	$3.39 \cdot 10^{4}$	0.99	∓ 0.7	$^{+6.0}_{-5.3}$	$^{+4.8}_{-4.5}$	± 2.4	$^{+2.3}_{-2.2}$	$^{+5.3}_{-5.0}$	± 2.8	$^{+1.5}_{-1.3}$	$^{+4.4}_{-4.1}$	$^{+0.3}_{-0.2}$	0.0	± 0.8	$^{+1.6}_{-1.5}$	0.0	± 0.1	± 1.5	± 0.2	± 1.0	0.47	1.00	0.18
80-110	$7.55 \cdot 10^{3}$	0.71	$^{-0.5}_{+0.4}$	$^{+5.7}_{-5.8}$	$^{+3.8}_{-3.9}$	$^{+2.6}_{-2.8}$	$^{+0.6}_{-1.0}$	$^{+4.3}_{-4.1}$	$^{+2.7}_{-2.9}$	$^{+1.0}_{-1.3}$	± 4.8	$^{+1.0}_{-1.3}$	0.0	∓ 0.3	$^{+3.9}_{-3.8}$	± 0.2	± 0.3	± 1.4	± 0.2	± 1.0	0.70	1.00	0.12
110-160	$1.28 \cdot 10^{3}$	0.50	0.0	$^{+5.6}_{-5.9}$	$^{+3.7}_{-3.8}$	± 2.5	$^{+0.8}_{-1.0}$	± 3.0	$^{+2.5}_{-2.6}$	$^{+0.7}_{-0.9}$	$^{+5.2}_{-5.1}$	$^{+1.6}_{-1.8}$	0.0	∓ 0.1	$^{+5.0}_{-5.3}$	± 0.2	0.0	± 1.7	± 0.1	± 1.0	0.63	1.00	0.08
160-210	$2.05 \cdot 10^{2}$	0.58	0.0	$^{+4.8}_{-4.0}$	$^{+3.9}_{-3.3}$	$^{+2.3}_{-1.9}$	$^{+1.8}_{-1.3}$	$^{+3.6}_{-3.1}$	$^{+2.3}_{-1.9}$	$^{+1.0}_{-0.4}$	$^{+5.9}_{-5.6}$	$^{+2.6}_{-2.0}$	$^{+0.4}_{+0.1}$	0.0	$^{+6.8}_{-6.1}$	± 0.2	0.0	± 1.2	± 0.1	± 1.0	0.63	1.00	0.06
210-260	$5.01 \cdot 10^{1}$	1.00	0.0	± 4.3	± 3.5	$^{+2.2}_{-1.9}$	$^{+1.8}_{-2.0}$	± 3.9	$^{+2.1}_{-1.8}$	$^{+0.2}_{-0.6}$	$^{+6.4}_{-6.0}$	$^{+3.3}_{-3.2}$	0.0	0.0	$^{+8.1}_{-7.3}$	± 0.1	0.0	± 1.6	0.0	± 1.0	0.53	1.00	0.06
260-310	$1.59 \cdot 10^{1}$	0.98	0.0	$^{+3.7}_{-3.5}$	$^{+2.7}_{-2.4}$	$^{+1.6}_{-1.2}$	$^{+2.6}_{-2.5}$	$^{+4.0}_{-3.7}$	$^{+1.8}_{-1.5}$	$^{+0.6}_{-0.3}$	$^{+6.6}_{-6.8}$	$^{+3.6}_{-3.7}$	$^{+0.2}_{0.0}$	0.0	$^{+8.5}_{-8.4}$	0.0	0.0	± 0.9	± 0.2	± 1.0	0.39	1.00	0.06
310-400	$4.38 \cdot 10^{0}$	1.06	0.0	$^{+3.3}_{-2.7}$	$^{+2.5}_{-2.2}$	$^{+1.4}_{-1.0}$	$^{+3.1}_{-2.5}$	$^{+4.2}_{-3.5}$	$^{+1.7}_{-1.2}$	$^{+0.4}_{-0.3}$	$^{+7.2}_{-6.1}$	$^{+4.1}_{-3.8}$	$^{+0.5}_{+0.2}$	0.0	$^{+9.6}_{-8.5}$	± 0.2	0.0	± 1.2	0.0	± 1.0	0.48	1.00	0.06
400-500	$9.18 \cdot 10^{-1}$	1.94	0.0	$^{+3.6}_{-4.0}$	$^{+2.8}_{-3.0}$	$^{+0.9}_{-0.7}$	$^{+2.8}_{-3.0}$	$^{+4.2}_{-4.6}$	$^{+1.2}_{-1.5}$	$^{+0.3}_{-0.4}$	$^{+6.7}_{-6.8}$	$^{+4.3}_{-4.8}$	0.0	0.0	± 9.9	± 0.2	0.0	± 1.2	0.0	± 1.0	0.43	1.00	0.06
500-600	$2.14 \cdot 10^{-1}$	3.67	0.0	$^{+3.4}_{-3.2}$	± 2.7	$^{+0.2}_{-0.3}$	$^{+2.3}_{-2.4}$	$^{+4.5}_{-4.3}$	$^{+1.4}_{-1.3}$	$^{+0.4}_{-0.5}$	$^{+7.3}_{-7.4}$	± 5.6	± 0.7	0.0	± 11	± 0.2	0.0	± 1.5	0.0	± 1.0	0.41	1.00	0.28
600-800	$4.07 \cdot 10^{-2}$	6.66	0.0	$^{+3.5}_{-3.9}$	$^{+0.9}_{-1.2}$	$^{+0.7}_{-0.8}$	± 2.3	$^{+5.0}_{-5.4}$	$^{+0.7}_{-1.1}$	$^{+0.3}_{-0.4}$	$^{+8.0}_{-8.1}$	$^{+7.0}_{-6.5}$	$^{+1.2}_{-1.3}$	0.0	$^{+14}_{-13}$	± 0.2	0.0	± 2.0	0.0	± 1.0	0.25	1.00	0.51
800-1000	$2.70 \cdot 10^{-3}$	22.3	0.0	$^{+5.9}_{-6.0}$	$^{+3.8}_{-3.3}$	$^{+1.1}_{-0.5}$	± 3.4	$^{+6.5}_{-5.8}$	$^{+1.0}_{-0.4}$	$^{+0.5}_{+0.1}$	$^{+11}_{-9.1}$	$^{+8.2}_{-7.7}$	$^{+3.6}_{-3.7}$	0.0	$^{+18}_{-16}$	± 0.5	0.0	± 0.8	0.0	± 1.0	0.26	1.00	0.87
1000-1200	$4.66 \cdot 10^{-4}$	61.7	0.0	$^{+7.8}_{-6.3}$	$^{+4.9}_{-4.4}$	$^{+0.6}_{-0.5}$	$^{+4.9}_{-4.0}$	$^{+8.0}_{-7.4}$	$^{+0.6}_{-1.1}$	$^{+0.7}_{-0.6}$	$^{+13}_{-10}$	$^{+11}_{-9.5}$	$^{+8.5}_{-7.8}$	0.0	$^{+24}_{-20}$	± 0.6	0.0	± 6.6	0.0	± 1.0	0.30	1.00	1.24
1200-1500	$1.02 \cdot 10^{-4}$	104	∓ 0.1	$^{+8.8}_{-11}$	$^{+6.9}_{-8.7}$	$^{+0.2}_{-1.8}$	$^{+5.1}_{-5.9}$	$^{+9.8}_{-11}$	$^{+0.4}_{-1.9}$	0.0	$^{+14}_{-16}$	$^{+13}_{-14}$	$^{+16}_{-17}$	0.0	$^{+33}_{-28}$	± 1.0	0.0	± 9.5	0.0	± 1.0	0.26	1.00	1.69

Table B.3: Measured jet cross section for $R = 0.4$ and $0.8 < |y| < 1.2$. See Table B.1 for a description of the columns. This table is available on HEPDATA [187].

p_{T}-bin [GeV]	σ [pb/GeV]	δ_{stat} %	γ_3	γ_9	γ_{15}	γ_{21}	γ_{27}	γ_{31}	γ_{34}	γ_{40}	γ_{46}	γ_{52}	γ_{58}	γ_{64}	γ_{70}	γ_{74}	γ_{75}	γ_{78}	γ_{82}	γ_{83}	u_1	u_2	u_3
20-30	$3.70 \cdot 10^{6}$	0.55	$^{+9.5}_{-9.0}$	$^{+7.0}_{-7.6}$	$^{+9.3}_{-9.1}$	$^{+9.5}_{-8.7}$	±3.7	±14	$^{+1.7}_{-1.8}$	±3.8	$^{+4.0}_{-4.1}$	0.0	0.0	$^{+2.5}_{-2.6}$	0.0	∓0.1	±0.9	±10	±0.6	±2.0	1.10	1.00	0.30
30-45	$5.62 \cdot 10^{5}$	1.17	$^{+4.7}_{-4.6}$	$^{+11}_{-9.5}$	$^{+6.8}_{-6.3}$	$^{+2.4}_{-1.9}$	$^{+2.3}_{-1.9}$	$^{+16}_{-14}$	$^{+2.3}_{-2.2}$	$^{+3.1}_{-3.0}$	$^{+4.4}_{-4.3}$	0.0	0.0	$^{+3.1}_{-3.0}$	∓0.2	0.0	±0.9	±4.7	0.0	±1.0	0.77	1.00	0.15
45-60	$1.09 \cdot 10^{5}$	2.01	$^{+2.0}_{-1.8}$	$^{+8.1}_{-6.7}$	$^{+6.3}_{-5.4}$	$^{+0.2}_{0.0}$	$^{+1.7}_{-1.4}$	$^{+12}_{-9.2}$	$^{+3.1}_{-2.8}$	$^{+2.0}_{-1.7}$	$^{+4.4}_{-3.8}$	$^{+0.2}_{+0.2}$	$^{+0.3}_{+0.0}$	$^{+2.8}_{-2.5}$	$^{+0.3}_{+0.0}$	0.0	±0.6	±1.8	0.0	±1.0	0.51	1.00	0.13
60-80	$2.67 \cdot 10^{4}$	0.73	∓0.5	$^{+6.7}_{-6.6}$	±5.4	±0.4	$^{+2.5}_{-2.6}$	$^{+8.0}_{-7.6}$	±3.1	$^{+1.5}_{-1.7}$	±4.9	$^{+0.3}_{-0.2}$	0.0	±0.9	$^{+1.7}_{-1.8}$	±0.1	±0.4	±0.6	0.0	±1.0	0.48	1.00	0.10
80-110	$5.84 \cdot 10^{3}$	1.11	∓0.4	$^{+6.5}_{-5.9}$	$^{+4.3}_{-4.1}$	$^{+0.9}_{-1.0}$	$^{+0.8}_{-1.0}$	$^{+5.8}_{-5.5}$	$^{+3.2}_{-3.1}$	$^{+1.2}_{-1.4}$	$^{+5.3}_{-5.0}$	$^{+1.2}_{-1.3}$	0.0	∓0.3	$^{+4.2}_{-4.0}$	±0.1	±0.2	±2.3	0.0	±1.0	0.42	1.00	0.07
110-160	$9.58 \cdot 10^{2}$	0.71	0.0	$^{+5.6}_{-5.7}$	±3.7	$^{+0.7}_{-1.1}$	±0.8	$^{+4.5}_{-4.4}$	±2.4	±0.7	$^{+5.1}_{-5.0}$	±1.5	0.0	∓0.1	$^{+4.9}_{-5.2}$	±0.2	0.0	±1.1	0.0	±1.0	0.49	1.00	0.05
160-210	$1.51 \cdot 10^{2}$	0.81	0.0	$^{+5.0}_{-4.3}$	$^{+4.2}_{-3.4}$	$^{+1.1}_{-0.7}$	$^{+1.7}_{-1.2}$	$^{+5.4}_{-5.1}$	$^{+2.4}_{-2.1}$	$^{+1.0}_{-0.5}$	$^{+6.3}_{-5.9}$	$^{+2.6}_{-2.2}$	$^{+0.4}_{+0.1}$	0.0	$^{+7.4}_{-6.3}$	±0.4	0.0	±1.2	0.0	±1.0	0.44	1.00	0.05
210-260	$3.38 \cdot 10^{1}$	0.66	0.0	$^{+4.2}_{-4.5}$	$^{+3.3}_{-3.7}$	±1.3	$^{+1.6}_{-2.2}$	$^{+5.8}_{-5.3}$	±2.0	$^{+0.2}_{-0.8}$	$^{+6.4}_{-6.3}$	$^{+3.0}_{-3.4}$	0.0	0.0	$^{+8.2}_{-7.7}$	±0.6	0.0	±1.3	0.0	±1.0	0.58	1.00	0.05
260-310	$9.58 \cdot 10^{0}$	1.28	0.0	$^{+4.1}_{-3.8}$	$^{+3.1}_{-2.6}$	$^{+1.7}_{-1.5}$	$^{+3.1}_{-2.8}$	$^{+6.3}_{-6.1}$	$^{+2.1}_{-1.7}$	$^{+0.6}_{-0.4}$	$^{+7.4}_{-7.1}$	$^{+3.9}_{-4.1}$	$^{+0.2}_{0.0}$	0.0	$^{+9.5}_{-8.7}$	±0.2	0.0	±0.9	±0.1	±1.0	0.47	1.00	0.06
310-400	$2.35 \cdot 10^{0}$	1.06	0.0	$^{+4.0}_{-3.2}$	$^{+2.8}_{-2.6}$	$^{+1.4}_{-1.0}$	$^{+3.6}_{-2.8}$	$^{+6.7}_{-6.3}$	$^{+1.9}_{-1.4}$	$^{+0.4}_{-0.3}$	$^{+8.0}_{-7.0}$	$^{+5.0}_{-4.5}$	$^{+0.5}_{+0.1}$	0.0	$^{+10}_{-9.7}$	0.0	0.0	±1.5	0.0	±1.0	0.38	1.00	0.06
400-500	$3.91 \cdot 10^{-1}$	1.98	0.0	$^{+3.9}_{-4.7}$	$^{+2.7}_{-3.6}$	$^{+1.5}_{-1.7}$	$^{+2.8}_{-3.6}$	$^{+7.4}_{-7.1}$	$^{+1.0}_{-1.8}$	$^{+0.3}_{-0.4}$	$^{+7.8}_{-7.9}$	$^{+5.0}_{-5.6}$	0.0	0.0	$^{+12}_{-11}$	±0.4	0.0	±1.0	±0.1	±1.0	0.46	1.00	0.07
500-600	$7.25 \cdot 10^{-2}$	4.72	0.0	$^{+4.1}_{-3.9}$	$^{+3.0}_{-2.9}$	$^{+2.2}_{-2.1}$	$^{+2.6}_{-2.7}$	$^{+8.4}_{-8.2}$	±1.5	±0.4	$^{+8.8}_{-9.0}$	$^{+6.8}_{-6.7}$	$^{+0.6}_{-0.7}$	0.0	±14	±0.5	0.0	±1.2	0.0	±1.0	0.44	1.00	0.58
600-800	$9.51 \cdot 10^{-3}$	8.77	0.0	$^{+4.9}_{-5.2}$	$^{+1.6}_{-2.0}$	$^{+1.1}_{-1.7}$	$^{+3.3}_{-3.2}$	$^{+11}_{-9.1}$	$^{+1.1}_{-1.6}$	$^{+0.5}_{-0.7}$	$^{+11}_{-9.9}$	$^{+9.8}_{-8.2}$	$^{+1.9}_{-2.2}$	0.0	$^{+20}_{-16}$	±0.6	0.0	±2.1	±0.2	±1.0	0.41	1.00	0.62
800-1000	$4.86 \cdot 10^{-4}$	39.2	0.0	$^{+8.2}_{-7.9}$	$^{+5.4}_{-4.5}$	$^{+0.8}_{-0.2}$	$^{+4.4}_{-4.6}$	±12	$^{+1.2}_{-0.6}$	$^{+0.7}_{+0.1}$	$^{+14}_{-13}$	$^{+11}_{-10}$	$^{+5.5}_{-5.2}$	0.0	$^{+25}_{-21}$	±1.1	0.0	±3.9	±0.3	±1.0	0.38	1.00	0.68
1000-1200	$6.93 \cdot 10^{-5}$	103	∓0.1	$^{+8.4}_{-8.8}$	$^{+6.7}_{-6.8}$	$^{+7.6}_{-8.1}$	$^{+6.5}_{-5.3}$	$^{+15}_{-14}$	$^{+0.5}_{-0.9}$	$^{+0.6}_{-0.4}$	$^{+16}_{-15}$	±14	$^{+11}_{-12}$	0.0	$^{+34}_{-27}$	±2.3	0.0	±9.2	±0.5	±1.0	0.15	1.00	0.77

Table B.4: Measured jet cross section for $R = 0.4$ and $1.2 < |y| < 2.1$. See Table B.1 for a description of the columns. This table is available on HEPDATA [187].

p_T-bin [GeV]	σ [pb/GeV]	δ_{stat} %	γ_4	γ_{10}	γ_{16}	γ_{22}	γ_{28}	γ_{31}	γ_{35}	γ_{41}	γ_{47}	γ_{53}	γ_{59}	γ_{65}	γ_{71}	γ_{74}	γ_{75}	γ_{79}	γ_{82}	γ_{84}	u_1	u_2	u_3
20-30	$2.76 \cdot 10^{6}$	0.69	$^{+10}_{-9.1}$	±7.4	$^{+10}_{-9.1}$	$^{+6.5}_{-6.1}$	±4.0	$^{+26}_{-23}$	$^{+2.0}_{-1.9}$	$^{+4.2}_{-4.1}$	$^{+4.4}_{-4.3}$	0.0	0.0	±2.7	0.0	0.0	±1.2	±15	±0.1	±2.0	1.27	1.00	0.02
30-45	$4.07 \cdot 10^{5}$	1.37	$^{+4.8}_{-4.3}$	$^{+11}_{-9.1}$	$^{+6.7}_{-5.8}$	$^{+4.7}_{-4.0}$	$^{+2.3}_{-1.8}$	$^{+28}_{-21}$	$^{+2.4}_{-2.2}$	$^{+3.3}_{-2.9}$	$^{+4.5}_{-4.1}$	0.0	0.0	$^{+3.2}_{-2.9}$	$^{-0.2}_{+0.1}$	0.0	±0.7	±5.1	0.0	±1.0	0.85	1.00	0.02
45-60	$8.00 \cdot 10^{4}$	2.84	$^{+2.5}_{-2.1}$	$^{+8.1}_{-7.1}$	$^{+6.7}_{-5.8}$	$^{+2.5}_{-2.0}$	$^{+2.1}_{-1.4}$	$^{+16}_{-13}$	$^{+3.5}_{-2.6}$	$^{+2.2}_{-1.7}$	$^{+4.7}_{-3.9}$	$^{+0.1}_{+0.2}$	$^{+0.3}_{+0.0}$	$^{+3.1}_{-2.6}$	$^{+0.3}_{+0.2}$	±0.2	±0.1	±1.6	0.0	±1.0	0.55	1.00	0.02
60-80	$1.71 \cdot 10^{4}$	1.05	$^{-0.5}_{+0.4}$	±7.0	$^{+5.5}_{-5.6}$	$^{+1.3}_{-1.5}$	$^{+2.5}_{-2.8}$	$^{+10}_{-9.4}$	$^{+3.1}_{-3.5}$	$^{+1.7}_{-1.9}$	$^{+5.0}_{-5.2}$	±0.3	0.0	$^{+0.8}_{-1.0}$	$^{+1.7}_{-1.9}$	±0.2	±0.3	±0.8	0.0	±1.0	0.57	1.00	0.02
80-110	$3.44 \cdot 10^{3}$	0.60	∓0.3	$^{+6.2}_{-6.3}$	$^{+3.9}_{-4.5}$	$^{+0.5}_{-0.7}$	$^{+0.6}_{-1.2}$	$^{+6.8}_{-6.7}$	$^{+2.8}_{-3.4}$	$^{+1.0}_{-1.5}$	$^{+5.0}_{-5.4}$	$^{+1.0}_{-1.5}$	0.0	$^{-0.3}_{+0.2}$	$^{+3.8}_{-4.4}$	±0.3	±0.1	±1.1	0.0	±1.0	0.78	1.00	0.02
110-160	$4.98 \cdot 10^{2}$	0.61	0.0	±6.4	$^{+4.2}_{-4.0}$	$^{+1.3}_{-1.1}$	$^{+1.1}_{-0.9}$	$^{+6.1}_{-6.2}$	$^{+2.9}_{-2.5}$	$^{+0.9}_{-0.8}$	$^{+6.1}_{-5.6}$	$^{+1.9}_{-1.7}$	0.0	∓0.1	$^{+5.9}_{-5.8}$	±0.4	0.0	±1.5	0.0	±1.0	0.66	1.00	0.00
160-210	$5.93 \cdot 10^{1}$	0.89	0.0	$^{+6.0}_{-5.0}$	$^{+5.1}_{-4.2}$	$^{+1.5}_{-0.9}$	$^{+2.3}_{-1.5}$	$^{+8.2}_{-6.8}$	$^{+3.2}_{-2.5}$	$^{+1.2}_{-0.5}$	$^{+7.4}_{-6.7}$	$^{+3.4}_{-2.8}$	$^{+0.4}_{+0.1}$	0.0	$^{+9.0}_{-7.3}$	±0.7	0.0	±1.6	0.0	±1.0	0.81	1.00	0.00
210-260	$1.00 \cdot 10^{1}$	1.31	0.0	±5.9	$^{+4.7}_{-4.9}$	$^{+0.8}_{-1.2}$	$^{+2.2}_{-2.7}$	$^{+9.5}_{-9.2}$	±2.4	$^{+0.3}_{-0.8}$	$^{+9.0}_{-8.8}$	$^{+4.6}_{-4.8}$	0.0	0.0	$^{+11}_{-10}$	±0.6	0.0	±1.9	0.0	±1.0	0.71	1.00	0.00
260-310	$1.85 \cdot 10^{0}$	2.04	0.0	$^{+6.2}_{-3.8}$	$^{+4.7}_{-2.6}$	$^{+3.6}_{-2.0}$	$^{+4.8}_{-2.9}$	$^{+10}_{-8.3}$	$^{+3.4}_{-1.8}$	$^{+1.0}_{-0.1}$	$^{+10.0}_{-8.6}$	$^{+6.1}_{-4.4}$	$^{+0.5}_{0.0}$	0.0	$^{+13}_{-12}$	±0.9	0.0	±2.8	±0.1	±1.0	0.56	1.00	0.22
310-400	$2.76 \cdot 10^{-1}$	3.07	0.0	$^{+6.5}_{-5.3}$	$^{+5.1}_{-4.2}$	$^{+3.3}_{-2.7}$	$^{+6.1}_{-4.5}$	$^{+14}_{-12}$	$^{+3.0}_{-2.5}$	$^{+0.5}_{-0.8}$	$^{+13}_{-11}$	$^{+8.4}_{-6.9}$	$^{+0.6}_{+0.1}$	0.0	$^{+18}_{-15}$	±0.7	0.0	±0.8	0.0	±1.0	0.92	1.00	0.13
400-500	$1.66 \cdot 10^{-2}$	11.5	0.0	$^{+9.3}_{-8.0}$	$^{+6.0}_{-6.1}$	$^{+1.0}_{-2.7}$	$^{+6.0}_{-6.1}$	$^{+17}_{-15}$	$^{+2.3}_{-3.1}$	$^{+1.2}_{-1.4}$	$^{+15}_{-14}$	$^{+11}_{-10}$	0.0	0.0	$^{+26}_{-19}$	±1.2	0.0	±5.6	±0.2	±1.0	1.07	1.00	0.14
500-600	$3.13 \cdot 10^{-4}$	91.4	0.0	±2.4	$^{+1.1}_{-2.6}$	±2.7	$^{+0.9}_{-2.6}$	$^{+9.5}_{-16}$	0.0	0.0	$^{+8.0}_{-16}$	$^{+5.4}_{-10}$	0.0	0.0	$^{+19}_{-25}$	±1.1	0.0	±8.0	±1.5	±1.0	-0.07	1.00	0.16

Table B.5: Measured jet cross section for $R = 0.4$ and $2.1 < |y| < 2.8$. See Table B.1 for a description of the columns. This table is available on HEPDATA [187].

p_{T}-bin [GeV]	σ [pb/GeV]	δ_{stat} %	γ_{5}	γ_{11}	γ_{17}	γ_{23}	γ_{29}	γ_{31}	γ_{36}	γ_{42}	γ_{48}	γ_{54}	γ_{60}	γ_{66}	γ_{72}	γ_{74}	γ_{75}	γ_{80}	γ_{82}	γ_{85}	u_{1}	u_{2}	u_{3}
20-30	$1.89 \cdot 10^{6}$	0.78	$^{+11}_{-9.0}$	$^{+7.8}_{-7.6}$	$^{+10}_{-9.2}$	$^{+17}_{-14}$	$^{+4.1}_{-3.9}$	$^{+37}_{-30}$	$^{+1.8}_{-1.9}$	$^{+4.3}_{-4.0}$	$^{+4.5}_{-4.2}$	0.0	0.0	$^{+2.7}_{-2.6}$	0.0	∓ 0.2	± 0.6	± 14	± 0.3	± 2.0	3.83	1.00	0.00
30-45	$2.67 \cdot 10^{5}$	1.67	$^{+4.9}_{-5.0}$	$^{+12}_{-11}$	$^{+6.8}_{-7.0}$	$^{+10}_{-9.3}$	$^{+2.5}_{-2.4}$	$^{+41}_{-28}$	$^{+2.6}_{-2.7}$	$^{+3.4}_{-3.6}$	$^{+4.8}_{-5.1}$	0.0	0.0	$^{+3.3}_{-3.6}$	∓ 0.1	0.0	± 0.9	± 6.5	0.0	± 1.0	2.67	1.00	0.00
45-60	$4.25 \cdot 10^{4}$	3.69	$^{+2.2}_{-2.0}$	$^{+9.1}_{-8.0}$	$^{+7.3}_{-6.5}$	$^{+7.5}_{-6.8}$	$^{+2.2}_{-1.7}$	$^{+28}_{-20}$	$^{+3.8}_{-3.3}$	$^{+2.4}_{-1.9}$	$^{+5.4}_{-4.7}$	$^{+0.3}_{+0.2}$	$^{+0.4}_{+0.0}$	$^{+3.1}_{-2.7}$	$^{+0.5}_{-0.1}$	± 0.3	± 0.2	± 2.1	0.0	± 1.0	1.78	1.00	0.00
60-80	$8.57 \cdot 10^{3}$	1.69	∓ 0.7	$^{+7.4}_{-6.4}$	$^{+5.6}_{-5.1}$	$^{+7.9}_{-6.7}$	± 2.5	$^{+18}_{-14}$	$^{+3.5}_{-3.2}$	$^{+1.7}_{-1.6}$	$^{+5.3}_{-4.6}$	± 0.4	0.0	$^{+1.0}_{-0.7}$	$^{+2.1}_{-2.0}$	± 0.3	± 0.3	± 1.7	0.0	± 1.0	3.35	1.00	0.00
80-110	$1.31 \cdot 10^{3}$	3.41	$^{-0.6}_{+0.5}$	$^{+7.5}_{-8.3}$	$^{+4.8}_{-5.4}$	$^{+8.1}_{-8.4}$	$^{+0.8}_{-1.0}$	± 13	$^{+3.2}_{-3.9}$	$^{+1.1}_{-1.5}$	$^{+6.4}_{-7.4}$	$^{+1.3}_{-1.7}$	0.0	$^{-0.5}_{+0.4}$	$^{+5.2}_{-5.8}$	± 0.2	± 0.7	± 2.2	± 0.1	± 1.0	4.17	1.00	0.00
110-160	$1.16 \cdot 10^{2}$	1.54	0.0	$^{+7.1}_{-8.6}$	$^{+4.6}_{-5.4}$	$^{+6.5}_{-7.6}$	± 1.3	$^{+14}_{-13}$	$^{+3.1}_{-3.5}$	± 1.0	$^{+7.0}_{-8.0}$	$^{+2.2}_{-2.5}$	0.0	∓ 0.2	$^{+7.0}_{-8.5}$	± 0.2	± 0.2	± 3.8	± 0.3	± 1.0	2.42	1.00	0.00
160-210	$5.57 \cdot 10^{0}$	3.92	0.0	$^{+10}_{-7.1}$	$^{+8.2}_{-5.8}$	$^{+12}_{-10}$	$^{+3.9}_{-2.4}$	$^{+22}_{-18}$	$^{+4.5}_{-3.0}$	$^{+1.7}_{-0.7}$	$^{+13}_{-11}$	$^{+5.1}_{-4.3}$	$^{+0.4}_{+0.1}$	0.0	$^{+16}_{-13}$	± 1.0	± 0.5	± 6.1	± 0.4	± 1.0	2.61	1.00	0.17
210-260	$2.89 \cdot 10^{-1}$	8.18	0.0	$^{+8.6}_{-8.3}$	$^{+6.6}_{-7.3}$	$^{+17}_{-16}$	$^{+4.0}_{-4.7}$	± 25	$^{+3.6}_{-3.3}$	$^{+0.3}_{-0.9}$	± 14	$^{+7.5}_{-8.1}$	0.0	0.0	$^{+18}_{-17}$	± 1.1	0.0	± 13	± 0.3	± 1.0	2.97	1.00	0.19
260-310	$9.17 \cdot 10^{-3}$	39.3	0.0	$^{+26}_{-14}$	$^{+20}_{-11}$	$^{+41}_{-28}$	$^{+22}_{-12}$	$^{+51}_{-38}$	± 12	$^{+3.1}_{+0.1}$	$^{+38}_{-28}$	$^{+28}_{-18}$	$^{+3.4}_{+0.1}$	0.0	$^{+41}_{-27}$	∓ 0.7	± 0.1	± 5.6	± 1.6	± 1.0	6.77	1.00	0.21

Table B.6: Measured jet cross section for $R = 0.4$ and $2.8 < |y| < 3.6$. See Table B.1 for a description of the columns. This table is available on HEPDATA [187].

p_{T}-bin [GeV]	σ [pb/GeV]	δ_{stat} %	γ_{6}	γ_{12}	γ_{18}	γ_{24}	γ_{30}	γ_{31}	γ_{37}	γ_{43}	γ_{49}	γ_{55}	γ_{61}	γ_{67}	γ_{73}	γ_{74}	γ_{75}	γ_{81}	γ_{82}	γ_{86}	u_1	u_2	u_3
20-30	$8.19 \cdot 10^{5}$	1.04	$^{+12}_{-10}$	$^{+8.8}_{-8.7}$	$^{+11}_{-10}$	$^{+3.3}_{-3.4}$	$^{+4.7}_{-4.5}$	$^{+68}_{-48}$	$^{+2.3}_{-2.2}$	$^{+4.9}_{-4.5}$	$^{+5.2}_{-4.9}$	0.0	0.0	$^{+3.1}_{-3.2}$	0.0	0.0	±0.3	±15	±1.0	±2.0	4.69	1.00	0.00
30-45	$8.64 \cdot 10^{4}$	1.13	±5.2	$^{+13}_{-11}$	$^{+7.9}_{-7.2}$	$^{+2.2}_{-2.0}$	$^{+2.6}_{-2.2}$	$^{+83}_{-44}$	$^{+2.8}_{-2.9}$	$^{+3.4}_{-3.5}$	$^{+5.4}_{-5.3}$	0.0	0.0	$^{+3.5}_{-3.6}$	0.0	0.0	±0.7	±4.4	±0.5	±1.0	7.98	1.00	0.00
45-60	$8.83 \cdot 10^{3}$	1.95	$^{+2.3}_{-2.6}$	$^{+10}_{-9.1}$	$^{+8.4}_{-7.8}$	$^{+1.7}_{-1.9}$	$^{+2.3}_{-2.6}$	$^{+60}_{-34}$	$^{+3.9}_{-4.2}$	$^{+2.4}_{-2.7}$	$^{+6.3}_{-5.5}$	$^{+0.3}_{+0.1}$	$^{+0.4}_{+0.0}$	$^{+3.3}_{-3.4}$	$^{+0.7}_{-0.5}$	±0.2	±0.7	±1.0	±0.4	±1.0	5.37	1.00	0.00
60-80	$9.20 \cdot 10^{2}$	2.78	∓0.9	$^{+11}_{-10}$	$^{+8.9}_{-8.4}$	$^{+3.0}_{-1.5}$	$^{+5.0}_{-3.6}$	$^{+41}_{-29}$	$^{+6.5}_{-5.7}$	$^{+3.8}_{-2.4}$	$^{+8.7}_{-8.1}$	$^{+1.1}_{-0.7}$	0.0	$^{+1.2}_{-1.1}$	$^{+5.0}_{-3.5}$	0.0	±1.8	±2.1	±0.4	±1.0	5.40	1.00	0.02
80-110	$5.38 \cdot 10^{1}$	3.94	∓0.6	±13	$^{+8.1}_{-9.9}$	$^{+1.1}_{-2.2}$	$^{+1.6}_{-3.0}$	$^{+31}_{-23}$	$^{+5.4}_{-7.7}$	$^{+2.2}_{-3.4}$	$^{+11}_{-12}$	$^{+2.6}_{-3.9}$	0.0	∓0.6	$^{+9.1}_{-11}$	±1.0	±0.2	±6.7	±0.7	±1.0	6.66	1.00	0.02
110-160	$5.42 \cdot 10^{-1}$	15.7	0.0	$^{+15}_{-17}$	$^{+13}_{-11}$	$^{+19}_{-30}$	$^{+2.9}_{-6.9}$	$^{+23}_{-30}$	$^{+8.9}_{-9.1}$	$^{+3.0}_{-5.8}$	$^{+16}_{-15}$	$^{+4.9}_{-8.8}$	0.0	∓0.3	$^{+17}_{-16}$	±1.3	0.0	±6.1	±0.5	±1.0	8.54	1.00	0.02

Table B.7: Measured jet cross section for $R = 0.4$ and $3.6 < |y| < 4.4$. See Table B.1 for a description of the columns. This table is available on HEPDATA [187].

p_{T}-bin [GeV]	σ [pb/GeV]	δ_{stat} %	γ_1	γ_7	γ_{13}	γ_{19}	γ_{25}	γ_{31}	γ_{32}	γ_{38}	γ_{44}	γ_{50}	γ_{56}	γ_{62}	γ_{68}	γ_{74}	γ_{75}	γ_{76}	γ_{82}	γ_{83}	u_1	u_2	u_3
20-30	$1.00 \cdot 10^{7}$	0.57	$^{+13}_{-12}$	± 11	$^{+16}_{-15}$	$^{+9.7}_{-9.1}$	$^{+5.7}_{-5.6}$	0.0	$^{+2.2}_{-2.3}$	$^{+5.6}_{-5.4}$	$^{+4.7}_{-5.1}$	0.0	0.0	$^{+2.1}_{-2.2}$	0.0	0.0	± 1.3	± 3.3	0.0	± 2.0	0.69	1.00	0.33
30-45	$1.23 \cdot 10^{6}$	1.21	$^{+8.4}_{-7.3}$	$^{+10}_{-8.9}$	$^{+10}_{-8.7}$	$^{+8.0}_{-6.9}$	$^{+2.4}_{-2.1}$	0.0	± 2.5	$^{+4.1}_{-3.8}$	$^{+4.4}_{-4.3}$	0.0	0.0	$^{+3.5}_{-3.6}$	0.0	0.0	± 0.8	± 3.0	0.0	± 1.0	0.47	1.00	0.22
45-60	$2.19 \cdot 10^{5}$	2.63	$^{+2.1}_{-1.2}$	$^{+8.4}_{-6.4}$	$^{+5.1}_{-3.5}$	$^{+4.6}_{-3.1}$	$^{+1.2}_{-0.5}$	0.0	$^{+3.5}_{-2.4}$	$^{+2.8}_{-1.8}$	$^{+4.9}_{-3.4}$	$^{+0.2}_{+0.2}$	$^{+0.4}_{+0.0}$	$^{+5.6}_{-4.1}$	0.0	0.0	± 1.0	± 1.4	± 0.1	± 1.0	0.30	1.00	0.19
60-80	$5.45 \cdot 10^{4}$	0.96	∓ 1.1	$^{+6.9}_{-5.9}$	$^{+1.1}_{-0.8}$	$^{+3.7}_{-3.1}$	$^{+0.8}_{-0.6}$	0.0	$^{+3.2}_{-2.7}$	$^{+1.7}_{-1.3}$	$^{+4.3}_{-3.6}$	$^{+0.4}_{-0.3}$	$^{+0.0}_{+0.1}$	$^{+4.6}_{-3.7}$	$^{-0.1}_{+0.2}$	0.0	± 0.4	± 1.3	0.0	± 1.0	0.28	1.00	0.15
80-110	$1.14 \cdot 10^{4}$	0.84	$^{-0.5}_{+0.4}$	$^{+6.4}_{-6.1}$	$^{+1.1}_{-1.6}$	$^{+3.9}_{-4.3}$	$^{+1.0}_{-1.5}$	0.0	$^{+3.0}_{-3.4}$	$^{+1.2}_{-1.8}$	$^{+4.9}_{-5.0}$	$^{+0.8}_{-1.0}$	0.0	$^{+2.5}_{-2.7}$	0.0	0.0	± 0.3	± 0.5	0.0	± 1.0	0.48	1.00	0.10
110-160	$1.93 \cdot 10^{3}$	0.61	0.0	$^{+3.9}_{-4.7}$	$^{+2.3}_{-3.0}$	$^{+3.0}_{-3.3}$	$^{+1.0}_{-1.2}$	0.0	$^{+3.0}_{-3.2}$	$^{+1.0}_{-1.2}$	$^{+4.9}_{-5.4}$	$^{+1.5}_{-1.7}$	0.0	0.0	$^{+1.1}_{-1.3}$	± 0.2	0.0	0.0	0.0	± 1.0	0.37	1.00	0.07
160-210	$3.21 \cdot 10^{2}$	0.67	0.0	$^{+5.9}_{-5.6}$	$^{+4.6}_{-4.0}$	$^{+2.2}_{-1.8}$	$^{+1.5}_{-1.1}$	0.0	$^{+2.7}_{-2.6}$	$^{+0.9}_{-0.6}$	$^{+6.1}_{-5.6}$	$^{+2.7}_{-2.2}$	$^{+0.4}_{+0.1}$	∓ 0.3	$^{+4.8}_{-4.4}$	± 0.1	0.0	± 0.8	0.0	± 1.0	0.45	1.00	0.06
210-260	$7.78 \cdot 10^{1}$	0.90	0.0	$^{+7.0}_{-6.8}$	± 3.6	$^{+1.0}_{-1.5}$	$^{+1.1}_{-1.6}$	0.0	$^{+2.2}_{-2.6}$	$^{+0.4}_{-0.6}$	$^{+5.6}_{-6.1}$	$^{+2.4}_{-3.1}$	± 0.2	0.0	$^{+5.7}_{-6.2}$	± 0.1	± 0.1	0.0	0.0	± 1.0	0.26	1.00	0.05
260-310	$2.54 \cdot 10^{1}$	0.83	0.0	$^{+5.2}_{-3.6}$	$^{+2.5}_{-2.2}$	$^{+1.4}_{-0.9}$	$^{+2.2}_{-1.8}$	0.0	$^{+2.5}_{-1.6}$	$^{+0.6}_{-0.2}$	$^{+6.2}_{-5.6}$	$^{+4.2}_{-3.3}$	$^{+0.6}_{-0.3}$	0.0	$^{+7.1}_{-6.3}$	± 0.2	± 0.3	± 0.7	0.0	± 1.0	0.24	1.00	0.05
310-400	$7.16 \cdot 10^{0}$	0.93	0.0	$^{+2.4}_{-2.5}$	$^{+2.8}_{-2.5}$	$^{+0.6}_{-0.5}$	$^{+2.5}_{-2.7}$	0.0	± 1.9	$^{+0.7}_{-0.2}$	± 6.3	$^{+4.3}_{-4.0}$	$^{+0.7}_{-0.2}$	0.0	± 6.9	± 0.2	± 0.2	± 0.4	0.0	± 1.0	0.27	1.00	0.05
400-500	$1.60 \cdot 10^{0}$	1.60	0.0	$^{+2.5}_{-3.3}$	$^{+1.8}_{-2.3}$	0.0	$^{+2.3}_{-2.4}$	0.0	$^{+1.1}_{-2.0}$	$^{+0.2}_{-0.8}$	$^{+6.5}_{-6.8}$	$^{+4.9}_{-5.6}$	0.0	0.0	$^{+7.7}_{-7.9}$	± 0.3	0.0	± 0.8	0.0	± 1.0	0.21	1.00	0.05
500-600	$4.10 \cdot 10^{-1}$	2.98	0.0	$^{+3.0}_{-2.7}$	$^{+2.3}_{-2.1}$	$^{+0.9}_{-0.8}$	$^{+3.1}_{-2.8}$	0.0	$^{+1.7}_{-1.4}$	± 0.5	$^{+7.0}_{-7.1}$	$^{+6.2}_{-5.6}$	± 0.7	0.0	$^{+9.4}_{-9.0}$	± 0.3	0.0	± 0.4	± 0.1	± 1.0	0.32	1.00	0.05
600-800	$7.61 \cdot 10^{-2}$	5.26	0.0	$^{+3.1}_{-3.4}$	± 4.8	± 0.9	$^{+3.3}_{-3.2}$	0.0	$^{+1.1}_{-1.6}$	$^{+0.3}_{-0.4}$	$^{+8.5}_{-7.1}$	$^{+6.5}_{-6.1}$	± 1.0	0.0	$^{+11}_{-9.3}$	± 0.2	0.0	± 0.6	0.0	± 1.0	0.14	1.00	0.21
800-1000	$1.18 \cdot 10^{-2}$	14.3	0.0	$^{+3.2}_{-2.7}$	$^{+6.3}_{-5.5}$	$^{+0.5}_{+0.2}$	$^{+2.5}_{-1.8}$	0.0	$^{+1.4}_{-0.8}$	$^{+0.5}_{+0.1}$	$^{+8.4}_{-8.0}$	$^{+7.8}_{-7.1}$	± 2.2	0.0	$^{+13}_{-11}$	± 0.5	0.0	± 0.7	0.0	± 1.0	0.17	1.00	0.21
1000-1200	$1.54 \cdot 10^{-3}$	34.0	0.0	$^{+2.4}_{-2.3}$	± 6.5	$^{+0.4}_{0.0}$	$^{+3.0}_{-2.9}$	0.0	$^{+1.1}_{-0.7}$	$^{+0.5}_{-0.3}$	$^{+8.6}_{-7.9}$	$^{+8.7}_{-8.5}$	$^{+4.9}_{-5.1}$	0.0	$^{+17}_{-14}$	± 0.7	0.0	± 1.3	0.0	± 1.0	0.10	1.00	0.21
1200-1500	$3.99 \cdot 10^{-4}$	58.9	0.0	$^{+1.7}_{-2.3}$	$^{+7.2}_{-7.4}$	$^{+0.8}_{-2.1}$	$^{+4.4}_{-5.1}$	0.0	$^{+0.3}_{-1.4}$	$^{+0.4}_{-0.8}$	$^{+9.3}_{-9.7}$	$^{+9.8}_{-10}$	$^{+8.9}_{-9.1}$	0.0	$^{+20}_{-18}$	± 0.6	0.0	± 2.2	± 0.1	± 1.0	0.13	1.00	0.21

Table B.8: Measured jet cross section for $R = 0.6$ and $|y| < 0.3$. See Table B.1 for a description of the columns. This table is available on HEPDATA [187].

p_{T}-bin	σ	δ_{stat}	γ_1	γ_7	γ_{13}	γ_{19}	γ_{25}	γ_{31}	γ_{32}	γ_{38}	γ_{44}	γ_{50}	γ_{56}	γ_{62}	γ_{68}	γ_{74}	γ_{75}	γ_{76}	γ_{82}	γ_{83}	u_1	u_2	u_3
[GeV]	[pb/GeV]	%																					
20-30	$9.95 \cdot 10^{6}$	0.48	$^{+12}_{-11}$	$^{+9.4}_{-9.5}$	$^{+14}_{-13}$	$^{+8.0}_{-8.3}$	$^{+4.7}_{-4.6}$	0.0	$^{+2.2}_{-2.1}$	$^{+4.4}_{-4.3}$	$^{+4.7}_{-4.6}$	0.0	0.0	$^{+3.0}_{-2.9}$	0.0	0.0	±0.9	±2.7	0.0	±2.0	0.71	1.00	0.30
30-45	$1.25 \cdot 10^{6}$	1.03	$^{+8.6}_{-7.6}$	$^{+9.9}_{-9.2}$	$^{+10}_{-9.3}$	$^{+7.9}_{-7.1}$	$^{+3.0}_{-2.5}$	0.0	$^{+2.6}_{-2.5}$	$^{+3.5}_{-3.2}$	$^{+4.9}_{-4.6}$	0.0	0.0	$^{+3.5}_{-3.2}$	$^{-0.2}_{+0.1}$	0.0	±0.7	±2.8	±0.1	±1.0	0.47	1.00	0.20
45-60	$2.25 \cdot 10^{5}$	2.04	$^{+2.2}_{-1.6}$	$^{+8.9}_{-7.2}$	$^{+7.4}_{-5.8}$	$^{+4.2}_{-3.4}$	$^{+1.9}_{-1.3}$	0.0	$^{+3.4}_{-2.7}$	$^{+2.1}_{-1.6}$	$^{+4.7}_{-3.9}$	$^{+0.2}_{+0.2}$	$^{+0.4}_{+0.0}$	$^{+2.9}_{-2.4}$	$^{+0.4}_{+0.1}$	0.0	±0.5	±1.6	±0.1	±1.0	0.31	1.00	0.19
60-80	$5.32 \cdot 10^{4}$	0.81	$^{-1.1}_{+1.0}$	$^{+6.4}_{-5.5}$	$^{+4.0}_{-3.5}$	$^{+2.7}_{-2.6}$	$^{+3.5}_{-3.4}$	0.0	$^{+3.0}_{-2.9}$	$^{+1.5}_{-1.3}$	$^{+4.7}_{-4.2}$	$^{+0.4}_{-0.2}$	0.0	$^{+0.9}_{-0.8}$	$^{+1.7}_{-1.5}$	0.0	±0.3	±1.2	0.0	±1.0	0.30	1.00	0.16
80-110	$1.13 \cdot 10^{4}$	0.47	∓0.5	$^{+5.3}_{-5.9}$	$^{+2.6}_{-3.2}$	$^{+2.4}_{-3.0}$	$^{+2.1}_{-2.6}$	0.0	$^{+2.5}_{-3.2}$	$^{+1.0}_{-1.4}$	$^{+4.6}_{-5.2}$	$^{+0.9}_{-1.4}$	0.0	∓0.3	$^{+3.5}_{-4.1}$	0.0	±0.3	±0.4	0.0	±1.0	0.44	1.00	0.11
110-160	$1.88 \cdot 10^{3}$	0.46	0.0	$^{+5.4}_{-5.2}$	$^{+2.5}_{-2.6}$	$^{+2.1}_{-2.3}$	$^{+0.4}_{-0.3}$	0.0	$^{+2.5}_{-2.3}$	±0.7	$^{+5.2}_{-4.9}$	$^{+1.6}_{-1.4}$	0.0	∓0.1	$^{+5.0}_{-5.1}$	±0.1	0.0	±0.8	0.0	±1.0	0.37	1.00	0.08
160-210	$3.03 \cdot 10^{2}$	0.49	0.0	$^{+4.0}_{-3.2}$	$^{+2.7}_{-2.5}$	$^{+2.4}_{-1.8}$	$^{+1.6}_{-1.1}$	0.0	$^{+2.6}_{-2.1}$	$^{+1.0}_{-0.5}$	$^{+6.1}_{-5.4}$	$^{+2.8}_{-2.1}$	$^{+0.4}_{+0.1}$	0.0	$^{+7.1}_{-5.9}$	±0.2	0.0	±0.5	0.0	±1.0	0.42	1.00	0.07
210-260	$7.47 \cdot 10^{1}$	0.62	0.0	$^{+2.8}_{-3.5}$	$^{+2.7}_{-3.3}$	$^{+1.1}_{-1.6}$	$^{+1.9}_{-2.5}$	0.0	$^{+1.7}_{-1.8}$	$^{+0.2}_{-0.7}$	$^{+6.2}_{-6.4}$	$^{+2.9}_{-3.4}$	0.0	0.0	$^{+8.0}_{-7.7}$	±0.2	0.0	±0.8	0.0	±1.0	0.33	1.00	0.07
260-310	$2.39 \cdot 10^{1}$	0.59	0.0	$^{+4.7}_{-3.6}$	$^{+2.9}_{-2.5}$	$^{+1.4}_{-1.5}$	$^{+2.9}_{-2.7}$	0.0	$^{+2.1}_{-1.7}$	$^{+0.8}_{-0.4}$	$^{+6.9}_{-6.7}$	$^{+3.7}_{-3.6}$	$^{+0.3}_{0.0}$	0.0	$^{+8.6}_{-8.3}$	±0.1	±0.1	±0.7	0.0	±1.0	0.27	1.00	0.07
310-400	$6.79 \cdot 10^{0}$	0.70	0.0	$^{+4.2}_{-3.5}$	$^{+3.1}_{-2.8}$	$^{+1.1}_{-0.5}$	$^{+3.4}_{-2.6}$	0.0	$^{+1.8}_{-1.2}$	±0.3	$^{+7.6}_{-6.1}$	$^{+4.5}_{-3.8}$	$^{+0.4}_{+0.1}$	0.0	$^{+9.8}_{-8.5}$	±0.2	±0.2	±0.4	0.0	±1.0	0.28	1.00	0.07
400-500	$1.44 \cdot 10^{0}$	1.47	0.0	$^{+4.3}_{-4.9}$	$^{+3.1}_{-3.2}$	0.0	$^{+1.8}_{-2.4}$	0.0	$^{+0.9}_{-1.4}$	$^{+0.2}_{-0.3}$	$^{+6.7}_{-6.5}$	$^{+4.2}_{-4.6}$	0.0	0.0	$^{+10}_{-9.2}$	±0.1	±0.2	±0.8	0.0	±1.0	0.23	1.00	0.07
500-600	$3.68 \cdot 10^{-1}$	2.72	0.0	$^{+3.5}_{-3.0}$	$^{+1.7}_{-1.4}$	$^{+0.9}_{-0.8}$	$^{+2.2}_{-2.3}$	0.0	$^{+1.3}_{-1.0}$	$^{+0.4}_{-0.3}$	$^{+6.7}_{-6.9}$	$^{+5.2}_{-5.1}$	$^{+0.6}_{-0.4}$	0.0	$^{+11}_{-10}$	±0.3	0.0	±0.5	0.0	±1.0	0.21	1.00	0.25
600-800	$7.50 \cdot 10^{-2}$	4.46	0.0	$^{+2.3}_{-2.5}$	$^{+0.8}_{-0.9}$	±0.4	$^{+3.3}_{-2.9}$	0.0	$^{+0.7}_{-1.2}$	$^{+0.4}_{-0.5}$	$^{+7.4}_{-7.2}$	$^{+6.4}_{-5.8}$	$^{+0.9}_{-1.3}$	0.0	$^{+13}_{-12}$	±0.3	0.0	±0.4	0.0	±1.0	0.18	1.00	0.25
800-1000	$9.09 \cdot 10^{-3}$	11.9	0.0	$^{+5.3}_{-4.7}$	$^{+1.8}_{-1.1}$	$^{+0.9}_{-0.4}$	$^{+3.5}_{-3.0}$	0.0	$^{+0.9}_{-0.3}$	$^{+0.4}_{+0.1}$	$^{+9.2}_{-7.8}$	$^{+7.2}_{-6.7}$	$^{+3.0}_{-3.1}$	0.0	$^{+16}_{-14}$	±0.4	0.0	±0.9	0.0	±1.0	0.14	1.00	0.25
1000-1200	$1.61 \cdot 10^{-3}$	28.8	0.0	$^{+6.1}_{-5.1}$	$^{+1.8}_{-1.9}$	$^{+0.8}_{-0.4}$	$^{+3.9}_{-3.3}$	0.0	$^{+0.7}_{-0.8}$	$^{+0.8}_{-0.4}$	$^{+11}_{-9.1}$	$^{+8.6}_{-7.9}$	$^{+6.6}_{-6.2}$	0.0	$^{+19}_{-17}$	±0.6	0.0	±1.4	0.0	±1.0	0.12	1.00	0.25
1200-1500	$2.35 \cdot 10^{-4}$	58.7	0.0	$^{+6.0}_{-7.5}$	$^{+1.6}_{-2.7}$	0.0	$^{+3.1}_{-4.3}$	0.0	$^{+0.4}_{-1.6}$	0.0	$^{+9.9}_{-11}$	$^{+8.8}_{-9.9}$	$^{+11}_{-12}$	0.0	$^{+23}_{-21}$	±0.3	0.0	±1.8	0.0	±1.0	0.13	1.00	0.25

Table B.9: Measured jet cross section for $R = 0.6$ and $0.3 < |y| < 0.8$. See Table B.1 for a description of the columns. This table is available on HEPDATA [187].

p_{T}-bin [GeV]	σ [pb/GeV]	δ_{stat} %	γ_2	γ_8	γ_{14}	γ_{20}	γ_{26}	γ_{31}	γ_{33}	γ_{39}	γ_{45}	γ_{51}	γ_{57}	γ_{63}	γ_{69}	γ_{74}	γ_{75}	γ_{77}	γ_{82}	γ_{83}	u_1	u_2	u_3
20-30	$8.54 \cdot 10^{6}$	0.55	$^{+10}_{-11}$	$^{+7.9}_{-8.6}$	±12	$^{+8.0}_{-8.4}$	$^{+3.9}_{-4.1}$	±4.2	±1.8	$^{+3.7}_{-3.8}$	$^{+3.9}_{-4.0}$	0.0	0.0	$^{+2.5}_{-2.6}$	0.0	0.0	±1.6	±8.1	±1.4	±2.0	0.97	1.00	0.25
30-45	$1.12 \cdot 10^{6}$	1.15	$^{+8.3}_{-7.6}$	$^{+9.6}_{-9.4}$	$^{+10}_{-9.5}$	$^{+5.3}_{-4.8}$	$^{+3.0}_{-2.6}$	$^{+5.3}_{-4.9}$	$^{+2.6}_{-2.5}$	$^{+3.5}_{-3.2}$	$^{+4.9}_{-4.6}$	0.0	0.0	$^{+3.5}_{-3.3}$	∓0.1	0.0	±0.4	±8.3	0.0	±1.0	0.84	1.00	0.20
45-60	$1.99 \cdot 10^{5}$	2.37	$^{+2.2}_{-1.8}$	$^{+9.2}_{-8.1}$	$^{+7.7}_{-6.5}$	$^{+3.6}_{-2.7}$	$^{+1.8}_{-1.5}$	$^{+4.9}_{-4.5}$	$^{+3.3}_{-3.0}$	$^{+2.0}_{-1.7}$	$^{+4.9}_{-4.5}$	$^{+0.2}_{+0.2}$	$^{+0.4}_{+0.0}$	$^{+2.8}_{-2.6}$	$^{+0.3}_{-0.1}$	±0.1	±0.3	±3.8	±0.4	±1.0	0.54	1.00	0.21
60-80	$4.84 \cdot 10^{4}$	0.91	∓1.1	$^{+6.8}_{-6.1}$	$^{+4.2}_{-3.7}$	$^{+2.0}_{-1.9}$	$^{+3.7}_{-3.5}$	$^{+4.0}_{-3.6}$	$^{+3.2}_{-3.1}$	±1.5	$^{+5.0}_{-4.5}$	$^{+0.4}_{-0.3}$	0.0	±0.9	±1.8	0.0	±0.2	±1.5	±0.2	±1.0	0.51	1.00	0.18
80-110	$1.03 \cdot 10^{4}$	0.61	∓0.5	$^{+5.5}_{-5.6}$	$^{+2.6}_{-3.0}$	$^{+0.8}_{-1.3}$	$^{+2.1}_{-2.6}$	$^{+3.0}_{-3.4}$	$^{+2.6}_{-3.1}$	$^{+1.0}_{-1.4}$	$^{+4.8}_{-5.0}$	$^{+1.0}_{-1.4}$	0.0	∓0.3	$^{+3.7}_{-4.0}$	0.0	±0.3	±1.3	±0.2	±1.0	0.71	1.00	0.12
110-160	$1.66 \cdot 10^{3}$	0.55	0.0	$^{+5.6}_{-5.3}$	$^{+2.6}_{-3.0}$	$^{+1.5}_{-2.0}$	$^{+0.4}_{-0.5}$	$^{+2.9}_{-3.0}$	$^{+2.5}_{-2.6}$	±0.8	$^{+5.5}_{-5.1}$	$^{+1.6}_{-1.8}$	0.0	∓0.1	$^{+5.3}_{-5.4}$	±0.1	0.0	±1.9	±0.2	±1.0	0.61	1.00	0.08
160-210	$2.60 \cdot 10^{2}$	0.64	0.0	$^{+3.7}_{-3.3}$	$^{+2.6}_{-2.4}$	$^{+2.4}_{-1.7}$	$^{+1.6}_{-1.1}$	±3.2	$^{+2.5}_{-2.0}$	$^{+1.0}_{-0.6}$	$^{+6.0}_{-5.7}$	$^{+2.7}_{-2.1}$	$^{+0.4}_{+0.1}$	0.0	$^{+7.0}_{-6.2}$	±0.2	0.0	±1.6	±0.1	±1.0	0.68	1.00	0.06
210-260	$6.17 \cdot 10^{1}$	0.96	0.0	$^{+2.8}_{-3.5}$	$^{+2.9}_{-3.3}$	$^{+1.6}_{-2.1}$	$^{+2.1}_{-2.5}$	$^{+3.3}_{-3.4}$	±1.9	$^{+0.2}_{-0.7}$	$^{+6.1}_{-6.6}$	$^{+3.0}_{-3.3}$	0.0	0.0	$^{+7.8}_{-7.9}$	±0.2	0.0	±1.5	±0.1	±1.0	0.52	1.00	0.06
260-310	$1.95 \cdot 10^{1}$	0.81	0.0	$^{+4.7}_{-3.8}$	$^{+2.6}_{-2.5}$	$^{+1.7}_{-1.6}$	$^{+2.7}_{-2.8}$	$^{+4.1}_{-3.5}$	±1.8	$^{+0.7}_{-0.3}$	$^{+7.1}_{-6.5}$	±3.8	$^{+0.3}_{0.0}$	0.0	$^{+9.1}_{-8.1}$	±0.2	±0.1	±1.7	0.0	±1.0	0.48	1.00	0.06
310-400	$5.24 \cdot 10^{0}$	1.12	0.0	$^{+4.3}_{-3.7}$	$^{+3.2}_{-3.0}$	±1.0	$^{+3.4}_{-2.7}$	$^{+3.8}_{-3.6}$	$^{+1.8}_{-1.3}$	±0.3	$^{+7.3}_{-6.3}$	$^{+4.6}_{-4.1}$	$^{+0.4}_{+0.1}$	0.0	$^{+9.7}_{-8.5}$	±0.1	±0.1	±1.4	±0.1	±1.0	0.47	1.00	0.06
400-500	$1.10 \cdot 10^{0}$	1.96	0.0	$^{+4.5}_{-4.9}$	±3.1	$^{+0.5}_{-1.0}$	$^{+1.7}_{-2.2}$	$^{+3.7}_{-3.6}$	$^{+0.9}_{-1.4}$	$^{+0.2}_{-0.3}$	$^{+6.5}_{-6.8}$	$^{+4.2}_{-4.7}$	0.0	0.0	$^{+9.5}_{-9.7}$	±0.2	±0.3	±0.7	±0.1	±1.0	0.35	1.00	0.06
500-600	$2.52 \cdot 10^{-1}$	3.33	0.0	$^{+3.6}_{-3.0}$	±1.5	$^{+1.0}_{-0.8}$	$^{+2.4}_{-2.5}$	$^{+4.0}_{-4.2}$	$^{+1.2}_{-1.0}$	±0.4	±7.2	±5.5	$^{+0.6}_{-0.4}$	0.0	±11	±0.3	±0.3	±0.2	±0.2	±1.0	0.37	1.00	0.28
600-800	$4.72 \cdot 10^{-2}$	6.53	0.0	$^{+2.3}_{-2.8}$	$^{+0.8}_{-0.9}$	0.0	±3.2	$^{+4.5}_{-4.3}$	$^{+0.6}_{-1.2}$	$^{+0.3}_{-0.4}$	$^{+8.3}_{-7.7}$	$^{+7.1}_{-6.1}$	$^{+0.9}_{-1.3}$	0.0	$^{+14}_{-13}$	±0.3	0.0	±2.3	0.0	±1.0	0.26	1.00	0.51
800-1000	$2.97 \cdot 10^{-3}$	22.0	0.0	$^{+6.3}_{-5.5}$	$^{+2.0}_{-1.3}$	$^{+0.4}_{+0.2}$	$^{+4.3}_{-3.5}$	$^{+5.7}_{-5.4}$	$^{+0.9}_{-0.3}$	$^{+0.5}_{+0.1}$	$^{+10}_{-8.8}$	$^{+8.3}_{-7.6}$	$^{+4.0}_{-3.7}$	0.0	$^{+18}_{-15}$	±0.5	0.0	±2.1	0.0	±1.0	0.25	1.00	0.87
1000-1200	$4.54 \cdot 10^{-4}$	62.5	0.0	$^{+7.3}_{-6.8}$	$^{+1.7}_{-2.7}$	$^{+0.6}_{-0.5}$	$^{+4.5}_{-4.4}$	$^{+7.1}_{-6.7}$	$^{+0.6}_{-1.3}$	$^{+0.7}_{-0.6}$	±12	±10	$^{+8.2}_{-8.6}$	0.0	$^{+23}_{-21}$	±0.6	0.0	±3.0	0.0	±1.0	0.28	1.00	1.24
1200-1500	$1.01 \cdot 10^{-4}$	114	$^{-0.2}_{+0.1}$	$^{+8.3}_{-11}$	$^{+2.4}_{-3.3}$	$^{+2.0}_{-2.2}$	$^{+4.2}_{-5.8}$	$^{+8.4}_{-9.7}$	$^{+1.3}_{-1.1}$	0.0	$^{+14}_{-16}$	$^{+13}_{-15}$	$^{+16}_{-18}$	0.0	$^{+33}_{-28}$	±1.3	0.0	±7.8	0.0	±1.0	0.17	1.00	1.69

Table B.10: Measured jet cross section for $R = 0.6$ and $0.8 < |y| < 1.2$. See Table B.1 for a description of the columns. This table is available on HEPDATA [187].

p_{T}-bin	σ	δ_{stat}	γ_{3}	γ_{9}	γ_{15}	γ_{21}	γ_{27}	γ_{31}	γ_{34}	γ_{40}	γ_{46}	γ_{52}	γ_{58}	γ_{64}	γ_{70}	γ_{74}	γ_{75}	γ_{78}	γ_{82}	γ_{83}	u_{1}	u_{2}	u_{3}
[GeV]	[pb/GeV]	%																					
20-30	$7.65 \cdot 10^{6}$	0.40	± 11	$^{+9.0}_{-9.2}$	± 13	$^{+11}_{-10}$	± 4.5	± 14	± 2.0	$^{+4.1}_{-4.2}$	$^{+4.5}_{-4.4}$	0.0	0.0	$^{+2.7}_{-2.8}$	0.0	0.0	± 1.3	± 11	± 0.6	± 2.0	1.18	1.00	0.30
30-45	$9.38 \cdot 10^{5}$	0.72	$^{+8.6}_{-8.0}$	$^{+10}_{-9.6}$	$^{+11}_{-9.8}$	$^{+5.8}_{-5.3}$	$^{+3.1}_{-2.8}$	$^{+15}_{-13}$	$^{+2.6}_{-2.7}$	$^{+3.5}_{-3.4}$	$^{+4.9}_{-4.7}$	0.0	0.0	$^{+3.5}_{-3.4}$	$^{-0.2}_{+0.1}$	0.0	± 0.6	± 7.0	0.0	± 1.0	0.86	1.00	0.15
45-60	$1.59 \cdot 10^{5}$	1.73	$^{+2.3}_{-1.6}$	$^{+9.2}_{-7.8}$	$^{+7.7}_{-6.3}$	$^{+3.8}_{-3.1}$	$^{+1.9}_{-1.3}$	$^{+10}_{-8.4}$	$^{+3.4}_{-2.8}$	$^{+2.1}_{-1.6}$	$^{+5.0}_{-4.1}$	$^{+0.1}_{+0.2}$	$^{+0.3}_{+0.0}$	$^{+3.0}_{-2.4}$	$^{+0.3}_{+0.1}$	0.0	± 0.7	± 2.1	0.0	± 1.0	0.54	1.00	0.13
60-80	$3.78 \cdot 10^{4}$	0.66	∓ 1.0	$^{+6.9}_{-6.0}$	$^{+4.3}_{-3.8}$	$^{+1.9}_{-1.6}$	$^{+3.7}_{-3.4}$	$^{+7.1}_{-6.1}$	$^{+3.2}_{-2.9}$	$^{+1.6}_{-1.4}$	$^{+5.1}_{-4.7}$	$^{+0.4}_{-0.3}$	0.0	± 0.9	$^{+1.9}_{-1.7}$	± 0.1	± 0.2	± 1.6	0.0	± 1.0	0.50	1.00	0.10
80-110	$7.76 \cdot 10^{3}$	0.93	$^{-0.5}_{+0.4}$	$^{+5.6}_{-6.0}$	$^{+2.7}_{-3.4}$	$^{+0.7}_{-1.2}$	$^{+2.2}_{-2.8}$	± 5.2	$^{+2.6}_{-3.3}$	$^{+1.0}_{-1.6}$	$^{+4.8}_{-5.3}$	$^{+1.0}_{-1.6}$	0.0	∓ 0.3	$^{+3.7}_{-4.2}$	± 0.1	± 0.3	± 1.0	0.0	± 1.0	0.40	1.00	0.07
110-160	$1.25 \cdot 10^{3}$	0.81	0.0	$^{+5.7}_{-5.5}$	$^{+2.7}_{-3.0}$	± 1.1	$^{+0.4}_{-0.5}$	$^{+4.6}_{-4.9}$	± 2.6	± 0.8	$^{+5.5}_{-5.3}$	± 1.7	0.0	∓ 0.1	$^{+5.2}_{-5.5}$	± 0.2	0.0	± 1.0	0.0	± 1.0	0.53	1.00	0.05
160-210	$1.86 \cdot 10^{2}$	0.74	0.0	$^{+4.1}_{-3.3}$	$^{+2.8}_{-2.5}$	$^{+1.1}_{-1.0}$	$^{+1.7}_{-1.2}$	$^{+5.7}_{-4.9}$	$^{+2.8}_{-2.2}$	$^{+1.1}_{-0.5}$	$^{+6.4}_{-6.0}$	$^{+3.0}_{-2.2}$	$^{+0.4}_{+0.1}$	0.0	$^{+7.4}_{-6.5}$	± 0.3	0.0	± 1.0	± 0.1	± 1.0	0.49	1.00	0.05
210-260	$4.12 \cdot 10^{1}$	0.71	0.0	$^{+2.9}_{-3.6}$	$^{+3.0}_{-3.4}$	$^{+0.1}_{-0.7}$	$^{+2.1}_{-2.6}$	$^{+5.4}_{-5.8}$	± 1.9	$^{+0.2}_{-0.7}$	$^{+6.5}_{-6.6}$	$^{+3.2}_{-3.5}$	0.0	0.0	$^{+8.2}_{-7.9}$	± 0.3	± 0.2	± 1.1	± 0.1	± 1.0	0.57	1.00	0.05
260-310	$1.14 \cdot 10^{1}$	1.28	0.0	$^{+5.0}_{-4.0}$	$^{+2.8}_{-2.6}$	$^{+0.2}_{0.0}$	± 2.9	$^{+6.2}_{-5.7}$	$^{+2.1}_{-1.9}$	$^{+0.6}_{-0.3}$	$^{+7.5}_{-7.3}$	$^{+3.8}_{-4.0}$	$^{+0.2}_{0.0}$	0.0	$^{+9.5}_{-9.0}$	± 0.3	± 0.1	± 0.8	0.0	± 1.0	0.42	1.00	0.06
310-400	$2.85 \cdot 10^{0}$	0.91	0.0	$^{+4.7}_{-4.0}$	$^{+3.6}_{-3.1}$	$^{+1.2}_{-0.4}$	$^{+3.9}_{-2.8}$	$^{+6.9}_{-5.7}$	$^{+2.1}_{-1.3}$	$^{+0.4}_{-0.3}$	$^{+8.0}_{-6.8}$	$^{+5.0}_{-4.4}$	$^{+0.5}_{+0.1}$	0.0	$^{+11}_{-9.6}$	± 0.2	0.0	± 1.7	0.0	± 1.0	0.40	1.00	0.06
400-500	$4.60 \cdot 10^{-1}$	1.87	0.0	$^{+5.3}_{-5.7}$	$^{+3.7}_{-3.8}$	$^{+1.7}_{-2.5}$	$^{+2.2}_{-3.0}$	$^{+7.2}_{-7.1}$	$^{+1.1}_{-1.8}$	$^{+0.4}_{-0.3}$	$^{+8.1}_{-7.7}$	$^{+5.5}_{-5.6}$	0.0	0.0	$^{+12}_{-11}$	± 0.3	0.0	± 1.3	0.0	± 1.0	0.47	1.00	0.07
500-600	$8.54 \cdot 10^{-2}$	4.18	0.0	$^{+4.2}_{-3.6}$	$^{+1.9}_{-1.8}$	$^{+2.4}_{-1.6}$	$^{+2.9}_{-3.1}$	$^{+8.7}_{-8.1}$	$^{+1.5}_{-1.4}$	$^{+0.5}_{-0.4}$	$^{+8.8}_{-8.9}$	$^{+6.7}_{-6.4}$	$^{+0.9}_{-0.8}$	0.0	$^{+14}_{-13}$	± 0.6	0.0	± 1.9	± 0.2	± 1.0	0.44	1.00	0.58
600-800	$1.15 \cdot 10^{-2}$	8.21	0.0	$^{+3.7}_{-3.8}$	$^{+1.3}_{-1.2}$	$^{+0.3}_{-1.0}$	$^{+4.9}_{-4.2}$	$^{+11}_{-9.8}$	$^{+0.8}_{-1.5}$	$^{+0.4}_{-0.7}$	$^{+12}_{-11}$	$^{+10}_{-8.9}$	$^{+1.6}_{-2.0}$	0.0	$^{+20}_{-17}$	± 0.6	0.0	± 2.7	± 0.2	± 1.0	0.35	1.00	0.62
800-1000	$6.85 \cdot 10^{-4}$	35.1	0.0	$^{+8.9}_{-7.4}$	$^{+2.9}_{-1.9}$	$^{+0.5}_{+0.3}$	$^{+5.8}_{-4.6}$	$^{+13}_{-11}$	$^{+1.5}_{-0.5}$	$^{+0.8}_{+0.1}$	$^{+15}_{-12}$	$^{+12}_{-10}$	$^{+5.8}_{-5.3}$	0.0	$^{+27}_{-21}$	± 1.1	0.0	± 3.7	± 0.3	± 1.0	0.41	1.00	0.68
1000-1200	$6.75 \cdot 10^{-5}$	104	∓ 0.1	$^{+10.0}_{-9.5}$	$^{+2.2}_{-3.1}$	± 2.4	$^{+6.1}_{-6.3}$	± 15	$^{+0.6}_{-1.5}$	$^{+0.6}_{-0.3}$	$^{+17}_{-15}$	± 14	± 13	0.0	$^{+39}_{-26}$	± 1.9	0.0	± 7.5	± 0.5	± 1.0	0.21	1.00	0.77

Table B.11: Measured jet cross section for $R = 0.6$ and $1.2 < |y| < 2.1$. See Table B.1 for a description of the columns. This table is available on HEPDATA [187].

p_{T}-bin [GeV]	σ [pb/GeV]	δ_{stat} %	γ_{4}	γ_{10}	γ_{16}	γ_{22}	γ_{28}	γ_{31}	γ_{35}	γ_{41}	γ_{47}	γ_{53}	γ_{59}	γ_{65}	γ_{71}	γ_{74}	γ_{75}	γ_{79}	γ_{82}	γ_{84}	u_1	u_2	u_3
20-30	$5.82 \cdot 10^{6}$	0.54	$^{+13}_{-11}$	$^{+9.9}_{-9.3}$	$^{+15}_{-13}$	$^{+5.7}_{-5.4}$	$^{+4.9}_{-4.8}$	$^{+22}_{-20}$	$^{+2.2}_{-2.1}$	$^{+4.5}_{-4.4}$	$^{+4.8}_{-4.6}$	0.0	0.0	$^{+3.0}_{-2.9}$	0.0	0.0	±0.4	±17	±0.5	±2.0	1.42	1.00	0.02
30-45	$6.89 \cdot 10^{5}$	1.02	$^{+8.9}_{-8.0}$	$^{+10}_{-9.8}$	$^{+11}_{-9.9}$	$^{+5.6}_{-5.4}$	$^{+3.1}_{-2.8}$	$^{+23}_{-18}$	$^{+2.6}_{-2.7}$	±3.5	$^{+5.0}_{-4.8}$	0.0	0.0	±3.5	$^{-0.2}_{+0.1}$	0.0	±0.5	±7.7	±0.2	±1.0	0.99	1.00	0.02
45-60	$1.19 \cdot 10^{5}$	2.32	$^{+2.7}_{-2.0}$	$^{+9.4}_{-8.0}$	$^{+7.9}_{-6.5}$	$^{+4.1}_{-3.5}$	$^{+2.1}_{-1.5}$	$^{+14}_{-11}$	$^{+3.6}_{-3.0}$	$^{+2.2}_{-1.7}$	$^{+5.0}_{-4.4}$	$^{+0.2}_{+0.2}$	$^{+0.4}_{+0.0}$	$^{+3.2}_{-2.5}$	$^{+0.3}_{-0.1}$	±0.2	±0.3	±2.4	±0.2	±1.0	0.59	1.00	0.02
60-80	$2.42 \cdot 10^{4}$	0.87	$^{-0.9}_{+0.8}$	$^{+7.0}_{-5.8}$	$^{+4.5}_{-3.7}$	$^{+2.4}_{-1.8}$	$^{+4.1}_{-3.3}$	$^{+8.5}_{-6.9}$	$^{+3.5}_{-2.7}$	$^{+2.1}_{-1.5}$	$^{+5.2}_{-4.5}$	$^{+0.6}_{-0.3}$	0.0	$^{+1.2}_{-0.8}$	$^{+2.1}_{-1.5}$	±0.2	±0.3	±1.5	0.0	±1.0	0.55	1.00	0.02
80-110	$4.72 \cdot 10^{3}$	0.58	$^{-0.4}_{+0.3}$	$^{+6.3}_{-5.9}$	$^{+3.5}_{-3.3}$	$^{+0.7}_{-0.6}$	±2.5	$^{+5.9}_{-5.6}$	$^{+3.2}_{-3.1}$	$^{+1.2}_{-1.4}$	$^{+5.5}_{-5.2}$	$^{+1.1}_{-1.3}$	0.0	$^{-0.3}_{+0.2}$	$^{+4.3}_{-4.1}$	±0.1	±0.2	±2.3	0.0	±1.0	0.80	1.00	0.02
110-160	$6.40 \cdot 10^{2}$	0.58	0.0	$^{+6.2}_{-6.0}$	$^{+2.9}_{-3.3}$	$^{+0.3}_{-0.5}$	$^{+0.4}_{-0.7}$	$^{+5.3}_{-5.2}$	$^{+2.8}_{-2.9}$	$^{+0.7}_{-1.0}$	$^{+6.0}_{-5.8}$	±1.9	0.0	0.0	$^{+5.7}_{-6.0}$	±0.2	0.0	±1.3	0.0	±1.0	0.69	1.00	0.00
160-210	$7.31 \cdot 10^{1}$	0.71	0.0	$^{+4.5}_{-4.1}$	$^{+2.9}_{-3.3}$	$^{+0.9}_{-0.6}$	±1.8	$^{+6.8}_{-6.5}$	±2.7	$^{+1.1}_{-0.7}$	$^{+7.4}_{-7.2}$	$^{+3.1}_{-3.0}$	$^{+0.4}_{+0.1}$	0.0	$^{+8.7}_{-7.9}$	±0.4	0.0	±2.2	0.0	±1.0	0.79	1.00	0.00
210-260	$1.21 \cdot 10^{1}$	1.25	0.0	$^{+3.9}_{-4.8}$	$^{+3.6}_{-4.4}$	$^{+1.3}_{-1.4}$	$^{+2.8}_{-3.6}$	$^{+7.7}_{-7.5}$	±2.4	0.0	±8.5	$^{+3.9}_{-4.6}$	0.0	0.0	±11	±0.5	±0.1	±1.6	0.0	±1.0	0.74	1.00	0.00
260-310	$2.26 \cdot 10^{0}$	1.80	0.0	$^{+7.5}_{-5.4}$	$^{+4.9}_{-3.3}$	$^{+2.1}_{-1.5}$	$^{+5.0}_{-3.6}$	$^{+9.7}_{-8.0}$	$^{+3.6}_{-2.3}$	$^{+1.4}_{-0.6}$	$^{+10}_{-9.6}$	$^{+6.0}_{-5.4}$	$^{+0.8}_{0.0}$	0.0	$^{+14}_{-12}$	±0.5	0.0	±1.7	0.0	±1.0	0.71	1.00	0.22
310-400	$3.24 \cdot 10^{-1}$	2.89	0.0	$^{+6.9}_{-6.6}$	$^{+5.1}_{-4.8}$	$^{+2.0}_{-1.5}$	$^{+5.3}_{-4.3}$	$^{+11}_{-9.7}$	$^{+2.8}_{-2.2}$	$^{+0.7}_{-0.5}$	$^{+13}_{-10}$	$^{+7.6}_{-7.1}$	$^{+0.8}_{+0.1}$	0.0	$^{+17}_{-14}$	±0.3	±0.2	±1.8	0.0	±1.0	0.84	1.00	0.13
400-500	$2.09 \cdot 10^{-2}$	11.7	0.0	$^{+11}_{-9.7}$	$^{+5.8}_{-6.3}$	$^{+2.7}_{-3.4}$	$^{+3.9}_{-5.6}$	$^{+15}_{-14}$	$^{+1.8}_{-2.7}$	$^{+0.7}_{-0.3}$	$^{+16}_{-14}$	$^{+12}_{-11}$	0.0	0.0	$^{+23}_{-20}$	±1.1	±0.3	±3.0	±0.5	±1.0	0.58	1.00	0.14
500-600	$5.83 \cdot 10^{-4}$	63.9	0.0	$^{+2.4}_{-1.1}$	$^{+1.1}_{+0.3}$	$^{+5.0}_{-4.0}$	$^{+0.8}_{-1.1}$	$^{+13}_{-5.1}$	$^{+1.1}_{+0.2}$	0.0	$^{+13}_{-7.8}$	$^{+9.2}_{-3.8}$	0.0	0.0	$^{+27}_{-16}$	±0.9	0.0	±12	±0.8	±1.0	0.08	1.00	0.16

Table B.12: Measured jet cross section for $R = 0.6$ and $2.1 < |y| < 2.8$. See Table B.1 for a description of the columns. This table is available on HEPDATA [187].

p_{T}-bin [GeV]	σ [pb/GeV]	δ_{stat} %	γ_5	γ_{11}	γ_{17}	γ_{23}	γ_{29}	γ_{31}	γ_{36}	γ_{42}	γ_{48}	γ_{54}	γ_{60}	γ_{66}	γ_{72}	γ_{74}	γ_{75}	γ_{80}	γ_{82}	γ_{85}	u_1	u_2	u_3
20-30	$3.90 \cdot 10^6$	0.61	$^{+14}_{-12}$	$^{+11}_{-9.8}$	$^{+16}_{-14}$	$^{+8.6}_{-7.8}$	$^{+5.2}_{-4.9}$	$^{+35}_{-28}$	$^{+2.3}_{-2.2}$	$^{+4.9}_{-4.5}$	$^{+5.2}_{-4.8}$	0.0	0.0	$^{+3.3}_{-3.0}$	0.0	0.0	±0.4	±16	±0.1	±2.0	4.37	1.00	0.00
30-45	$4.26 \cdot 10^5$	1.42	$^{+9.0}_{-7.8}$	$^{+11}_{-10.0}$	$^{+11}_{-9.9}$	$^{+9.4}_{-8.0}$	$^{+3.1}_{-2.8}$	$^{+37}_{-26}$	±2.8	$^{+3.5}_{-3.6}$	$^{+5.3}_{-5.2}$	0.0	0.0	$^{+3.6}_{-3.7}$	∓0.1	0.0	±0.8	±9.7	±0.1	±1.0	2.99	1.00	0.00
45-60	$6.42 \cdot 10^4$	3.20	$^{+2.1}_{-2.4}$	$^{+8.8}_{-9.4}$	$^{+7.2}_{-7.9}$	$^{+7.1}_{-7.8}$	$^{+2.1}_{-2.3}$	$^{+24}_{-19}$	$^{+3.5}_{-3.8}$	$^{+2.2}_{-2.3}$	$^{+4.8}_{-5.5}$	$^{+0.1}_{+0.2}$	$^{+0.3}_{+0.0}$	$^{+3.0}_{-3.3}$	$^{+0.5}_{-0.3}$	±0.2	±0.4	±1.3	0.0	±1.0	1.83	1.00	0.00
60-80	$1.24 \cdot 10^4$	1.36	$^{-1.2}_{+1.1}$	$^{+7.5}_{-6.6}$	$^{+4.4}_{-4.0}$	$^{+5.9}_{-5.3}$	$^{+4.1}_{-3.7}$	$^{+17}_{-13}$	$^{+3.7}_{-3.2}$	$^{+2.0}_{-1.4}$	$^{+5.6}_{-4.9}$	$^{+0.6}_{-0.4}$	0.0	$^{+1.0}_{-0.8}$	$^{+2.5}_{-2.0}$	±0.3	±0.5	±2.3	0.0	±1.0	3.47	1.00	0.00
80-110	$1.78 \cdot 10^3$	2.35	∓0.5	$^{+6.8}_{-6.7}$	$^{+3.9}_{-3.7}$	±6.1	$^{+2.6}_{-3.0}$	±11	$^{+3.6}_{-3.8}$	$^{+1.3}_{-1.8}$	$^{+6.1}_{-6.2}$	$^{+1.5}_{-2.0}$	0.0	∓0.4	$^{+5.2}_{-5.1}$	±0.3	±0.2	±3.4	0.0	±1.0	4.12	1.00	0.00
110-160	$1.51 \cdot 10^2$	1.36	0.0	$^{+8.0}_{-8.1}$	$^{+3.9}_{-4.3}$	$^{+9.7}_{-9.6}$	$^{+0.7}_{-0.9}$	$^{+13}_{-12}$	$^{+3.5}_{-3.7}$	$^{+1.0}_{-1.3}$	$^{+8.1}_{-8.2}$	$^{+2.4}_{-2.7}$	0.0	∓0.2	$^{+8.1}_{-8.6}$	±0.2	0.0	±2.4	±0.1	±1.0	2.62	1.00	0.00
160-210	$7.23 \cdot 10^0$	3.16	0.0	$^{+7.6}_{-5.2}$	$^{+5.3}_{-4.2}$	$^{+9.4}_{-7.4}$	$^{+3.5}_{-2.4}$	$^{+21}_{-17}$	$^{+5.1}_{-3.5}$	$^{+2.0}_{-0.4}$	$^{+13}_{-10}$	$^{+5.9}_{-4.3}$	$^{+0.7}_{+0.1}$	0.0	$^{+16}_{-12}$	±0.6	0.0	±4.7	±0.1	±1.0	2.56	1.00	0.17
210-260	$3.75 \cdot 10^{-1}$	6.88	0.0	$^{+8.3}_{-7.7}$	$^{+7.5}_{-6.6}$	$^{+8.0}_{-6.0}$	$^{+5.2}_{-5.7}$	$^{+26}_{-20}$	$^{+3.5}_{-4.0}$	$^{+0.6}_{-1.2}$	$^{+17}_{-14}$	$^{+8.8}_{-7.3}$	0.0	0.0	$^{+21}_{-18}$	±1.0	0.0	±6.1	±0.4	±1.0	3.36	1.00	0.19
260-310	$1.09 \cdot 10^{-2}$	35.8	0.0	$^{+14}_{-8.1}$	$^{+8.4}_{-6.1}$	$^{+11}_{-5.5}$	$^{+9.4}_{-6.7}$	$^{+41}_{-31}$	$^{+3.8}_{-3.9}$	$^{+2.2}_{+0.4}$	$^{+25}_{-20}$	$^{+12}_{-8.8}$	$^{+2.6}_{+0.2}$	0.0	$^{+35}_{-22}$	∓0.3	±0.7	±19	±1.3	±1.0	3.53	1.00	0.21

Table B.13: Measured jet cross section for $R = 0.6$ and $2.8 < |y| < 3.6$. See Table B.1 for a description of the columns. This table is available on HEPDATA [187].

p_{T}-bin [GeV]	σ [pb/GeV]	δ_{stat} %	γ_{6}	γ_{12}	γ_{18}	γ_{24}	γ_{30}	γ_{31}	γ_{37}	γ_{43}	γ_{49}	γ_{55}	γ_{61}	γ_{67}	γ_{73}	γ_{74}	γ_{75}	γ_{81}	γ_{82}	γ_{86}	u_1	u_2	u_3
20-30	$1.51 \cdot 10^{6}$	0.81	$^{+14}_{-13}$	±11	$^{+17}_{-15}$	$^{+3.1}_{-3.2}$	$^{+5.3}_{-5.5}$	$^{+60}_{-42}$	$^{+2.4}_{-2.5}$	$^{+5.0}_{-5.1}$	$^{+5.3}_{-5.4}$	0.0	0.0	$^{+3.2}_{-3.4}$	0.0	0.0	±0.3	±13	±1.2	±2.0	5.01	1.00	0.00
30-45	$1.38 \cdot 10^{5}$	0.86	$^{+10}_{-8.9}$	$^{+13}_{-11}$	$^{+13}_{-11}$	$^{+3.0}_{-2.8}$	$^{+3.6}_{-2.9}$	$^{+65}_{-37}$	$^{+3.3}_{-3.0}$	$^{+4.1}_{-3.8}$	$^{+6.3}_{-5.7}$	0.0	0.0	$^{+4.1}_{-3.9}$	0.0	0.0	±0.9	±6.2	±0.7	±1.0	9.22	1.00	0.00
45-60	$1.29 \cdot 10^{4}$	2.08	$^{+2.5}_{-2.4}$	$^{+12}_{-11}$	$^{+9.8}_{-9.4}$	$^{+2.0}_{-1.8}$	$^{+2.9}_{-2.6}$	$^{+39}_{-26}$	$^{+5.0}_{-4.7}$	$^{+2.5}_{-2.6}$	±6.8	$^{+0.6}_{+0.2}$	$^{+0.7}_{+0.0}$	$^{+3.7}_{-3.3}$	$^{+1.0}_{-0.2}$	±0.4	±0.5	±1.5	±0.3	±1.0	5.64	1.00	0.00
60-80	$1.27 \cdot 10^{3}$	2.23	$^{-1.3}_{+1.2}$	$^{+8.9}_{-11}$	$^{+5.9}_{-7.4}$	$^{+0.8}_{-2.6}$	$^{+5.0}_{-7.0}$	$^{+24}_{-19}$	$^{+4.4}_{-6.4}$	$^{+2.0}_{-4.0}$	$^{+7.7}_{-8.8}$	$^{+0.3}_{-1.7}$	0.0	$^{+0.5}_{-2.2}$	$^{+3.5}_{-4.9}$	±0.3	±0.6	±4.3	±0.8	±1.0	5.27	1.00	0.02
80-110	$7.70 \cdot 10^{1}$	3.19	∓0.5	$^{+13}_{-10}$	$^{+6.1}_{-5.1}$	$^{+4.7}_{-2.6}$	$^{+4.6}_{-3.2}$	$^{+17}_{-13}$	$^{+6.0}_{-4.7}$	±1.9	$^{+11}_{-9.5}$	$^{+2.2}_{-2.3}$	0.0	∓0.5	$^{+8.3}_{-7.7}$	∓0.2	±0.2	±5.1	±0.6	±1.0	5.55	1.00	0.02
110-160	$8.28 \cdot 10^{-1}$	12.2	0.0	$^{+10}_{-15}$	$^{+7.1}_{-9.4}$	$^{+9.3}_{-11}$	$^{+0.3}_{-3.7}$	$^{+13}_{-14}$	$^{+2.7}_{-9.7}$	$^{+0.8}_{-4.2}$	$^{+10}_{-15}$	$^{+3.5}_{-6.9}$	0.0	$^{-0.2}_{+0.4}$	$^{+11}_{-16}$	±2.3	±0.1	±11	±3.1	±1.0	8.01	1.00	0.02

Table B.14: Measured jet cross section for $R = 0.6$ and $3.6 < |y| < 4.4$. See Table B.1 for a description of the columns. This table is available on HEPDATA [187].

B.2 Dijet Tables

m_{12}-bin [TeV]	σ [pb/TeV]	δ_{stat} %	γ_1	γ_7	γ_{13}	γ_{19}	γ_{25}	γ_{31}	γ_{32}	γ_{38}	γ_{44}	γ_{50}	γ_{56}	γ_{62}	γ_{68}	γ_{74}	γ_{75}	γ_{76}	γ_{82}	γ_{83}	u_1	u_2	u_3
0.07-0.11	$2.4 \cdot 10^{8}$	1.3	$^{+4.0}_{-4.1}$	$^{+8.2}_{-7.7}$	$^{+5.9}_{-5.8}$	$^{+4.3}_{-4.2}$	$^{+1.5}_{-1.7}$	$^{+9.8}_{-8.5}$	$^{+2.0}_{-2.3}$	$^{+2.5}_{-2.7}$	$^{+3.7}_{-3.9}$	0.0	0.02	$^{+2.7}_{-2.8}$	$^{+0.15}_{-0.14}$	2.0	N/A	2.1	0.01	2.1	$^{+2.4}_{-2.7}$	1.0	1.0
0.11-0.16	$3.4 \cdot 10^{7}$	0.67	$^{+0.95}_{-0.93}$	$^{+6.4}_{-6.2}$	$^{+4.9}_{-4.8}$	2.7	1.9	$^{+5.6}_{-4.9}$	2.6	$^{+1.7}_{-1.6}$	$^{+4.1}_{-4.0}$	$^{+0.18}_{-0.24}$	$^{+0.0}_{-0.03}$	$^{+1.9}_{-1.7}$	$^{+0.81}_{-0.87}$	0.8	N/A	0.76	0.12	2.0	$^{+1.6}_{-1.7}$	1.0	1.0
0.16-0.21	$7.1 \cdot 10^{6}$	0.52	$^{+0.35}_{-0.33}$	$^{+6.0}_{-5.5}$	$^{+3.9}_{-3.7}$	$^{+2.2}_{-2.0}$	$^{+1.3}_{-1.2}$	$^{+3.3}_{-3.0}$	$^{+2.8}_{-2.5}$	$^{+1.3}_{-1.1}$	$^{+4.5}_{-4.1}$	$^{+0.85}_{-0.77}$	$^{+0.06}_{-0.04}$	$^{+0.49}_{-0.47}$	$^{+2.5}_{-2.4}$	0.6	N/A	0.61	0.1	2.0	$^{+1.2}_{-1.1}$	1.0	1.0
0.21-0.26	$2.0 \cdot 10^{6}$	0.88	0.12	$^{+5.7}_{-5.6}$	$^{+3.7}_{-4.0}$	2.2	$^{+0.79}_{-0.84}$	$^{+2.2}_{-2.3}$	2.6	$^{+0.99}_{-0.98}$	$^{+4.7}_{-4.8}$	$^{+1.3}_{-1.4}$	$^{+0.04}_{-0.07}$	$^{+0.03}_{-0.02}$	$^{+3.4}_{-3.7}$	0.3	N/A	0.34	0.04	2.0	$^{+1.0}_{-0.98}$	1.0	1.0
0.26-0.31	$7.2 \cdot 10^{5}$	0.67	0.03	$^{+5.5}_{-4.9}$	$^{+3.9}_{-3.2}$	$^{+2.5}_{-2.4}$	$^{+1.2}_{-1.0}$	$^{+2.6}_{-2.1}$	$^{+2.7}_{-2.4}$	$^{+0.88}_{-0.9}$	$^{+5.5}_{-4.8}$	$^{+1.7}_{-1.6}$	$^{+0.06}_{-0.04}$	$^{+0.03}_{-0.04}$	$^{+4.8}_{-4.3}$	0.6	N/A	0.62	0.11	2.0	$^{+0.77}_{-0.83}$	1.0	1.0
0.31-0.37	$2.8 \cdot 10^{5}$	0.55	0.0	$^{+4.9}_{-4.6}$	$^{+3.4}_{-3.3}$	$^{+2.5}_{-2.2}$	$^{+1.4}_{-1.3}$	$^{+2.4}_{-2.3}$	$^{+2.5}_{-2.3}$	0.67	$^{+5.7}_{-5.3}$	$^{+2.1}_{-2.0}$	$^{+0.08}_{-0.07}$	$^{+0.01}_{-0.02}$	$^{+5.5}_{-5.1}$	0.6	N/A	0.57	0.03	2.0	$^{+0.64}_{-0.67}$	1.0	1.0
0.37-0.44	$1.1 \cdot 10^{5}$	0.61	0.0	$^{+4.3}_{-4.2}$	$^{+3.7}_{-3.8}$	$^{+1.9}_{-2.0}$	1.4	$^{+2.3}_{-2.0}$	$^{+2.0}_{-2.1}$	$^{+0.55}_{-0.59}$	5.5	$^{+2.2}_{-2.3}$	$^{+0.1}_{-0.12}$	0.0	$^{+6.0}_{-5.9}$	0.3	N/A	0.29	0.01	2.0	$^{+0.56}_{-0.65}$	1.0	1.0
0.44-0.51	$4.3 \cdot 10^{4}$	0.64	0.0	$^{+4.5}_{-4.3}$	$^{+4.1}_{-3.9}$	$^{+1.9}_{-2.0}$	$^{+1.7}_{-1.8}$	2.1	$^{+2.1}_{-2.0}$	$^{+0.61}_{-0.63}$	$^{+6.0}_{-5.7}$	$^{+3.0}_{-2.9}$	$^{+0.13}_{-0.16}$	0.0	$^{+6.8}_{-6.6}$	0.2	N/A	0.24	0.0	2.0	$^{+0.63}_{-0.75}$	1.0	1.0
0.51-0.59	$1.8 \cdot 10^{4}$	0.82	0.0	$^{+4.5}_{-3.8}$	$^{+3.3}_{-2.6}$	$^{+2.0}_{-1.6}$	$^{+2.2}_{-1.7}$	$^{+2.5}_{-1.8}$	$^{+2.1}_{-1.7}$	$^{+0.64}_{-0.42}$	$^{+6.4}_{-5.8}$	$^{+3.6}_{-2.9}$	$^{+0.27}_{-0.15}$	0.0	$^{+7.7}_{-6.8}$	0.7	N/A	0.66	0.16	2.0	$^{+0.7}_{-0.52}$	1.0	1.0
0.59-0.67	$7.9 \cdot 10^{3}$	1.1	0.0	$^{+3.5}_{-3.8}$	$^{+2.6}_{-2.9}$	$^{+1.3}_{-1.4}$	$^{+2.0}_{-2.4}$	$^{+1.7}_{-2.2}$	$^{+1.6}_{-1.7}$	$^{+0.31}_{-0.4}$	$^{+6.2}_{-6.4}$	$^{+3.2}_{-3.7}$	$^{+0.13}_{-0.2}$	0.0	$^{+7.4}_{-7.6}$	0.1	N/A	0.12	0.0	2.0	$^{+0.36}_{-0.51}$	1.0	1.0
0.67-0.76	$3.7 \cdot 10^{3}$	1.3	0.0	$^{+3.2}_{-3.3}$	$^{+2.3}_{-2.4}$	$^{+1.2}_{-1.3}$	$^{+2.3}_{-2.4}$	$^{+1.6}_{-1.9}$	$^{+1.4}_{-1.6}$	$^{+0.33}_{-0.39}$	$^{+6.5}_{-6.2}$	$^{+3.8}_{-3.9}$	$^{+0.12}_{-0.18}$	0.0	$^{+8.3}_{-7.9}$	0.3	N/A	0.3	0.0	2.0	$^{+0.34}_{-0.39}$	1.0	1.0
0.76-0.85	$1.8 \cdot 10^{3}$	1.8	0.0	$^{+3.2}_{-3.1}$	$^{+2.0}_{-1.9}$	$^{+1.5}_{-1.4}$	$^{+2.6}_{-2.5}$	$^{+2.2}_{-1.8}$	$^{+1.7}_{-1.6}$	$^{+0.48}_{-0.38}$	$^{+6.8}_{-6.3}$	$^{+4.5}_{-4.3}$	$^{+0.26}_{-0.17}$	0.0	$^{+9.0}_{-8.1}$	0.4	N/A	0.41	0.06	2.0	$^{+0.46}_{-0.39}$	1.0	1.0
0.85-0.95	$8.6 \cdot 10^{2}$	2.2	0.0	$^{+3.2}_{-3.0}$	$^{+2.3}_{-2.2}$	$^{+1.5}_{-1.4}$	$^{+2.6}_{-2.5}$	$^{+1.9}_{-1.8}$	$^{+1.5}_{-1.4}$	$^{+0.28}_{-0.44}$	$^{+6.9}_{-6.8}$	$^{+4.8}_{-4.7}$	$^{+0.12}_{-0.23}$	0.0	$^{+9.2}_{-8.6}$	0.3	N/A	0.34	0.0	2.0	$^{+0.27}_{-0.42}$	1.0	1.0
0.95-1.06	$4.2 \cdot 10^{2}$	3.2	0.0	2.7	$^{+2.5}_{-2.6}$	1.4	$^{+2.4}_{-2.3}$	1.7	1.3	$^{+0.35}_{-0.36}$	$^{+7.1}_{-6.5}$	$^{+5.1}_{-4.8}$	$^{+0.23}_{-0.1}$	0.0	$^{+9.5}_{-9.2}$	0.4	N/A	0.37	0.0	2.0	$^{+0.3}_{-0.31}$	1.0	1.0
1.06-1.18	$2.1 \cdot 10^{2}$	4.4	0.0	$^{+3.2}_{-3.1}$	2.4	$^{+1.1}_{-1.3}$	$^{+2.3}_{-2.5}$	1.8	$^{+1.4}_{-1.5}$	$^{+0.45}_{-0.43}$	$^{+7.4}_{-6.6}$	$^{+5.5}_{-5.3}$	$^{+0.49}_{-0.55}$	0.0	$^{+11}_{-9.1}$	0.5	N/A	0.55	0.0	2.0	$^{+0.47}_{-0.36}$	1.0	1.0
1.18-1.31	$9.6 \cdot 10^{1}$	5.8	0.0	$^{+3.3}_{-3.4}$	$^{+1.1}_{-1.4}$	$^{+0.48}_{-0.7}$	$^{+1.9}_{-2.0}$	$^{+1.5}_{-1.3}$	$^{+0.99}_{-1.3}$	$^{+0.33}_{-0.32}$	6.7	5.4	$^{+0.43}_{-0.73}$	0.0	10	0.1	N/A	0.1	0.0	2.0	$^{+0.26}_{-0.3}$	1.0	1.0
1.31-1.45	$4.7 \cdot 10^{1}$	7.7	0.0	$^{+3.7}_{-3.6}$	1.6	$^{+0.84}_{-0.58}$	$^{+2.2}_{-2.0}$	$^{+1.3}_{-1.2}$	$^{+1.2}_{-0.92}$	$^{+0.34}_{-0.26}$	$^{+7.5}_{-7.2}$	$^{+6.1}_{-5.9}$	$^{+0.97}_{-0.77}$	0.0	$^{+12}_{-11}$	0.2	N/A	0.23	0.06	2.0	0.2	1.0	1.0
1.45-1.6	$2.1 \cdot 10^{1}$	13	0.0	3.9	$^{+2.8}_{-2.9}$	$^{+1.1}_{-1.2}$	2.6	$^{+1.3}_{-1.4}$	$^{+1.1}_{-1.2}$	$^{+0.34}_{-0.31}$	$^{+8.3}_{-7.5}$	$^{+6.6}_{-6.2}$	$^{+1.4}_{-1.5}$	0.0	$^{+12}_{-11}$	0.3	N/A	0.35	0.0	2.0	$^{+0.22}_{-0.18}$	1.0	1.0
1.6-1.94	$7.2 \cdot 10^{0}$	14	0.0	$^{+4.3}_{-4.2}$	$^{+3.7}_{-3.8}$	$^{+1.3}_{-1.2}$	2.6	1.1	$^{+1.0}_{-0.99}$	$^{+0.37}_{-0.34}$	$^{+8.6}_{-8.0}$	$^{+7.2}_{-6.7}$	$^{+2.2}_{-2.3}$	0.0	$^{+14}_{-12}$	0.5	N/A	0.52	0.03	2.0	$^{+0.25}_{-0.21}$	1.0	1.0
1.94-2.78	$6.4 \cdot 10^{-1}$	35	$^{+0.0}_{-0.01}$	$^{+4.3}_{-4.2}$	$^{+4.2}_{-4.1}$	$^{+0.61}_{-0.83}$	$^{+2.9}_{-3.0}$	$^{+0.76}_{-0.74}$	$^{+0.72}_{-0.92}$	$^{+0.35}_{-0.46}$	$^{+8.5}_{-8.4}$	7.7	$^{+4.4}_{-4.6}$	0.0	$^{+16}_{-15}$	0.4	N/A	0.45	0.01	2.0	$^{+0.12}_{-0.2}$	1.0	1.0

Table B.15: Measured dijet cross section for $R = 0.4$ and $y^* < 0.5$. σ is the measured cross section. δ_{stat} is the statistical uncertainty. γ_i and u_i are the correlated and uncorrelated systematic uncertainties, as described in Sec. 7.13 and Table 7.4. All uncertainties are given in %. An overall luminosity uncertainty of 3.4%, which is applicable to all ATLAS data samples based on 2010 data, is not shown. This table is available on HEPDATA [187].

m_{12}-bin [TeV]	σ [pb/TeV]	δ_{stat} %	γ_1	γ_7	γ_{13}	γ_{19}	γ_{25}	γ_{31}	γ_{32}	γ_{38}	γ_{44}	γ_{50}	γ_{56}	γ_{62}	γ_{68}	γ_{74}	γ_{75}	γ_{76}	γ_{82}	γ_{83}	u_1	u_2	u_3
0.11-0.16	$7.9 \cdot 10^{7}$	1.2	$^{+3.9}_{-3.5}$	$^{+7.8}_{-7.2}$	$^{+6.2}_{-5.6}$	$^{+4.2}_{-3.8}$	$^{+1.9}_{-1.7}$	$^{+10}_{-8.3}$	$^{+2.5}_{-2.3}$	$^{+2.6}_{-2.3}$	$^{+4.1}_{-3.8}$	$^{+0.02}_{-0.0}$	$^{+0.02}_{-0.0}$	$^{+2.7}_{-2.5}$	$^{+0.04}_{-0.0}$	2.0	N/A	2.1	0.25	2.1	$^{+2.7}_{-2.3}$	1.0	1.0
0.16-0.21	$1.6 \cdot 10^{7}$	0.77	$^{+0.48}_{-0.63}$	6.2	$^{+4.4}_{-4.6}$	$^{+2.0}_{-2.7}$	$^{+1.8}_{-2.5}$	$^{+4.4}_{-4.9}$	$^{+2.9}_{-3.5}$	$^{+1.2}_{-1.9}$	$^{+4.3}_{-4.7}$	$^{+0.4}_{-0.93}$	$^{+0.0}_{-0.04}$	$^{+1.3}_{-1.9}$	$^{+1.4}_{-2.2}$	0.0	N/A	0.0	0.0	1.9	$^{+1.0}_{-2.3}$	1.0	1.0
0.21-0.26	$4.7 \cdot 10^{6}$	0.62	$^{+0.39}_{-0.45}$	$^{+6.0}_{-5.9}$	$^{+4.0}_{-4.1}$	$^{+2.2}_{-2.3}$	$^{+1.2}_{-1.3}$	$^{+3.4}_{-3.6}$	2.8	1.1	$^{+4.5}_{-4.6}$	$^{+0.8}_{-0.87}$	$^{+0.04}_{-0.03}$	$^{+0.43}_{-0.39}$	$^{+2.5}_{-2.7}$	0.3	N/A	0.26	0.0	2.0	$^{+1.1}_{-1.4}$	1.0	1.0
0.26-0.31	$1.7 \cdot 10^{6}$	0.66	0.11	$^{+6.2}_{-6.1}$	$^{+4.2}_{-4.1}$	$^{+2.4}_{-2.2}$	$^{+0.96}_{-0.67}$	$^{+2.9}_{-3.1}$	$^{+2.7}_{-2.6}$	$^{+1.1}_{-0.88}$	5.0	$^{+1.3}_{-1.1}$	$^{+0.08}_{-0.05}$	$^{+0.11}_{-0.0}$	$^{+3.6}_{-3.7}$	0.6	N/A	0.6	0.0	2.0	$^{+1.2}_{-0.96}$	1.0	1.0
0.31-0.37	$6.5 \cdot 10^{5}$	0.63	0.02	$^{+5.5}_{-5.2}$	3.7	2.4	$^{+0.95}_{-1.0}$	$^{+3.0}_{-2.6}$	$^{+2.7}_{-2.5}$	$^{+0.88}_{-0.84}$	$^{+5.1}_{-4.8}$	$^{+1.7}_{-1.6}$	$^{+0.06}_{-0.07}$	$^{+0.0}_{-0.04}$	$^{+4.3}_{-4.2}$	0.5	N/A	0.54	0.1	2.0	$^{+0.89}_{-0.9}$	1.0	1.0
0.37-0.44	$2.5 \cdot 10^{5}$	0.77	0.0	$^{+4.9}_{-5.2}$	$^{+3.4}_{-3.7}$	$^{+2.2}_{-2.8}$	$^{+1.4}_{-1.6}$	$^{+2.8}_{-3.1}$	$^{+2.4}_{-2.8}$	$^{+0.88}_{-1.1}$	$^{+5.3}_{-5.6}$	$^{+1.8}_{-2.3}$	$^{+0.06}_{-0.13}$	0.0	$^{+4.9}_{-5.4}$	0.1	N/A	0.14	0.02	2.0	$^{+0.79}_{-1.2}$	1.0	1.0
0.44-0.51	$1.0 \cdot 10^{5}$	0.68	0.0	$^{+4.7}_{-4.4}$	3.4	$^{+1.9}_{-2.0}$	$^{+1.2}_{-1.4}$	$^{+2.5}_{-2.6}$	$^{+2.0}_{-2.1}$	$^{+0.61}_{-0.68}$	$^{+5.7}_{-5.2}$	$^{+1.9}_{-2.1}$	0.09	0.0	$^{+5.8}_{-5.4}$	0.6	N/A	0.55	0.03	2.0	$^{+0.66}_{-0.68}$	1.0	1.0
0.51-0.59	$4.4 \cdot 10^{4}$	0.82	0.0	$^{+4.9}_{-4.1}$	$^{+4.2}_{-3.7}$	$^{+2.0}_{-1.7}$	$^{+1.7}_{-1.5}$	$^{+2.9}_{-2.5}$	$^{+2.2}_{-1.8}$	$^{+0.6}_{-0.56}$	$^{+6.6}_{-5.2}$	$^{+2.8}_{-2.4}$	$^{+0.1}_{-0.14}$	0.0	$^{+7.3}_{-5.8}$	0.8	N/A	0.82	0.14	2.0	$^{+0.75}_{-0.65}$	1.0	1.0
0.59-0.67	$1.9 \cdot 10^{4}$	0.94	0.0	$^{+4.3}_{-4.6}$	$^{+3.8}_{-3.6}$	$^{+1.8}_{-1.7}$	$^{+1.8}_{-1.7}$	$^{+2.8}_{-2.7}$	$^{+2.1}_{-2.0}$	$^{+0.62}_{-0.52}$	$^{+6.1}_{-6.3}$	3.1	$^{+0.19}_{-0.16}$	0.0	$^{+7.1}_{-7.3}$	0.4	N/A	0.42	0.06	2.0	$^{+0.69}_{-0.66}$	1.0	1.0
0.67-0.76	$9.0 \cdot 10^{3}$	1.0	0.0	$^{+3.9}_{-4.4}$	$^{+3.0}_{-3.3}$	$^{+1.6}_{-2.0}$	$^{+2.0}_{-2.4}$	$^{+2.6}_{-2.9}$	$^{+1.8}_{-2.3}$	$^{+0.3}_{-0.56}$	$^{+5.9}_{-6.5}$	$^{+3.2}_{-3.7}$	$^{+0.05}_{-0.15}$	0.0	$^{+7.1}_{-7.9}$	0.0	N/A	0.0	0.0	2.0	$^{+0.37}_{-0.77}$	1.0	1.0
0.76-0.85	$4.3 \cdot 10^{3}$	1.3	0.0	$^{+4.7}_{-3.2}$	$^{+3.4}_{-2.4}$	$^{+2.0}_{-1.4}$	$^{+2.9}_{-2.2}$	$^{+3.4}_{-2.3}$	$^{+2.2}_{-1.6}$	$^{+0.62}_{-0.48}$	$^{+7.9}_{-6.0}$	$^{+4.5}_{-3.2}$	$^{+0.31}_{-0.15}$	0.0	$^{+9.6}_{-7.5}$	1.0	N/A	0.99	0.12	2.0	$^{+0.75}_{-0.53}$	1.0	1.0
0.85-0.95	$2.1 \cdot 10^{3}$	1.6	0.0	$^{+3.3}_{-3.6}$	$^{+2.4}_{-2.5}$	$^{+1.3}_{-1.4}$	$^{+2.4}_{-2.6}$	$^{+2.5}_{-2.8}$	$^{+1.6}_{-1.7}$	$^{+0.49}_{-0.33}$	$^{+6.8}_{-7.0}$	$^{+3.9}_{-4.1}$	$^{+0.24}_{-0.09}$	0.0	$^{+9.0}_{-8.5}$	0.3	N/A	0.33	0.0	2.0	$^{+0.55}_{-0.33}$	1.0	1.0
0.95-1.06	$9.8 \cdot 10^{2}$	2.1	0.0	$^{+3.4}_{-3.3}$	$^{+2.4}_{-2.2}$	1.3	$^{+2.7}_{-2.6}$	$^{+2.8}_{-2.7}$	1.6	$^{+0.37}_{-0.44}$	$^{+7.1}_{-6.7}$	$^{+4.6}_{-4.3}$	$^{+0.16}_{-0.21}$	0.0	$^{+9.1}_{-8.7}$	0.4	N/A	0.36	0.0	2.0	$^{+0.36}_{-0.45}$	1.0	1.0
1.06-1.18	$4.9 \cdot 10^{2}$	2.7	0.0	$^{+3.3}_{-3.0}$	$^{+2.3}_{-2.2}$	$^{+1.5}_{-1.4}$	$^{+2.6}_{-2.4}$	$^{+2.7}_{-2.6}$	$^{+1.6}_{-1.5}$	$^{+0.37}_{-0.43}$	$^{+7.1}_{-6.3}$	$^{+4.7}_{-4.4}$	$^{+0.21}_{-0.23}$	0.0	$^{+9.2}_{-8.6}$	0.4	N/A	0.37	0.03	2.0	$^{+0.34}_{-0.42}$	1.0	1.0
1.18-1.31	$2.3 \cdot 10^{2}$	3.9	0.0	$^{+3.8}_{-3.2}$	$^{+3.1}_{-2.7}$	$^{+1.4}_{-1.5}$	$^{+3.0}_{-2.7}$	$^{+3.3}_{-2.9}$	$^{+1.6}_{-1.5}$	$^{+0.5}_{-0.3}$	$^{+7.9}_{-7.0}$	$^{+5.7}_{-5.1}$	$^{+0.31}_{-0.19}$	0.0	$^{+11}_{-10}$	0.7	N/A	0.66	0.0	2.0	$^{+0.52}_{-0.3}$	1.0	1.0
1.31-1.45	$1.1 \cdot 10^{2}$	5.2	0.0	$^{+3.3}_{-3.4}$	$^{+2.4}_{-2.6}$	1.2	2.4	$^{+2.8}_{-2.7}$	$^{+1.4}_{-1.3}$	$^{+0.38}_{-0.34}$	$^{+7.3}_{-7.4}$	$^{+5.4}_{-5.5}$	$^{+0.42}_{-0.21}$	0.0	10	0.3	N/A	0.28	0.02	2.0	$^{+0.36}_{-0.32}$	1.0	1.0
1.45-1.6	$5.2 \cdot 10^{1}$	6.8	0.0	$^{+2.9}_{-3.7}$	$^{+1.8}_{-2.4}$	$^{+0.91}_{-0.94}$	$^{+1.8}_{-2.3}$	$^{+2.4}_{-3.2}$	$^{+1.0}_{-1.3}$	$^{+0.34}_{-0.41}$	$^{+6.5}_{-7.8}$	$^{+4.9}_{-6.5}$	$^{+0.41}_{-0.63}$	0.0	$^{+11}_{-10}$	0.0	N/A	0.0	0.08	2.0	$^{+0.26}_{-0.34}$	1.0	1.0
1.6-1.76	$2.0 \cdot 10^{1}$	11	0.0	$^{+3.7}_{-4.0}$	2.0	$^{+0.83}_{-0.82}$	$^{+2.1}_{-2.3}$	$^{+3.2}_{-3.3}$	1.1	$^{+0.2}_{-0.29}$	$^{+8.4}_{-7.7}$	$^{+6.4}_{-6.3}$	$^{+0.79}_{-0.76}$	0.0	$^{+13}_{-12}$	0.4	N/A	0.4	0.0	2.0	$^{+0.08}_{-0.23}$	1.0	1.0
1.76-2.12	$7.6 \cdot 10^{0}$	13	0.0	$^{+4.3}_{-4.0}$	$^{+2.3}_{-2.4}$	$^{+0.98}_{-1.1}$	$^{+2.7}_{-2.5}$	$^{+3.2}_{-3.1}$	$^{+1.0}_{-1.1}$	$^{+0.41}_{-0.42}$	$^{+8.5}_{-7.9}$	$^{+7.0}_{-6.6}$	$^{+1.3}_{-1.5}$	0.0	$^{+14}_{-13}$	0.4	N/A	0.44	0.11	2.0	$^{+0.32}_{-0.21}$	1.0	1.0
2.12-3.31	$9.8 \cdot 10^{-1}$	24	0.0	$^{+5.6}_{-5.1}$	$^{+4.1}_{-3.7}$	$^{+0.94}_{-0.86}$	$^{+3.6}_{-3.3}$	$^{+3.6}_{-3.4}$	$^{+1.0}_{-0.86}$	$^{+0.42}_{-0.45}$	$^{+10}_{-8.9}$	$^{+8.6}_{-7.6}$	$^{+3.9}_{-3.6}$	0.0	$^{+17}_{-15}$	1.0	N/A	0.99	0.05	2.0	0.31	1.0	1.0

Table B.16: Measured dijet cross section for $R = 0.4$ and $0.5 < y^* < 1.0$. See Table B.15 for a description of the columns. This table is available on HEPDATA [187].

m_{12}-bin	σ	δ_{stat}	γ_{2}	γ_{8}	γ_{14}	γ_{20}	γ_{26}	γ_{31}	γ_{33}	γ_{39}	γ_{45}	γ_{51}	γ_{57}	γ_{63}	γ_{69}	γ_{74}	γ_{75}	γ_{77}	γ_{82}	γ_{83}	u_{1}	u_{2}	u_{3}
[TeV]	[pb/TeV]	%																					
0.16-0.21	$4.3 \cdot 10^{7}$	1.5	$^{+4.2}_{-3.9}$	$^{+8.3}_{-7.8}$	$^{+6.5}_{-6.1}$	$^{+4.4}_{-4.1}$	$^{+2.0}_{-1.9}$	$^{+13}_{-11}$	2.5	$^{+2.7}_{-2.6}$	$^{+4.2}_{-4.0}$	$^{+0.08}_{-0.07}$	0.01	2.8	$^{+0.1}_{-0.04}$	2.0	N/A	2.3	0.2	2.1	$^{+3.1}_{-2.8}$	2.0	1.0
0.21-0.26	$1.3 \cdot 10^{7}$	1.1	$^{+0.37}_{-0.61}$	6.5	$^{+5.0}_{-5.3}$	$^{+2.1}_{-2.3}$	$^{+1.4}_{-1.7}$	$^{+7.9}_{-7.4}$	$^{+2.8}_{-2.9}$	$^{+1.4}_{-1.5}$	$^{+4.2}_{-4.6}$	$^{+0.26}_{-0.36}$	$^{+0.03}_{-0.04}$	1.8	$^{+0.71}_{-0.85}$	0.2	N/A	0.22	0.12	1.9	$^{+1.5}_{-2.1}$	2.0	1.0
0.26-0.31	$4.8 \cdot 10^{6}$	1.0	$^{+0.04}_{-0.09}$	$^{+7.0}_{-6.4}$	$^{+4.8}_{-4.5}$	$^{+2.5}_{-2.2}$	$^{+1.8}_{-1.5}$	$^{+6.7}_{-5.7}$	$^{+3.0}_{-2.6}$	$^{+1.3}_{-1.1}$	$^{+4.7}_{-4.4}$	$^{+0.49}_{-0.32}$	$^{+0.06}_{-0.02}$	$^{+1.1}_{-0.93}$	$^{+1.8}_{-1.6}$	0.8	N/A	0.76	0.12	2.0	$^{+1.4}_{-1.5}$	2.0	1.0
0.31-0.37	$1.9 \cdot 10^{6}$	0.95	0.14	$^{+6.1}_{-5.8}$	$^{+4.5}_{-4.0}$	$^{+2.5}_{-2.2}$	$^{+1.6}_{-1.4}$	$^{+5.1}_{-4.6}$	$^{+3.1}_{-2.5}$	$^{+1.5}_{-1.2}$	$^{+4.7}_{-4.4}$	$^{+0.88}_{-0.8}$	$^{+0.05}_{-0.03}$	$^{+0.57}_{-0.36}$	$^{+2.8}_{-2.6}$	0.8	N/A	0.8	0.0	2.0	$^{+1.7}_{-1.4}$	2.0	1.0
0.37-0.44	$7.3 \cdot 10^{5}$	0.89	0.07	$^{+5.9}_{-5.3}$	$^{+4.0}_{-3.7}$	2.1	$^{+1.0}_{-0.98}$	$^{+4.2}_{-3.8}$	$^{+2.5}_{-2.6}$	1.1	$^{+4.8}_{-4.4}$	$^{+1.1}_{-1.2}$	$^{+0.1}_{-0.07}$	$^{+0.06}_{-0.07}$	$^{+3.3}_{-3.5}$	0.5	N/A	0.51	0.0	2.0	$^{+1.2}_{-1.3}$	2.0	1.0
0.44-0.51	$3.0 \cdot 10^{5}$	1.1	0.02	$^{+6.3}_{-6.1}$	$^{+4.3}_{-4.2}$	$^{+2.3}_{-2.5}$	1.1	$^{+4.0}_{-4.1}$	3.0	1.0	$^{+5.6}_{-5.5}$	$^{+1.8}_{-1.6}$	$^{+0.05}_{-0.04}$	$^{+0.01}_{-0.04}$	$^{+4.7}_{-4.6}$	1.0	N/A	1.0	0.0	2.0	$^{+1.1}_{-1.3}$	2.0	1.0
0.51-0.59	$1.3 \cdot 10^{5}$	1.3	0.0	$^{+5.8}_{-5.9}$	$^{+3.9}_{-4.3}$	$^{+2.3}_{-2.2}$	$^{+1.4}_{-1.2}$	$^{+4.0}_{-4.6}$	$^{+2.7}_{-2.9}$	$^{+1.0}_{-0.66}$	$^{+6.0}_{-5.8}$	$^{+2.1}_{-1.9}$	$^{+0.05}_{-0.13}$	$^{+0.0}_{-0.02}$	5.7	0.7	N/A	0.7	0.02	2.0	$^{+1.2}_{-0.85}$	2.0	1.0
0.59-0.67	$5.7 \cdot 10^{4}$	1.4	0.0	$^{+5.5}_{-5.3}$	$^{+3.9}_{-3.6}$	$^{+2.1}_{-2.0}$	$^{+1.3}_{-1.4}$	$^{+4.0}_{-3.9}$	$^{+2.3}_{-2.5}$	$^{+0.77}_{-0.8}$	$^{+6.3}_{-5.7}$	$^{+2.0}_{-2.3}$	$^{+0.12}_{-0.06}$	$^{+0.0}_{-0.01}$	$^{+6.4}_{-5.9}$	0.7	N/A	0.69	0.0	2.0	$^{+0.82}_{-0.92}$	2.0	1.0
0.67-0.76	$2.6 \cdot 10^{4}$	1.1	0.0	$^{+5.1}_{-4.3}$	$^{+4.0}_{-3.4}$	$^{+2.0}_{-1.8}$	$^{+1.6}_{-1.4}$	$^{+4.1}_{-3.2}$	$^{+2.3}_{-2.0}$	$^{+0.8}_{-0.72}$	$^{+6.1}_{-5.7}$	$^{+2.4}_{-2.2}$	0.07	0.0	$^{+6.5}_{-6.1}$	0.3	N/A	0.34	0.31	2.0	$^{+0.78}_{-0.91}$	2.0	1.0
0.76-0.85	$1.3 \cdot 10^{4}$	1.4	0.0	$^{+4.9}_{-5.1}$	4.0	$^{+1.9}_{-1.7}$	$^{+1.9}_{-2.0}$	$^{+3.9}_{-4.4}$	$^{+2.4}_{-2.2}$	$^{+0.63}_{-0.67}$	$^{+6.2}_{-6.3}$	$^{+2.7}_{-3.0}$	$^{+0.15}_{-0.13}$	0.0	$^{+7.2}_{-7.0}$	0.4	N/A	0.4	0.0	2.0	$^{+0.96}_{-0.85}$	2.0	1.0
0.85-0.95	$6.1 \cdot 10^{3}$	1.5	0.0	$^{+5.2}_{-5.0}$	$^{+4.5}_{-4.0}$	1.8	$^{+2.3}_{-2.4}$	$^{+5.1}_{-4.5}$	$^{+2.4}_{-2.3}$	$^{+0.47}_{-0.39}$	$^{+7.7}_{-6.7}$	$^{+3.8}_{-3.4}$	$^{+0.14}_{-0.08}$	0.0	$^{+8.6}_{-8.2}$	0.7	N/A	0.72	0.0	2.0	$^{+0.75}_{-0.77}$	2.0	1.0
0.95-1.06	$3.1 \cdot 10^{3}$	1.6	0.0	$^{+4.8}_{-4.6}$	$^{+3.4}_{-3.3}$	1.7	$^{+2.0}_{-2.2}$	$^{+4.6}_{-4.2}$	1.9	$^{+0.67}_{-0.52}$	$^{+7.1}_{-7.2}$	$^{+3.6}_{-3.5}$	$^{+0.08}_{-0.16}$	0.0	$^{+8.8}_{-8.7}$	0.7	N/A	0.73	0.12	2.0	$^{+0.9}_{-0.79}$	2.0	1.0
1.06-1.18	$1.4 \cdot 10^{3}$	2.1	0.0	$^{+4.1}_{-4.2}$	$^{+2.8}_{-2.6}$	$^{+1.4}_{-1.8}$	$^{+2.5}_{-2.2}$	$^{+3.8}_{-4.5}$	$^{+1.8}_{-2.1}$	$^{+0.48}_{-0.95}$	$^{+7.2}_{-8.0}$	$^{+4.0}_{-4.2}$	$^{+0.16}_{-0.22}$	0.0	9.3	0.3	N/A	0.26	0.0	2.0	$^{+0.66}_{-1.0}$	2.0	1.0
1.18-1.31	$7.2 \cdot 10^{2}$	2.7	0.0	$^{+2.9}_{-4.0}$	$^{+2.4}_{-2.9}$	$^{+1.1}_{-1.8}$	$^{+2.6}_{-3.0}$	$^{+3.5}_{-4.5}$	$^{+1.3}_{-1.9}$	$^{+0.25}_{-0.54}$	$^{+6.7}_{-6.9}$	$^{+3.4}_{-4.4}$	$^{+0.23}_{-0.07}$	0.0	$^{+9.4}_{-8.1}$	0.5	N/A	0.49	0.03	2.0	$^{+0.35}_{-0.89}$	2.0	1.0
1.31-1.45	$3.5 \cdot 10^{2}$	2.9	0.0	$^{+5.6}_{-3.4}$	$^{+4.1}_{-2.7}$	$^{+2.5}_{-1.6}$	$^{+4.1}_{-3.0}$	$^{+6.7}_{-4.6}$	$^{+2.8}_{-1.5}$	$^{+0.9}_{-0.36}$	$^{+9.7}_{-7.0}$	$^{+6.3}_{-4.0}$	$^{+0.18}_{-0.16}$	0.0	$^{+13}_{-8.9}$	2.0	N/A	1.7	0.12	2.0	$^{+1.2}_{-0.48}$	2.0	1.0
1.45-1.6	$1.5 \cdot 10^{2}$	4.5	0.0	$^{+4.2}_{-4.0}$	$^{+3.0}_{-3.1}$	1.5	$^{+3.2}_{-3.3}$	$^{+5.1}_{-4.8}$	$^{+1.8}_{-1.7}$	$^{+0.43}_{-0.38}$	$^{+7.6}_{-7.2}$	$^{+5.1}_{-4.8}$	$^{+0.04}_{-0.12}$	0.0	$^{+10}_{-9.9}$	0.6	N/A	0.58	0.1	2.0	0.46	2.0	1.0
1.6-1.76	$7.3 \cdot 10^{1}$	6.0	0.0	$^{+4.2}_{-4.1}$	$^{+3.2}_{-2.7}$	$^{+1.6}_{-1.1}$	$^{+3.1}_{-2.7}$	$^{+5.8}_{-5.1}$	$^{+2.0}_{-1.4}$	$^{+0.48}_{-0.37}$	$^{+8.1}_{-7.9}$	$^{+5.9}_{-5.2}$	$^{+0.34}_{-0.22}$	0.0	11	0.5	N/A	0.51	0.02	2.0	$^{+0.54}_{-0.42}$	2.0	1.0
1.76-1.94	$2.9 \cdot 10^{1}$	8.5	0.0	4.0	$^{+2.8}_{-3.1}$	$^{+1.4}_{-1.3}$	$^{+2.3}_{-2.9}$	$^{+5.3}_{-6.4}$	$^{+1.5}_{-1.6}$	$^{+0.56}_{-0.43}$	8.5	$^{+5.9}_{-6.3}$	$^{+0.34}_{-0.18}$	0.0	$^{+13}_{-12}$	0.5	N/A	0.47	0.04	2.0	$^{+0.62}_{-0.43}$	2.0	1.0
1.94-2.12	$1.7 \cdot 10^{1}$	11	0.0	$^{+4.3}_{-4.8}$	$^{+3.1}_{-3.9}$	$^{+1.2}_{-2.2}$	$^{+2.8}_{-3.6}$	$^{+7.0}_{-6.9}$	$^{+1.4}_{-2.4}$	$^{+0.61}_{-0.72}$	$^{+9.2}_{-8.6}$	$^{+6.8}_{-7.1}$	$^{+0.36}_{-0.63}$	0.0	13	0.2	N/A	0.17	0.02	2.0	$^{+0.6}_{-0.72}$	2.0	1.0
2.12-2.55	$5.2 \cdot 10^{0}$	16	0.0	$^{+5.0}_{-4.7}$	$^{+2.9}_{-2.6}$	$^{+1.0}_{-1.3}$	$^{+3.0}_{-2.5}$	$^{+6.2}_{-6.6}$	$^{+1.2}_{-1.4}$	$^{+0.24}_{-0.45}$	9.2	6.8	$^{+0.53}_{-1.1}$	0.0	$^{+16}_{-14}$	0.7	N/A	0.71	0.0	2.0	$^{+0.23}_{-0.43}$	2.0	1.0
2.55-3.61	$4.3 \cdot 10^{-1}$	39	0.01	$^{+5.9}_{-5.4}$	$^{+3.0}_{-2.2}$	$^{+1.5}_{-0.82}$	$^{+4.2}_{-3.3}$	$^{+8.9}_{-8.4}$	$^{+2.2}_{-0.95}$	$^{+0.37}_{-0.42}$	$^{+11}_{-10}$	$^{+9.6}_{-8.9}$	$^{+3.4}_{-2.0}$	0.0	$^{+19}_{-17}$	1.0	N/A	1.3	0.0	2.0	$^{+0.26}_{-0.29}$	2.0	1.0

Table B.17: Measured dijet cross section for $R = 0.4$ and $1.0 < y^{*} < 1.5$. See Table B.15 for a description of the columns. This table is available on HEPDATA [187].

m_{12}-bin [TeV]	σ [pb/TeV]	δ_{stat} %	γ_{3}	γ_{9}	γ_{15}	γ_{21}	γ_{27}	γ_{31}	γ_{34}	γ_{40}	γ_{46}	γ_{52}	γ_{58}	γ_{64}	γ_{70}	γ_{74}	γ_{75}	γ_{78}	γ_{82}	γ_{83}	u_{1}	u_{2}	u_{3}
0.26-0.31	$1.3 \cdot 10^{7}$	2.6	$^{+4.2}_{-3.6}$	$^{+8.8}_{-8.6}$	$^{+6.7}_{-6.8}$	$^{+4.1}_{-3.8}$	$^{+1.9}_{-2.1}$	$^{+18}_{-15}$	$^{+2.8}_{-2.7}$	$^{+2.8}_{-2.5}$	$^{+4.5}_{-4.4}$	$^{+0.1}_{-0.01}$	$^{+0.02}_{-0.0}$	$^{+3.2}_{-2.9}$	$^{+0.14}_{-0.07}$	3.0	N/A	2.6	0.22	$^{+2.1}_{-2.0}$	$^{+3.7}_{-3.2}$	2.0	1.0
0.31-0.37	$5.4 \cdot 10^{6}$	1.9	$^{+2.0}_{-1.7}$	$^{+8.4}_{-6.6}$	$^{+7.3}_{-5.6}$	$^{+3.6}_{-2.6}$	$^{+2.2}_{-1.7}$	$^{+15}_{-11}$	$^{+3.4}_{-2.6}$	$^{+2.2}_{-1.9}$	$^{+5.4}_{-4.3}$	$^{+0.17}_{-0.13}$	$^{+0.01}_{-0.03}$	$^{+2.4}_{-2.1}$	$^{+0.62}_{-0.52}$	2.0	N/A	1.6	0.04	2.0	$^{+3.2}_{-2.5}$	2.0	1.0
0.37-0.44	$2.2 \cdot 10^{6}$	1.7	$^{+0.92}_{-0.67}$	$^{+8.3}_{-6.9}$	$^{+6.4}_{-5.3}$	$^{+2.7}_{-2.1}$	2.2	$^{+13}_{-9.6}$	$^{+3.4}_{-2.7}$	$^{+1.9}_{-1.7}$	$^{+5.6}_{-4.8}$	$^{+0.65}_{-0.47}$	0.0	$^{+1.6}_{-1.4}$	$^{+1.7}_{-1.2}$	1.0	N/A	1.5	0.38	2.0	$^{+2.5}_{-2.2}$	2.0	1.0
0.44-0.51	$8.9 \cdot 10^{5}$	1.7	$^{+0.0}_{-0.36}$	$^{+6.8}_{-7.6}$	$^{+4.3}_{-5.6}$	$^{+1.7}_{-2.5}$	$^{+1.4}_{-2.2}$	$^{+9.3}_{-9.4}$	$^{+2.4}_{-3.5}$	$^{+0.9}_{-1.7}$	$^{+4.1}_{-5.7}$	$^{+0.17}_{-0.85}$	$^{+0.03}_{-0.05}$	$^{+0.39}_{-1.0}$	$^{+1.6}_{-3.1}$	0.4	N/A	0.45	0.0	2.0	$^{+1.5}_{-2.4}$	2.0	1.0
0.51-0.59	$3.7 \cdot 10^{5}$	1.6	$^{+0.0}_{-0.08}$	$^{+5.8}_{-6.1}$	$^{+4.2}_{-4.3}$	$^{+2.2}_{-2.8}$	$^{+1.2}_{-1.9}$	6.4	$^{+2.7}_{-3.3}$	$^{+0.99}_{-1.8}$	$^{+4.6}_{-4.7}$	$^{+0.67}_{-1.6}$	$^{+0.02}_{-0.13}$	$^{+0.08}_{-0.64}$	$^{+3.4}_{-3.6}$	1.0	N/A	0.96	0.0	2.0	$^{+1.4}_{-2.6}$	2.0	1.0
0.59-0.67	$1.7 \cdot 10^{5}$	1.9	$^{+0.08}_{-0.02}$	7.0	$^{+5.2}_{-5.0}$	$^{+2.7}_{-2.8}$	$^{+1.7}_{-1.4}$	$^{+6.7}_{-6.6}$	$^{+3.8}_{-3.6}$	$^{+2.1}_{-1.5}$	$^{+6.0}_{-5.7}$	$^{+2.3}_{-1.9}$	$^{+0.06}_{-0.14}$	$^{+0.05}_{-0.02}$	$^{+5.1}_{-4.9}$	0.7	N/A	0.74	0.39	2.0	2.4	2.0	1.0
0.67-0.76	$8.1 \cdot 10^{4}$	1.9	$^{+0.04}_{-0.02}$	$^{+7.4}_{-6.5}$	$^{+4.7}_{-4.3}$	2.2	$^{+1.1}_{-0.97}$	$^{+6.7}_{-6.4}$	$^{+3.2}_{-2.7}$	$^{+1.2}_{-0.89}$	$^{+6.1}_{-5.7}$	$^{+1.6}_{-1.5}$	$^{+0.04}_{-0.07}$	$^{+0.09}_{-0.03}$	$^{+5.4}_{-5.1}$	0.9	N/A	0.9	0.19	2.0	$^{+1.4}_{-1.5}$	2.0	1.0
0.76-0.85	$4.0 \cdot 10^{4}$	2.1	0.0	$^{+8.2}_{-5.8}$	$^{+5.2}_{-4.3}$	$^{+3.8}_{-1.6}$	$^{+1.4}_{-1.2}$	$^{+7.7}_{-5.6}$	$^{+3.7}_{-2.8}$	$^{+1.2}_{-0.95}$	$^{+7.6}_{-5.6}$	$^{+2.8}_{-1.8}$	$^{+0.05}_{-0.14}$	$^{+0.0}_{-0.03}$	$^{+7.2}_{-5.4}$	2.0	N/A	1.7	0.0	2.0	$^{+2.7}_{-1.2}$	2.0	1.0
0.85-0.95	$1.9 \cdot 10^{4}$	2.5	0.0	$^{+7.0}_{-6.3}$	$^{+5.1}_{-4.4}$	$^{+2.8}_{-2.6}$	$^{+1.9}_{-1.7}$	$^{+6.5}_{-5.8}$	3.2	$^{+0.87}_{-0.73}$	$^{+7.1}_{-6.5}$	$^{+2.9}_{-2.6}$	$^{+0.02}_{-0.04}$	$^{+0.0}_{-0.02}$	$^{+7.1}_{-6.6}$	1.0	N/A	1.3	0.0	2.0	$^{+1.7}_{-1.6}$	2.0	1.0
0.95-1.06	$9.5 \cdot 10^{3}$	2.2	0.0	$^{+6.0}_{-5.2}$	$^{+3.9}_{-2.9}$	$^{+1.6}_{-1.2}$	$^{+0.97}_{-1.2}$	$^{+6.2}_{-5.6}$	$^{+2.1}_{-1.6}$	$^{+0.57}_{-0.58}$	$^{+6.4}_{-5.9}$	$^{+2.1}_{-1.5}$	$^{+0.04}_{-0.03}$	$^{+0.01}_{-0.0}$	$^{+6.8}_{-6.3}$	0.9	N/A	0.89	0.0	2.0	$^{+0.42}_{-0.95}$	2.0	1.0
1.06-1.18	$4.6 \cdot 10^{3}$	2.8	0.0	$^{+5.0}_{-6.0}$	$^{+3.5}_{-5.0}$	$^{+1.6}_{-1.8}$	$^{+1.8}_{-2.1}$	$^{+5.7}_{-6.9}$	$^{+2.2}_{-2.9}$	$^{+0.33}_{-1.5}$	$^{+6.3}_{-7.8}$	$^{+2.4}_{-3.4}$	$^{+0.05}_{-0.14}$	0.0	$^{+6.8}_{-9.4}$	0.0	N/A	0.0	0.03	2.0	$^{+1.1}_{-1.7}$	2.0	1.0
1.18-1.31	$2.2 \cdot 10^{3}$	2.9	0.0	$^{+5.5}_{-7.2}$	$^{+4.6}_{-5.7}$	$^{+1.9}_{-2.8}$	$^{+2.5}_{-3.6}$	$^{+6.9}_{-8.2}$	$^{+3.0}_{-4.2}$	$^{+0.87}_{-1.1}$	$^{+7.5}_{-8.5}$	$^{+3.7}_{-4.5}$	$^{+0.21}_{-0.08}$	0.0	$^{+8.8}_{-9.4}$	0.1	N/A	0.14	0.0	2.0	$^{+1.3}_{-1.5}$	2.0	1.0
1.31-1.45	$1.0 \cdot 10^{3}$	3.3	0.0	$^{+6.2}_{-5.7}$	$^{+4.8}_{-3.3}$	$^{+2.0}_{-1.1}$	$^{+2.4}_{-1.4}$	$^{+7.6}_{-7.4}$	$^{+2.6}_{-1.5}$	$^{+0.61}_{-0.45}$	$^{+8.3}_{-7.4}$	$^{+4.4}_{-3.2}$	$^{+0.14}_{-0.12}$	0.0	$^{+9.9}_{-8.8}$	1.0	N/A	1.0	0.23	2.0	$^{+0.98}_{-0.57}$	2.0	1.0
1.45-1.6	$4.9 \cdot 10^{2}$	4.0	0.0	$^{+4.8}_{-3.6}$	$^{+4.0}_{-3.4}$	$^{+1.5}_{-1.3}$	$^{+2.7}_{-1.6}$	5.9	$^{+1.9}_{-1.5}$	$^{+0.12}_{-0.37}$	$^{+7.3}_{-6.8}$	$^{+3.8}_{-3.4}$	$^{+0.0}_{-0.4}$	0.0	$^{+10}_{-8.1}$	2.0	N/A	1.9	0.0	2.0	$^{+0.56}_{-0.21}$	2.0	1.0
1.6-1.76	$2.3 \cdot 10^{2}$	4.5	0.0	$^{+4.2}_{-2.7}$	$^{+2.7}_{-2.9}$	$^{+1.4}_{-1.3}$	$^{+2.8}_{-2.1}$	$^{+7.7}_{-4.0}$	$^{+2.0}_{-1.5}$	$^{+0.8}_{-0.42}$	$^{+8.3}_{-5.0}$	$^{+3.6}_{-3.0}$	$^{+0.22}_{-0.08}$	0.0	$^{+11}_{-7.9}$	2.0	N/A	1.6	0.2	2.0	$^{+1.2}_{-1.1}$	2.0	1.0
1.76-1.94	$9.8 \cdot 10^{1}$	6.5	0.0	$^{+4.1}_{-6.1}$	$^{+2.0}_{-3.6}$	$^{+1.2}_{-0.34}$	$^{+2.2}_{-3.5}$	$^{+7.5}_{-9.1}$	$^{+1.9}_{-1.2}$	$^{+0.34}_{-0.0}$	$^{+9.0}_{-9.7}$	$^{+4.2}_{-5.9}$	$^{+0.15}_{-0.0}$	0.0	11	0.3	N/A	0.32	0.0	2.0	$^{+0.92}_{-0.1}$	2.0	1.0
1.94-2.12	$4.3 \cdot 10^{1}$	9.5	0.0	$^{+4.3}_{-5.7}$	$^{+2.6}_{-3.5}$	$^{+1.7}_{-4.1}$	$^{+2.5}_{-4.3}$	$^{+5.9}_{-8.3}$	$^{+0.62}_{-3.3}$	$^{+0.0}_{-1.4}$	$^{+6.9}_{-10}$	$^{+4.6}_{-6.1}$	$^{+0.04}_{-0.0}$	0.0	$^{+9.9}_{-13}$	0.0	N/A	0.0	0.0	2.0	$^{+0.2}_{-2.5}$	2.0	1.0
2.12-2.33	$2.3 \cdot 10^{1}$	12	0.0	$^{+6.0}_{-5.7}$	$^{+5.0}_{-4.9}$	$^{+1.0}_{-2.0}$	$^{+2.8}_{-3.4}$	$^{+9.4}_{-11}$	$^{+0.78}_{-2.1}$	$^{+0.0}_{-0.44}$	$^{+10}_{-11}$	$^{+7.3}_{-6.3}$	$^{+0.0}_{-0.21}$	0.0	$^{+14}_{-13}$	1.0	N/A	1.2	0.05	2.0	$^{+0.23}_{-0.7}$	2.0	1.0
2.33-2.78	$5.9 \cdot 10^{0}$	14	0.0	$^{+5.7}_{-4.4}$	$^{+3.9}_{-3.3}$	$^{+2.4}_{-1.7}$	$^{+4.2}_{-3.1}$	$^{+9.0}_{-7.9}$	$^{+2.8}_{-1.9}$	$^{+1.1}_{-0.63}$	$^{+9.1}_{-8.7}$	$^{+6.9}_{-6.2}$	$^{+0.73}_{-0.66}$	0.0	12	0.9	N/A	0.9	0.0	2.0	$^{+1.1}_{-0.51}$	2.0	1.0
2.78-3.93	$5.4 \cdot 10^{-1}$	34	0.01	$^{+10}_{-7.1}$	$^{+7.2}_{-4.5}$	$^{+2.3}_{-2.4}$	$^{+6.3}_{-4.3}$	$^{+15}_{-11}$	$^{+2.7}_{-2.0}$	1.2	$^{+17}_{-11}$	$^{+13}_{-9.3}$	$^{+0.84}_{-0.93}$	0.0	$^{+24}_{-17}$	3.0	N/A	3.1	0.0	2.0	1.2	2.0	1.0

Table B.18: Measured dijet cross section for $R = 0.4$ and $1.5 < y^{*} < 2.0$. See Table B.15 for a description of the columns. This table is available on HEPDATA [187].

m_{12}-bin	σ	δ_{stat}	γ_4	γ_{10}	γ_{16}	γ_{22}	γ_{28}	γ_{31}	γ_{35}	γ_{41}	γ_{47}	γ_{53}	γ_{59}	γ_{65}	γ_{71}	γ_{74}	γ_{75}	γ_{79}	γ_{82}	γ_{84}	u_1	u_2	u_3
[TeV]	[pb/TeV]	%																					
0.37-0.44	$5.8 \cdot 10^{6}$	3.9	$^{+5.1}_{-5.2}$	$^{+11}_{-9.3}$	$^{+7.9}_{-7.5}$	$^{+4.1}_{-4.5}$	$^{+2.1}_{-2.7}$	$^{+30}_{-22}$	$^{+2.8}_{-3.2}$	$^{+3.0}_{-3.5}$	5.3	$^{+0.0}_{-0.08}$	$^{+0.02}_{-0.08}$	$^{+3.0}_{-3.7}$	$^{+0.12}_{-0.07}$	5.0	N/A	4.8	0.0	2.1	$^{+5.7}_{-4.3}$	1.0	$^{+1.6}_{-0.44}$
0.44-0.51	$2.6 \cdot 10^{6}$	3.7	$^{+4.7}_{-3.9}$	$^{+11}_{-9.3}$	$^{+8.6}_{-7.6}$	$^{+4.3}_{-3.8}$	$^{+2.4}_{-2.5}$	$^{+28}_{-20}$	$^{+4.0}_{-3.4}$	$^{+3.5}_{-3.0}$	$^{+6.0}_{-5.3}$	$^{+0.28}_{-0.24}$	$^{+0.03}_{-0.02}$	$^{+3.8}_{-3.2}$	$^{+0.44}_{-0.4}$	4.0	N/A	3.7	0.07	2.0	$^{+5.2}_{-4.3}$	1.0	$^{+1.1}_{-0.92}$
0.51-0.59	$1.1 \cdot 10^{6}$	2.7	$^{+2.4}_{-2.0}$	$^{+9.4}_{-7.9}$	$^{+7.6}_{-6.6}$	$^{+3.7}_{-2.6}$	$^{+2.4}_{-2.2}$	$^{+21}_{-16}$	$^{+3.5}_{-3.3}$	$^{+2.7}_{-2.1}$	$^{+5.9}_{-4.9}$	$^{+0.39}_{-0.17}$	$^{+0.02}_{-0.0}$	$^{+2.7}_{-2.2}$	$^{+0.96}_{-0.92}$	2.0	N/A	2.1	0.0	2.0	$^{+3.6}_{-3.7}$	1.0	$^{+0.9}_{-1.1}$
0.59-0.67	$5.2 \cdot 10^{5}$	2.2	$^{+0.99}_{-0.86}$	$^{+8.3}_{-7.3}$	$^{+6.8}_{-5.9}$	$^{+2.9}_{-2.5}$	$^{+2.6}_{-2.2}$	$^{+17}_{-13}$	$^{+3.4}_{-3.0}$	$^{+2.1}_{-1.8}$	$^{+5.4}_{-4.8}$	$^{+0.55}_{-0.41}$	$^{+0.03}_{-0.0}$	$^{+1.6}_{-1.4}$	$^{+1.8}_{-1.6}$	2.0	N/A	1.9	0.14	2.0	$^{+3.1}_{-3.0}$	1.0	$^{+0.96}_{-1.0}$
0.67-0.76	$2.4 \cdot 10^{5}$	2.1	$^{+0.36}_{-0.33}$	$^{+8.1}_{-7.5}$	$^{+6.0}_{-5.9}$	2.8	$^{+2.2}_{-2.1}$	$^{+15}_{-13}$	3.4	$^{+1.6}_{-1.7}$	$^{+5.4}_{-5.6}$	$^{+0.63}_{-0.82}$	$^{+0.02}_{-0.03}$	$^{+0.86}_{-0.98}$	$^{+2.5}_{-2.8}$	3.0	N/A	2.7	1.9	2.0	$^{+2.9}_{-3.1}$	1.0	$^{+0.99}_{-1.0}$
0.76-0.85	$1.2 \cdot 10^{5}$	1.9	$^{+0.04}_{-0.0}$	$^{+7.8}_{-7.4}$	$^{+5.7}_{-5.4}$	$^{+2.5}_{-2.8}$	1.9	$^{+13}_{-11}$	$^{+3.3}_{-3.4}$	$^{+1.5}_{-1.7}$	5.8	$^{+0.91}_{-0.97}$	$^{+0.03}_{-0.06}$	$^{+0.34}_{-0.5}$	$^{+3.4}_{-3.6}$	3.0	N/A	2.6	1.6	2.0	$^{+2.4}_{-2.9}$	1.0	1.0
0.85-0.95	$5.8 \cdot 10^{4}$	1.9	$^{+0.09}_{-0.06}$	$^{+8.1}_{-7.4}$	$^{+5.6}_{-4.9}$	$^{+2.4}_{-2.1}$	$^{+1.7}_{-1.3}$	$^{+12}_{-10}$	$^{+3.4}_{-2.9}$	$^{+1.6}_{-1.3}$	$^{+6.4}_{-5.6}$	$^{+1.4}_{-1.1}$	$^{+0.05}_{-0.07}$	$^{+0.19}_{-0.08}$	$^{+4.4}_{-3.8}$	3.0	N/A	3.1	1.8	2.0	$^{+2.5}_{-2.1}$	1.0	1.0
0.95-1.06	$2.8 \cdot 10^{4}$	2.2	$^{+0.04}_{-0.05}$	$^{+6.9}_{-7.1}$	$^{+4.7}_{-4.9}$	$^{+2.3}_{-2.2}$	$^{+1.1}_{-1.0}$	$^{+9.5}_{-9.2}$	$^{+2.7}_{-3.0}$	$^{+1.2}_{-1.1}$	$^{+5.6}_{-5.7}$	1.3	$^{+0.04}_{-0.01}$	$^{+0.06}_{-0.0}$	4.8	2.0	N/A	2.3	0.43	2.0	$^{+1.9}_{-1.8}$	1.0	1.0
1.06-1.18	$1.4 \cdot 10^{4}$	2.1	0.02	$^{+8.6}_{-7.5}$	$^{+6.1}_{-5.4}$	$^{+3.2}_{-2.7}$	$^{+1.8}_{-1.3}$	$^{+11}_{-9.5}$	$^{+4.3}_{-3.6}$	$^{+1.5}_{-1.1}$	$^{+7.5}_{-6.7}$	$^{+2.4}_{-1.9}$	$^{+0.08}_{-0.0}$	$^{+0.02}_{-0.03}$	$^{+7.0}_{-6.1}$	4.0	N/A	4.3	2.8	2.0	$^{+2.9}_{-2.4}$	1.0	1.0
1.18-1.31	$6.7 \cdot 10^{3}$	2.6	0.0	$^{+8.1}_{-7.3}$	$^{+5.5}_{-5.1}$	$^{+2.6}_{-2.7}$	1.5	$^{+9.7}_{-8.7}$	$^{+3.8}_{-3.4}$	$^{+1.2}_{-1.1}$	$^{+7.3}_{-6.9}$	$^{+2.3}_{-2.2}$	$^{+0.06}_{-0.15}$	$^{+0.01}_{-0.03}$	$^{+6.9}_{-6.7}$	2.0	N/A	1.7	0.86	2.0	2.2	1.0	1.0
1.31-1.45	$3.2 \cdot 10^{3}$	3.1	0.0	$^{+6.4}_{-7.5}$	$^{+4.3}_{-4.9}$	$^{+1.7}_{-2.6}$	$^{+1.1}_{-2.0}$	$^{+8.2}_{-8.8}$	$^{+2.3}_{-3.4}$	$^{+0.71}_{-1.2}$	$^{+6.3}_{-7.5}$	$^{+1.8}_{-2.7}$	$^{+0.01}_{-0.18}$	$^{+0.0}_{-0.01}$	$^{+6.2}_{-7.8}$	0.2	N/A	0.23	0.0	2.0	$^{+1.2}_{-1.8}$	1.0	1.0
1.45-1.6	$1.5 \cdot 10^{3}$	3.9	0.0	$^{+7.7}_{-6.4}$	$^{+5.2}_{-4.3}$	$^{+2.7}_{-2.0}$	$^{+2.2}_{-1.6}$	$^{+10}_{-8.7}$	$^{+3.1}_{-2.6}$	$^{+1.2}_{-0.8}$	$^{+8.3}_{-7.1}$	$^{+3.1}_{-2.3}$	$^{+0.08}_{-0.0}$	$^{+0.0}_{-0.01}$	$^{+9.0}_{-7.6}$	1.0	N/A	1.3	0.36	2.0	$^{+2.0}_{-1.5}$	1.0	1.0
1.6-1.76	$7.3 \cdot 10^{2}$	3.9	0.0	$^{+7.9}_{-6.2}$	$^{+5.8}_{-4.5}$	$^{+3.1}_{-2.4}$	$^{+2.8}_{-2.0}$	$^{+11}_{-8.5}$	$^{+4.1}_{-2.6}$	$^{+1.2}_{-1.1}$	$^{+9.4}_{-7.4}$	$^{+3.9}_{-2.7}$	$^{+0.26}_{-0.29}$	0.0	$^{+10}_{-8.0}$	0.3	N/A	0.3	0.0	2.0	$^{+2.3}_{-1.9}$	1.0	1.0
1.76-1.94	$3.1 \cdot 10^{2}$	4.5	0.0	$^{+5.2}_{-8.1}$	$^{+3.8}_{-6.5}$	$^{+1.6}_{-3.5}$	$^{+1.4}_{-3.2}$	$^{+8.6}_{-11}$	$^{+2.4}_{-4.3}$	$^{+0.8}_{-1.3}$	$^{+7.4}_{-9.7}$	$^{+2.8}_{-5.6}$	$^{+0.13}_{-0.19}$	0.0	$^{+8.5}_{-11}$	0.0	N/A	0.0	0.0	2.0	$^{+0.81}_{-2.3}$	1.0	1.0
1.94-2.12	$1.5 \cdot 10^{2}$	5.9	0.0	$^{+5.1}_{-6.6}$	$^{+4.3}_{-5.5}$	$^{+2.3}_{-2.4}$	$^{+1.7}_{-2.9}$	$^{+9.0}_{-10}$	$^{+1.8}_{-3.1}$	$^{+0.83}_{-1.1}$	$^{+7.9}_{-9.3}$	$^{+3.3}_{-4.3}$	$^{+0.05}_{-0.0}$	0.0	$^{+9.5}_{-11}$	0.7	N/A	0.66	0.0	2.0	$^{+1.2}_{-2.0}$	1.0	1.0
2.12-2.33	$7.3 \cdot 10^{1}$	7.7	0.0	$^{+8.5}_{-5.6}$	$^{+7.1}_{-3.9}$	$^{+4.7}_{-2.1}$	$^{+4.6}_{-2.3}$	$^{+13}_{-9.5}$	$^{+4.3}_{-2.1}$	$^{+0.89}_{-0.95}$	$^{+12}_{-8.8}$	$^{+6.4}_{-3.5}$	$^{+0.21}_{-0.46}$	0.0	$^{+14}_{-9.9}$	2.0	N/A	2.4	0.42	2.0	$^{+3.4}_{-1.3}$	1.0	1.0
2.33-2.55	$2.6 \cdot 10^{1}$	9.7	0.0	$^{+6.6}_{-5.9}$	$^{+4.5}_{-4.6}$	$^{+2.4}_{-3.3}$	$^{+3.0}_{-3.5}$	$^{+12}_{-9.9}$	$^{+2.6}_{-2.7}$	$^{+0.85}_{-1.2}$	$^{+11}_{-8.7}$	$^{+4.9}_{-5.2}$	$^{+0.28}_{-0.37}$	0.0	$^{+14}_{-11}$	1.0	N/A	1.3	0.21	2.0	$^{+1.7}_{-2.0}$	1.0	1.0
2.55-3.04	8.0	12	0.0	$^{+7.6}_{-6.7}$	$^{+5.6}_{-5.2}$	$^{+3.6}_{-3.2}$	$^{+4.8}_{-4.2}$	$^{+14}_{-11}$	$^{+3.7}_{-3.0}$	0.69	$^{+13}_{-11}$	$^{+7.2}_{-6.5}$	$^{+0.14}_{-0.23}$	0.0	$^{+15}_{-14}$	3.0	N/A	2.8	0.08	2.0	$^{+1.7}_{-1.6}$	1.0	1.0
3.04-4.27	$2.3 \cdot 10^{-1}$	51	0.0	$^{+7.4}_{-6.7}$	$^{+5.4}_{-4.8}$	3.4	$^{+5.6}_{-5.1}$	$^{+16}_{-13}$	$^{+2.6}_{-3.3}$	$^{+0.7}_{-0.78}$	$^{+15}_{-13}$	$^{+8.6}_{-8.0}$	$^{+0.3}_{-0.29}$	0.0	$^{+20}_{-18}$	2.0	N/A	2.5	0.18	2.0	$^{+1.3}_{-1.4}$	1.0	1.0

Table B.19: Measured dijet cross section for $R = 0.4$ and $2.0 < y^{*} < 2.5$. See Table B.15 for a description of the columns. This table is available on HEPDATA [187].

m_{12}-bin [TeV]	σ [pb/TeV]	δ_{stat} %	$\gamma 4$	γ_{10}	γ_{16}	γ_{22}	γ_{28}	γ_{31}	γ_{35}	γ_{41}	γ_{47}	γ_{53}	γ_{59}	γ_{65}	γ_{71}	γ_{74}	γ_{75}	γ_{79}	γ_{82}	γ_{84}	u_1	u_2	u_3
0.67-0.76	$7.3 \cdot 10^5$	7.1	$^{+4.9}_{-4.8}$	10	8.0	4.2	$^{+2.8}_{-2.6}$	$^{+43}_{-28}$	$^{+3.5}_{-3.3}$	$^{+3.5}_{-3.3}$	$^{+5.3}_{-5.6}$	$^{+0.19}_{-0.09}$	$^{+0.04}_{-0.01}$	$^{+3.6}_{-3.4}$	$^{+0.35}_{-0.22}$	5.0	N/A	4.8	0.17	2.1	$^{+5.5}_{-5.9}$	1.0	$^{+0.75}_{-1.2}$
0.76-0.85	$3.9 \cdot 10^5$	8.5	$^{+4.2}_{-3.0}$	$^{+11}_{-8.9}$	$^{+9.0}_{-7.4}$	$^{+4.2}_{-3.5}$	$^{+2.7}_{-2.4}$	$^{+39}_{-23}$	$^{+4.1}_{-3.3}$	$^{+3.5}_{-2.6}$	$^{+6.7}_{-5.6}$	$^{+0.16}_{-0.14}$	$^{+0.05}_{-0.0}$	$^{+3.6}_{-2.7}$	$^{+0.68}_{-0.5}$	5.0	N/A	4.7	0.4	2.0	$^{+6.1}_{-4.4}$	1.0	$^{+0.94}_{-1.1}$
0.85-0.95	$1.9 \cdot 10^5$	4.9	$^{+2.5}_{-2.0}$	$^{+10}_{-8.5}$	$^{+9.0}_{-6.9}$	$^{+4.4}_{-3.1}$	2.6	$^{+32}_{-21}$	$^{+3.9}_{-3.6}$	$^{+2.6}_{-2.4}$	$^{+7.2}_{-5.4}$	$^{+0.31}_{-0.25}$	$^{+0.02}_{-0.0}$	$^{+2.5}_{-2.2}$	$^{+1.2}_{-1.1}$	3.0	N/A	3.1	0.11	2.0	$^{+5.6}_{-4.0}$	1.0	$^{+1.1}_{-0.95}$
0.95-1.06	$9.1 \cdot 10^4$	3.3	1.3	$^{+9.4}_{-8.1}$	$^{+7.7}_{-6.6}$	$^{+3.4}_{-3.5}$	$^{+2.6}_{-2.7}$	$^{+25}_{-19}$	$^{+3.6}_{-4.0}$	$^{+2.0}_{-2.4}$	$^{+6.0}_{-5.6}$	$^{+0.56}_{-0.53}$	0.0	$^{+1.7}_{-1.9}$	$^{+2.0}_{-2.1}$	2.0	N/A	2.0	0.08	2.0	$^{+4.2}_{-4.5}$	1.0	$^{+1.0}_{-0.97}$
1.06-1.18	$4.3 \cdot 10^4$	3.4	$^{+0.63}_{-0.61}$	$^{+8.8}_{-8.5}$	$^{+6.5}_{-6.7}$	$^{+3.2}_{-3.6}$	$^{+2.7}_{-2.6}$	$^{+20}_{-17}$	$^{+3.8}_{-4.0}$	$^{+2.2}_{-2.1}$	$^{+5.8}_{-6.3}$	$^{+0.8}_{-0.81}$	$^{+0.09}_{-0.12}$	$^{+1.3}_{-1.2}$	$^{+2.7}_{-3.0}$	2.0	N/A	2.2	0.87	2.0	$^{+3.9}_{-4.5}$	1.0	$^{+1.0}_{-0.99}$
1.18-1.31	$2.1 \cdot 10^4$	3.5	$^{+0.18}_{-0.16}$	$^{+8.6}_{-9.4}$	$^{+6.1}_{-6.9}$	3.5	2.1	$^{+20}_{-17}$	$^{+3.4}_{-3.7}$	1.7	$^{+6.1}_{-6.8}$	$^{+0.84}_{-0.96}$	$^{+0.07}_{-0.08}$	$^{+0.75}_{-0.58}$	$^{+3.2}_{-3.8}$	1.0	N/A	1.2	0.0	2.0	$^{+3.3}_{-4.1}$	1.0	1.0
1.31-1.45	$9.9 \cdot 10^3$	3.0	$^{+0.03}_{-0.06}$	$^{+9.5}_{-8.6}$	$^{+6.7}_{-6.1}$	$^{+3.4}_{-3.2}$	$^{+1.6}_{-1.7}$	$^{+20}_{-15}$	$^{+4.2}_{-3.5}$	1.5	$^{+7.2}_{-6.6}$	$^{+1.1}_{-1.2}$	$^{+0.05}_{-0.08}$	$^{+0.24}_{-0.3}$	$^{+4.9}_{-4.5}$	0.0	N/A	0.0	0.0	2.0	$^{+4.1}_{-3.4}$	1.0	1.0
1.45-1.6	$4.9 \cdot 10^3$	3.4	0.07	$^{+9.4}_{-8.1}$	$^{+6.8}_{-5.8}$	$^{+3.8}_{-3.4}$	$^{+1.8}_{-1.7}$	$^{+16}_{-13}$	$^{+4.4}_{-3.8}$	$^{+1.8}_{-1.6}$	$^{+7.8}_{-6.6}$	$^{+1.8}_{-1.7}$	$^{+0.01}_{-0.12}$	$^{+0.09}_{-0.18}$	$^{+5.9}_{-5.3}$	0.9	N/A	0.93	0.0	2.0	$^{+3.9}_{-3.5}$	1.0	1.0
1.6-1.76	$2.4 \cdot 10^3$	4.2	0.04	$^{+9.2}_{-7.4}$	$^{+6.6}_{-5.2}$	$^{+4.0}_{-3.4}$	$^{+1.6}_{-1.1}$	$^{+15}_{-12}$	$^{+3.9}_{-3.5}$	$^{+1.4}_{-1.1}$	$^{+7.9}_{-6.4}$	$^{+2.0}_{-1.7}$	$^{+0.0}_{-0.09}$	$^{+0.03}_{-0.0}$	$^{+6.7}_{-5.6}$	3.0	N/A	3.4	2.4	2.0	$^{+3.2}_{-2.9}$	1.0	1.0
1.76-1.94	$1.0 \cdot 10^3$	5.5	0.02	$^{+9.5}_{-9.3}$	$^{+6.4}_{-6.7}$	$^{+4.3}_{-4.8}$	$^{+1.8}_{-2.0}$	$^{+15}_{-13}$	$^{+4.2}_{-4.3}$	$^{+1.5}_{-2.2}$	8.5	$^{+2.5}_{-2.8}$	$^{+0.07}_{-0.1}$	$^{+0.08}_{-0.02}$	$^{+7.9}_{-8.0}$	3.0	N/A	3.0	0.92	2.0	$^{+3.1}_{-3.4}$	1.0	1.0
1.94-2.12	$4.7 \cdot 10^2$	6.0	0.0	8.7	$^{+5.9}_{-6.1}$	$^{+4.5}_{-4.3}$	$^{+1.9}_{-1.5}$	13	$^{+4.0}_{-3.6}$	1.5	$^{+8.2}_{-8.4}$	$^{+2.8}_{-2.4}$	$^{+0.17}_{-0.04}$	0.03	$^{+7.9}_{-8.2}$	0.9	N/A	0.89	0.0	2.0	$^{+2.9}_{-2.6}$	1.0	1.0
2.12-2.33	$2.2 \cdot 10^2$	9.0	0.0	$^{+8.9}_{-10}$	$^{+5.9}_{-7.6}$	$^{+4.7}_{-6.1}$	$^{+2.1}_{-4.0}$	$^{+14}_{-15}$	$^{+3.6}_{-5.4}$	$^{+1.3}_{-1.0}$	$^{+9.0}_{-10}$	$^{+2.9}_{-4.7}$	$^{+0.12}_{-0.13}$	$^{+0.0}_{-0.02}$	$^{+9.0}_{-11}$	0.8	N/A	0.76	0.0	2.0	$^{+3.0}_{-4.5}$	1.0	1.0
2.33-2.55	$9.6 \cdot 10^1$	11	0.0	$^{+10}_{-8.3}$	$^{+6.9}_{-5.9}$	$^{+5.5}_{-4.7}$	$^{+2.5}_{-3.1}$	$^{+16}_{-13}$	4.3	$^{+1.3}_{-1.0}$	$^{+11}_{-8.9}$	$^{+3.9}_{-4.1}$	$^{+0.09}_{-0.14}$	0.0	$^{+11}_{-9.7}$	4.0	N/A	4.4	2.6	2.0	$^{+3.6}_{-3.2}$	1.0	1.0
2.55-2.78	$4.6 \cdot 10^1$	19	0.0	$^{+8.0}_{-8.5}$	$^{+5.8}_{-6.5}$	$^{+4.9}_{-5.3}$	$^{+2.4}_{-2.9}$	$^{+16}_{-15}$	$^{+3.8}_{-4.1}$	$^{+0.97}_{-1.6}$	$^{+9.9}_{-10}$	$^{+3.8}_{-4.4}$	$^{+0.07}_{-0.14}$	0.0	$^{+11}_{-12}$	3.0	N/A	3.4	0.67	2.0	$^{+3.0}_{-2.5}$	1.0	1.0
2.78-3.31	8.0	16	0.0	$^{+8.8}_{-7.7}$	$^{+5.7}_{-6.1}$	$^{+4.9}_{-5.1}$	$^{+3.3}_{-2.9}$	$^{+18}_{-16}$	$^{+3.8}_{-3.5}$	$^{+0.83}_{-1.1}$	$^{+12}_{-10}$	4.5	$^{+0.2}_{-0.13}$	0.0	$^{+14}_{-12}$	4.0	N/A	3.5	0.24	2.0	$^{+2.2}_{-3.0}$	1.0	1.0
3.31-4.64	$5.5 \cdot 10^{-1}$	46	0.0	11	$^{+8.5}_{-9.2}$	$^{+8.3}_{-9.1}$	$^{+5.3}_{-5.5}$	$^{+22}_{-21}$	$^{+4.6}_{-4.9}$	$^{+1.7}_{-0.78}$	$^{+16}_{-15}$	$^{+8.5}_{-8.4}$	$^{+0.55}_{-0.13}$	0.0	$^{+19}_{-18}$	3.0	N/A	2.5	0.0	2.0	$^{+4.0}_{-4.7}$	1.0	1.0

Table B.20: Measured dijet cross section for $R = 0.4$ and $2.5 < y^* < 3.0$. See Table B.15 for a description of the columns. This table is available on HEPDATA [187].

m_{12}-bin	σ	δ_{stat}	$\gamma5$	γ_{11}	γ_{17}	γ_{23}	γ_{29}	γ_{31}	γ_{36}	γ_{42}	γ_{48}	γ_{54}	γ_{60}	γ_{66}	γ_{72}	γ_{74}	γ_{75}	γ_{80}	γ_{82}	γ_{85}	u_1	u_2	u_3
[TeV]	[pb/TeV]	%																					
1.18-1.31	$5.6 \cdot 10^4$	6.6	$^{+3.8}_{-4.4}$	$^{+12}_{-11}$	$^{+8.9}_{-8.7}$	$^{+4.7}_{-4.8}$	$^{+2.3}_{-3.0}$	$^{+59}_{-33}$	$^{+3.7}_{-4.2}$	$^{+2.7}_{-3.4}$	$^{+6.0}_{-6.6}$	$^{+0.17}_{-0.16}$	0.02	$^{+2.9}_{-3.5}$	$^{+0.53}_{-0.59}$	6.0	N/A	5.8	0.69	2.0	$^{+6.6}_{-7.1}$	2.0	$^{+0.95}_{-1.1}$
1.31-1.45	$2.6 \cdot 10^4$	6.2	$^{+2.9}_{-3.1}$	$^{+12}_{-10}$	$^{+8.6}_{-8.5}$	$^{+5.3}_{-4.5}$	$^{+2.4}_{-2.9}$	$^{+44}_{-30}$	$^{+4.1}_{-4.5}$	$^{+2.6}_{-2.9}$	$^{+6.3}_{-6.7}$	$^{+0.26}_{-0.27}$	$^{+0.04}_{-0.0}$	$^{+2.8}_{-3.0}$	$^{+1.1}_{-1.2}$	3.0	N/A	3.0	0.7	2.0	$^{+5.6}_{-6.8}$	2.0	$^{+0.78}_{-1.2}$
1.45-1.6	$1.4 \cdot 10^4$	7.2	$^{+2.4}_{-2.1}$	$^{+11}_{-10}$	$^{+8.2}_{-8.3}$	$^{+5.0}_{-4.9}$	$^{+3.2}_{-3.0}$	$^{+40}_{-27}$	$^{+4.6}_{-4.3}$	$^{+3.0}_{-2.8}$	6.7	$^{+0.48}_{-0.44}$	$^{+0.05}_{-0.0}$	$^{+2.9}_{-2.7}$	1.8	3.0	N/A	3.3	1.4	2.0	$^{+5.6}_{-6.3}$	2.0	$^{+0.88}_{-1.1}$
1.6-1.76	$7.2 \cdot 10^3$	7.3	$^{+1.6}_{-1.3}$	11	8.4	5.1	$^{+3.6}_{-3.3}$	$^{+39}_{-25}$	$^{+4.9}_{-4.6}$	$^{+3.1}_{-2.6}$	$^{+7.3}_{-7.2}$	$^{+0.73}_{-0.77}$	0.03	$^{+2.2}_{-1.9}$	2.8	3.0	N/A	3.1	0.94	2.0	$^{+6.1}_{-6.6}$	2.0	$^{+0.96}_{-1.0}$
1.76-1.94	$3.1 \cdot 10^3$	5.0	$^{+0.54}_{-0.43}$	11	$^{+8.5}_{-8.8}$	$^{+5.3}_{-5.5}$	3.2	$^{+34}_{-25}$	$^{+4.7}_{-5.2}$	$^{+2.6}_{-2.4}$	8.0	$^{+0.9}_{-1.1}$	$^{+0.04}_{-0.05}$	$^{+1.0}_{-1.1}$	$^{+3.7}_{-4.3}$	4.0	N/A	3.6	1.8	2.0	$^{+6.3}_{-6.4}$	2.0	$^{+0.99}_{-1.0}$
1.94-2.12	$1.5 \cdot 10^3$	4.4	$^{+0.06}_{-0.02}$	$^{+11}_{-10}$	$^{+7.7}_{-7.8}$	5.5	$^{+2.7}_{-2.5}$	$^{+30}_{-22}$	$^{+4.6}_{-4.7}$	2.1	7.9	$^{+1.2}_{-1.4}$	$^{+0.09}_{-0.06}$	$^{+0.59}_{-0.63}$	$^{+4.6}_{-4.8}$	6.0	N/A	5.7	3.5	2.0	5.4	2.0	1.0
2.12-2.33	$6.4 \cdot 10^2$	5.3	$^{+0.1}_{-0.11}$	$^{+11}_{-9.6}$	$^{+7.5}_{-6.8}$	$^{+5.8}_{-5.4}$	$^{+2.3}_{-1.9}$	$^{+26}_{-20}$	$^{+4.6}_{-4.2}$	$^{+2.1}_{-1.7}$	$^{+8.2}_{-7.5}$	$^{+1.7}_{-1.5}$	$^{+0.1}_{-0.07}$	$^{+0.37}_{-0.42}$	$^{+5.8}_{-5.3}$	0.09	N/A	0.09	0.0	2.0	$^{+5.1}_{-4.8}$	2.0	1.0
2.33-2.55	$2.7 \cdot 10^2$	7.2	$^{+0.0}_{-0.1}$	$^{+10}_{-9.3}$	$^{+7.1}_{-6.8}$	5.7	1.8	$^{+23}_{-20}$	$^{+4.2}_{-4.5}$	$^{+1.7}_{-1.8}$	$^{+8.2}_{-7.9}$	$^{+1.8}_{-2.0}$	$^{+0.05}_{-0.07}$	$^{+0.11}_{-0.28}$	$^{+6.3}_{-6.6}$	0.0	N/A	0.0	0.0	2.0	$^{+4.4}_{-4.7}$	2.0	1.0
2.55-2.78	$1.1 \cdot 10^2$	9.9	$^{+0.0}_{-0.07}$	11	$^{+7.3}_{-7.9}$	$^{+7.0}_{-7.4}$	$^{+1.8}_{-2.6}$	$^{+32}_{-20}$	$^{+4.5}_{-5.5}$	$^{+1.7}_{-2.5}$	$^{+9.4}_{-9.6}$	$^{+2.3}_{-3.1}$	$^{+0.1}_{-0.12}$	$^{+0.02}_{-0.05}$	$^{+8.1}_{-8.6}$	0.0	N/A	0.0	0.0	2.0	$^{+4.4}_{-5.5}$	2.0	1.0
2.78-3.04	$4.3 \cdot 10^1$	11	$^{+0.05}_{-0.04}$	$^{+13}_{-12}$	$^{+9.1}_{-8.0}$	$^{+9.1}_{-8.3}$	$^{+2.2}_{-2.7}$	$^{+30}_{-21}$	$^{+5.9}_{-5.4}$	$^{+1.8}_{-2.3}$	$^{+12}_{-11}$	$^{+3.2}_{-3.5}$	$^{+0.15}_{-0.13}$	$^{+0.07}_{-0.03}$	$^{+11}_{-9.8}$	5.0	N/A	5.1	3.1	2.0	$^{+5.5}_{-5.1}$	2.0	1.0
3.04-3.61	$1.2 \cdot 10^1$	17	$^{+0.03}_{-0.02}$	$^{+14}_{-12}$	$^{+10}_{-8.3}$	$^{+12}_{-9.7}$	$^{+3.1}_{-2.9}$	$^{+28}_{-22}$	$^{+6.7}_{-5.4}$	2.1	$^{+14}_{-12}$	$^{+4.6}_{-4.1}$	$^{+0.09}_{-0.11}$	$^{+0.07}_{-0.05}$	$^{+14}_{-12}$	10	N/A	9.6	5.6	2.0	$^{+5.9}_{-4.5}$	2.0	1.0
3.61-5.04	$4.4 \cdot 10^{-1}$	54	$^{+0.01}_{-0.0}$	$^{+18}_{-15}$	$^{+13}_{-11}$	$^{+17}_{-15}$	$^{+5.0}_{-4.4}$	$^{+35}_{-28}$	$^{+7.7}_{-6.3}$	$^{+2.0}_{-2.5}$	$^{+21}_{-17}$	$^{+7.6}_{-6.1}$	$^{+0.14}_{-0.16}$	0.03	$^{+22}_{-19}$	10	N/A	9.9	2.6	2.0	$^{+5.9}_{-4.6}$	2.0	1.0

Table B.21: Measured dijet cross section for $R = 0.4$ and $3.0 < y^* < 3.5$. See Table B.15 for a description of the columns. This table is available on HEPDATA [187].

m_{12}-bin	σ	δ_{stat}	$\gamma 6$	γ_{12}	γ_{18}	γ_{24}	γ_{30}	γ_{31}	γ_{37}	γ_{43}	γ_{49}	γ_{55}	γ_{61}	γ_{67}	γ_{73}	γ_{74}	γ_{75}	γ_{81}	γ_{82}	γ_{86}	u_1	u_2	u_3
[TeV]	[pb/TeV]	%																					
1.76-1.94	$8.9 \cdot 10^{3}$	13	$^{+6.2}_{-5.2}$	$^{+14}_{-12}$	$^{+10}_{-9.1}$	4.9	$^{+3.2}_{-3.0}$	$^{+100}_{-46}$	$^{+4.4}_{-4.1}$	$^{+4.1}_{-3.8}$	$^{+7.4}_{-6.7}$	$^{+0.07}_{-0.2}$	0.01	$^{+4.3}_{-4.0}$	$^{+0.22}_{-0.48}$	7.0	N/A	6.8	0.0	2.1	$^{+11}_{-8.1}$	2.0	$^{+2.3}_{-0.0}$
1.94-2.12	$3.6 \cdot 10^{3}$	14	$^{+4.3}_{-4.4}$	$^{+13}_{-11}$	$^{+9.5}_{-9.1}$	$^{+4.1}_{-5.1}$	$^{+3.1}_{-2.8}$	$^{+76}_{-37}$	4.1	$^{+3.6}_{-3.3}$	$^{+7.0}_{-6.9}$	$^{+0.06}_{-0.18}$	$^{+0.0}_{-0.02}$	$^{+3.5}_{-3.6}$	$^{+0.58}_{-0.79}$	3.0	N/A	2.8	0.0	2.0	$^{+7.3}_{-6.9}$	2.0	$^{+0.72}_{-1.3}$
2.12-2.33	$1.3 \cdot 10^{3}$	8.9	$^{+1.7}_{-3.0}$	$^{+12}_{-9.6}$	$^{+9.9}_{-8.4}$	$^{+2.8}_{-3.6}$	$^{+2.3}_{-2.0}$	$^{+58}_{-42}$	$^{+3.6}_{-3.5}$	$^{+2.2}_{-2.3}$	6.2	$^{+0.43}_{-0.32}$	0.02	$^{+2.1}_{-2.3}$	$^{+0.81}_{-0.59}$	0.0	N/A	0.0	0.0	2.0	$^{+4.9}_{-6.3}$	2.0	$^{+0.33}_{-1.7}$
2.33-2.55	$6.1 \cdot 10^{2}$	8.8	$^{+1.9}_{-2.4}$	$^{+18}_{-12}$	$^{+13}_{-9.9}$	$^{+2.8}_{-4.1}$	$^{+3.6}_{-3.2}$	$^{+86}_{-42}$	$^{+4.3}_{-4.8}$	$^{+3.1}_{-3.0}$	$^{+7.6}_{-7.9}$	$^{+0.27}_{-0.42}$	$^{+0.05}_{-0.02}$	$^{+2.8}_{-2.5}$	$^{+1.8}_{-2.3}$	1.0	N/A	1.3	0.0	2.0	$^{+6.5}_{-7.9}$	2.0	$^{+0.68}_{-1.3}$
2.55-2.78	$3.0 \cdot 10^{2}$	8.4	$^{+4.0}_{-1.5}$	$^{+18}_{-16}$	13	$^{+4.5}_{-8.3}$	$^{+6.6}_{-7.4}$	$^{+71}_{-41}$	$^{+7.9}_{-8.8}$	$^{+5.8}_{-6.7}$	$^{+11}_{-12}$	$^{+3.5}_{-4.5}$	$^{+0.09}_{-0.03}$	$^{+4.9}_{-5.8}$	$^{+5.8}_{-6.9}$	5.0	N/A	4.9	4.5	2.0	$^{+9.1}_{-11}$	2.0	$^{+0.91}_{-1.1}$
2.78-3.04	$1.0 \cdot 10^{2}$	11	$^{+1.7}_{-0.78}$	$^{+20}_{-15}$	$^{+16}_{-12}$	$^{+9.6}_{-7.3}$	$^{+5.2}_{-5.9}$	$^{+64}_{-37}$	$^{+11}_{-8.2}$	$^{+3.9}_{-5.3}$	$^{+15}_{-12}$	$^{+2.3}_{-2.9}$	$^{+0.06}_{-0.03}$	$^{+2.4}_{-3.7}$	$^{+9.8}_{-7.1}$	10	N/A	13	0.32	2.0	$^{+13}_{-9.2}$	2.0	$^{+0.98}_{-1.0}$
3.04-3.31	$4.0 \cdot 10^{1}$	15	$^{+0.0}_{-0.2}$	$^{+20}_{-14}$	$^{+16}_{-11}$	$^{+7.8}_{-5.7}$	$^{+4.3}_{-3.9}$	$^{+60}_{-34}$	$^{+9.0}_{-6.9}$	$^{+3.3}_{-3.6}$	$^{+14}_{-12}$	$^{+2.0}_{-1.5}$	$^{+0.06}_{-0.02}$	$^{+0.99}_{-0.91}$	$^{+8.9}_{-7.5}$	9.0	N/A	8.7	0.0	2.0	$^{+9.9}_{-6.9}$	2.0	1.0
3.31-3.93	$9.3 \cdot 10^{0}$	21	$^{+0.1}_{-0.33}$	$^{+19}_{-16}$	$^{+13}_{-11}$	$^{+5.6}_{-4.9}$	$^{+3.6}_{-3.2}$	$^{+57}_{-35}$	$^{+7.4}_{-7.2}$	$^{+3.3}_{-3.0}$	$^{+14}_{-13}$	$^{+2.6}_{-2.4}$	$^{+0.15}_{-0.07}$	$^{+0.53}_{-0.12}$	$^{+9.5}_{-9.2}$	5.0	N/A	5.0	0.39	2.0	$^{+6.6}_{-6.5}$	2.0	1.0
3.93-5.47	$8.6 \cdot 10^{-2}$	68	$^{+0.18}_{-0.24}$	$^{+22}_{-18}$	$^{+15}_{-11}$	$^{+9.2}_{-7.9}$	$^{+3.3}_{-3.5}$	$^{+65}_{-36}$	$^{+11}_{-9.2}$	$^{+3.0}_{-3.5}$	$^{+19}_{-15}$	$^{+4.6}_{-4.7}$	$^{+0.12}_{-0.15}$	$^{+0.22}_{-0.0}$	$^{+17}_{-13}$	20	N/A	17	13	2.0	$^{+7.4}_{-6.0}$	2.0	1.0

Table B.22: Measured dijet cross section for $R = 0.4$ and $3.5 < y^{*} < 4.0$. See Table B.15 for a description of the columns. This table is available on HEPDATA [187].

m_{12}-bin [TeV]	σ [pb/TeV]	δ_{stat} %	$\gamma 6$	γ_{12}	γ_{18}	γ_{24}	γ_{30}	γ_{31}	γ_{37}	γ_{43}	γ_{49}	γ_{55}	γ_{61}	γ_{67}	γ_{73}	γ_{74}	γ_{75}	γ_{81}	γ_{82}	γ_{86}	u_1	u_2	u_3
2.55-3.04	$2.6 \cdot 10^2$	21	$^{+5.8}_{-6.2}$	$^{+16}_{-14}$	12	$^{+2.0}_{-2.4}$	$^{+2.8}_{-3.1}$	$^{+120}_{-59}$	$^{+4.5}_{-4.7}$	$^{+3.9}_{-4.0}$	$^{+7.7}_{-8.4}$	$^{+0.08}_{-0.29}$	0.0	$^{+4.1}_{-4.5}$	$^{+0.42}_{-0.87}$	7.0	N/A	7.2	3.2	$^{+2.1}_{-2.0}$	$^{+8.9}_{-9.0}$	2.0	1.0
3.04-4.27	$1.8 \cdot 10^1$	24	$^{+3.9}_{-2.8}$	$^{+18}_{-15}$	$^{+14}_{-13}$	$^{+4.2}_{-2.6}$	$^{+5.8}_{-4.3}$	$^{+110}_{-50}$	7.7	$^{+5.4}_{-3.1}$	11	$^{+2.1}_{-1.1}$	$^{+0.0}_{-0.28}$	$^{+5.1}_{-3.0}$	$^{+4.1}_{-2.5}$	3.0	N/A	2.9	4.1	2.0	$^{+7.9}_{-9.3}$	2.0	1.0

Table B.23: Measured dijet cross section for $R = 0.4$ and $4.0 < y^* < 4.4$. See Table B.15 for a description of the columns. This table is available on HEPDATA [187].

m_{12}-bin [TeV]	σ [pb/TeV]	δ_{stat} %	γ_1	γ_7	γ_{13}	γ_{19}	γ_{25}	γ_{31}	γ_{32}	γ_{38}	γ_{44}	γ_{50}	γ_{56}	γ_{62}	γ_{68}	γ_{74}	γ_{75}	γ_{76}	γ_{82}	γ_{83}	u_1	u_2	u_3
0.07-0.11	$4.6 \cdot 10^{8}$	0.97	$^{+6.9}_{-6.2}$	$^{+9.3}_{-8.5}$	$^{+9.6}_{-8.6}$	$^{+5.6}_{-5.1}$	$^{+2.4}_{-2.3}$	$^{+9.6}_{-7.5}$	$^{+2.7}_{-2.6}$	$^{+3.1}_{-2.9}$	$^{+4.5}_{-4.3}$	$^{+0.03}_{-0.02}$	0.0	$^{+3.3}_{-3.1}$	$^{+0.11}_{-0.12}$	3.0	N/A	2.8	0.45	2.1	$^{+5.5}_{-4.9}$	1.0	1.0
0.11-0.16	$5.6 \cdot 10^{7}$	0.59	$^{+0.91}_{-0.87}$	$^{+6.9}_{-6.5}$	$^{+5.2}_{-4.8}$	$^{+3.2}_{-2.9}$	$^{+2.5}_{-2.4}$	$^{+4.9}_{-4.2}$	$^{+2.8}_{-2.6}$	1.7	$^{+4.3}_{-4.1}$	$^{+0.22}_{-0.25}$	$^{+0.04}_{-0.03}$	$^{+2.0}_{-1.9}$	$^{+0.74}_{-0.76}$	0.9	N/A	0.89	0.17	2.0	$^{+2.8}_{-2.9}$	1.0	1.0
0.16-0.21	$1.1 \cdot 10^{7}$	0.44	$^{+0.57}_{-0.6}$	$^{+6.0}_{-5.6}$	$^{+2.9}_{-2.7}$	2.1	$^{+2.5}_{-2.3}$	$^{+3.1}_{-2.9}$	$^{+3.0}_{-2.9}$	1.3	$^{+4.8}_{-4.5}$	$^{+0.92}_{-0.86}$	$^{+0.05}_{-0.03}$	$^{+0.47}_{-0.49}$	$^{+2.9}_{-2.7}$	0.6	N/A	0.58	0.15	2.0	$^{+1.9}_{-2.2}$	1.0	1.0
0.21-0.26	$2.9 \cdot 10^{6}$	0.6	$^{+0.14}_{-0.15}$	$^{+5.7}_{-5.3}$	$^{+2.8}_{-2.9}$	$^{+1.9}_{-2.0}$	1.1	2.3	$^{+2.6}_{-2.7}$	$^{+0.99}_{-1.1}$	$^{+5.0}_{-4.7}$	$^{+1.3}_{-1.4}$	$^{+0.03}_{-0.07}$	$^{+0.04}_{-0.03}$	$^{+3.7}_{-3.6}$	0.5	N/A	0.51	0.05	2.0	$^{+1.6}_{-1.7}$	1.0	1.0
0.26-0.31	$1.0 \cdot 10^{6}$	0.65	0.03	$^{+5.2}_{-4.7}$	$^{+2.7}_{-2.4}$	$^{+2.0}_{-1.7}$	$^{+0.76}_{-0.69}$	$^{+2.3}_{-2.1}$	$^{+2.6}_{-2.3}$	$^{+0.89}_{-0.69}$	$^{+5.3}_{-5.0}$	$^{+1.7}_{-1.6}$	$^{+0.04}_{-0.03}$	$^{+0.03}_{-0.0}$	$^{+4.6}_{-4.4}$	0.6	N/A	0.65	0.06	2.0	$^{+1.3}_{-1.1}$	1.0	1.0
0.31-0.37	$3.8 \cdot 10^{5}$	0.54	0.0	$^{+4.7}_{-4.5}$	$^{+2.5}_{-2.4}$	$^{+2.0}_{-1.9}$	$^{+1.1}_{-1.0}$	$^{+2.2}_{-2.1}$	$^{+2.5}_{-2.3}$	$^{+0.78}_{-0.71}$	5.4	$^{+2.1}_{-2.0}$	0.11	0.02	5.3	0.4	N/A	0.45	0.07	2.0	$^{+1.2}_{-1.3}$	1.0	1.0
0.37-0.44	$1.4 \cdot 10^{5}$	0.5	0.0	$^{+3.7}_{-3.4}$	$^{+3.0}_{-2.8}$	$^{+1.6}_{-1.3}$	$^{+1.6}_{-1.3}$	$^{+2.4}_{-2.0}$	$^{+2.2}_{-2.0}$	$^{+0.69}_{-0.63}$	$^{+6.0}_{-5.3}$	$^{+2.5}_{-2.2}$	$^{+0.1}_{-0.12}$	0.0	$^{+6.3}_{-5.6}$	0.6	N/A	0.55	0.09	2.0	$^{+1.2}_{-0.99}$	1.0	1.0
0.44-0.51	$5.8 \cdot 10^{4}$	0.59	0.0	$^{+3.9}_{-3.6}$	$^{+3.4}_{-3.1}$	$^{+1.4}_{-1.3}$	$^{+2.2}_{-2.0}$	$^{+2.2}_{-2.1}$	$^{+2.3}_{-2.1}$	$^{+0.61}_{-0.57}$	$^{+6.3}_{-5.7}$	$^{+3.1}_{-2.9}$	$^{+0.21}_{-0.15}$	0.0	$^{+7.1}_{-6.4}$	0.4	N/A	0.45	0.0	2.0	$^{+0.99}_{-1.1}$	1.0	1.0
0.51-0.59	$2.4 \cdot 10^{4}$	0.67	0.0	$^{+4.5}_{-4.6}$	$^{+2.6}_{-2.8}$	1.3	$^{+2.2}_{-2.5}$	$^{+1.9}_{-2.1}$	$^{+1.8}_{-1.9}$	$^{+0.51}_{-0.5}$	6.4	$^{+3.2}_{-3.4}$	$^{+0.19}_{-0.14}$	0.0	$^{+7.5}_{-7.6}$	0.2	N/A	0.19	0.0	2.0	1.0	1.0	1.0
0.59-0.67	$1.1 \cdot 10^{4}$	1.0	0.0	$^{+3.6}_{-3.5}$	2.2	$^{+0.91}_{-0.98}$	$^{+2.4}_{-2.5}$	$^{+1.7}_{-1.9}$	$^{+1.5}_{-1.7}$	$^{+0.39}_{-0.35}$	6.2	3.3	$^{+0.13}_{-0.16}$	0.0	$^{+7.8}_{-7.4}$	0.4	N/A	0.41	0.0	2.0	$^{+0.6}_{-0.7}$	1.0	1.0
0.67-0.76	$4.8 \cdot 10^{3}$	1.3	0.0	$^{+3.6}_{-3.5}$	$^{+3.0}_{-2.9}$	$^{+0.96}_{-0.85}$	$^{+2.9}_{-2.7}$	$^{+1.9}_{-1.8}$	$^{+1.7}_{-1.6}$	$^{+0.45}_{-0.37}$	$^{+6.9}_{-6.6}$	4.1	$^{+0.21}_{-0.16}$	0.0	$^{+8.8}_{-8.3}$	0.4	N/A	0.36	0.08	2.0	$^{+0.73}_{-0.6}$	1.0	1.0
0.76-0.85	$2.3 \cdot 10^{3}$	1.7	0.0	$^{+3.8}_{-4.1}$	$^{+3.5}_{-3.7}$	$^{+0.54}_{-0.64}$	$^{+2.4}_{-2.5}$	$^{+1.8}_{-1.9}$	1.6	$^{+0.31}_{-0.44}$	$^{+6.4}_{-6.6}$	$^{+4.2}_{-4.4}$	$^{+0.14}_{-0.18}$	0.0	8.5	0.08	N/A	0.08	0.0	2.0	$^{+0.56}_{-0.65}$	1.0	1.0
0.85-0.95	$1.1 \cdot 10^{3}$	2.1	0.0	$^{+4.2}_{-4.1}$	3.1	$^{+0.61}_{-0.75}$	$^{+2.2}_{-2.3}$	1.7	1.5	$^{+0.32}_{-0.37}$	$^{+6.7}_{-6.2}$	$^{+4.6}_{-4.5}$	$^{+0.11}_{-0.23}$	0.0	$^{+9.1}_{-8.3}$	0.4	N/A	0.35	0.0	2.0	$^{+0.48}_{-0.57}$	1.0	1.0
0.95-1.06	$5.5 \cdot 10^{2}$	2.7	0.0	$^{+4.2}_{-4.0}$	$^{+2.3}_{-2.1}$	$^{+0.95}_{-0.9}$	2.3	$^{+1.9}_{-1.6}$	1.5	$^{+0.38}_{-0.42}$	$^{+7.1}_{-6.8}$	$^{+5.2}_{-4.8}$	$^{+0.24}_{-0.23}$	0.0	$^{+10}_{-9.1}$	0.4	N/A	0.43	0.07	2.0	$^{+0.57}_{-0.59}$	1.0	1.0
1.06-1.18	$2.6 \cdot 10^{2}$	3.6	0.0	$^{+3.7}_{-3.3}$	$^{+1.8}_{-1.6}$	$^{+0.95}_{-0.78}$	$^{+2.9}_{-2.6}$	$^{+1.8}_{-1.6}$	$^{+1.5}_{-1.3}$	$^{+0.41}_{-0.32}$	$^{+7.4}_{-7.2}$	5.6	$^{+0.55}_{-0.42}$	0.0	10	0.2	N/A	0.25	0.0	2.0	$^{+0.58}_{-0.44}$	1.0	1.0
1.18-1.31	$1.3 \cdot 10^{2}$	5.0	0.0	$^{+2.2}_{-2.5}$	$^{+1.7}_{-2.0}$	$^{+0.81}_{-0.73}$	$^{+2.6}_{-3.0}$	$^{+1.2}_{-1.5}$	$^{+1.0}_{-1.1}$	$^{+0.39}_{-0.45}$	$^{+7.2}_{-6.9}$	$^{+5.8}_{-5.6}$	$^{+0.52}_{-0.59}$	0.0	11	0.1	N/A	0.1	0.0	2.0	$^{+0.49}_{-0.46}$	1.0	1.0
1.31-1.45	$5.4 \cdot 10^{1}$	7.0	0.0	$^{+2.4}_{-2.7}$	$^{+2.0}_{-2.3}$	$^{+0.51}_{-0.55}$	$^{+3.0}_{-3.1}$	$^{+1.2}_{-1.3}$	$^{+1.1}_{-1.2}$	$^{+0.29}_{-0.37}$	$^{+7.2}_{-7.3}$	$^{+6.0}_{-6.1}$	$^{+0.94}_{-0.96}$	0.0	11	0.09	N/A	0.09	0.0	2.0	$^{+0.28}_{-0.4}$	1.0	1.0
1.45-1.6	$2.2 \cdot 10^{1}$	9.8	0.0	$^{+3.5}_{-3.4}$	$^{+2.6}_{-2.3}$	$^{+0.33}_{-0.31}$	$^{+2.9}_{-2.8}$	$^{+1.1}_{-1.2}$	$^{+1.1}_{-0.98}$	$^{+0.33}_{-0.29}$	$^{+8.1}_{-7.6}$	$^{+6.5}_{-6.2}$	$^{+1.3}_{-1.2}$	0.0	$^{+12}_{-11}$	0.3	N/A	0.32	0.0	2.0	$^{+0.32}_{-0.3}$	1.0	1.0
1.6-1.94	$9.2 \cdot 10^{0}$	11	0.0	$^{+4.2}_{-4.3}$	$^{+2.9}_{-3.0}$	$^{+0.3}_{-0.49}$	$^{+2.9}_{-3.0}$	1.0	$^{+0.95}_{-1.2}$	$^{+0.33}_{-0.49}$	$^{+8.7}_{-8.1}$	$^{+7.2}_{-6.9}$	$^{+2.1}_{-2.5}$	0.0	$^{+14}_{-13}$	0.3	N/A	0.31	0.0	2.0	$^{+0.33}_{-0.46}$	1.0	1.0
1.94-2.78	$9.2 \cdot 10^{-1}$	29	0.0	$^{+4.2}_{-3.8}$	$^{+3.6}_{-3.4}$	$^{+0.61}_{-0.53}$	$^{+3.0}_{-2.7}$	$^{+0.74}_{-0.68}$	$^{+0.95}_{-0.86}$	$^{+0.47}_{-0.43}$	$^{+9.0}_{-8.2}$	$^{+8.2}_{-7.5}$	$^{+4.7}_{-4.5}$	0.0	$^{+17}_{-14}$	0.8	N/A	0.85	0.09	2.0	$^{+0.29}_{-0.28}$	1.0	1.0

Table B.24: Measured dijet cross section for $R = 0.6$ and $y^* < 0.5$. See Table B.15 for a description of the columns. This table is available on HEPDATA [187].

m_{12}-bin	σ	δ_{stat}	γ_1	γ_7	γ_{13}	γ_{19}	γ_{25}	γ_{31}	γ_{32}	γ_{38}	γ_{44}	γ_{50}	γ_{56}	γ_{62}	γ_{68}	γ_{74}	γ_{75}	γ_{76}	γ_{82}	γ_{83}	u_1	u_2	u_3
[TeV]	[pb/TeV]	%																					
0.11-0.16	$1.4 \cdot 10^8$	0.91	$^{+5.3}_{-4.9}$	$^{+8.8}_{-8.1}$	$^{+8.8}_{-8.0}$	$^{+4.9}_{-4.6}$	$^{+2.2}_{-2.3}$	$^{+9.1}_{-7.8}$	$^{+2.5}_{-2.6}$	2.7	$^{+4.4}_{-4.2}$	$^{+0.07}_{-0.03}$	$^{+0.0}_{-0.01}$	2.8	$^{+0.07}_{-0.06}$	2.0	N/A	2.3	0.28	2.1	$^{+5.3}_{-4.6}$	1.0	1.0
0.16-0.21	$2.5 \cdot 10^7$	0.69	1.2	$^{+6.4}_{-6.0}$	$^{+3.3}_{-3.1}$	2.0	2.4	$^{+4.0}_{-3.6}$	$^{+3.0}_{-2.9}$	$^{+1.2}_{-1.1}$	$^{+4.4}_{-4.3}$	$^{+0.43}_{-0.38}$	0.03	1.2	1.4	0.07	N/A	0.07	0.0	1.9	$^{+1.8}_{-2.6}$	1.0	1.0
0.21-0.26	$7.1 \cdot 10^6$	0.59	$^{+0.58}_{-0.59}$	$^{+5.8}_{-5.4}$	$^{+2.8}_{-2.5}$	$^{+2.0}_{-1.9}$	$^{+2.4}_{-2.1}$	$^{+3.1}_{-2.9}$	$^{+2.8}_{-2.6}$	$^{+1.2}_{-1.1}$	$^{+4.4}_{-4.3}$	$^{+0.82}_{-0.83}$	$^{+0.06}_{-0.04}$	0.43	$^{+2.7}_{-2.5}$	0.6	N/A	0.63	0.0	2.0	$^{+2.0}_{-2.1}$	1.0	1.0
0.26-0.31	$2.5 \cdot 10^6$	0.49	$^{+0.12}_{-0.13}$	$^{+6.0}_{-5.9}$	$^{+3.1}_{-3.0}$	2.1	$^{+1.5}_{-1.3}$	$^{+3.1}_{-3.0}$	$^{+2.8}_{-2.7}$	$^{+1.2}_{-1.1}$	$^{+5.3}_{-5.1}$	1.3	0.04	$^{+0.22}_{-0.04}$	$^{+3.9}_{-3.8}$	0.6	N/A	0.61	0.0	2.0	2.1	1.0	1.0
0.31-0.37	$9.4 \cdot 10^5$	0.61	0.02	$^{+5.5}_{-5.4}$	$^{+2.7}_{-2.8}$	2.0	$^{+0.87}_{-0.91}$	$^{+2.6}_{-2.8}$	2.6	$^{+0.92}_{-0.94}$	$^{+5.1}_{-5.2}$	1.6	$^{+0.06}_{-0.1}$	$^{+0.01}_{-0.02}$	$^{+4.2}_{-4.4}$	0.5	N/A	0.48	0.15	2.0	$^{+1.6}_{-1.7}$	1.0	1.0
0.37-0.44	$3.5 \cdot 10^5$	0.73	0.0	$^{+5.1}_{-4.8}$	$^{+2.6}_{-2.7}$	$^{+1.9}_{-1.7}$	$^{+1.0}_{-0.94}$	$^{+2.7}_{-2.6}$	2.5	$^{+0.83}_{-0.68}$	$^{+5.6}_{-5.4}$	$^{+1.9}_{-1.8}$	$^{+0.07}_{-0.06}$	$^{+0.0}_{-0.03}$	$^{+5.3}_{-5.2}$	0.5	N/A	0.54	0.08	2.0	$^{+1.3}_{-1.4}$	1.0	1.0
0.44-0.51	$1.4 \cdot 10^5$	0.71	0.0	$^{+4.5}_{-4.0}$	$^{+3.0}_{-2.7}$	1.6	1.3	$^{+2.8}_{-2.4}$	$^{+2.4}_{-2.3}$	$^{+0.75}_{-0.72}$	$^{+6.1}_{-5.5}$	$^{+2.4}_{-2.2}$	$^{+0.1}_{-0.13}$	0.0	$^{+6.3}_{-5.8}$	0.6	N/A	0.63	0.17	2.0	$^{+1.2}_{-1.4}$	1.0	1.0
0.51-0.59	$5.9 \cdot 10^4$	0.74	0.0	3.9	$^{+3.2}_{-3.1}$	$^{+1.4}_{-1.5}$	$^{+1.7}_{-1.8}$	$^{+2.8}_{-2.6}$	2.2	0.68	$^{+6.3}_{-6.1}$	2.8	$^{+0.17}_{-0.12}$	0.0	$^{+6.9}_{-6.7}$	0.5	N/A	0.54	0.06	2.0	$^{+1.3}_{-1.2}$	1.0	1.0
0.59-0.67	$2.6 \cdot 10^4$	0.82	0.0	$^{+4.2}_{-3.6}$	$^{+3.3}_{-2.8}$	1.3	$^{+2.3}_{-2.0}$	$^{+2.8}_{-2.6}$	2.1	0.56	$^{+6.9}_{-5.6}$	$^{+3.2}_{-2.8}$	$^{+0.13}_{-0.14}$	0.0	$^{+7.9}_{-6.6}$	0.7	N/A	0.7	0.1	2.0	$^{+1.0}_{-1.2}$	1.0	1.0
0.67-0.76	$1.2 \cdot 10^4$	1.0	0.0	$^{+4.1}_{-4.0}$	2.8	$^{+1.1}_{-1.0}$	$^{+2.4}_{-2.5}$	$^{+2.3}_{-2.4}$	$^{+2.0}_{-1.8}$	$^{+0.4}_{-0.43}$	$^{+6.3}_{-6.5}$	$^{+3.4}_{-3.5}$	$^{+0.1}_{-0.15}$	0.0	$^{+7.7}_{-7.9}$	0.2	N/A	0.21	0.12	2.0	$^{+0.98}_{-0.93}$	1.0	1.0
0.76-0.85	$5.6 \cdot 10^3$	1.2	0.0	$^{+4.3}_{-4.1}$	$^{+2.8}_{-2.9}$	$^{+1.0}_{-1.2}$	$^{+2.9}_{-3.0}$	2.8	$^{+1.9}_{-2.0}$	$^{+0.34}_{-0.57}$	$^{+7.1}_{-6.8}$	$^{+4.1}_{-3.8}$	$^{+0.17}_{-0.22}$	0.0	$^{+8.5}_{-8.3}$	0.4	N/A	0.37	0.0	2.0	$^{+0.87}_{-1.1}$	1.0	1.0
0.85-0.95	$2.7 \cdot 10^3$	1.4	0.0	$^{+4.3}_{-4.2}$	$^{+3.4}_{-3.0}$	$^{+0.93}_{-0.81}$	$^{+3.1}_{-2.8}$	$^{+3.0}_{-2.7}$	$^{+1.8}_{-1.7}$	$^{+0.56}_{-0.34}$	$^{+7.4}_{-7.0}$	$^{+4.6}_{-4.3}$	$^{+0.23}_{-0.07}$	0.0	$^{+9.6}_{-9.0}$	0.4	N/A	0.43	0.17	2.0	$^{+0.82}_{-0.61}$	1.0	1.0
0.95-1.06	$1.3 \cdot 10^3$	1.8	0.0	$^{+4.0}_{-4.1}$	3.5	$^{+0.74}_{-0.64}$	2.8	$^{+2.6}_{-2.7}$	$^{+1.6}_{-1.7}$	$^{+0.38}_{-0.39}$	$^{+7.3}_{-7.1}$	$^{+4.4}_{-4.6}$	$^{+0.13}_{-0.2}$	0.0	$^{+9.3}_{-9.0}$	0.2	N/A	0.19	0.0	2.0	$^{+0.62}_{-0.63}$	1.0	1.0
1.06-1.18	$6.4 \cdot 10^2$	2.6	0.0	$^{+4.1}_{-4.0}$	$^{+3.2}_{-3.0}$	$^{+0.7}_{-0.71}$	$^{+2.3}_{-2.2}$	$^{+2.6}_{-2.5}$	$^{+1.5}_{-1.4}$	$^{+0.33}_{-0.39}$	$^{+6.8}_{-6.6}$	4.7	$^{+0.18}_{-0.16}$	0.0	$^{+9.4}_{-8.8}$	0.5	N/A	0.49	0.0	2.0	$^{+0.58}_{-0.65}$	1.0	1.0
1.18-1.31	$3.0 \cdot 10^2$	3.5	0.0	$^{+4.5}_{-4.6}$	2.9	$^{+1.2}_{-1.3}$	$^{+2.5}_{-2.7}$	$^{+2.8}_{-3.2}$	$^{+1.6}_{-1.8}$	$^{+0.49}_{-0.52}$	$^{+7.5}_{-7.4}$	$^{+5.2}_{-5.3}$	$^{+0.36}_{-0.42}$	0.0	$^{+11}_{-9.9}$	0.3	N/A	0.25	0.0	2.0	$^{+0.76}_{-0.71}$	1.0	1.0
1.31-1.45	$1.4 \cdot 10^2$	4.8	0.0	$^{+3.9}_{-3.3}$	$^{+2.0}_{-1.9}$	$^{+1.0}_{-0.88}$	$^{+2.4}_{-2.1}$	$^{+2.7}_{-2.4}$	$^{+1.3}_{-1.1}$	$^{+0.45}_{-0.26}$	$^{+7.6}_{-6.6}$	$^{+5.3}_{-5.0}$	$^{+0.24}_{-0.18}$	0.0	$^{+11}_{-10}$	0.5	N/A	0.49	0.02	2.0	$^{+0.59}_{-0.34}$	1.0	1.0
1.45-1.6	$6.5 \cdot 10^1$	7.1	0.0	$^{+3.9}_{-2.5}$	$^{+2.4}_{-1.5}$	$^{+0.97}_{-0.87}$	$^{+3.6}_{-2.3}$	$^{+3.5}_{-2.1}$	$^{+1.3}_{-1.0}$	$^{+0.37}_{-0.4}$	$^{+8.8}_{-6.3}$	$^{+7.0}_{-4.9}$	$^{+0.62}_{-0.46}$	0.0	$^{+13}_{-10}$	1.0	N/A	1.1	0.14	2.0	$^{+0.45}_{-0.51}$	1.0	1.0
1.6-1.76	$3.0 \cdot 10^1$	8.4	0.0	$^{+2.7}_{-3.2}$	$^{+1.9}_{-2.2}$	$^{+0.81}_{-1.0}$	$^{+3.1}_{-3.4}$	$^{+2.8}_{-3.1}$	$^{+1.4}_{-1.3}$	$^{+0.35}_{-0.44}$	$^{+7.7}_{-7.9}$	6.5	$^{+1.0}_{-0.88}$	0.0	$^{+13}_{-12}$	0.2	N/A	0.18	0.13	2.0	$^{+0.55}_{-0.64}$	1.0	1.0
1.76-2.12	$9.2 \cdot 10^0$	13	0.0	$^{+3.3}_{-3.6}$	$^{+1.9}_{-2.2}$	$^{+0.49}_{-0.37}$	$^{+3.1}_{-3.2}$	$^{+3.0}_{-3.2}$	$^{+1.1}_{-1.3}$	$^{+0.36}_{-0.32}$	$^{+8.3}_{-8.4}$	$^{+6.5}_{-6.8}$	$^{+1.4}_{-1.6}$	0.0	$^{+14}_{-13}$	0.2	N/A	0.24	0.12	2.0	$^{+0.41}_{-0.36}$	1.0	1.0
2.12-3.31	$1.1 \cdot 10^0$	20	0.0	$^{+5.1}_{-5.0}$	$^{+2.2}_{-2.1}$	$^{+0.41}_{-0.33}$	$^{+3.5}_{-3.4}$	$^{+3.2}_{-3.1}$	$^{+0.97}_{-0.93}$	$^{+0.42}_{-0.37}$	$^{+10}_{-9.2}$	$^{+8.2}_{-7.9}$	3.7	0.0	$^{+17}_{-16}$	0.6	N/A	0.61	0.0	2.0	$^{+0.38}_{-0.34}$	1.0	1.0

Table B.25: Measured dijet cross section for $R = 0.6$ and $0.5 < y^* < 1.0$. See Table B.15 for a description of the columns. This table is available on HEPDATA [187].

m_{12}-bin	σ	δ_{stat}	γ_{2}	γ_{8}	γ_{14}	γ_{20}	γ_{26}	γ_{31}	γ_{33}	γ_{39}	γ_{45}	γ_{51}	γ_{57}	γ_{63}	γ_{69}	γ_{74}	γ_{75}	γ_{77}	γ_{82}	γ_{83}	u_{1}	u_{2}	u_{3}
[TeV]	[pb/TeV]	%																					
0.16-0.21	$7.9 \cdot 10^{7}$	1.5	$^{+6.2}_{-5.8}$	$^{+9.3}_{-8.9}$	$^{+9.7}_{-8.9}$	$^{+5.2}_{-5.0}$	$^{+2.6}_{-2.5}$	$^{+12}_{-11}$	2.8	$^{+3.1}_{-3.0}$	4.7	$^{+0.01}_{-0.06}$	$^{+0.01}_{-0.0}$	3.2	$^{+0.0}_{-0.02}$	3.0	N/A	2.8	0.4	2.1	$^{+6.5}_{-5.7}$	2.0	1.0
0.21-0.26	$2.2 \cdot 10^{7}$	0.99	$^{+0.48}_{-0.62}$	$^{+8.0}_{-7.0}$	$^{+5.5}_{-5.2}$	$^{+3.2}_{-3.3}$	$^{+2.4}_{-2.5}$	$^{+7.3}_{-6.4}$	$^{+3.2}_{-3.3}$	$^{+2.0}_{-1.7}$	$^{+4.8}_{-4.7}$	$^{+0.37}_{-0.2}$	$^{+0.01}_{-0.0}$	$^{+2.3}_{-2.1}$	$^{+1.0}_{-0.82}$	0.7	N/A	0.72	0.27	1.9	$^{+3.3}_{-4.1}$	2.0	1.0
0.26-0.31	$7.5 \cdot 10^{6}$	0.97	$^{+0.39}_{-0.41}$	6.8	$^{+3.8}_{-4.1}$	$^{+2.4}_{-2.6}$	$^{+2.8}_{-2.9}$	$^{+5.5}_{-5.7}$	$^{+2.9}_{-3.2}$	$^{+1.3}_{-1.6}$	$^{+4.5}_{-5.0}$	$^{+0.4}_{-0.42}$	$^{+0.06}_{-0.07}$	$^{+1.0}_{-1.2}$	1.9	0.2	N/A	0.2	0.09	2.0	$^{+2.8}_{-3.7}$	2.0	1.0
0.31-0.37	$2.9 \cdot 10^{6}$	0.92	$^{+0.21}_{-0.28}$	$^{+6.2}_{-6.6}$	$^{+3.1}_{-3.4}$	2.1	$^{+2.2}_{-2.4}$	$^{+4.5}_{-4.7}$	$^{+2.6}_{-2.8}$	$^{+1.3}_{-1.5}$	$^{+4.9}_{-5.1}$	$^{+0.78}_{-1.0}$	$^{+0.03}_{-0.09}$	$^{+0.45}_{-0.75}$	$^{+2.5}_{-3.0}$	0.3	N/A	0.34	0.0	2.0	$^{+2.6}_{-2.9}$	2.0	1.0
0.37-0.44	$1.1 \cdot 10^{6}$	0.8	$^{+0.07}_{-0.08}$	$^{+5.6}_{-5.5}$	$^{+3.1}_{-2.9}$	$^{+1.7}_{-1.9}$	$^{+1.4}_{-1.5}$	3.7	2.7	1.0	4.7	$^{+1.1}_{-1.3}$	$^{+0.08}_{-0.05}$	$^{+0.11}_{-0.1}$	$^{+3.4}_{-3.5}$	0.8	N/A	0.85	0.0	2.0	$^{+2.2}_{-2.3}$	2.0	1.0
0.44-0.51	$4.3 \cdot 10^{5}$	1.0	0.02	$^{+5.6}_{-5.8}$	$^{+3.1}_{-3.0}$	$^{+1.9}_{-1.7}$	$^{+1.1}_{-0.87}$	3.7	$^{+2.8}_{-2.7}$	$^{+0.9}_{-0.81}$	$^{+5.1}_{-5.5}$	$^{+1.5}_{-1.4}$	$^{+0.01}_{-0.0}$	$^{+0.04}_{-0.02}$	$^{+4.5}_{-4.8}$	0.7	N/A	0.71	0.0	2.0	$^{+2.1}_{-1.9}$	2.0	1.0
0.51-0.59	$1.8 \cdot 10^{5}$	1.1	0.0	$^{+6.1}_{-5.3}$	$^{+3.1}_{-3.0}$	$^{+2.1}_{-1.8}$	$^{+1.1}_{-1.0}$	$^{+4.3}_{-3.5}$	$^{+2.8}_{-2.7}$	$^{+0.85}_{-0.89}$	$^{+6.4}_{-5.5}$	$^{+2.1}_{-1.9}$	$^{+0.1}_{-0.07}$	$^{+0.04}_{-0.01}$	$^{+5.9}_{-5.2}$	0.8	N/A	0.82	0.06	2.0	$^{+2.0}_{-1.7}$	2.0	1.0
0.59-0.67	$7.9 \cdot 10^{4}$	1.1	0.0	$^{+5.1}_{-4.9}$	$^{+2.8}_{-2.6}$	1.7	$^{+1.2}_{-1.1}$	$^{+3.6}_{-3.8}$	$^{+2.5}_{-2.4}$	$^{+0.82}_{-0.8}$	$^{+5.7}_{-6.0}$	$^{+2.2}_{-2.0}$	$^{+0.14}_{-0.19}$	$^{+0.01}_{-0.0}$	$^{+5.8}_{-6.3}$	0.3	N/A	0.27	0.0	2.0	$^{+1.6}_{-1.9}$	2.0	1.0
0.67-0.76	$3.7 \cdot 10^{4}$	1.1	0.0	$^{+4.0}_{-4.5}$	$^{+2.8}_{-3.3}$	$^{+1.5}_{-1.8}$	$^{+1.4}_{-1.8}$	$^{+3.4}_{-3.9}$	$^{+2.4}_{-2.6}$	$^{+0.64}_{-1.2}$	6.2	$^{+2.4}_{-2.9}$	$^{+0.0}_{-0.09}$	0.0	$^{+6.9}_{-6.5}$	0.5	N/A	0.5	0.0	2.0	$^{+1.6}_{-1.8}$	2.0	1.0
0.76-0.85	$1.7 \cdot 10^{4}$	1.4	0.0	$^{+4.0}_{-3.8}$	$^{+3.3}_{-3.2}$	$^{+1.5}_{-1.2}$	$^{+2.1}_{-1.8}$	$^{+4.0}_{-3.9}$	$^{+2.7}_{-2.5}$	$^{+0.83}_{-0.7}$	6.4	$^{+3.1}_{-2.9}$	$^{+0.17}_{-0.1}$	0.0	$^{+7.4}_{-7.0}$	0.7	N/A	0.69	0.0	2.0	$^{+1.6}_{-1.5}$	2.0	1.0
0.85-0.95	$8.4 \cdot 10^{3}$	1.3	0.0	$^{+4.1}_{-4.4}$	$^{+2.9}_{-3.3}$	1.1	$^{+2.1}_{-2.5}$	4.4	$^{+2.0}_{-2.4}$	$^{+0.37}_{-0.39}$	$^{+7.2}_{-7.3}$	$^{+3.0}_{-3.7}$	$^{+0.1}_{-0.02}$	0.0	$^{+8.0}_{-8.8}$	0.2	N/A	0.18	0.0	2.0	$^{+1.1}_{-1.7}$	2.0	1.0
0.95-1.06	$4.1 \cdot 10^{3}$	1.5	0.0	$^{+4.6}_{-4.1}$	$^{+3.4}_{-2.9}$	1.3	$^{+3.0}_{-2.6}$	$^{+4.2}_{-3.8}$	$^{+2.3}_{-2.1}$	$^{+0.81}_{-0.77}$	$^{+7.7}_{-6.5}$	$^{+3.9}_{-3.4}$	$^{+0.39}_{-0.17}$	0.0	$^{+9.3}_{-8.0}$	0.7	N/A	0.73	0.24	2.0	$^{+1.5}_{-1.6}$	2.0	1.0
1.06-1.18	$2.0 \cdot 10^{3}$	1.9	0.0	$^{+3.7}_{-3.9}$	$^{+2.9}_{-3.3}$	$^{+1.1}_{-1.3}$	$^{+2.8}_{-3.1}$	$^{+3.7}_{-3.9}$	$^{+2.0}_{-2.1}$	$^{+0.84}_{-0.7}$	$^{+6.7}_{-6.5}$	$^{+3.8}_{-3.7}$	$^{+0.22}_{-0.35}$	0.0	$^{+8.3}_{-7.7}$	0.6	N/A	0.65	0.08	2.0	$^{+1.1}_{-1.4}$	2.0	1.0
1.18-1.31	$9.0 \cdot 10^{2}$	2.6	0.0	$^{+3.6}_{-5.5}$	$^{+2.7}_{-4.1}$	$^{+1.2}_{-0.76}$	$^{+2.7}_{-3.6}$	$^{+4.3}_{-5.2}$	$^{+1.5}_{-2.1}$	$^{+0.21}_{-0.52}$	$^{+7.5}_{-8.8}$	$^{+3.5}_{-5.5}$	$^{+0.11}_{-0.14}$	0.0	$^{+9.9}_{-11}$	0.0	N/A	0.0	0.0	2.0	1.1	2.0	1.0
1.31-1.45	$4.6 \cdot 10^{2}$	3.3	0.0	$^{+4.6}_{-5.0}$	3.8	$^{+0.95}_{-1.0}$	$^{+3.3}_{-3.5}$	$^{+4.7}_{-4.8}$	2.1	$^{+0.53}_{-0.36}$	$^{+7.3}_{-7.9}$	$^{+4.7}_{-5.2}$	$^{+0.18}_{-0.26}$	0.0	$^{+10}_{-11}$	0.4	N/A	0.39	0.0	2.0	$^{+1.1}_{-0.98}$	2.0	1.0
1.45-1.6	$2.1 \cdot 10^{2}$	3.7	0.0	$^{+5.8}_{-4.4}$	$^{+4.1}_{-3.5}$	$^{+1.6}_{-1.0}$	$^{+3.2}_{-2.9}$	$^{+6.0}_{-4.6}$	$^{+2.0}_{-1.7}$	$^{+0.86}_{-0.39}$	$^{+9.5}_{-7.8}$	$^{+6.2}_{-4.7}$	$^{+0.53}_{-0.19}$	0.0	$^{+13}_{-10}$	1.0	N/A	0.98	0.26	2.0	$^{+1.3}_{-0.77}$	2.0	1.0
1.6-1.76	$9.3 \cdot 10^{1}$	5.3	0.0	$^{+4.9}_{-4.7}$	$^{+3.6}_{-3.4}$	1.2	$^{+2.6}_{-2.5}$	$^{+5.1}_{-4.8}$	1.6	$^{+0.34}_{-0.52}$	$^{+8.2}_{-7.6}$	5.3	$^{+0.18}_{-0.14}$	0.0	$^{+12}_{-10}$	0.6	N/A	0.63	0.04	2.0	$^{+0.65}_{-0.74}$	2.0	1.0
1.76-1.94	$3.8 \cdot 10^{1}$	9.3	0.0	$^{+5.6}_{-5.0}$	$^{+3.2}_{-3.0}$	$^{+1.4}_{-1.3}$	$^{+2.9}_{-2.4}$	$^{+5.8}_{-5.6}$	$^{+1.7}_{-1.5}$	$^{+0.44}_{-0.28}$	$^{+9.1}_{-7.8}$	$^{+6.5}_{-6.0}$	$^{+0.38}_{-0.0}$	0.0	12	0.4	N/A	0.42	0.0	2.0	$^{+0.6}_{-0.58}$	2.0	1.0
1.94-2.12	$2.1 \cdot 10^{1}$	10	0.0	$^{+4.2}_{-3.8}$	$^{+2.1}_{-2.4}$	1.3	$^{+2.7}_{-2.8}$	$^{+4.8}_{-5.7}$	$^{+1.0}_{-1.4}$	$^{+0.07}_{-0.59}$	$^{+8.2}_{-7.2}$	$^{+6.0}_{-5.7}$	$^{+0.19}_{-0.74}$	0.0	$^{+12}_{-11}$	0.3	N/A	0.31	0.06	2.0	$^{+0.74}_{-0.79}$	2.0	1.0
2.12-2.55	$6.9 \cdot 10^{0}$	14	0.0	$^{+4.7}_{-4.3}$	$^{+2.9}_{-1.9}$	$^{+2.1}_{-1.6}$	$^{+4.5}_{-3.9}$	$^{+7.5}_{-6.4}$	$^{+2.2}_{-1.3}$	$^{+0.63}_{-0.19}$	$^{+9.9}_{-9.6}$	$^{+8.1}_{-7.4}$	$^{+1.1}_{-0.74}$	0.0	$^{+17}_{-14}$	0.9	N/A	0.9	0.0	2.0	$^{+1.0}_{-0.5}$	2.0	1.0
2.55-3.61	$5.8 \cdot 10^{-1}$	33	0.0	$^{+4.9}_{-3.9}$	$^{+1.8}_{-1.2}$	$^{+0.39}_{-0.34}$	$^{+4.5}_{-3.3}$	$^{+8.0}_{-6.2}$	$^{+1.5}_{-0.91}$	$^{+0.43}_{-0.35}$	$^{+11}_{-8.5}$	$^{+9.4}_{-7.1}$	2.2	0.0	$^{+19}_{-16}$	2.0	N/A	1.8	0.11	2.0	$^{+0.44}_{-0.39}$	2.0	1.0

Table B.26: Measured dijet cross section for $R = 0.6$ and $1.0 < y^{*} < 1.5$. See Table B.15 for a description of the columns. This table is available on HEPDATA [187].

m_{12}-bin [TeV]	σ [pb/TeV]	δ_{stat} %	γ_3	γ_9	γ_{15}	γ_{21}	γ_{27}	γ_{31}	γ_{34}	γ_{40}	γ_{46}	γ_{52}	γ_{58}	γ_{64}	γ_{70}	γ_{74}	γ_{75}	γ_{78}	γ_{82}	γ_{83}	u_1	u_2	u_3
0.26-0.31	$2.5 \cdot 10^{7}$	2.3	$^{+5.9}_{-5.5}$	$^{+10}_{-9.1}$	$^{+9.8}_{-8.9}$	$^{+5.2}_{-4.9}$	$^{+2.6}_{-2.5}$	$^{+16}_{-14}$	$^{+3.2}_{-3.1}$	$^{+3.2}_{-2.9}$	$^{+5.0}_{-4.9}$	$^{+0.03}_{-0.0}$	$^{+0.01}_{-0.0}$	$^{+3.5}_{-3.3}$	$^{+0.05}_{-0.0}$	3.0	N/A	3.2	0.35	$^{+2.1}_{-2.0}$	$^{+7.4}_{-6.8}$	2.0	1.0
0.31-0.37	$9.6 \cdot 10^{6}$	2.3	$^{+1.8}_{-1.9}$	$^{+8.9}_{-7.6}$	$^{+7.3}_{-6.3}$	$^{+3.3}_{-3.2}$	2.3	$^{+12}_{-9.6}$	$^{+3.0}_{-2.9}$	$^{+2.0}_{-2.1}$	$^{+4.6}_{-4.8}$	$^{+0.07}_{-0.17}$	$^{+0.02}_{-0.1}$	$^{+2.4}_{-2.5}$	$^{+0.53}_{-0.71}$	2.0	N/A	1.7	0.13	2.0	$^{+4.9}_{-5.0}$	2.0	1.0
0.37-0.44	$3.6 \cdot 10^{6}$	1.4	$^{+0.38}_{-0.35}$	$^{+7.9}_{-7.1}$	$^{+5.5}_{-5.2}$	$^{+3.4}_{-3.0}$	$^{+2.9}_{-3.0}$	$^{+9.4}_{-8.5}$	$^{+3.2}_{-3.0}$	$^{+1.7}_{-1.8}$	$^{+5.3}_{-4.8}$	$^{+0.54}_{-0.43}$	0.07	$^{+1.6}_{-1.8}$	1.4	1.0	N/A	1.4	0.06	2.0	$^{+4.9}_{-4.7}$	2.0	1.0
0.44-0.51	$1.4 \cdot 10^{6}$	1.5	$^{+0.0}_{-0.14}$	$^{+7.1}_{-8.0}$	$^{+4.6}_{-4.7}$	$^{+2.8}_{-2.9}$	3.4	$^{+8.0}_{-8.3}$	$^{+3.7}_{-3.8}$	$^{+1.8}_{-2.0}$	$^{+5.6}_{-5.8}$	$^{+0.85}_{-1.1}$	0.0	$^{+0.73}_{-1.0}$	$^{+3.1}_{-3.0}$	0.6	N/A	0.63	0.0	2.0	$^{+4.5}_{-5.1}$	2.0	1.0
0.51-0.59	$5.9 \cdot 10^{5}$	1.5	$^{+0.1}_{-0.12}$	$^{+7.2}_{-7.0}$	$^{+3.8}_{-3.9}$	$^{+1.7}_{-2.4}$	$^{+2.4}_{-2.7}$	$^{+7.4}_{-6.6}$	$^{+3.1}_{-3.3}$	$^{+1.1}_{-1.5}$	$^{+5.4}_{-5.5}$	$^{+0.63}_{-1.0}$	$^{+0.0}_{-0.06}$	$^{+0.17}_{-0.15}$	$^{+3.5}_{-3.7}$	0.5	N/A	0.54	0.0	2.0	$^{+3.3}_{-4.0}$	2.0	1.0
0.59-0.67	$2.6 \cdot 10^{5}$	1.6	$^{+0.09}_{-0.07}$	$^{+6.5}_{-6.0}$	$^{+3.6}_{-3.4}$	$^{+2.1}_{-2.2}$	2.0	5.7	$^{+2.8}_{-3.0}$	$^{+1.4}_{-1.3}$	$^{+5.4}_{-5.2}$	$^{+1.5}_{-1.4}$	$^{+0.24}_{-0.07}$	$^{+0.07}_{-0.0}$	$^{+4.0}_{-4.1}$	1.0	N/A	1.0	0.0	2.0	3.0	2.0	1.0
0.67-0.76	$1.2 \cdot 10^{5}$	1.7	0.02	6.4	3.6	$^{+2.0}_{-2.3}$	$^{+1.5}_{-1.3}$	$^{+5.8}_{-5.5}$	$^{+3.1}_{-3.3}$	$^{+1.2}_{-0.99}$	$^{+6.0}_{-6.1}$	$^{+2.2}_{-1.7}$	$^{+0.09}_{-0.04}$	0.03	$^{+5.2}_{-5.3}$	0.9	N/A	0.87	0.26	2.0	$^{+3.1}_{-3.2}$	2.0	1.0
0.76-0.85	$5.7 \cdot 10^{4}$	2.1	0.0	$^{+7.0}_{-6.8}$	$^{+3.3}_{-3.2}$	$^{+1.7}_{-1.6}$	$^{+0.94}_{-0.54}$	6.0	$^{+3.0}_{-2.7}$	$^{+0.57}_{-0.58}$	6.6	$^{+1.9}_{-1.4}$	$^{+0.12}_{-0.0}$	$^{+0.02}_{-0.07}$	6.3	0.8	N/A	0.85	0.33	2.0	$^{+2.6}_{-2.3}$	2.0	1.0
0.85-0.95	$2.8 \cdot 10^{4}$	2.1	0.0	$^{+5.6}_{-5.4}$	$^{+2.4}_{-2.6}$	$^{+1.4}_{-1.5}$	$^{+0.89}_{-0.83}$	$^{+5.1}_{-4.9}$	$^{+2.1}_{-2.3}$	$^{+0.6}_{-1.0}$	$^{+5.8}_{-6.2}$	$^{+1.5}_{-1.9}$	$^{+0.0}_{-0.13}$	$^{+0.0}_{-0.02}$	$^{+6.1}_{-6.8}$	0.08	N/A	0.08	0.17	2.0	$^{+1.8}_{-2.2}$	2.0	1.0
0.95-1.06	$1.4 \cdot 10^{4}$	2.3	0.0	$^{+5.2}_{-5.6}$	$^{+3.7}_{-3.4}$	$^{+1.5}_{-1.6}$	$^{+1.7}_{-2.1}$	$^{+6.0}_{-6.1}$	$^{+3.7}_{-3.1}$	$^{+1.4}_{-0.94}$	$^{+6.6}_{-6.4}$	$^{+3.2}_{-3.0}$	$^{+0.17}_{-0.1}$	0.0	$^{+6.9}_{-7.1}$	0.6	N/A	0.58	0.25	2.0	$^{+2.6}_{-3.1}$	2.0	1.0
1.06-1.18	$6.3 \cdot 10^{3}$	2.5	0.0	$^{+5.6}_{-4.0}$	$^{+4.1}_{-2.7}$	$^{+2.3}_{-1.2}$	$^{+2.6}_{-1.7}$	$^{+6.9}_{-5.8}$	$^{+3.5}_{-2.4}$	$^{+1.2}_{-0.58}$	$^{+8.0}_{-7.2}$	$^{+3.6}_{-2.6}$	$^{+0.17}_{-0.04}$	0.0	$^{+8.6}_{-7.7}$	1.0	N/A	1.4	1.0	2.0	$^{+2.9}_{-2.1}$	2.0	1.0
1.18-1.31	$3.1 \cdot 10^{3}$	2.6	0.0	$^{+3.5}_{-3.3}$	$^{+1.5}_{-2.9}$	$^{+1.2}_{-1.6}$	$^{+1.2}_{-2.0}$	$^{+6.2}_{-5.3}$	$^{+1.3}_{-2.3}$	$^{+0.53}_{-1.1}$	$^{+8.1}_{-6.6}$	$^{+1.2}_{-3.1}$	$^{+0.0}_{-0.07}$	0.0	$^{+9.1}_{-7.5}$	2.0	N/A	1.6	0.38	2.0	$^{+1.1}_{-2.1}$	2.0	1.0
1.31-1.45	$1.4 \cdot 10^{3}$	3.2	0.0	$^{+5.3}_{-4.1}$	$^{+4.3}_{-3.8}$	1.2	$^{+2.3}_{-3.2}$	$^{+7.3}_{-6.1}$	$^{+2.2}_{-2.9}$	$^{+0.58}_{-0.66}$	$^{+9.1}_{-7.3}$	$^{+4.7}_{-3.7}$	$^{+0.24}_{-0.26}$	0.0	$^{+10}_{-9.6}$	0.1	N/A	0.15	0.0	2.0	$^{+2.6}_{-2.0}$	2.0	1.0
1.45-1.6	$6.7 \cdot 10^{2}$	3.7	0.0	$^{+5.5}_{-4.7}$	$^{+5.3}_{-4.0}$	$^{+1.6}_{-1.3}$	$^{+4.7}_{-3.3}$	$^{+7.7}_{-6.0}$	$^{+3.9}_{-2.3}$	$^{+0.52}_{-1.0}$	$^{+8.2}_{-7.7}$	$^{+5.6}_{-4.4}$	0.26	0.0	$^{+11}_{-9.0}$	2.0	N/A	1.8	0.0	2.0	$^{+3.1}_{-1.7}$	2.0	1.0
1.6-1.76	$3.0 \cdot 10^{2}$	4.5	0.0	$^{+3.3}_{-4.0}$	$^{+2.2}_{-2.1}$	$^{+0.93}_{-0.76}$	$^{+1.6}_{-2.3}$	$^{+5.9}_{-6.6}$	$^{+1.2}_{-0.88}$	$^{+0.72}_{-0.0}$	$^{+7.9}_{-8.2}$	$^{+3.1}_{-3.5}$	$^{+0.0}_{-0.03}$	0.0	$^{+11}_{-9.8}$	2.0	N/A	1.9	0.42	2.0	$^{+1.3}_{-0.51}$	2.0	1.0
1.76-1.94	$1.4 \cdot 10^{2}$	5.0	0.0	$^{+6.1}_{-4.3}$	$^{+4.1}_{-3.9}$	$^{+1.5}_{-1.9}$	$^{+3.6}_{-3.2}$	$^{+8.6}_{-6.3}$	$^{+2.7}_{-3.0}$	$^{+0.64}_{-1.2}$	$^{+11}_{-7.3}$	$^{+6.1}_{-4.6}$	$^{+0.11}_{-0.02}$	0.0	$^{+13}_{-9.8}$	1.0	N/A	1.5	0.02	2.0	$^{+1.4}_{-3.1}$	2.0	1.0
1.94-2.12	$6.0 \cdot 10^{1}$	7.9	0.0	$^{+6.1}_{-6.4}$	$^{+5.5}_{-5.7}$	2.2	$^{+5.3}_{-5.1}$	$^{+9.0}_{-7.9}$	2.7	$^{+1.1}_{-0.33}$	$^{+11}_{-8.5}$	$^{+6.1}_{-5.7}$	$^{+0.87}_{-0.02}$	0.0	$^{+12}_{-9.9}$	0.8	N/A	0.76	0.0	2.0	$^{+2.3}_{-1.8}$	2.0	1.0
2.12-2.33	$2.8 \cdot 10^{1}$	10	0.0	$^{+8.4}_{-7.0}$	$^{+6.2}_{-4.4}$	$^{+1.6}_{-1.8}$	$^{+5.3}_{-4.1}$	$^{+9.7}_{-9.0}$	$^{+2.2}_{-2.3}$	$^{+0.43}_{-0.15}$	$^{+11}_{-9.5}$	$^{+8.6}_{-7.1}$	$^{+0.4}_{-0.28}$	0.0	15	0.7	N/A	0.73	0.0	2.0	$^{+1.4}_{-1.1}$	2.0	1.0
2.33-2.78	$9.8 \cdot 10^{0}$	11	0.0	$^{+5.8}_{-4.4}$	$^{+3.5}_{-3.2}$	$^{+1.2}_{-1.5}$	$^{+2.6}_{-2.4}$	$^{+7.3}_{-6.3}$	1.5	$^{+0.46}_{-0.73}$	$^{+9.4}_{-7.9}$	$^{+5.7}_{-4.6}$	$^{+0.14}_{-0.27}$	0.0	$^{+13}_{-12}$	2.0	N/A	1.6	0.0	2.0	$^{+0.81}_{-0.86}$	2.0	1.0
2.78-3.93	$6.2 \cdot 10^{-1}$	29	0.02	$^{+7.4}_{-6.8}$	$^{+4.0}_{-3.5}$	$^{+2.8}_{-1.8}$	$^{+5.2}_{-3.9}$	$^{+12}_{-13}$	$^{+3.0}_{-2.1}$	$^{+0.29}_{-0.32}$	14	$^{+11}_{-10}$	$^{+0.36}_{-0.35}$	0.0	$^{+21}_{-19}$	1.0	N/A	1.1	0.0	2.0	$^{+1.5}_{-0.86}$	2.0	1.0

Table B.27: Measured dijet cross section for $R = 0.6$ and $1.5 < y^{*} < 2.0$. See Table B.15 for a description of the columns. This table is available on HEPDATA [187].

m_{12}-bin [TeV]	σ [pb/TeV]	δ_{stat} %	γ_4	γ_{10}	γ_{16}	γ_{22}	γ_{28}	γ_{31}	γ_{35}	γ_{41}	γ_{47}	γ_{53}	γ_{59}	γ_{65}	γ_{71}	γ_{74}	γ_{75}	γ_{79}	γ_{82}	γ_{84}	u_1	u_2	u_3
0.37-0.44	$1.3 \cdot 10^{7}$	3.2	$^{+10}_{-7.3}$	$^{+14}_{-11}$	$^{+15}_{-11}$	$^{+7.8}_{-5.8}$	$^{+3.7}_{-2.6}$	$^{+29}_{-21}$	$^{+3.8}_{-3.1}$	$^{+4.2}_{-3.3}$	$^{+6.8}_{-4.6}$	$^{+0.09}_{-0.0}$	$^{+0.01}_{-0.0}$	$^{+4.3}_{-3.5}$	$^{+0.06}_{-0.0}$	7.0	N/A	7.0	1.1	2.1	$^{+16}_{-8.4}$	1.0	$^{+2.7}_{-0.0}$
0.44-0.51	$4.8 \cdot 10^{6}$	3.2	$^{+5.6}_{-5.5}$	$^{+11}_{-10}$	$^{+10}_{-9.4}$	$^{+5.0}_{-5.2}$	$^{+3.2}_{-2.9}$	$^{+25}_{-18}$	$^{+3.6}_{-3.5}$	$^{+3.3}_{-3.2}$	$^{+5.3}_{-5.7}$	$^{+0.1}_{-0.17}$	$^{+0.02}_{-0.04}$	$^{+3.5}_{-3.4}$	$^{+0.28}_{-0.25}$	4.0	N/A	4.2	0.74	2.0	$^{+9.2}_{-8.6}$	1.0	$^{+1.2}_{-0.83}$
0.51-0.59	$2.0 \cdot 10^{6}$	3.0	$^{+1.9}_{-2.6}$	$^{+8.6}_{-8.3}$	$^{+7.7}_{-7.5}$	$^{+3.5}_{-3.9}$	$^{+2.7}_{-3.2}$	$^{+18}_{-15}$	$^{+3.4}_{-3.6}$	$^{+2.2}_{-2.5}$	5.5	$^{+0.32}_{-0.29}$	$^{+0.0}_{-0.02}$	$^{+2.3}_{-2.7}$	$^{+0.82}_{-0.91}$	2.0	N/A	2.3	0.31	2.0	$^{+6.3}_{-7.4}$	1.0	$^{+0.67}_{-1.3}$
0.59-0.67	$8.9 \cdot 10^{5}$	1.9	$^{+0.67}_{-0.97}$	$^{+8.6}_{-8.2}$	6.4	$^{+2.7}_{-3.3}$	$^{+2.7}_{-3.5}$	$^{+15}_{-13}$	$^{+3.0}_{-3.7}$	$^{+1.7}_{-2.2}$	$^{+5.3}_{-5.8}$	$^{+0.4}_{-0.45}$	$^{+0.04}_{-0.0}$	$^{+1.4}_{-1.7}$	$^{+1.3}_{-1.9}$	2.0	N/A	2.1	0.64	2.0	$^{+6.0}_{-6.7}$	1.0	$^{+0.91}_{-1.1}$
0.67-0.76	$3.9 \cdot 10^{5}$	1.9	$^{+0.24}_{-0.21}$	$^{+8.6}_{-7.7}$	$^{+5.6}_{-5.0}$	$^{+2.7}_{-2.6}$	$^{+3.5}_{-3.4}$	$^{+13}_{-11}$	$^{+3.6}_{-3.4}$	$^{+1.7}_{-1.8}$	$^{+5.9}_{-5.7}$	$^{+0.47}_{-0.59}$	0.03	$^{+0.84}_{-0.88}$	$^{+2.7}_{-2.6}$	3.0	N/A	2.9	1.3	2.0	$^{+6.3}_{-5.9}$	1.0	$^{+0.99}_{-1.0}$
0.76-0.85	$1.9 \cdot 10^{5}$	1.5	$^{+0.0}_{-0.02}$	$^{+7.5}_{-7.3}$	$^{+4.6}_{-4.2}$	$^{+2.6}_{-2.4}$	$^{+3.4}_{-3.0}$	$^{+11}_{-9.9}$	$^{+3.6}_{-3.3}$	$^{+1.8}_{-1.7}$	$^{+5.7}_{-5.5}$	$^{+0.91}_{-1.0}$	$^{+0.03}_{-0.07}$	$^{+0.44}_{-0.55}$	$^{+3.3}_{-3.4}$	2.0	N/A	2.4	0.85	2.0	$^{+5.4}_{-5.1}$	1.0	1.0
0.85-0.95	$9.4 \cdot 10^{4}$	1.4	$^{+0.06}_{-0.07}$	$^{+8.0}_{-7.3}$	$^{+4.6}_{-4.5}$	2.5	3.0	$^{+10}_{-9.1}$	3.7	$^{+1.6}_{-1.5}$	$^{+6.6}_{-6.0}$	1.3	$^{+0.01}_{-0.1}$	$^{+0.14}_{-0.26}$	$^{+4.7}_{-4.5}$	1.0	N/A	1.5	0.06	2.0	$^{+5.3}_{-5.1}$	1.0	1.0
0.95-1.06	$4.3 \cdot 10^{4}$	1.6	$^{+0.05}_{-0.04}$	$^{+7.5}_{-6.9}$	$^{+4.2}_{-4.1}$	$^{+2.4}_{-2.3}$	2.2	$^{+9.0}_{-7.9}$	$^{+3.6}_{-3.4}$	1.3	$^{+6.4}_{-5.9}$	1.6	0.05	$^{+0.04}_{-0.0}$	$^{+5.0}_{-5.1}$	1.0	N/A	1.1	0.0	2.0	4.7	1.0	1.0
1.06-1.18	$2.0 \cdot 10^{4}$	1.9	0.02	$^{+7.6}_{-7.8}$	$^{+4.0}_{-4.3}$	$^{+2.2}_{-2.4}$	$^{+1.5}_{-1.6}$	$^{+8.8}_{-8.6}$	$^{+3.4}_{-3.6}$	1.2	$^{+6.7}_{-7.2}$	1.8	$^{+0.05}_{-0.06}$	$^{+0.06}_{-0.01}$	$^{+6.1}_{-6.5}$	2.0	N/A	2.3	1.3	2.0	$^{+4.2}_{-4.6}$	1.0	1.0
1.18-1.31	$9.9 \cdot 10^{3}$	2.5	0.0	$^{+7.8}_{-7.1}$	3.8	$^{+2.1}_{-2.4}$	$^{+1.3}_{-1.2}$	$^{+9.2}_{-7.9}$	3.3	$^{+1.3}_{-1.2}$	$^{+7.7}_{-6.8}$	2.1	$^{+0.11}_{-0.04}$	$^{+0.02}_{-0.03}$	$^{+7.5}_{-6.5}$	4.0	N/A	3.6	2.0	2.0	$^{+3.8}_{-3.7}$	1.0	1.0
1.31-1.45	$4.7 \cdot 10^{3}$	2.7	0.0	$^{+7.0}_{-6.7}$	$^{+3.8}_{-3.6}$	$^{+2.1}_{-2.0}$	$^{+1.4}_{-1.1}$	8.1	$^{+3.4}_{-3.1}$	$^{+0.9}_{-1.0}$	$^{+7.2}_{-7.0}$	$^{+2.4}_{-2.2}$	$^{+0.06}_{-0.03}$	$^{+0.02}_{-0.01}$	$^{+7.2}_{-7.1}$	2.0	N/A	2.3	0.81	2.0	3.6	1.0	1.0
1.45-1.6	$2.2 \cdot 10^{3}$	3.5	0.0	$^{+6.0}_{-6.5}$	$^{+3.0}_{-3.6}$	$^{+2.0}_{-2.1}$	$^{+1.4}_{-1.9}$	$^{+8.7}_{-8.3}$	$^{+2.9}_{-3.3}$	$^{+0.92}_{-1.1}$	$^{+8.2}_{-8.1}$	$^{+2.3}_{-3.0}$	$^{+0.05}_{-0.1}$	0.0	$^{+8.5}_{-8.6}$	0.0	N/A	0.0	0.0	2.0	$^{+3.2}_{-3.7}$	1.0	1.0
1.6-1.76	$1.0 \cdot 10^{3}$	3.9	0.0	$^{+6.3}_{-5.6}$	$^{+4.2}_{-3.4}$	$^{+2.1}_{-1.8}$	$^{+2.6}_{-2.2}$	$^{+8.7}_{-8.0}$	$^{+3.8}_{-3.0}$	$^{+1.2}_{-0.78}$	$^{+8.6}_{-7.5}$	$^{+4.0}_{-3.3}$	$^{+0.09}_{-0.13}$	0.0	$^{+9.0}_{-8.3}$	0.0	N/A	0.0	0.0	2.0	3.7	1.0	1.0
1.76-1.94	$4.6 \cdot 10^{2}$	4.1	0.0	$^{+5.0}_{-4.6}$	$^{+3.2}_{-3.6}$	$^{+1.5}_{-1.4}$	$^{+2.0}_{-1.7}$	$^{+9.0}_{-9.2}$	$^{+2.4}_{-2.7}$	$^{+0.84}_{-0.55}$	$^{+8.8}_{-8.4}$	$^{+2.9}_{-3.2}$	$^{+0.14}_{-0.1}$	0.0	$^{+9.8}_{-9.7}$	1.0	N/A	1.1	0.0	2.0	3.0	1.0	1.0
1.94-2.12	$2.1 \cdot 10^{2}$	4.7	0.0	$^{+5.9}_{-3.8}$	$^{+4.9}_{-3.4}$	$^{+2.1}_{-1.7}$	$^{+3.5}_{-2.4}$	$^{+9.7}_{-8.6}$	$^{+3.3}_{-2.7}$	$^{+1.3}_{-0.9}$	$^{+9.4}_{-7.5}$	$^{+4.8}_{-3.0}$	$^{+0.32}_{-0.02}$	0.0	$^{+11}_{-9.3}$	2.0	N/A	2.2	0.18	2.0	$^{+3.9}_{-2.9}$	1.0	1.0
2.12-2.33	$1.0 \cdot 10^{2}$	7.0	0.0	$^{+4.8}_{-6.2}$	$^{+3.9}_{-4.4}$	$^{+1.7}_{-1.8}$	$^{+2.8}_{-3.4}$	10	$^{+3.0}_{-2.9}$	$^{+0.65}_{-0.93}$	$^{+9.5}_{-10}$	$^{+4.2}_{-6.1}$	$^{+0.05}_{-0.44}$	0.0	$^{+11}_{-12}$	0.4	N/A	0.44	0.0	2.0	$^{+3.0}_{-3.3}$	1.0	1.0
2.33-2.55	$4.1 \cdot 10^{1}$	9.9	0.0	$^{+5.0}_{-5.7}$	$^{+2.8}_{-4.4}$	$^{+1.6}_{-2.0}$	$^{+2.3}_{-4.0}$	$^{+10}_{-8.6}$	$^{+2.8}_{-3.2}$	$^{+0.51}_{-1.1}$	$^{+10}_{-9.0}$	$^{+4.4}_{-5.3}$	$^{+0.34}_{-0.5}$	0.0	$^{+13}_{-11}$	2.0	N/A	1.6	0.33	2.0	$^{+2.4}_{-3.4}$	1.0	1.0
2.55-3.04	$1.1 \cdot 10^{1}$	10	0.0	$^{+9.5}_{-6.9}$	$^{+8.1}_{-5.0}$	$^{+2.4}_{-2.3}$	$^{+7.9}_{-4.7}$	$^{+14}_{-10}$	$^{+3.1}_{-3.2}$	$^{+0.8}_{-0.86}$	$^{+15}_{-11}$	$^{+9.1}_{-6.3}$	$^{+0.25}_{-0.18}$	0.0	$^{+18}_{-14}$	3.0	N/A	2.6	0.46	2.0	$^{+3.4}_{-3.2}$	1.0	1.0
3.04-4.27	$5.1 \cdot 10^{-1}$	35	0.01	$^{+8.7}_{-8.1}$	$^{+6.4}_{-6.2}$	$^{+2.8}_{-3.0}$	$^{+5.6}_{-5.2}$	$^{+13}_{-12}$	$^{+3.1}_{-3.2}$	$^{+0.69}_{-0.88}$	$^{+15}_{-13}$	$^{+8.9}_{-8.8}$	$^{+0.23}_{-0.4}$	0.0	$^{+20}_{-18}$	2.0	N/A	2.1	0.11	2.0	$^{+2.8}_{-3.0}$	1.0	1.0

Table B.28: Measured dijet cross section for $R = 0.6$ and $2.0 < y^{*} < 2.5$. See Table B.15 for a description of the columns. This table is available on HEPDATA [187].

m_{12}-bin [TeV]	σ [pb/TeV]	$\delta_{\rm stat}$ %	$\gamma 4$	γ_{10}	γ_{16}	γ_{22}	γ_{28}	γ_{31}	γ_{35}	γ_{41}	γ_{47}	γ_{53}	γ_{59}	γ_{65}	γ_{71}	γ_{74}	γ_{75}	γ_{79}	γ_{82}	γ_{84}	u_1	u_2	u_3
0.67-0.76	$1.4 \cdot 10^{6}$	5.4	$^{+7.6}_{-5.9}$	$^{+13}_{-10}$	$^{+13}_{-10}$	$^{+5.2}_{-4.6}$	$^{+3.2}_{-2.6}$	$^{+37}_{-26}$	$^{+3.5}_{-3.1}$	$^{+3.6}_{-3.2}$	$^{+6.1}_{-5.3}$	$^{+0.05}_{-0.08}$	$^{+0.04}_{-0.05}$	$^{+3.7}_{-3.4}$	$^{+0.18}_{-0.06}$	6.0	N/A	6.4	0.28	2.1	$^{+15}_{-11}$	1.0	$^{+1.6}_{-0.4}$
0.76-0.85	$7.3 \cdot 10^{5}$	6.5	$^{+5.0}_{-4.3}$	$^{+12}_{-11}$	$^{+11}_{-9.7}$	$^{+5.2}_{-4.8}$	$^{+3.5}_{-3.2}$	$^{+30}_{-21}$	$^{+4.5}_{-4.0}$	$^{+3.8}_{-3.2}$	$^{+6.6}_{-6.0}$	$^{+0.54}_{-0.24}$	0.0	$^{+4.0}_{-3.3}$	$^{+1.1}_{-0.55}$	4.0	N/A	3.7	0.69	2.0	$^{+11}_{-10}$	1.0	$^{+0.95}_{-1.1}$
0.85-0.95	$3.2 \cdot 10^{5}$	3.8	$^{+2.6}_{-2.7}$	10	$^{+8.4}_{-9.1}$	$^{+4.0}_{-4.2}$	$^{+3.2}_{-3.5}$	$^{+23}_{-19}$	4.2	$^{+2.8}_{-2.5}$	$^{+6.4}_{-6.8}$	$^{+0.45}_{-0.27}$	$^{+0.02}_{-0.0}$	$^{+2.9}_{-2.6}$	$^{+1.4}_{-1.1}$	2.0	N/A	2.4	0.83	2.0	$^{+9.5}_{-9.7}$	1.0	$^{+0.86}_{-1.1}$
0.95-1.06	$1.5 \cdot 10^{5}$	2.9	$^{+1.3}_{-1.4}$	$^{+9.9}_{-9.2}$	$^{+7.9}_{-7.2}$	3.5	$^{+3.5}_{-3.7}$	$^{+22}_{-17}$	$^{+4.0}_{-3.9}$	$^{+2.2}_{-2.3}$	$^{+6.6}_{-6.4}$	$^{+0.54}_{-0.57}$	$^{+0.01}_{-0.03}$	1.9	1.7	3.0	N/A	2.7	0.8	2.0	$^{+9.1}_{-8.8}$	1.0	$^{+0.95}_{-1.0}$
1.06-1.18	$7.7 \cdot 10^{4}$	3.3	$^{+0.54}_{-0.6}$	$^{+9.2}_{-8.4}$	$^{+6.2}_{-5.8}$	$^{+3.3}_{-2.8}$	$^{+3.7}_{-3.6}$	$^{+19}_{-15}$	3.7	$^{+2.0}_{-2.1}$	$^{+6.0}_{-6.1}$	0.66	$^{+0.0}_{-0.04}$	$^{+1.4}_{-1.3}$	$^{+2.5}_{-2.6}$	2.0	N/A	1.9	0.59	2.0	$^{+8.8}_{-8.5}$	1.0	$^{+0.99}_{-1.0}$
1.18-1.31	$3.6 \cdot 10^{4}$	2.8	$^{+0.11}_{-0.16}$	$^{+9.7}_{-8.0}$	$^{+5.5}_{-5.1}$	$^{+3.5}_{-3.2}$	$^{+3.7}_{-4.0}$	$^{+18}_{-14}$	4.0	$^{+1.7}_{-2.0}$	$^{+6.7}_{-6.1}$	$^{+0.89}_{-0.98}$	$^{+0.1}_{-0.04}$	$^{+0.91}_{-0.85}$	$^{+3.6}_{-3.8}$	2.0	N/A	2.2	0.7	2.0	$^{+8.4}_{-8.2}$	1.0	1.0
1.31-1.45	$1.6 \cdot 10^{4}$	2.4	$^{+0.06}_{-0.05}$	$^{+9.5}_{-8.8}$	$^{+5.8}_{-5.2}$	$^{+3.4}_{-3.3}$	3.6	$^{+15}_{-13}$	$^{+4.6}_{-4.2}$	$^{+2.4}_{-1.8}$	$^{+7.5}_{-7.2}$	$^{+1.3}_{-1.5}$	$^{+0.08}_{-0.04}$	$^{+0.27}_{-0.4}$	$^{+5.1}_{-5.0}$	2.0	N/A	1.8	0.0	2.0	$^{+8.7}_{-7.4}$	1.0	1.0
1.45-1.6	$7.8 \cdot 10^{3}$	2.8	$^{+0.06}_{-0.05}$	$^{+9.0}_{-8.5}$	$^{+5.2}_{-5.1}$	$^{+3.0}_{-3.2}$	$^{+2.8}_{-2.9}$	$^{+14}_{-12}$	4.1	1.7	$^{+7.3}_{-7.2}$	$^{+1.4}_{-1.8}$	$^{+0.05}_{-0.07}$	$^{+0.06}_{-0.1}$	5.7	1.0	N/A	1.2	0.0	2.0	$^{+7.3}_{-6.8}$	1.0	1.0
1.6-1.76	$3.8 \cdot 10^{3}$	3.2	0.03	$^{+8.8}_{-8.0}$	$^{+4.6}_{-4.5}$	$^{+3.1}_{-3.2}$	$^{+2.3}_{-2.5}$	$^{+13}_{-10}$	3.9	$^{+1.6}_{-1.8}$	$^{+7.4}_{-7.0}$	2.1	$^{+0.08}_{-0.1}$	$^{+0.02}_{-0.15}$	$^{+6.3}_{-6.2}$	3.0	N/A	2.6	1.4	2.0	$^{+7.1}_{-6.2}$	1.0	1.0
1.76-1.94	$1.6 \cdot 10^{3}$	4.6	$^{+0.01}_{-0.02}$	$^{+8.8}_{-8.1}$	$^{+4.6}_{-4.7}$	$^{+3.4}_{-3.5}$	1.9	$^{+12}_{-11}$	3.9	$^{+1.4}_{-1.6}$	$^{+8.2}_{-7.7}$	$^{+2.4}_{-2.3}$	$^{+0.06}_{-0.09}$	$^{+0.0}_{-0.03}$	$^{+7.4}_{-7.2}$	2.0	N/A	2.1	0.08	2.0	$^{+6.3}_{-6.2}$	1.0	1.0
1.94-2.12	$7.0 \cdot 10^{2}$	4.8	0.0	$^{+9.7}_{-8.7}$	$^{+5.3}_{-5.4}$	4.4	$^{+1.9}_{-1.5}$	$^{+13}_{-12}$	$^{+4.6}_{-4.7}$	$^{+1.6}_{-1.3}$	$^{+9.8}_{-8.6}$	$^{+3.0}_{-3.5}$	$^{+0.16}_{-0.07}$	$^{+0.04}_{-0.02}$	$^{+9.3}_{-8.5}$	1.0	N/A	1.3	0.0	2.0	$^{+6.5}_{-6.6}$	1.0	1.0
2.12-2.33	$3.2 \cdot 10^{2}$	7.9	0.0	$^{+8.8}_{-7.5}$	$^{+4.8}_{-3.9}$	$^{+4.1}_{-3.4}$	$^{+1.8}_{-1.5}$	$^{+13}_{-11}$	$^{+4.3}_{-3.6}$	$^{+1.4}_{-1.0}$	$^{+9.6}_{-8.4}$	$^{+3.3}_{-2.8}$	$^{+0.14}_{-0.08}$	$^{+0.02}_{-0.01}$	$^{+9.7}_{-8.6}$	2.0	N/A	2.2	0.63	2.0	$^{+6.3}_{-5.4}$	1.0	1.0
2.33-2.55	$1.4 \cdot 10^{2}$	9.2	0.0	$^{+7.9}_{-8.2}$	$^{+4.5}_{-4.6}$	$^{+3.9}_{-4.0}$	$^{+2.1}_{-2.4}$	13	$^{+4.2}_{-4.3}$	$^{+1.2}_{-1.7}$	9.9	$^{+3.7}_{-3.8}$	$^{+0.08}_{-0.04}$	$^{+0.01}_{-0.0}$	10	5.0	N/A	5.1	4.0	2.0	5.9	1.0	1.0
2.55-2.78	$5.8 \cdot 10^{1}$	15	0.0	$^{+7.8}_{-7.6}$	$^{+4.8}_{-5.1}$	$^{+3.8}_{-4.0}$	$^{+2.8}_{-2.9}$	$^{+15}_{-13}$	$^{+4.2}_{-4.3}$	$^{+1.2}_{-1.9}$	11	$^{+4.3}_{-4.6}$	$^{+0.09}_{-0.23}$	0.0	$^{+13}_{-12}$	5.0	N/A	4.8	2.5	2.0	$^{+6.0}_{-5.7}$	1.0	1.0
2.78-3.31	$1.2 \cdot 10^{1}$	13	0.0	$^{+7.3}_{-6.5}$	$^{+5.1}_{-4.9}$	$^{+4.1}_{-4.3}$	$^{+3.1}_{-3.5}$	$^{+16}_{-13}$	$^{+3.8}_{-4.0}$	$^{+1.3}_{-0.96}$	$^{+13}_{-10}$	$^{+4.8}_{-5.1}$	$^{+0.18}_{-0.33}$	0.0	$^{+14}_{-12}$	3.0	N/A	3.1	0.0	2.0	$^{+6.0}_{-6.8}$	1.0	1.0
3.31-4.64	$4.9 \cdot 10^{-1}$	39	0.0	$^{+8.5}_{-8.0}$	$^{+7.2}_{-6.9}$	$^{+6.4}_{-5.7}$	$^{+5.9}_{-5.3}$	$^{+22}_{-18}$	4.9	$^{+0.84}_{-1.5}$	$^{+16}_{-13}$	$^{+7.9}_{-7.7}$	$^{+0.14}_{-0.31}$	0.0	$^{+21}_{-16}$	4.0	N/A	3.8	0.0	2.0	$^{+8.1}_{-7.4}$	1.0	1.0

Table B.29: Measured dijet cross section for $R = 0.6$ and $2.5 < y^{*} < 3.0$. See Table B.15 for a description of the columns. This table is available on HEPDATA [187].

m_{12}-bin [TeV]	σ [pb/TeV]	δ_{stat} %	γ_5	γ_{11}	γ_{17}	γ_{23}	γ_{29}	γ_{31}	γ_{36}	γ_{42}	γ_{48}	γ_{54}	γ_{60}	γ_{66}	γ_{72}	γ_{74}	γ_{75}	γ_{80}	γ_{82}	γ_{85}	u_1	u_2	u_3
1.18-1.31	$1.3 \cdot 10^5$	9.7	$^{+5.5}_{-6.4}$	13	12	$^{+4.4}_{-4.9}$	2.9	$^{+48}_{-29}$	3.9	$^{+3.1}_{-3.4}$	$^{+6.3}_{-7.3}$	$^{+0.27}_{-0.23}$	$^{+0.15}_{-0.04}$	$^{+3.2}_{-3.5}$	$^{+0.48}_{-0.54}$	5.0	N/A	5.0	0.23	2.0	$^{+15}_{-16}$	2.0	$^{+0.0}_{-2.4}$
1.31-1.45	$5.4 \cdot 10^4$	6.8	$^{+3.3}_{-3.8}$	$^{+13}_{-11}$	$^{+11}_{-9.7}$	$^{+4.9}_{-4.4}$	$^{+3.5}_{-3.4}$	$^{+37}_{-25}$	$^{+4.3}_{-4.2}$	2.9	$^{+6.7}_{-7.3}$	$^{+0.22}_{-0.24}$	$^{+0.07}_{-0.05}$	$^{+3.0}_{-3.2}$	$^{+0.85}_{-1.0}$	3.0	N/A	3.1	0.49	2.0	$^{+15}_{-13}$	2.0	$^{+0.66}_{-1.3}$
1.45-1.6	$2.4 \cdot 10^4$	6.5	2.4	$^{+13}_{-10}$	$^{+10}_{-8.3}$	$^{+4.8}_{-4.3}$	$^{+4.2}_{-4.0}$	$^{+33}_{-23}$	$^{+4.9}_{-4.5}$	$^{+2.8}_{-3.0}$	$^{+8.0}_{-7.0}$	$^{+0.58}_{-0.47}$	$^{+0.0}_{-0.04}$	$^{+2.6}_{-2.8}$	$^{+1.9}_{-1.7}$	4.0	N/A	3.9	1.9	2.0	$^{+14}_{-13}$	2.0	$^{+1.2}_{-0.84}$
1.6-1.76	$1.2 \cdot 10^4$	5.5	$^{+1.2}_{-1.1}$	$^{+11}_{-10}$	$^{+8.5}_{-7.4}$	$^{+4.3}_{-3.9}$	$^{+4.4}_{-4.2}$	$^{+29}_{-22}$	$^{+4.8}_{-4.3}$	$^{+2.6}_{-2.5}$	$^{+7.7}_{-6.8}$	$^{+0.78}_{-0.72}$	$^{+0.0}_{-0.05}$	$^{+1.9}_{-1.8}$	$^{+2.7}_{-2.6}$	3.0	N/A	3.4	0.15	2.0	14	2.0	$^{+1.1}_{-0.9}$
1.76-1.94	$5.6 \cdot 10^3$	4.4	$^{+0.55}_{-0.33}$	$^{+11}_{-10}$	$^{+8.0}_{-7.0}$	$^{+4.7}_{-3.9}$	$^{+5.1}_{-4.5}$	$^{+27}_{-21}$	$^{+5.3}_{-4.6}$	$^{+2.8}_{-2.4}$	$^{+8.2}_{-7.3}$	$^{+0.99}_{-0.93}$	$^{+0.14}_{-0.03}$	$^{+1.6}_{-1.2}$	$^{+4.0}_{-3.8}$	3.0	N/A	3.2	0.53	2.0	$^{+14}_{-12}$	2.0	$^{+1.0}_{-0.97}$
1.94-2.12	$2.4 \cdot 10^3$	4.2	$^{+0.18}_{-0.09}$	$^{+11}_{-10}$	$^{+6.9}_{-6.5}$	$^{+4.9}_{-4.2}$	$^{+4.5}_{-4.2}$	$^{+25}_{-20}$	$^{+5.0}_{-4.6}$	$^{+2.4}_{-2.3}$	$^{+8.2}_{-8.0}$	$^{+1.2}_{-1.1}$	$^{+0.08}_{-0.03}$	$^{+0.86}_{-0.7}$	$^{+4.6}_{-4.5}$	4.0	N/A	4.0	2.3	2.0	12	2.0	$^{+1.0}_{-0.99}$
2.12-2.33	$1.1 \cdot 10^3$	3.0	$^{+0.0}_{-0.06}$	11	$^{+6.3}_{-6.1}$	4.9	$^{+3.8}_{-3.9}$	$^{+22}_{-17}$	4.7	2.0	$^{+8.8}_{-8.2}$	$^{+1.4}_{-1.5}$	$^{+0.0}_{-0.07}$	$^{+0.28}_{-0.37}$	$^{+5.8}_{-5.6}$	4.0	N/A	3.8	1.6	2.0	$^{+13}_{-11}$	2.0	$^{+1.0}_{-0.99}$
2.33-2.55	$4.5 \cdot 10^2$	5.0	$^{+0.05}_{-0.09}$	$^{+11}_{-10}$	$^{+6.2}_{-5.7}$	$^{+5.7}_{-5.4}$	$^{+3.6}_{-3.4}$	$^{+20}_{-16}$	$^{+5.0}_{-4.6}$	$^{+2.2}_{-2.0}$	$^{+9.3}_{-8.4}$	$^{+2.2}_{-2.0}$	$^{+0.13}_{-0.09}$	$^{+0.23}_{-0.15}$	$^{+7.2}_{-6.6}$	0.6	N/A	0.61	0.0	2.0	$^{+12}_{-10}$	2.0	1.0
2.55-2.78	$1.9 \cdot 10^2$	7.7	0.05	$^{+11}_{-9.4}$	$^{+5.8}_{-5.2}$	$^{+6.3}_{-5.6}$	$^{+2.9}_{-2.6}$	$^{+19}_{-22}$	$^{+4.9}_{-4.4}$	$^{+2.1}_{-2.0}$	$^{+9.6}_{-8.7}$	$^{+2.6}_{-2.4}$	$^{+0.15}_{-0.05}$	$^{+0.14}_{-0.04}$	$^{+8.1}_{-7.5}$	0.0	N/A	0.0	0.0	2.0	$^{+10}_{-8.8}$	2.0	1.0
2.78-3.04	$7.3 \cdot 10^1$	9.7	0.03	$^{+12}_{-11}$	6.2	$^{+7.7}_{-7.3}$	2.6	20	5.3	2.0	$^{+11}_{-10}$	$^{+3.2}_{-3.0}$	$^{+0.15}_{-0.11}$	$^{+0.03}_{-0.0}$	$^{+9.9}_{-9.6}$	1.0	N/A	1.2	0.0	2.0	$^{+10}_{-9.3}$	2.0	1.0
3.04-3.61	$1.9 \cdot 10^1$	15	0.01	$^{+14}_{-12}$	$^{+7.6}_{-6.6}$	$^{+10}_{-8.9}$	$^{+2.9}_{-2.5}$	$^{+23}_{-18}$	$^{+6.4}_{-5.8}$	$^{+2.2}_{-1.8}$	$^{+14}_{-12}$	$^{+4.4}_{-4.0}$	$^{+0.2}_{-0.22}$	$^{+0.03}_{-0.05}$	$^{+14}_{-12}$	10	N/A	9.9	4.4	2.0	$^{+11}_{-10}$	2.0	1.0
3.61-5.04	$8.9 \cdot 10^{-1}$	38	0.0	$^{+15}_{-12}$	$^{+8.2}_{-7.3}$	$^{+14}_{-12}$	$^{+4.0}_{-3.6}$	$^{+29}_{-22}$	$^{+7.1}_{-6.4}$	$^{+2.5}_{-2.1}$	$^{+19}_{-16}$	$^{+6.7}_{-6.2}$	$^{+0.41}_{-0.37}$	$^{+0.02}_{-0.03}$	$^{+20}_{-17}$	9.0	N/A	9.2	1.6	2.0	$^{+12}_{-10}$	2.0	1.0

Table B.30: Measured dijet cross section for $R = 0.6$ and $3.0 < y^* < 3.5$. See Table B.15 for a description of the columns. This table is available on HEPDATA [187].

m_{12}-bin [TeV]	σ [pb/TeV]	δ_{stat} %	$\gamma6$	γ_{12}	γ_{18}	γ_{24}	γ_{30}	γ_{31}	γ_{37}	γ_{43}	γ_{49}	γ_{55}	γ_{61}	γ_{67}	γ_{73}	γ_{74}	γ_{75}	γ_{81}	γ_{82}	γ_{86}	u_1	u_2	u_3
1.76-1.94	$1.8 \cdot 10^4$	11	$^{+9.7}_{-8.4}$	$^{+18}_{-15}$	$^{+17}_{-15}$	$^{+6.0}_{-5.3}$	4.6	$^{+85}_{-42}$	$^{+5.4}_{-5.3}$	5.1	$^{+8.9}_{-9.0}$	$^{+0.26}_{-0.08}$	$^{+0.0}_{-0.02}$	$^{+5.4}_{-5.3}$	$^{+0.48}_{-0.24}$	8.0	N/A	8.3	0.71	2.1	$^{+32}_{-19}$	2.0	$^{+0.89}_{-1.1}$
1.94-2.12	$8.0 \cdot 10^3$	12	$^{+6.3}_{-5.0}$	$^{+15}_{-8.9}$	$^{+14}_{-7.8}$	4.3	$^{+3.5}_{-2.9}$	$^{+72}_{-32}$	$^{+5.0}_{-3.9}$	$^{+3.6}_{-3.0}$	$^{+8.2}_{-3.2}$	$^{+0.48}_{-0.18}$	$^{+0.1}_{-0.0}$	$^{+4.2}_{-3.1}$	$^{+0.99}_{-0.66}$	7.0	N/A	6.7	0.42	2.0	$^{+25}_{-10}$	2.0	$^{+2.5}_{-0.0}$
2.12-2.33	$3.4 \cdot 10^3$	19	$^{+4.3}_{-3.5}$	$^{+14}_{-7.0}$	$^{+11}_{-5.3}$	$^{+4.5}_{-3.8}$	$^{+4.3}_{-3.5}$	$^{+50}_{-25}$	$^{+5.4}_{-4.2}$	$^{+3.9}_{-3.0}$	$^{+8.0}_{-2.3}$	$^{+0.59}_{-0.26}$	$^{+0.12}_{-0.03}$	$^{+4.0}_{-3.0}$	$^{+1.8}_{-1.1}$	5.0	N/A	4.6	0.0	2.0	$^{+17}_{-9.5}$	2.0	$^{+1.5}_{-0.48}$
2.33-2.55	$1.2 \cdot 10^3$	9.7	$^{+2.6}_{-2.0}$	$^{+12}_{-28}$	$^{+9.5}_{-26}$	$^{+4.2}_{-2.9}$	$^{+4.0}_{-3.4}$	$^{+39}_{-41}$	$^{+4.8}_{-4.0}$	$^{+2.9}_{-2.5}$	$^{+7.6}_{-25}$	$^{+0.62}_{-0.43}$	$^{+0.06}_{-0.03}$	$^{+2.7}_{-2.3}$	$^{+2.2}_{-1.7}$	0.0	N/A	0.0	0.0	2.0	$^{+15}_{-31}$	2.0	$^{+1.1}_{-0.94}$
2.55-2.78	$4.8 \cdot 10^2$	8.0	$^{+1.5}_{-1.4}$	$^{+13}_{-22}$	$^{+10}_{-19}$	$^{+4.0}_{-3.9}$	$^{+4.4}_{-5.1}$	$^{+39}_{-36}$	$^{+4.9}_{-5.6}$	$^{+2.8}_{-3.1}$	$^{+8.8}_{-18}$	$^{+0.6}_{-0.84}$	$^{+0.02}_{-0.03}$	$^{+2.1}_{-2.3}$	$^{+2.8}_{-3.3}$	0.0	N/A	0.0	0.0	2.0	$^{+17}_{-25}$	2.0	$^{+1.0}_{-0.99}$
2.78-3.04	$2.0 \cdot 10^2$	8.4	$^{+0.65}_{-0.77}$	$^{+16}_{-12}$	$^{+11}_{-8.1}$	$^{+4.8}_{-4.9}$	$^{+6.6}_{-6.7}$	$^{+42}_{-28}$	$^{+6.8}_{-7.0}$	$^{+3.2}_{-3.7}$	$^{+12}_{-8.7}$	$^{+1.2}_{-1.6}$	$^{+0.01}_{-0.09}$	$^{+1.7}_{-2.3}$	$^{+4.7}_{-5.2}$	3.0	N/A	2.8	0.0	2.0	$^{+19}_{-13}$	2.0	$^{+1.0}_{-0.99}$
3.04-3.31	$8.0 \cdot 10^1$	13	0.21	$^{+16}_{-12}$	$^{+10}_{-7.4}$	$^{+5.5}_{-5.4}$	$^{+6.9}_{-6.2}$	$^{+42}_{-25}$	$^{+7.4}_{-6.7}$	$^{+3.6}_{-3.5}$	$^{+12}_{-9.3}$	$^{+2.0}_{-2.2}$	$^{+0.15}_{-0.09}$	$^{+1.5}_{-1.4}$	$^{+7.2}_{-6.6}$	5.0	N/A	4.6	0.0	2.0	$^{+16}_{-13}$	2.0	$^{+1.0}_{-0.99}$
3.31-3.93	$1.3 \cdot 10^1$	17	$^{+0.02}_{-0.0}$	$^{+17}_{-15}$	$^{+9.6}_{-8.8}$	6.4	6.2	$^{+37}_{-25}$	7.4	$^{+3.4}_{-3.3}$	$^{+13}_{-12}$	$^{+2.8}_{-2.7}$	0.12	$^{+0.84}_{-0.55}$	$^{+9.0}_{-9.3}$	5.0	N/A	5.4	0.0	2.0	$^{+17}_{-15}$	2.0	1.0
3.93-5.47	$1.7 \cdot 10^{-1}$	43	$^{+0.12}_{-0.14}$	$^{+24}_{-20}$	$^{+13}_{-11}$	$^{+11}_{-9.4}$	$^{+6.3}_{-5.6}$	$^{+37}_{-26}$	$^{+10}_{-9.5}$	$^{+3.7}_{-3.0}$	$^{+21}_{-18}$	$^{+5.3}_{-4.1}$	$^{+0.23}_{-0.32}$	$^{+0.0}_{-0.24}$	$^{+18}_{-16}$	20	N/A	16	8.7	2.0	$^{+22}_{-17}$	2.0	1.0

Table B.31: Measured dijet cross section for $R = 0.6$ and $3.5 < y^* < 4.0$. See Table B.15 for a description of the columns. This table is available on HEPDATA [187].

m_{12}-bin [TeV]	σ [pb/TeV]	δ_{stat} %	$\gamma6$	γ_{12}	γ_{18}	γ_{24}	γ_{30}	γ_{31}	γ_{37}	γ_{43}	γ_{49}	γ_{55}	γ_{61}	γ_{67}	γ_{73}	γ_{74}	γ_{75}	γ_{81}	γ_{82}	γ_{86}	u_1	u_2	u_3
2.55-3.04	$4.3 \cdot 10^2$	20	${}^{+9.5}_{-9.3}$	17	16	${}^{+4.2}_{-4.6}$	${}^{+4.2}_{-4.7}$	${}^{+98}_{-47}$	${}^{+5.5}_{-5.8}$	${}^{+5.1}_{-5.7}$	${}^{+8.3}_{-8.7}$	${}^{+0.14}_{-0.49}$	${}^{+0.01}_{-0.07}$	${}^{+5.6}_{-5.7}$	${}^{+0.5}_{-0.98}$	8.0	N/A	7.8	2.8	${}^{+2.1}_{-2.0}$	${}^{+27}_{-21}$	2.0	1.0
3.04-4.27	$2.8 \cdot 10^1$	19	${}^{+5.9}_{-2.4}$	${}^{+25}_{-16}$	${}^{+22}_{-14}$	${}^{+3.8}_{-2.0}$	${}^{+6.7}_{-7.1}$	${}^{+94}_{-36}$	${}^{+8.9}_{-8.0}$	${}^{+5.1}_{-4.1}$	${}^{+14}_{-12}$	${}^{+0.66}_{-0.86}$	${}^{+0.04}_{-0.15}$	${}^{+5.6}_{-5.0}$	${}^{+3.5}_{-2.3}$	10	N/A	9.7	0.0	2.0	${}^{+29}_{-18}$	2.0	1.0

Table B.32: Measured dijet cross section for $R = 0.6$ and $4.0 < y^* < 4.4$. See Table B.15 for a description of the columns. This table is available on HEPDATA [187].

REFERENCES

[1] E. Feng and J.E. Pilcher. Triggering ATLAS with Minimum Bias Trigger Scintillators. ATL-TILECAL-INT-2007-004, 2007. URL: https://cdsweb.cern.ch/record/1034461/.

[2] ATLAS Collaboration. Performance of the Minimum Bias Trigger in *pp* Collisions at $\sqrt{s} = 900$ GeV. ATLAS-CONF-2010-025, 2010. URL: http://atlas.web.cern.ch/Atlas/GROUPS/PHYSICS/CONFNOTES/ATLAS-CONF-2010-025/.

[3] ATLAS Collaboration. Performance of the ATLAS Trigger System in 2010. *Eur. Phys. J. C*, 72:1849, 2012. `doi:10.1140/epjc/s10052-011-1849-1`.

[4] ATLAS Collaboration. Performance of the Minimum Bias Trigger in *pp* Collisions at $\sqrt{s} = 7$ TeV. ATLAS-CONF-2010-068, 2010. URL: http://atlas.web.cern.ch/Atlas/GROUPS/PHYSICS/CONFNOTES/ATLAS-CONF-2010-068/.

[5] W. Bell, E. Feng, B. Heinemann, E. Nurse, P. Steinberg, and L. Tompkins. Offline Performance of the ATLAS Minimum Bias Trigger Scintillator Detector at $\sqrt{s} = 7$ TeV. ATL-COM-LUM-2010-033, 2010. URL: https://cdsweb.cern.ch/record/1309184.

[6] G. Aad et al. Readiness of the ATLAS Tile Calorimeter for LHC collisions. *Eur. Phys. J. C*, 70:1193–1236, 2010. `doi:10.1140/epjc/s10052-010-1508-y`.

[7] ATLAS Collaboration. Properties of Jets and Inputs to Jet Reconstruction and Calibration with the ATLAS Detector Using Proton-Proton Collisions at $\sqrt{s} = 7$ TeV. ATLAS-CONF-2010-053, 2010. URL: http://atlas.web.cern.ch/Atlas/GROUPS/PHYSICS/CONFNOTES/ATLAS-CONF-2010-053/.

[8] S. Kolos, E. Feng, and A. Iakovlev. Remote monitoring evaluation report. ATL-DQ-TR-0019, 2009. URL: https://edms.cern.ch/document/986115.

[9] S. Kolos, E. Alexandrov, E. Feng, R. Hauser, A. Iakovlev, and A. Zaytsev. Online remote monitoring facilities for the ATLAS experiment. *J. Phys. Conf. Ser.*, 331:022013, 2011. Proceedings of CHEP 2010, Taipei. `doi:10.1088/1742-6596/331/2/022013`.

[10] K. Koeneke et al. A new data format for the commissioning phase of the ATLAS detector. *J. Phys. Conf. Ser.*, 219(3):032047. Proceedings of CHEP 2009, Prague. `doi:10.1088/1742-6596/219/3/032047`.

[11] G. Choudalakis and E. Feng. Use of Tracks to Reconstruct Jets in Damaged Calorimeter Regions. ATL-PHYS-INT-2009-017, 2009. URL: https://cdsweb.cern.ch/record/1155161.

[12] L. Asquith et al. Performance of Jet Algorithms in the ATLAS Detector. ATL-PHYS-INT-2010-129, 2010. URL: https://cdsweb.cern.ch/record/1311867.

[13] G. Choudalakis, E. Feng, A. Messina, and L. Pribyl. In-Situ Jet Energy Scale Calibration Using Direct Photon+Jet Balance. ATL-PHYS-INT-2010-023, 2010. URL: https://cdsweb.cern.ch/record/1245511.

[14] ATLAS Collaboration. Jet energy measurement with the ATLAS detector in proton-proton collisions at $\sqrt{s} = 7$ TeV. 2011. Submitted to *Eur. Phys. J. C*. `arXiv:1112.6426`.

[15] ATLAS Collaboration. Determination of the ATLAS jet energy measurement uncertainty using photon-jet events in proton-proton collisions at $\sqrt{s} = 7$ TeV. ATLAS-CONF-2011-031, 2011. URL: https://atlas.web.cern.ch/Atlas/GROUPS/PHYSICS/CONFNOTES/ATLAS-CONF-2011-031/.

[16] N. Boelaert et al. ATLAS sensitivity to contact interactions and gravity mediated effects in large extra dimensions using dijet events at $\sqrt{s} = 7$ TeV. ATL-COM-PHYS-2010-136, 2010. URL: https://cdsweb.cern.ch/record/1248604.

[17] ATLAS Collaboration. Search for New Particles in Two-Jet Final States in 7 TeV Proton-Proton Collisions with the ATLAS Detector at the LHC. *Phys. Rev. Lett.*, 105:161801, 2010. `doi:10.1103/PhysRevLett.105.161801`.

[18] ATLAS Collaboration. Search for quark contact interactions in dijet angular distributions in pp collisions at $\sqrt{s} = 7$ TeV measured with the ATLAS detector. *Phys. Lett. B*, 694(4-5):327–345, 2011. `doi:10.1016/j.physletb.2010.10.021`.

[19] ATLAS Collaboration. Observation of a Centrality-Dependent Dijet Asymmetry in Lead-Lead Collisions at $\sqrt{s_{NN}} = 2.76$ TeV with the ATLAS Detector at the LHC. *Phys. Rev. Lett.*, 105:252303, 2010. `doi:10.1103/PhysRevLett.105.252303`.

[20] E. Feng et al. Observation of Energetic Jet Production in pp Collisions at $\sqrt{s} = 7$ TeV using the ATLAS Experiment at the LHC. 2010. Proceedings of PLHC 2010, DESY. `arXiv:1010.1974`.

[21] ATLAS Collaboration. Measurement of inclusive jet and dijet cross sections in proton-proton collisions at 7 TeV centre-of-mass energy with the ATLAS detector. *Eur. Phys. J. C*, 71:1512, 2011. `doi:10.1140/epjc/s10052-010-1512-2`.

[22] ATLAS Collaboration. Measurement of jet production in proton-proton collisions at 7 TeV centre-of-mass energy with the ATLAS detector. ATLAS-CONF-2010-050, 2010. URL: https://atlas.web.cern.ch/Atlas/GROUPS/PHYSICS/CONFNOTES/ATLAS-CONF-2010-050/.

[23] ATLAS Collaboration. Measurement of inclusive jet and dijet production in pp collisions at $\sqrt{s} = 7$ TeV using the ATLAS detector. 2011. Submitted to *Phys. Rev. D*. `arXiv:1112.6297`.

[24] ATLAS Collaboration. Measurement of inclusive jet and dijet cross sections in proton-proton collision data at 7 TeV centre-of-mass energy using the ATLAS detector. ATLAS-CONF-2011-047, 2011. URL: https://atlas.web.cern.ch/Atlas/GROUPS/PHYSICS/CONFNOTES/ATLAS-CONF-2011-047/.

[25] UA1 Collaboration. Angular distributions and structure functions from two-jet events at the CERN SPS $p\bar{p}$ collider. *Phys. Lett. B*, 136:294–300, 1984. `doi:10.1016/0370-2693(84)91164-X`.

[26] L3 Collaboration. Determination of α_s from jet multiplicities measured on the Z^0 resonance. *Phys. Lett. B*, 248:464–472, 1990. `doi:10.1016/0370-2693(90)90323-X`.

[27] UA2 Collaboration. Inclusive jet cross-section and a search for quark compositeness at the CERN $\bar{p}p$ collider. *Phys. Lett. B*, 257:232–240, 1991. `doi:10.1016/0370-2693(91)90887-V`.

[28] ZEUS Collaboration. Dijet photoproduction at HERA and the structure of the photon. *Eur. Phys. J. C*, 23:615–631, 2002. `doi:10.1007/s100520200936`.

[29] ZEUS Collaboration. Inclusive jet cross sections in the Breit frame in neutral current deep inelastic scattering at HERA and determination of α_s. *Phys. Lett. B*, 547:164–180, 2002. `doi:10.1016/S0370-2693(02)02763-6`.

[30] ALEPH Collaboration. Measurements of the strong coupling constant and the QCD colour factors using four-jet observables from hadronic Z decays. *Eur. Phys. J. C*, 27:1–17, 2003. `doi:10.1140/epjc/s2002-01114-2`.

[31] DELPHI Collaboration. Measurement of the energy dependence of hadronic jet rates and the strong coupling α_s from the four-jet rate with the DELPHI detector at LEP. *Eur. Phys. J. C*, 38:413–426, 2005. `doi:10.1140/epjc/s2004-02060-7`.

[32] ZEUS Collaboration. An NLO QCD analysis of inclusive cross-section and jet-production data from the ZEUS experiment. *Eur. Phys. J. C*, 42:1–16, 2005. `doi:10.1140/epjc/s2005-02293-x`.

[33] OPAL Collaboration. Measurement of the strong coupling α_s from four-jet observables in e^+e^- annihilation. *Eur. Phys. J. C*, 47:295–307, 2006. `doi:10.1140/epjc/s2006-02581-y`.

[34] CDF Collaboration. Measurement of the inclusive jet cross section using the k_T algorithm in $p\bar{p}$ collisions at $\sqrt{s} = 1.96$ TeV with the CDF II detector. *Phys. Rev. D*, 75:092006, 2007. `doi:10.1103/PhysRevD.75.092006`.

[35] D0 Collaboration. Measurement of the Inclusive Jet Cross Section in $p\bar{p}$ Collisions at $\sqrt{s}$ =1.96 TeV. *Phys. Rev. Lett.*, 101:062001, 2008. `doi:10.1103/PhysRevLett.101.062001`.

[36] CDF Collaboration. Measurement of the inclusive jet cross section at the Fermilab Tevatron $p\bar{p}$ collider using a cone-based jet algorithm. *Phys. Rev. D*, 78:052006, 2008. `doi:10.1103/PhysRevD.78.052006`.

[37] D0 Collaboration. Determination of the strong coupling constant from the inclusive jet cross section in $p\bar{p}$ collisions at $\sqrt{s} = 1.96$ TeV. *Phys. Rev. D*, 80:111107, 2009. `doi:10.1103/PhysRevD.80.111107`.

[38] D0 Collaboration. Measurement of Dijet Angular Distributions at $\sqrt{s} = 1.96$ TeV and Searches for Quark Compositeness and Extra Spatial Dimensions. *Phys. Rev. Lett.*, 103:191803, 2009. `doi:10.1103/PhysRevLett.103.191803`.

[39] H1 Collaboration. Jet production in *ep* collisions at low Q^2 and determination of α_s. *Eur. Phys. J. C*, 67:1–24, 2010. `doi:10.1140/epjc/s10052-010-1282-x`.

[40] H1 Collaboration. Jet production in *ep* collisions at high Q^2 and determination of α_s. *Eur. Phys. J. C*, 65:363–383, 2010. `doi:10.1140/epjc/s10052-009-1208-7`.

[41] ZEUS Collaboration. Inclusive-jet cross sections in NC DIS at HERA and a comparison of the k_T, anti-k_T and SIScone jet algorithms. *Phys. Lett. B*, 691:127–137, 2010. `doi:10.1016/j.physletb.2010.06.015`.

[42] D0 Collaboration. Measurement of the dijet invariant mass cross section in $p\bar{p}$ collisions at $\sqrt{s} = 1.96$ TeV. *Phys. Lett. B*, 693:531–538, 2010. `doi:10.1016/j.physletb.2010.09.013`.

[43] CMS Collaboration. Measurement of the Inclusive Jet Cross Section in *pp* Collisions at $\sqrt{s} = 7$ TeV. *Phys. Rev. Lett.*, 107:132001, 2011. `doi:10.1103/PhysRevLett.107.132001`.

[44] CMS Collaboration. Measurement of the differential dijet production cross section in proton-proton collisions at $\sqrt{s} = 7$ TeV. *Phys. Lett. B*, 700:187–206, 2011. `doi:10.1016/j.physletb.2011.05.027`.

[45] Particle Data Group. Review of Particle Physics. *J. Phys. G*, 37:075021, 2010. `doi:10.1088/0954-3899/37/7A/075021`.

[46] S.D. Ellis, J. Huston, K. Hatakeyama, P. Loch, and M. Tönnesmann. Jets in hadron-hadron collisions. *Prog. Part. Nucl. Phys.*, 60(2):484–551, 2008. `doi:10.1016/j.ppnp.2007.12.002`.

[47] A.D. Martin, W.J. Stirling, R.S. Thorne, and G. Watt. Parton distributions for the LHC. *Eur. Phys. J. C*, 63:189–285, 2009. `doi:10.1140/epjc/s10052-009-1072-5`.

[48] M. Gell-Mann. Symmetries of Baryons and Mesons. *Phys. Rev.*, 125:1067–1084, 1962. `doi:10.1103/PhysRev.125.1067`.

[49] O.W. Greenberg. Spin and Unitary-Spin Independence in a Paraquark Model of Baryons and Mesons. *Phys. Rev. Lett.*, 13:598–602, 1964. `doi:10.1103/PhysRevLett.13.598`.

[50] M.Y. Han and Y. Nambu. Three-Triplet Model with Double SU(3) Symmetry. *Phys. Rev.*, 139:B1006–B1010, 1965. `doi:10.1103/PhysRev.139.B1006`.

[51] E.D. Bloom et al. High-Energy Inelastic e-p Scattering at 6° and 10°. *Phys. Rev. Lett.*, 23:930–934, 1969. `doi:10.1103/PhysRevLett.23.930`.

[52] D.J. Gross and F. Wilczek. Ultraviolet Behavior of Non-Abelian Gauge Theories. *Phys. Rev. Lett.*, 30:1343–1346, 1973. `doi:10.1103/PhysRevLett.30.1343`.

[53] H.D. Politzer. Reliable Perturbative Results for Strong Interactions? *Phys. Rev. Lett.*, 30:1346–1349, 1973. `doi:10.1103/PhysRevLett.30.1346`.

[54] M.E. Peskin and D.V. Schroeder. *An Introduction to Quantum Field Theory.* Addison-Wesley, Reading, 1995.

[55] S. Bethke. The 2009 world average of α_{s}. *Eur. Phys. J. C*, 64:689–703, 2009. `doi:10.1140/epjc/s10052-009-1173-1`.

[56] T. Sjöstrand. A model for initial state parton showers. *Phys. Lett. B*, 157(4):321 – 325, 1985. `doi:10.1016/0370-2693(85)90674-4`.

[57] R.K. Ellis, W.J. Stirling, and B.R. Webber. *QCD and Collider Physics.* Cambridge University Press, Cambridge, 2003.

[58] V.V. Sudakov. Vertex parts at very high-energies in quantum electrodynamics. *Sov. Phys. JETP*, 3:65–71, 1956.

[59] P.Z. Skands. Tuning Monte Carlo generators: The Perugia tunes. *Phys. Rev. D*, 82:074018, 2010. `doi:10.1103/PhysRevD.82.074018`.

[60] ATLAS Collaboration. New ATLAS event generator tunes to 2010 data. ATL-PHYS-PUB-2011-008, 2011. URL: https://cdsweb.cern.ch/record/1345343.

[61] ATLAS Collaboration. ATLAS tunes of PYTHIA 6 and PYTHIA 8 for MC11. ATL-PHYS-PUB-2011-009, 2011. URL: https://cdsweb.cern.ch/record/1363300.

[62] ATLAS Collaboration. Charged particle multiplicities in pp interactions at $\sqrt{s} =$ 0.9 and 7 TeV in a diffractive limited phase-space measured with the ATLAS detector at the LHC and new PYTHIA 6 tune. ATLAS-CONF-2010-031, 2010. URL: http://cdsweb.cern.ch/record/1277665.

[63] ATLAS Collaboration. First tuning of HERWIG/JIMMY to ATLAS data. ATL-PHYS-PUB-2010-014, 2010. URL: https://cdsweb.cern.ch/record/1303025.

[64] T. Sjöstrand, S. Mrenna, and P.Z. Skands. PYTHIA 6.4 physics and manual. *JHEP*, 0605:026, 2006. `doi:10.1088/1126-6708/2006/05/026`.

[65] G. Corcella et al. HERWIG 6: An event generator for hadron emission reactions with interfering gluons (including supersymmetric processes). *JHEP*, 01:010, 2001. `doi:10.1088/1126-6708/2001/01/010`.

[66] R.P. Feynman. Very High-Energy Collisions of Hadrons. *Phys. Rev. Lett.*, 23:1415–1417, 1969. `doi:10.1103/PhysRevLett.23.1415`.

[67] V.N. Gribov and L.N. Lipatov. Deep inelastic e-p scattering in perturbation theory. *Sov. J. Nucl. Phys.*, 15:438–450, 1972.

[68] G. Altarelli and G. Parisi. Asymptotic freedom in parton language. *Nucl. Phys. B*, 126:298, 1977. `doi:10.1016/0550-3213(77)90384-4`.

[69] Y.L. Dokshitzer. Calculation of the Structure Functions for Deep Inelastic Scattering and e^+e^- Annihilation by Perturbation Theory in Quantum Chromodynamics. *Sov. Phys. JETP*, 46:641–653, 1977.

[70] C.M. Buttar et al. The Underlying Event. 2005. URL: https://cdsweb.cern.ch/record/941461/.

[71] B. Flaugher and K. Meier. A Compilation of Jet Finding Algorithms. FERMILAB-Conf-90-248-E, 1990. URL: http://lss.fnal.gov/archive/preprint/fermilab-conf-90-248-e.shtml.

[72] M. Cacciari, G.P. Salam, and G. Soyez. The anti-k_t jet clustering algorithm. *JHEP*, 0804:063, 2008. `doi:10.1088/1126-6708/2008/04/063`.

[73] M. Cacciari, G.P. Salam, and G. Soyez. FastJet user manual. 2011. `arXiv:1111.6097`.

[74] J.E. Huth et al. Toward a standardization of jet definitions. FERMILAB-Conf-90-249-E, 1990. URL: http://lss.fnal.gov/archive/preprint/fermilab-conf-90-249-e.shtml.

[75] Y.L. Dokshitzer, G.D. Leder, S. Moretti, and B.R. Webber. Better jet clustering algorithms. *JHEP*, 9708:001, 1997. `doi:10.1088/1126-6708/1997/08/001`.

[76] M. Wobisch and T. Wengler. Hadronization corrections to jet cross sections in deep-inelastic scattering. 1998. `arXiv:hep-ph/9907280`.

[77] S. Catani, Y.L. Dokshitzer, M.H. Seymour, and B.R. Webber. Longitudinally-invariant $k_\perp$-clustering algorithms for hadron-hadron collisions. *Nucl. Phys. B*, 406:187–224, 1993. `doi:10.1016/0550-3213(93)90166-M`.

[78] S.D. Ellis and D.E. Soper. Successive combination jet algorithm for hadron collisions. *Phys. Rev. D*, 48:3160–3166, 1993. `doi:10.1103/PhysRevD.48.3160`.

[79] G.P. Salam and G. Soyez. A Practical Seedless Infrared-Safe Cone jet algorithm. *JHEP*, 0705:086, 2007. `doi:10.1088/1126-6708/2007/05/086`.

[80] C. Buttar et al. Standard Model Handles and Candles Working Group: Tools and Jets Summary Report, 2008. `arXiv:0803.0678`.

[81] L. Evans and P. Bryant. LHC Machine. *JINST*, 3:S08001, 2008. `doi:10.1088/1748-0221/3/08/S08001`.

[82] O.S. Brüning et al. LHC Design Report, Vol. 1: The LHC Main Ring. CERN-2004-003-V-1, 2004. URL: http://cdsweb.cern.ch/record/782076.

[83] O.S. Brüning et al. LHC Design Report, Vol. 2: The LHC Infrastructure and General Services. CERN-2004-003-V-2, 2004. URL: http://cdsweb.cern.ch/record/815187.

[84] M. Benedikt et al. LHC Design Report, Vol. 3: The LHC Injector Chain. CERN-2004-003-V-3, 2004. URL: http://cdsweb.cern.ch/record/823808.

[85] M. Bajko et al. Report of the Task Force on the Incident of 19th September 2008 at the LHC. CERN-LHC-PROJECT-Report-1168, 2009. URL: http://cdsweb.cern.ch/record/1168025.

[86] LEP. LEP Design Report, Vol. 1: The LEP injector chain. CERN-LEP-TH-83-29, CERN-PS-DL-83-31, CERN-SPS-83-26, 1983. URL: https://cdsweb.cern.ch/record/98881.

[87] LEP. LEP Design Report, Vol. 2: The LEP main ring. CERN-LEP-84-01, 1984. URL: https://cdsweb.cern.ch/record/102083.

[88] M. Ferro-Luzzi. LHC 2010 Operation — As Viewed From The Experiments. Proceedings of the Chamonix 2011 LHC Performance Workshop. URL: https://espace.cern.ch/acc-tec-sector/Chamonix/Chamx2011/papers/MFL_1_01.pdf.

[89] ATLAS Collaboration. The ATLAS Experiment at the CERN Large Hadron Collider. *JINST*, 3:S08003, 2008. `doi:10.1088/1748-0221/3/08/S08003`.

[90] ATLAS Collaboration. ATLAS Inner Detector: Technical Design Report, 1. ATLAS-TDR-004, CERN-LHCC-97-016, 1997. URL: http://cdsweb.cern.ch/record/331063.

[91] ATLAS Collaboration. ATLAS Inner Detector: Technical Design Report, 2. ATLAS-TDR-005, CERN-LHCC-97-017, 1997. URL: http://cdsweb.cern.ch/record/331064.

[92] ATLAS Collaboration. ATLAS Central Solenoid: Technical Design Report. ATLAS-TDR-009, CERN-LHCC-97-021, 1997. URL: http://cdsweb.cern.ch/record/331067.

[93] A. Yamamoto et al. The ATLAS central solenoid. *Nucl. Instrum. Meth. A*, 584(1):53–74, 2008. `doi:10.1016/j.nima.2007.09.047`.

[94] ATLAS Collaboration. ATLAS Liquid-argon Calorimeter: Technical Design Report. ATLAS-TDR-002, CERN-LHCC-96-041, 1996. URL: http://cdsweb.cern.ch/record/331061.

[95] ATLAS Collaboration. ATLAS Tile Calorimeter: Technical Design Report. ATLAS-TDR-003, CERN-LHCC-96-042, 1996. URL: http://cdsweb.cern.ch/record/331062.

[96] ATLAS Collaboration. ATLAS Muon Spectrometer: Technical Design Report. ATLAS-TDR-010, CERN-LHCC-97-022, 1997. URL: http://cdsweb.cern.ch/record/331068.

[97] ATLAS Collaboration. ATLAS Barrel Toroid: Technical Design Report. ATLAS-TDR-007, CERN-LHCC-97-019, 1997. URL: http://cdsweb.cern.ch/record/331065.

[98] ATLAS Collaboration. ATLAS End-cap Toroids: Technical Design Report. ATLAS-TDR-008, CERN-LHCC-97-020, 1997. URL: http://cdsweb.cern.ch/record/331066.

[99] ATLAS Collaboration. Charged-particle multiplicities in *pp* interactions measured with the ATLAS detector at the LHC. *New J. Phys.*, 13:053033, 2011. `doi:10.1088/1367-2630/13/5/053033`.

[100] ATLAS Collaboration. ATLAS Pixel Detector: Technical Design Report. ATLAS-TDR-011, CERN-LHCC-98-013, 1998. URL: https://cdsweb.cern.ch/record/381263.

[101] I. Peric et al. The FEI3 readout chip for the ATLAS pixel detector. *Nucl. Instrum. Meth. A*, 565(1):178–187, 2006. `doi:10.1016/j.nima.2006.05.032`.

[102] J.N. Jackson et al. The ATLAS semiconductor tracker (SCT). *Nucl. Instrum. Meth. A*, 541(1-2):89–95, 2005. `doi:10.1016/j.nima.2005.01.043`.

[103] F. Campabadal et al. Design and performance of the ABCD3TA ASIC for readout of silicon strip detectors in the ATLAS semiconductor tracker. *Nucl. Instrum. Meth. A*, 552(3):292–328, 2005. `doi:10.1016/j.nima.2005.07.002`.

[104] E. Abat et al. The ATLAS TRT barrel detector. *JINST*, 3:P02014, 2008. `doi:10.1088/1748-0221/3/02/P02014`.

[105] E. Abat et al. The ATLAS TRT end-cap detectors. *JINST*, 3:P10003, 2008. `doi:10.1088/1748-0221/3/10/P10003`.

[106] R. Wigmans. *Calorimetry: Energy Measurement in Particle Physics.* Oxford University Press, New York, 2000.

[107] ATLAS Collaboration. Expected Performance of the ATLAS Experiment - Detector, Trigger and Physics. 2009. `arXiv:0901.0512`.

[108] E. Abat et al. Combined performance studies for electrons at the 2004 ATLAS combined test-beam. *JINST*, 5:P11006, 2010. `doi:10.1088/1748-0221/5/11/P11006`.

[109] M. Aharrouche et al. Measurement of the response of the ATLAS liquid argon barrel calorimeter to electrons at the 2004 combined test-beam. *Nucl. Instrum. Meth. A*, 614(3):400–432, 2010. `doi:10.1016/j.nima.2009.12.055`.

[110] M. Aharrouche et al. Response uniformity of the ATLAS liquid argon electromagnetic calorimeter. *Nucl. Instrum. Meth. A*, 582(2):429–455, 2007. `doi:10.1016/j.nima.2007.08.157`.

[111] M. Aharrouche et al. Energy linearity and resolution of the ATLAS electromagnetic barrel calorimeter in an electron test-beam. *Nucl. Instrum. Meth. A*, 568(2):601–623, 2006. `doi:10.1016/j.nima.2006.07.053`.

[112] J. Pinfold et al. Performance of the ATLAS liquid argon endcap calorimeter in the pseudorapidity region $2.5 < |\eta| < 4.0$ in beam tests. *Nucl. Instrum. Meth. A*, 593(3):324 – 342, 2008. `doi:10.1016/j.nima.2008.05.033`.

[113] C. Cojocaru et al. Hadronic calibration of the ATLAS liquid argon end-cap calorimeter in the pseudorapidity region $1.6 < |\eta| < 1.8$ in beam tests. *Nucl. Instrum. Meth. A*, 531(3):481–514, 2004. `doi:10.1016/j.nima.2004.05.133`.

[114] P. Adragna et al. Measurement of pion and proton response and longitudinal shower profiles up to 20 nuclear interaction lengths with the ATLAS Tile calorimeter. *Nucl. Instr. Meth. A*, 615(2):158–181, 2010. `doi:10.1016/j.nima.2010.01.037`.

[115] P. Adragna et al. Testbeam studies of production modules of the ATLAS Tile Calorimeter. *Nucl. Instrum. Meth. A*, 606(3):362–394, 2009. `doi:10.1016/j.nima.2009.04.009`.

[116] E. Abat et al. Response and Shower Topology of 2 to 180 GeV Pions Measured with the ATLAS Barrel Calorimeter at the CERN Test-beam and Comparison to Monte Carlo Simulations. ATL-CAL-PUB-2010-001, 2010. URL: https://cdsweb.cern.ch/record/1263861.

[117] M. Aharrouche et al. Study of the response of ATLAS electromagnetic liquid argon calorimeters to muons. *Nucl. Instrum. Meth. A*, 606(3):419–431, 2009. `doi:10.1016/j.nima.2009.05.021`.

[118] G. Aad et al. Drift Time Measurement in the ATLAS Liquid Argon Electromagnetic Calorimeter using Cosmic Muons. *Eur. Phys. J. C*, 70:755–785, 2010. `doi:10.1140/epjc/s10052-010-1403-6`.

[119] ATLAS Collaboration. Readiness of the ATLAS liquid argon calorimeter for LHC collisions. *Eur. Phys. J. C*, 70:723–753, 2010. `doi:10.1140/epjc/s10052-010-1354-y`.

[120] W.E. Cleland and E.G. Stern. Signal processing considerations for liquid ionization calorimeters in a high rate environment. *Nucl. Instrum. Meth. A*, 338(23):467–497, 1994. `doi:10.1016/0168-9002(94)91332-3`.

[121] A. Artamonov et al. The ATLAS Forward Calorimeter. *JINST*, 3:P02010, 2008. `doi:10.1088/1748-0221/3/02/P02010`.

[122] G. Aad et al. Commissioning of the ATLAS Muon Spectrometer with cosmic rays. *Eur. Phys. J. C*, 70:875–916. `doi:10.1140/epjc/s10052-010-1415-2`.

[123] V. Cindro et al. The ATLAS Beam Conditions Monitor. *JINST*, 3:P02004, 2008. `doi:10.1088/1748-0221/3/02/P02004`.

[124] ATLAS Collaboration. ATLAS Forward Detectors for Measurement of Elastic Scattering and Luminosity. ATLAS-TDR-018, CERN-LHCC-2008-004, 2008. URL: https://cdsweb.cern.ch/record/1095847.

[125] S. van der Meer. Calibration of the effective beam height in the ISR. CERN-ISR-PO-68-31, 1968. URL: https://cdsweb.cern.ch/record/296752.

[126] ATLAS Collaboration. ATLAS Level-1 Trigger: Technical Design Report. ATLAS-TDR-012, CERN-LHCC-98-014, 1998. URL: https://cdsweb.cern.ch/record/381429.

[127] M. Grothe et al. Architecture of the ATLAS high level trigger event selection software. *Nucl. Instrum. Meth. A*, 518:537–541, 2004. `doi:10.1016/j.nima.2003.11.079`.

[128] ATLAS Collaboration. ATLAS High-Level Trigger, Data-Acquisition and Controls: Technical Design Report. ATLAS-TDR-016, CERN-LHCC-2003-022, 2003. URL: https://cdsweb.cern.ch/record/616089.

[129] S. Ask et al. The ATLAS central level-1 trigger logic and TTC system. *JINST*, 3:P08002, 2008. `doi:10.1088/1748-0221/3/08/P08002`.

[130] S. Agostinelli et al. GEANT4: A simulation toolkit. *Nucl. Instrum. Meth. A*, 506:250–303, 2003. `doi:10.1016/S0168-9002(03)01368-8`.

[131] ATLAS Collaboration. The ATLAS Simulation Infrastructure. *Eur. Phys. J. C*, 70:823–874, 2010. `doi:10.1140/epjc/s10052-010-1429-9`.

[132] G. Folger and J.P. Wellisch. String parton models in GEANT4. *eConf*, C0303241:MOMT007, 2003. `arXiv:nucl-th/0306007`.

[133] H.W. Bertini. Intranuclear Cascade Calculation of the Secondary Nucleon Spectra from Nucleon-Nucleus Interactions in the Energy Range 340 to 2900 MeV and Comparisons with Experiment. *Phys. Rev.*, 188:1711–1730, 1969. `doi:10.1103/PhysRev.188.1711`.

[134] ATLAS Collaboration. The ATLAS Inner Detector commissioning and calibration. *Eur. Phys. J. C*, 70:787–821, 2010. `doi:10.1140/epjc/s10052-010-1366-7`.

[135] ATLAS Collaboration. A measurement of the material in the ATLAS inner detector using secondary hadronic interactions. *JINST*, 7:P01013, 2012. `doi:10.1088/1748-0221/7/01/P01013`.

[136] ATLAS Collaboration. Photon Conversions at $\sqrt{s} = 900$ GeV measured with the ATLAS Detector. ATLAS-CONF-2010-007, 2010. URL: http://atlas.web.cern.ch/Atlas/GROUPS/PHYSICS/CONFNOTES/ATLAS-CONF-2010-007/.

[137] ATLAS Collaboration. ATLAS Calorimeter Response to Single Isolated Hadrons and Estimation of the Calorimeter Jet Scale Uncertainty. ATLAS-CONF-2011-028, 2011. URL: http://cdsweb.cern.ch/record/1337075.

[138] ATLAS Collaboration. Performance of Missing Transverse Momentum Reconstruction in Proton-Proton Collisions at 7 TeV with ATLAS. *Eur. Phys. J. C*, 72:1844, 2012. `doi:10.1140/epjc/s10052-011-1844-6`.

[139] F. Bergsma. Calibration of Hall sensors in three dimensions. 2003. Proceedings of the 13th International Magnetic Measurement Workshop, SLAC. URL: https://cdsweb.cern.ch/record/1072471.

[140] I.I. Rabi, J.R. Zacharias, S. Millman, and P. Kusch. A New Method of Measuring the Nuclear Magnetic Moment. *Phys. Rev.*, 53:318–318, 1938. `doi:10.1103/PhysRev.53.318`.

[141] M. Aleksa et al. Measurement of the ATLAS solenoid magnetic field. *JINST*, 3:P04003, 2008. `doi:10.1088/1748-0221/3/04/P04003`.

[142] A. Sherstnev and R.S. Thorne. Different PDF approximations useful for LO Monte Carlo generators, 2008. `arXiv:0807.2132`.

[143] J.M. Butterworth, J.R. Forshaw, and M.H. Seymour. Multiparton interactions in photoproduction at HERA. *Z. Phys. C*, 72:637–646, 1996. `doi:10.1007/s002880050286`.

[144] M. Bahr et al. Herwig++ Physics and Manual. *Eur. Phys. J. C*, 58:639–707, 2008. `doi:10.1140/epjc/s10052-008-0798-9`.

[145] Z. Nagy. Next-to-leading order calculation of three jet observables in hadron hadron collision. *Phys. Rev. D*, 68:094002, 2003. `doi:10.1103/PhysRevD.68.094002`.

[146] S. Alioli, K. Hamilton, P. Nason, C. Oleari, and E. Re. Jet pair production in POWHEG. *JHEP*, 04:081, 2011. `doi:10.1007/JHEP04(2011)081`.

[147] P. Nason. MINT: a Computer Program for Adaptive Monte Carlo Integration and Generation of Unweighted Distributions, 2007. `arXiv:0709.2085`.

[148] H.-L. Lai et al. New parton distributions for collider physics. *Phys. Rev. D*, 82:074024, 2010. `doi:10.1103/PhysRevD.82.074024`.

[149] S.D. Ellis, Z. Kunszt, and D.E. Soper. Two jet production in hadron collisions at order α_s^3 in QCD. *Phys. Rev. Lett.*, 69:1496–1499, 1992. `doi:10.1103/PhysRevLett.69.1496`.

[150] R.D. Ball et al. A first unbiased global NLO determination of parton distributions and their uncertainties. *Nucl. Phys. B*, 838:136–206, 2010. `doi:10.1016/j.nuclphysb.2010.05.008`.

[151] S. Forte, E. Laenen, P. Nason, and J. Rojo. Heavy quarks in deep-inelastic scattering. *Nucl. Phys. B*, 834:116–162, 2010. `doi:10.1016/j.nuclphysb.2010.03.014`.

[152] H1 and ZEUS Collaborations. HERAPDF 1.5. H1prelim-10-142, ZEUS-prel-10-018. URL: https://www.desy.de/h1zeus/combined_results/index.php?do=proton_structure.

[153] T. Carli et al. A posteriori inclusion of parton density functions in NLO QCD final-state calculations at hadron colliders: The APPLGRID Project. *Eur. Phys. J. C*, 66:503–524, 2010. `doi:10.1140/epjc/s10052-010-1255-0`.

[154] H.-L. Lai et al. Uncertainty induced by QCD coupling in the CTEQ global analysis of parton distributions. *Phys. Rev. D*, 82:054021, 2010. `doi:10.1103/PhysRevD.82.054021`.

[155] S. Moretti, M.R. Nolten, and D.A. Ross. Weak corrections to four-parton processes. *Nucl. Phys. B*, 759:50–82, 2006. `doi:10.1016/j.nuclphysb.2006.09.028`.

[156] P. Nason. A new method for combining NLO QCD with shower Monte Carlo algorithms. *JHEP*, 11:040, 2004. `doi:10.1088/1126-6708/2004/11/040`.

[157] S. Frixione, P. Nason, and C. Oleari. Matching NLO QCD computations with Parton Shower simulations: the POWHEG method. *JHEP*, 11:070, 2007. `doi:10.1088/1126-6708/2007/11/070`.

[158] S. Alioli, P. Nason, C. Oleari, and E. Re. A general framework for implementing NLO calculations in shower Monte Carlo programs: the POWHEG BOX. *JHEP*, 1006:043, 2010. `doi:10.1007/JHEP06(2010)043`.

[159] W Lampl et al. Calorimeter Clustering Algorithms: Description and Performance. ATLAS-LARG-PUB-2008-002, 2008. URL: https://cdsweb.cern.ch/record/1099735.

[160] ATLAS Collaboration. In-situ jet energy scale and jet shape corrections for multiple interactions in the first ATLAS data at the LHC. ATLAS-CONF-2011-030, 2011. URL: https://atlas.web.cern.ch/Atlas/GROUPS/PHYSICS/CONFNOTES/ATLAS-CONF-2011-030/.

[161] S. Frixione and G. Ridolfi. Jet photoproduction at HERA. *Nucl. Phys. B*, 507:315–333, 1997. `doi:10.1016/S0550-3213(97)00575-0`.

[162] ATLAS Collaboration. Charged-particle multiplicities in pp interactions at $\sqrt{s} =$ 900 GeV measured with the ATLAS detector at the LHC. *Phys. Lett. B*, 688:21–42, 2010. `doi:10.1016/j.physletb.2010.03.064`.

[163] V. Lendermann et al. Combining Triggers in HEP Data Analysis. *Nucl. Instrum. Meth. A*, 604:707–718, 2009. `doi:10.1016/j.nima.2009.03.173`.

[164] ATLAS Collaboration. Data-Quality Requirements and Event Cleaning for Jets and Missing Transverse Energy Reconstruction with the ATLAS Detector in Proton-Proton Collisions at a Center-of-Mass Energy of $\sqrt{s} = 7$ TeV. ATLAS-CONF-2010-038, 2010. URL: https://atlas.web.cern.ch/Atlas/GROUPS/PHYSICS/CONFNOTES/ATLAS-CONF-2010-038/.

[165] ATLAS Collaboration. Updated Luminosity Determination in pp Collisions at $\sqrt{s} = 7$ TeV using the ATLAS Detector. ATLAS-CONF-2011-011, 2011. URL: http://cdsweb.cern.ch/record/1334563.

[166] ATLAS Collaboration. Luminosity Determination in pp Collisions at $\sqrt{s} = 7$ TeV Using the ATLAS Detector at the LHC. *Eur. Phys. J. C*, 71:1630, 2011. `doi:10.1140/epjc/s10052-011-1630-5`.

[167] G. Anders et al. LHC Bunch Current Normalisation for the April-May 2010 Luminosity Calibration Measurements. CERN-ATS-Note-2011-004, 2011. URL: https://cdsweb.cern.ch/record/1325370.

[168] A. Alice et al. LHC Bunch Current Normalisation for the October 2010 Luminosity Calibration Measurements. CERN-ATS-Note-2011-016, 2011. URL: https://cdsweb.cern.ch/record/1333997.

[169] L. Lyons, D. Gibaut, and P. Clifford. How to combine correlated estimates of a single physical quantity. *Nucl. Instrum. Meth. A*, 270:110, 1988. `doi:10.1016/0168-9002(88)90018-6`.

[170] A. Valassi. Combining correlated measurements of several different physical quantities. *Nucl. Instrum. Meth. A*, 500:391, 2003. `doi:10.1016/S0168-9002(03)00329-2`.

[171] B. Malaescu. An iterative, dynamically stabilized method of data unfolding, 2009. `arXiv:0907.3791`.

[172] G. D'Agostini. A multidimensional unfolding method based on Bayes' theorem. *Nucl. Instrum. Meth. A*, 362:487–498, 1995. `doi:10.1016/0168-9002(95)00274-X`.

[173] ATLAS Collaboration. ATLAS Calorimeter Response to Single Isolated Hadrons and Estimation of the Calorimeter Jet Scale Uncertainty. ATLAS-CONF-2010-052, 2010. URL: http://cdsweb.cern.ch/record/1281309.

[174] ATLAS Collaboration. In-situ pseudorapidity intercalibration for evaluation of jet energy scale uncertainty using dijet events in proton-proton collisions at $\sqrt{s} = 7$ TeV. ATLAS-CONF-2011-014, 2011. URL: https://atlas.web.cern.ch/Atlas/GROUPS/PHYSICS/CONFNOTES/ATLAS-CONF-2011-014/.

[175] ATLAS Collaboration. Jet energy scale and its systematic uncertainty in proton-proton collisions at $\sqrt{s} = 7$ TeV in ATLAS 2010 data. ATLAS-CONF-2011-032, 2011. URL: https://atlas.web.cern.ch/Atlas/GROUPS/PHYSICS/CONFNOTES/ATLAS-CONF-2011-032/.

[176] E. Khramov et al. Study of the Response of the Hadronic Barrel Calorimeter in the ATLAS Combined Test-beam to Pions of Energies from 20 to 350 GeV for Beam Impact Points from 0.2 to 0.65. ATL-TILECAL-PUB-2009-007, 2009. URL: http://cdsweb.cern.ch/record/1172156.

[177] ATLAS Collaboration. Response of isolated particles identified using resonances in proton-proton collisions at $\sqrt{s} = 7$ TeV with the ATLAS detector. ATLAS-CONF-2011-019, 2011. URL: https://atlas.web.cern.ch/Atlas/GROUPS/PHYSICS/CONFNOTES/ATLAS-CONF-2011-019/.

[178] ATLAS Collaboration. Electron performance measurements with the ATLAS detector using the 2010 LHC proton-proton collision data. 2011. Submitted to *Eur. Phys. J. C*. `arXiv:1110.3174`.

[179] ATLAS Collaboration. Validation of the ATLAS jet energy measurement uncertainties using tracks in proton-proton collisions at $\sqrt{s} = 7$ TeV. ATLAS-CONF-2011-067, 2011. URL: https://atlas.web.cern.ch/Atlas/GROUPS/PHYSICS/CONFNOTES/ATLAS-CONF-2011-067/.

[180] ATLAS Collaboration. Probing the jet energy measurement at the TeV-scale with the multi-jet balance technique in proton-proton collisions at $\sqrt{s} = 7$ TeV with the ATLAS detector. ATLAS-CONF-2011-029, 2011. URL: https://atlas.web.cern.ch/Atlas/GROUPS/PHYSICS/CONFNOTES/ATLAS-CONF-2011-029/.

[181] ATLAS Collaboration. Measurement of the jet fragmentation function and transverse profile in proton-proton collisions at a center-of-mass energy of 7 TeV with the ATLAS detector. *Eur. Phys. J. C*, 71:1795, 2011. `doi:10.1140/epjc/s10052-011-1795-y`.

[182] ATLAS Collaboration. Measurement of the inclusive isolated prompt photon cross section in pp collisions at $\sqrt{s} = 7$ TeV with the ATLAS detector. *Phys. Rev. D*, 83:052005, 2011. `doi:10.1103/PhysRevD.83.052005`.

[183] ATLAS Collaboration. Jet energy resolution and reconstruction efficiencies from in-situ techniqes with the ATLAS Detector using proton-proton collisions at a center-of-mass energy $\sqrt{s} = 7$ TeV. ATLAS-CONF-2010-054, 2010. URL: https://atlas.web.cern.ch/Atlas/GROUPS/PHYSICS/CONFNOTES/ATLAS-CONF-2010-054/.

[184] A. Höcker and V. Kartvelishvili. SVD approach to data unfolding. *Nucl. Instrum. Meth. A*, 372:469–481, 1996. `doi:10.1016/0168-9002(95)01478-0`.

[185] K. Tackmann, A. Höcker, and H. Lacker. TSVDUnfold: SVD Approach to Data Unfolding, 2010. URL: http://root.cern.ch/root/html/TSVDUnfold.html.

[186] ATLAS Collaboration. Study of Jet Shapes in Inclusive Jet Production in pp Collisions at $\sqrt{s} = 7$ TeV using the ATLAS Detector. *Phys. Rev. D*, 83:052003, 2011. `doi:10.1103/PhysRevD.83.052003`.

[187] ATLAS Collaboration. Measurement of inclusive jet and dijet production in pp collisions at $\sqrt{s} = 7$ TeV using the ATLAS detector, 2011. HEPDATA. URL: http://hepdata.cedar.ac.uk/view/irn9320911.